

Dissertation
submitted to the
Combined Faculty of Natural Sciences and Mathematics
of the Ruperto Carola University Heidelberg, Germany
for the degree of
Doctor of Natural Sciences

Presented by
Paul Gerald Layague Sanchez
born in Mandaluyong, Philippines

Oral examination: 4th of December 2020

**Entrainment of coupled, phase-shifted signaling
oscillations in the presomitic mesoderm**

Referees:

Dr. Justin Crocker

Prof. Dr. Ulrich Schwarz

Joint PhD between EMBL and the University of Heidelberg

European Molecular Biology Laboratory (EMBL)
Developmental Biology Unit
Timing in Embryonic Development Group

Developmental Biology and Dynamical Systems Theory

Entrainment of coupled, phase-shifted signaling oscillations in the presomitic mesoderm

Paul Gerald Layague Sanchez

<i>First Examiner (Erstgutachter)</i>	Justin Crocker Developmental Biology Unit European Molecular Biology Laboratory (EMBL)
<i>Second Examiner (Zweitgutachter)</i>	Ulrich Schwarz Institute for Theoretical Physics University of Heidelberg
<i>Member (Mitglied)</i>	Lars Hufnagel Cell Biology and Biophysics Unit, EMBL currently with Luxendo GmbH, Bruker
<i>Member (Mitglied)</i>	Nicholas S. Foulkes Institute of Biological and Chemical Systems Karlsruhe Institute of Technology
<i>Supervisor</i>	Alexander Aulehla

December 2020

Paul Gerald Layague Sanchez

Entrainment of coupled, phase-shifted signaling oscillations in the presomitic mesoderm

Developmental Biology and Dynamical Systems Theory, December 2020

Examiners (Gutachter): Justin Crocker and Ulrich Schwarz

Members (Mitglied): Lars Hufnagel and Nicholas S. Foulkes

Supervisor: Alexander Aulehla

Joint PhD between EMBL and the University of Heidelberg

Timing in Embryonic Development Group

Developmental Biology Unit

European Molecular Biology Laboratory (EMBL)

Meyerhofstrasse 1

69117 Heidelberg, Germany

Summary

Synchronization is everywhere in nature. It is an emergent property arising in systems of interacting oscillatory entities, regardless if these entities are physical (e.g. in an electrical circuit) or biological (e.g. a group of fireflies). In vertebrate embryos, synchronization of intracellular signaling oscillations regulates the precise and periodic formation of somites, the precursors of vertebrae. In this system, oscillations are coordinated between neighbors via intercellular coupling, and such coordination results in a phase shift between oscillations, giving the impression of a spatiotemporal wave pattern travelling through the presomitic mesoderm (PSM) from posterior to anterior. Where this wave arrests at the anterior PSM, a new somite forms. The timing of such an event is mediated by the segmentation clock, an elaborate molecular signaling network between Notch, Wnt, and FGF signaling.

While there are numerous studies focusing on the molecular details underlying such spatiotemporal regulation from the bottom-up, research delving into (1) the nature and mechanism of its synchronization and (2) its impact on tissue patterning during embryogenesis remains limited. To address this, we thus instead focus on a principles-based, top-down, approach. Accordingly, we recently developed a microfluidics-based experimental platform allowing entrainment of the signaling oscillations in the PSM to periodic pulses of signaling modulators, leveraging fundamental entrainment principles that have also been studied in other complex physical and biological oscillatory systems (e.g. the circadian clock).

In this current research, we use such experimental platform to map Arnold tongues, to systematically control both the period and the phase of oscillations in the PSM, and to precisely modulate the segmentation clock. We report how the systems-level entrainment behavior of oscillations in an embryonic tissue follows dynamical systems theory, despite its complexity. Furthermore, we uncover- and elaborate on a peculiar behavior in our system (i.e. emergence of a period gradient even upon tissue-level entrainment), providing insight into the nature of the underlying oscillatory network in the PSM. This finding has enabled us to generate testable hypotheses about the importance of the period gradient for the processing of spatiotemporal cues and proper tissue patterning. Moreover, experiments with intact embryonic tissue have allowed us to link modulation of the segmentation clock and its consequences on

patterning of the PSM. We specifically record observations in apparent contradiction with traditional interpretations of a well-known model of periodic patterning during somitogenesis (i.e. the classical clock and wavefront model). Our observations instead support the proposition that the oscillatory dynamics encode both the timing and spacing of somite formation.

More generally, we here highlight the power of our experimental approach to precisely control the period and phase of a complex spatially-extended system of coupled and phase-shifted oscillations in an embryonic tissue, which had not been possible before using genetics and pharmacological intervention. We hope this research provides further experimental evidence of the universality of fundamental entrainment principles, and offers an alternative top-down approach to the study of synchronization of biological oscillations in embryonic development.

Zusammenfassung

Synchronisation ist überall in der Natur zu finden. Es ist eine emergente Eigenschaft, die in Systemen interagierender, oszillierender Einheiten auftritt, unabhängig davon, ob diese Einheiten physikalisch (z.B. in einem Stromkreis) oder biologisch (z.B. in einer Gruppe von Leuchtkäfern) sind. Bei Wirbeltierembryonen reguliert die Synchronisation intrazellulärer Signalschwingungen die präzise und periodische Bildung von Somiten, den Vorläufern von Wirbeln. In diesem System werden Oszillationen über interzelluläre Kopplung zwischen Nachbarzellen koordiniert; diese Koordination führt zu einer Phasenverschiebung zwischen Oszillationen, was den Eindruck eines raumzeitlichen Wellenmusters ergibt, welches sich durch das präsomitische Mesoderm (PSM) von posterior nach anterior fortbewegt. Wo diese Welle am anterior PSM anhält, bildet sich ein neuer Somit. Die Zeiteinteilung eines solchen Ereignisses wird durch die Segmentierungsuhr bestimmt, ein ausgeklügeltes molekulares Signalnetzwerk zwischen Notch-, Wnt- und FGF-Signalen.

Während es zahlreiche Studien gibt, die sich auf die molekularen Details einer solchen raumzeitlichen Regulation im Bottom-Up Prinzip konzentrieren, ist die bisherige Forschung über (1) die Art und den Mechanismus der Synchronisation und (2) deren Auswirkung auf die Gewebestrukturierung während der Embryogenese begrenzt. Um dies zu adressieren, konzentrieren wir uns stattdessen auf einen prinzipienbasierten Top-Down-Ansatz. Dementsprechend haben wir kürzlich eine auf Mikrofluidik basierende, experimentelle Plattform entwickelt, die das Entrainment der Signalschwingungen im PSM mit periodischen Impulsen von Signalmodulatoren ermöglicht und dabei grundlegende Entrainmentprinzipien nutzt, die auch in anderen komplexen physikalischen und biologischen Schwingungssystemen (z. B. in der circadianen Uhr) untersucht wurden.

In dieser Forschungsarbeit verwenden wir solche experimentelle Plattform um Arnold-Zungen abzubilden, und dadurch sowohl die Periode als auch die Phase der Schwingungen im PSM systematisch zu steuern und die Segmentierungsuhr präzise zu modulieren. Wir zeigen auf, wie in einem embryonalen Gewebe das Systemebene Entrainment von Schwingungen trotz seiner Komplexität der Theorie dynamischer Systeme folgt. Darüber hinaus enthüllen und präzisieren wir ein besonderes Verhalten in unserem System (d.h. das Auftreten eines Periodengra-

dienten selbst bei Entrainment auf Gewebeebene), wodurch wir Einblick in die Natur des zugrunde liegenden Oszillationsnetzwerks im PSM erhalten. Diese Entdeckung hat es uns ermöglicht, überprüfbare Hypothesen über die Bedeutung des Periodengradienten für die Verarbeitung raumzeitlicher Signale und richtige Gewebestrukturierung aufzustellen. Darüber hinaus haben Experimente mit intaktem embryonalem Gewebe es uns ermöglicht, die Modulation der Segmentierungsuhr und ihre Konsequenzen für die Strukturierung des PSM zu verknüpfen. Spezifisch erfassen wir Beobachtungen, die in scheinbarem Gegensatz zu klassischen Interpretationen eines wohlbekannten Modells der periodischen Strukturierung während der Somitogenese (d.h. des klassischen "Clock and Wavefront" Modells) stehen. Unsere Beobachtungen unterstützen hingegen das Argument, dass die Schwingungsdynamik sowohl den zeitlichen als auch den räumlichen Aspekt der Somitenbildung codiert.

Im Allgemeinen betonen wir hier die Fähigkeit unseres experimentellen Ansatzes, die Periode und Phase eines komplexen, räumlich ausgedehnten Systems gekoppelter und phasenverschobener Schwingungen in einem embryonalen Gewebe präzise zu steuern, was zuvor mit Genetik und pharmakologischer Intervention nicht möglich war. Wir hoffen, dass diese Forschung weitere experimentelle Beweise für die Universalität grundlegender Entrainmentprinzipien liefert und einen alternativen Top-Down-Ansatz zur Untersuchung der Synchronisation biologischer Schwingungen in der Embryonalentwicklung bietet.

Acknowledgement

I am thankful to Alexander Aulehla for introducing me to nonlinear dynamics and developmental biology, scientific fields which I have become really passionate about. Thank you for your guidance and your support. Thank you also for sharing with me your knowledge and your wisdom.

I am also very grateful to Justin Crocker, Lars Hufnagel, and Ulrich Schwarz who have been guiding me in the progress of this PhD research over the last years. I also thank Nicholas S. Foulkes for accepting the invitation to be part of my thesis examination committee.

I thank the past and current members of Alexander's lab at the European Molecular Biology Laboratory (EMBL). It has been very transformative doing science with all of you! Special thanks to Katharina Sonnen, who taught me microfluidics and who mentored me especially when I was starting in my PhD, and to Gregor Mönke, who established the wavelet analysis workflow we use in the lab and who helped me a lot when I was starting to learn dynamical systems theory. I also thank my active collaborators in the lab, Takehito Tomita and Hidenobu Miyazawa, for working with me closely on the link between FGF and the period gradient and on entrainment via periodic perturbation of glycolytic flux.

I am grateful to Miki Ebisuya, Anne Ephrussi, Paul François, Adrián Granada, Hanspeter Herzel, Mogens Høgh Jensen, Ryoichiro Kageyama, Istvan Kiss, Sandeep Krishna, Andy Oates, Eric Siggia, Ben Steventon, and Stefano Vianello for discussions and feedback that enriched this research. I thank the lab of Christoph Merten at EMBL, especially Nachiket Satish Shembekar and Ramesh Utharala, for discussions and feedback on microfluidics. Thanks also to the labs of Takashi Hiiragi and Aissam Ikmi for the joint self-organization meetings.

I am thankful to Nobuko Tsuchida-Straeten for maintaining the LuVeLu mouse line. Thanks to Nobuko also for generating the Axin2-GSAGS-Achilles mouse line and the PFKFB3 mutant mouse line, in collaboration with Marteinn Snaebjornsson and Yvonne Petersen.

I thank Antonio Politi for providing the Pipeline Constructor macro for automated live microscopy, and I acknowledge the assistance from Maximilian Beckers, Aliaksandr Halavaty, Oleksandr Maistreko, Gregor Mönke, and Takehito Tomita in writing scripts for data analysis.

I also thank the EMBL Szilárd Library, most especially Natalia Garea Garcia and Tijana Ilić, for helping me buy books and for finding copies (and English translations) of old research articles.

I am very grateful to the EMBL Laboratory Animal Resources (LAR), the EMBL Advanced Light Microscopy Facility (ALMF), the EMBL Cleaning Services, the EMBL Graduate Office, the EMBL Mechanical Workshop, the EMBL Photolab, and the EMBL Purchase Department. Special thanks also to Anthi Papasavva, our administrator at the Developmental Biology Unit. Thank you all very much for your service!

I thank Stefano Vianello for some of the illustrations in this thesis, and I thank Anna Boldo and Léonie Strömich, with some help from Carlos Rojas-Cordova and Philipp Stachel-Braum, for the German translation of my thesis summary (Zusammenfassung). I am also thankful to Ali Seleit, Silvija Švambarytė, and Mark Vincent dela Cerna for going through an earlier version of the text.

I am grateful to the people whom I met and interacted with during my stay at the Marine Biological Laboratory in Woods Hole. Thanks in particular to Michael Akam, Andrea Attardi, Richard Behringer, Melvin Bonilla, Cynthia Bradham, Maximilien Courgeon, Hernan Garcia, Andrew Gillis, Bob Goldstein, Jonathan Henry, Raymond Keller, Jane Kondev, David Matus, Catherine May, David McClay, Nipam Patel, Rob Phillips, Manu Prakash, Alvaro Sanchez, Elaine Seaver, Claudio Stern, Julie Theriot, Eric Wieschaus, Laurel Yohe, and Xinwen Zhu for inspiring me and affecting how I approach science, one way or another! I will cherish the knowledge and wisdom you shared with me. I am also very grateful to the the Burroughs Wellcome Fund, the Helmsley Charitable Trust, the Horace W. Stunkard Scholarship Fund, the Arthur Klorfein Scholarship and Fellowship Fund, and The Company of Biologists for the financial support to go to Woods Hole and meet these wonderful people.

To Alexandra Elbakyan, thank you very much for making scientific knowledge more accessible.

To the people whom I worked with in advocating for diversity and inclusion at EMBL, Sofia Forslund, Antje Keppler, Antonio Politi, David Puga, Daniel Rios, Carlos Rojas-Cordova, Malvika Sharan, Marzia Sidri, and Jesús Alvarado Valverde, thank you very much!

To my friends who, like me, were writing their theses in the middle of the COVID19 crisis, Lucia Cassella, Esther Kim, Dimitrios Konstantinidis, Carlos Rojas-Cordova, Luigi Russo, Samantha Seah, and Francesca Vianello, thank you for keeping me (socially-distanced) company!

To my friends whom I started my formal science training with at the University of the Philippines (UP) Manila, Isabella Enriquez, Tere Frias, Sheryl Grijaldo, and Valerie Santos, thank you for making those years of learning fun and enjoyable! To my mentors at UP, Nelson Villarante (Doc V) and Maria Constanca Carrillo (Doc Carrillo), thank you for believing in me and for encouraging me to pursue a career in science.

I also thank Clara Buenconsejo, who in 2015 started a crowdfunding campaign to financially help me apply for and pursue graduate school. Many thanks as well to those who donated. I am very grateful.

To Chih-Yen King, Chang-I Yu, Yu-Wen Huang, Shenq-Huey Wong, and Lucy Chen, my former labmates in Academia Sinica in Taiwan, thank you for making me feel for the first time how it is to be part of a lab. To Marija Buljan, thank you for mentoring me when I first came to Heidelberg as a research intern in 2014.

To my closest friends in Heidelberg, Anniek, Anthi, Carina, Carlos, Christine, Daniel, Emilia, Hidenobu, Lucia, Philipp, Samantha, Silvija, and Takehito, thank you very much for the friendship! Carina, Emilia, Philipp, and Silvija, thank you for reaching out to me especially when I struggle with my mental health! To my psychotherapist, Florian Theis, thank you very much!

To Anna, Francesca, and Alvis, thank you very much for accepting me and for making me feel like a part of your family.

To RG, Baby, Kay, Patrick, Paula, Penpen, and Angel, maraming maraming salamat sa pagmamahal at suporta. To Anna and PT, maraming salamat sa pag-gabay niyo sa amin. Mahal na mahal ko kayong lahat!

To Stefano, thank you very much for your unconditional love, your unwavering support, and your overflowing patience. Ti amo tantissimo! Ngayon at kailanman.

To You, maraming salamat po.

It really does take a village. I am where I am and I am empowered to go further because of the path paved by people who have come before me, and because of the love and support I have received. I am grateful, and I am eager to pay it forward!

A las Flores de Heidelberg

*¡Id a mi patria, id extranjeras flores
sembradas del viajero en el camino,
y bajo su azul cielo,
que guarda mis amores,
contad del peregrino
la fé que alienta por su patrio suelo!*

*Id y decid...; decid que cuando el alba
vuestro cáliz abrió por vez primera,
cabe el Neckar helado,
le visteis silencioso a vuestro lado
pensando en su constante primavera.*

*Decid que cuando el alba,
que roba vuestro aroma,
cantos de amor jugando os susurraba,
él también murmuraba
cantos de amor en su natal idioma;
que cuando el sol la cumbre
del Koenigsthul en la mañana dora
y con su tibia lumbre
anima el valle, el bosque y la espesura,
saluda en ese sol, aún en su aurora,
al que en su patria en su cenit fulgura.*

*Y contad aquel día
cuando os cojía al borde del sendero,
entre las ruinas del feudal castillo
orilla al Neckar o en la selva umbría.
Contad lo que os decía,
cuando, con gran cuidado,
entre las páginas de un libro usado
vuestras flexibles hojas oprimia.*

*Llevad, llevad ¡oh flores!
amor a mis amores
paz a mi país y a su fecunda tierra,
fé a sus hombres, virtud a sus mujeres,
salud a dulces seres
que el paternal sagrado hogar encierra...*

*Cuando toquéis la playa,
el beso que os imprimo
depositadlo en alas de la brisa,
porque con ella vaya,
y bese cuando adoro, amo y estimo.*

*Mas ¡ay! llegaréis, flores,
conservaréis, quizás, vuestros colores;
pero lejos del patrio, heroico suelo,
a quién debéis la vida
perderéis los olores;*

*que aroma es alma, y no abandona el cielo
cuya luz viera en su nacer, ni olvida.*

**Jose Rizal, National Hero of the Philippines
Heidelberg, Germany, 1886**

To the Flowers of Heidelberg

Go to my country, go, O foreign flowers,
sown by the traveler along the road,
and under that blue heaven
that watches over my loved ones,
recount the devotion
the pilgrim nurses for his native sod!

Go and say say that when dawn
opened your chalices for the first time
beside the icy Neckar,
you saw him silent beside you,
thinking of her constant vernal clime.

Say that when dawn
which steals your aroma
was whispering playful love songs to your young
sweet petals, he, too, murmured
canticles of love in his native tongue;
that in the morning when the sun first traces
the topmost peak of Koenigsstul in gold
and with a mild warmth raises
to life again the valley, the glade, the forest,
he hails that sun, still in its dawning,
that in his country in full zenith blazes.

And tell of that day
when he collected you along the way
among the ruins of a feudal castle,
on the banks of the Neckar, or in a forest nook.
Recount the words he said
as, with great care,
between the pages of a worn-out book
he pressed the flexible petals that he took.

Carry, carry, O flowers,
my love to my loved ones,
peace to my country and its fecund loam,
faith to its men and virtue to its women,
health to the gracious beings
that dwell within the sacred paternal home.

When you reach that shore,
deposit the kiss I gave you
on the wings of the wind above
that with the wind it may rove
and I may kiss all that I worship, honor and love!

But O you will arrive there, flowers,
and you will keep perhaps your vivid hues;
but far from your native heroic earth
to which you owe your life and worth,
your fragrances you will lose!

For fragrance is a spirit that never can forsake
and never forgets the sky that saw its birth.

translated by Nick Joaquin

၂၆၆၆၆၆ နှစ် ဝမ်း ကပ်
Sinisid ko ang dagat

၆၆၆၆၆၆ နှစ် ဝမ်း ဝမ်း
Nalibot ko ang mundo

၆၆၆၆၆၆ နှစ် ဝမ်း
Nasa puso ko pala

၆၆၆၆၆၆ နှစ် ဝမ်း
hinahanap kong kulo

Noypi, Bamboo Mañalac

To RG and Baby

To Kay, Patrick, Paula, Penpen, and Angel

To Anna and PT

To Dando, Ansing, Ruben, and Nida

To Stefano

To those we lost and to us trying to get by in the middle of a global health crisis

To curious and queer minds of the past, the present, and the future

Contents

1	Introduction	1
1.1	Complex systems in the natural world: their collective dynamics and emergent behavior	2
1.1.1	Collective dynamics and emergence	2
1.1.2	Coarse-graining in studying complex systems	4
1.1.3	Recommended reading	6
1.2	Collective dynamics of oscillations: synchronization and entrainment	7
1.3	Entrainment of electrical circuits, of chemical reactions, and of biological systems	10
1.3.1	Entrainment of electrical circuits	10
1.3.2	Entrainment of chemical reactions	10
1.3.3	Entrainment of biological systems	12
1.4	Somitogenesis, a complex spatially-extended biological system of coupled and phase-shifted signaling oscillations	17
1.4.1	Segmented tissue patterning in vertebrate embryos	17
1.4.2	Theoretical models of tissue patterning	19
1.4.3	Signaling oscillations in the PSM: the segmentation clock	21
1.4.4	Notch signaling and intercellular coupling of intracellular signaling oscillations in the mouse PSM	21
1.4.5	Some recent advances in studying signaling oscillations in the mouse PSM	25
1.4.6	Some findings from our lab regarding signaling oscillations during somitogenesis	28
2	Aims of the study	29
3	Does the segmentation clock obey unifying physical principles in synchronization?	31
3.1	Results	32
3.1.1	A microfluidics-based experimental platform enables entrainment of the segmentation clock to periodic pulses of DAPT	32
3.1.2	Entrainment to periodic pulses of DAPT allows control over the period of the segmentation clock	34

3.1.3	The segmentation clock establishes a stable phase relationship with the periodic DAPT pulses via phase-locking	38
3.1.4	Detuning between the free-running segmentation clock and the periodic pulses of DAPT affects the entrainment phase . .	40
3.1.5	The segmentation clock is amenable to higher-order entrainment	41
3.1.6	Entrainment results in the emergence of an altered period gradient along the AP axis	44
3.2	Discussion	47
3.3	Conclusion	50
3.4	Outlook	51
4	Is an emergent period gradient important for segmentation of the pre-somitic mesoderm?	55
4.1	Results	56
4.1.1	The rhythm of the segmentation clock matches the rhythm of oscillations in the posterior PSM (i.e. the center of spreadouts) regardless whether the clock is sped up or slowed down . . .	56
4.1.2	A higher (or lower) period gradient correlates with a higher (or lower) amplitude gradient	59
4.1.3	The frequency gradient precedes the phase gradient in samples subjected to periodic pulses of DAPT	62
4.1.4	Entrainment of the segmentation clock results in a less steep phase gradient	62
4.1.5	When the segmentation clock is entrained to periodic DAPT pulses, a change in slope of the frequency gradient translates less to a corresponding change in slope of the phase gradient	63
4.1.6	Entrained samples undergo segmentation despite having a flatter phase gradient than controls	67
4.1.7	Increasing entrainment strength abolishes the period gradient and its consequent phase wave	68
4.1.8	Oscillations of Wnt signaling are also entrained to periodic pulses of DAPT and are phase-shifted to entrained oscillations of Notch signaling	72
4.2	Discussion	75
4.3	Conclusion	82
4.4	Outlook	83
5	Does modulating the segmentation clock affect somitogenesis according to the classical clock and wavefront model?	87
5.1	Results	88
5.1.1	Intact PSM can be cultured within PDMS microfluidics chips for entrainment	88

5.1.2	Microfluidics-based entrainment enables precise adjustment of the segmentation clock in intact PSM	88
5.1.3	Segment polarity is preserved in somites formed from intact PSM subjected to microfluidics-based entrainment	92
5.1.4	Left-right asymmetry is present in some samples adjusted to a slower segmentation clock with periodic DAPT pulses	94
5.1.5	A slower segmentation clock does not always result in a proportionally bigger somite	94
5.2	Discussion	96
5.3	Conclusion	101
5.4	Outlook	102
6	Materials and methods	107
6.1	Animals	107
6.1.1	Mouse lines	107
6.1.2	Genotyping	108
6.2	Working with mouse embryos	109
6.2.1	Media preparation	109
6.2.2	Mouse dissection and embryo recovery	109
6.2.3	In situ hybridization using digoxigenin-labeled probes	110
6.2.4	Hybridization chain reaction of intact embryo tails	115
6.2.5	Correlative live imaging and immunofluorescence	117
6.3	Microfluidics	120
6.3.1	Making of PDMS mold	120
6.3.2	Making of microfluidics device from pre-existing mold	122
6.3.3	Preparations for microfluidics-based entrainment of ex vivo model of somitogenesis (spreadout)	124
6.3.4	Preparations for microfluidics-based entrainment of intact PSM125	125
6.3.5	Loading embryonic tissues in microfluidics device and mounting for live imaging	126
6.3.6	Setting up automated pumping	127
6.4	Confocal microscopy	128
6.5	Data analysis	130
6.5.1	Extracting timeseries from global intensity and re-orientation of spreadouts for subsequent gradient analyses	130
6.5.2	Monitoring period-locking and phase-locking	131
6.5.3	Generating wavelet movies	133
6.5.4	Examining period/frequency gradient and phase gradient in spreadouts	133
7	Abbreviations	135
8	Supplementary files and figures	137

8.1	Supplementary files	137
8.1.1	Codes and accompanying sample data	137
8.1.2	Movies	137
8.1.3	Text files	138
8.2	Supplementary figures	138

Bibliography		161
---------------------	--	------------

Introduction

“*While I was forced to stay in bed for a few days and made observations on my two clocks of the new workshop, I noticed a wonderful effect that nobody could have thought of before.*

— **Christiaan Huygens**

translated from French by Carsten Henkel

Synchronization – that is, the establishment of a constant phase relationship between different oscillating objects – is extremely prevalent throughout the natural world. Whether one looks at the coordinated swinging of the pendulums of lifeless clocks hanging on a beam (first documented by Christiaan Huygens in 1665, reported in a letter he wrote to his father) or at the orchestrated blinking of lively fireflies in Southeast Asia (Buck and Buck, 1968; Buck, 1988), synchronizing behaviors are all around us. Regardless if the oscillating entities are inanimate or animate, and whether they belong to the physical or to the biological world, the concepts underlying synchronization are universal. One of such unifying principles is entrainment, whereby an autonomous oscillation synchronizes to the cycling of another one. Oscillations are integral to rhythms in biology, such as the circadian clock and the cell cycle. In vertebrate embryos, signaling oscillations govern the periodic segmentation of the presomitic mesoderm (PSM) during a process called somitogenesis, fundamentally marking the metameric patterning of the major axis of the embryo (Palmeirim et al., 1997; Dequéant and Pourquié, 2008; Hubaud and Pourquié, 2014). Somites, generated by this process, will later give rise to the vertebrae. Investigation on the extent to which signaling oscillations in the PSM follow universal principles underlying synchronization is limited. To this point, this current research focuses on systematic analysis of their entrainment dynamics, as oscillating entities are expected to obey fundamental principles of entrainment, and we are certain such an approach can be used to probe the mechanism of synchronization in somitogenesis. This section contains an introduction to the concept of entrainment, a background on the signaling oscillations in the presomitic mesoderm during somitogenesis, and a summary of our recent effort, using microfluidics-based entrainment, in broadening mechanistic insight into synchronization during embryonic development.

1.1 Complex systems in the natural world: their collective dynamics and emergent behavior

1.1.1 Collective dynamics and emergence

Collective dynamics emerging in complex systems are ubiquitous in nature. For instance, we see collective dynamics as frost patterns on windows after a snowfall in winter, as magnetism, as traffic jams in urban cities, as hurricanes, and also as flocking in birds (Figure 1.1). These emergent behaviors arise from the nonlinear interactions between components of a complex system (Haan, 2006; Manson, 2001). In complex systems, these behaviors self-organize and form amongst the individual components in the absence of a blueprint or master plan (Camazine et al., 2003).

The emergent properties of a complex system are not attributable to any property of its constituent parts (Haan, 2006; Baas and Emmeche, 1997). In fact, having arisen from interactions in the system, collective dynamics or a system's emergent property is more than the mere addition of each of its components' properties (Haan, 2006; Manson, 2001; Mazzocchi, 2008). This was beautifully conveyed by Aristotle in *Metaphysics* (Book VIII 1045a 8-10), translated to English by William David Ross (available at <http://classics.mit.edu/Aristotle/metaphysics.8.viii.html>):

In the case of all things which have several parts and in which the totality is not, as it were, a mere heap, but the whole is something beside the parts, there is a cause; for even in bodies contact is the cause of unity in some cases, and in others viscosity or some other such quality.

which is now more simply referred to as "the whole is more than the sum of its parts." For instance, an image on a screen is an emergent property of tiny pixels of either red, green, or blue, organized in space at a given time and none of which project a tiny version of the image. Monitoring a single car in a city will not give us any information on how traffic jams would form, how long they would last, or where they would happen. Similarly, just observing a single bird in a flock will not give us an idea how precisely the entire flock would behave.

On a deeper and much higher level, collective dynamics in complex systems do not result only in unique, emergent behavior of the entire system. In fact, each part would also elicit unique behaviors when part of a group, compared to when in isolation (Mazzocchi, 2008). For example, when a population of cells with slow signaling oscillations is mixed with another population of cells with fast signaling

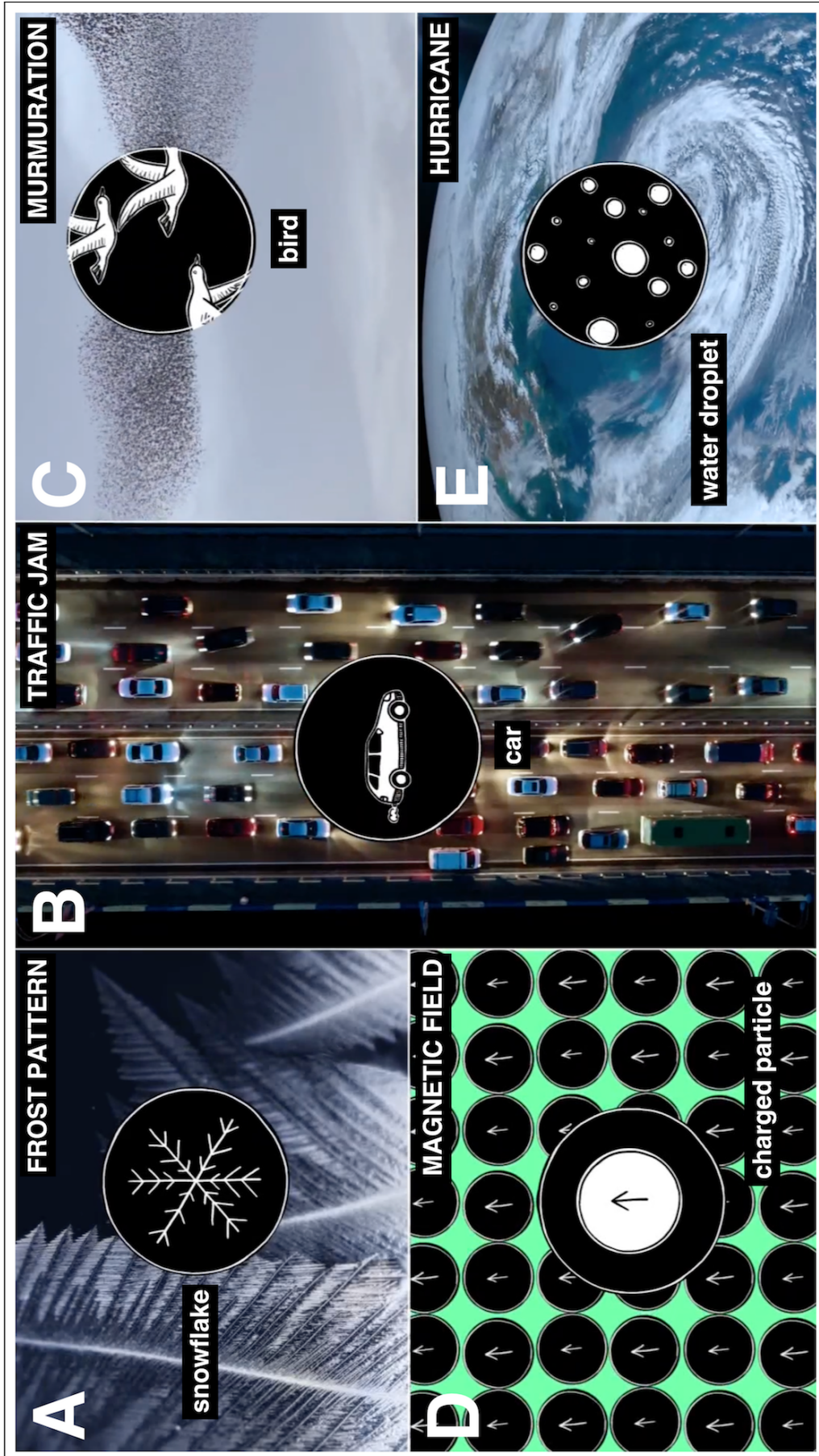


Figure 1.1 Collective dynamics emerging in complex systems are ubiquitous in nature. (A) Frost patterns emerge from snowflakes on windows. (B) Traffic jams emerge from cars in a busy road. (C) Murmurations emerge from a flock of birds. (D) Magnetic fields emerge from alignment of charged particles. (E) Hurricanes emerge from water droplets. Photo credit: Lottie Kingslake for Quanta Magazine.

oscillations (Tsiairis and Aulehla, 2016), not only is the collective period of the oscillations equal to the average of the two starting periods, but also each of the oscillations adjusts to the average period. Fast oscillations slow down, while slow oscillations speed up. Synchronization, an emergent property of such complex system of oscillatory entities, constrains the individual components, adjusting their periods to a value which neither population had in isolation.

1.1.2 Coarse-graining in studying complex systems

Complex systems are characterized by hierarchical levels of organization (Mazzocchi, 2008), which span different length scales. In biology, these span from the subatomic, to the cellular, to the organismal, and even to the ecosystems level and beyond. Taking this into account, a different level of understanding about a system is attained based on the chosen level of organization subjected to scientific inquiry. This is pointed out by David Marr and Tomaso Poggio in what is now more commonly known as the Level of Understanding manifesto (Marr and Poggio, 1976):

Complex systems, like a nervous system or a developing embryo, must be analyzed and understood at several different levels. Of course, there are logical and causal relationships among them, but the important point is that these levels of description are only loosely related.

While all levels of organization in a system are important and can be investigated independent of each other, Marr and Poggio go on arguing that knowing all about a lower level (i.e. constituent parts) does not directly enable construction of a higher level (i.e. the system) in studying complex systems (Marr and Poggio, 1976). More precisely, "reductionism does not imply constructionism." As earlier elaborated by Philip W. Anderson in *More is Different* (Anderson, 1972),

The ability to reduce everything to simple fundamental laws does not imply the ability to start from those laws and reconstruct the universe.

This is also echoed by François Jacob in *Evolution and Tinkering* (Jacob, 1977):

The properties of a system can be explained by the properties of its components. They cannot be deduced from them.

Dissection of a system's microscopic property does not allow direct reconstruction of a mesoscopic/macroscopic one (i.e. bottom-up), as higher levels of organization acquire new emergent properties (Mazzocchi, 2008; Anderson, 1972; Jacob, 1977). For instance, the gross domestic product (GDP) of a country at a given instant (i.e. macroeconomics) can not be projected from the economic activities of one single person (i.e. microeconomics) (example given by Simon DeDeo in a lecture on renormalization, available at <https://www.complexityexplorer.org/courses/67-introduction-to-renormalization/>). Another example is how a protein's 3D structure can not always be deduced from its amino acid sequence. In yeast, a translation termination factor protein (i.e. Sup35) can fold into very different heritable conformations (i.e. prion strains) depending on genetic background (i.e. yeast strain) (King, 2001; Yu and King, 2019; Huang and King, 2020). These highlight the importance of unique approaches in capturing collective dynamics and emergent behavior in complex systems, while not getting too overwhelmed by often highly parameterized microscopic/molecular details.

Indeed, with the realization from -omics studies that biology is inherently complex (Mazzocchi, 2008), theory-driven top-down approaches, based on renormalization and coarse-graining, are becoming more and more valuable in studying complex biological systems (Mazzocchi, 2008; van Regenmortel, 2004; Trepast and Sahai, 2018; Bialek, 2015). In these approaches, the microscopic description of a system is coarse-grained to a rather mesoscopic/macroscopic one. Molecular signatures are coarse-grained to the level of the cell that confines them. Cell states are coarse-grained to the level of the tissue where they belong. By shifting focus on a higher level description, principles that describe a system phenomenon could be identified. As systems that have the same phenomenology often share same fundamental principles, theoretical and experimental insights from one complex system could guide investigation of another complex system, despite the two having entirely different constituent parts. For instance, jamming, like between cars in road congestion, has been studied in self-propelled polystyrene beads (Geyer et al., 2019), in huddling penguins in the Antarctic (Zitterbart et al., 2011), and in a developing fish embryo (Mongera et al., 2018). In studying complex systems, theory is proving to be very important in generating hypotheses, guiding experiments, and predicting outcomes (Bialek, 2015; Phillips, 2015).

1.1.3 Recommended reading

Here are some recommended reading on complex systems and theory in biology (titles arranged alphabetically), with link to downloadable PDF.

Complexity in Biology

Fulvio Mazzocchi

<https://doi.org/10.1038/sj.embor.7401147>

Evolution and Tinkering

François Jacob

<https://doi.org/10.1126/science.860134>

From Understanding Computation to Understanding Neural Circuitry

David Marr and Tomaso Poggio

<https://dspace.mit.edu/handle/1721.1/5782>

How Emergence Arises

Hans de Haan

<https://doi.org/10.1016/j.ecocom.2007.02.003>

More is Different

Philip W. Anderson

<https://doi.org/10.1126/science.177.4047.393>

Perspectives on Theory at the Interface of Physics and Biology

William Bialek

<https://doi.org/10.1088/1361-6633/aa995b>

<https://arxiv.org/abs/1512.08954>

Simplifying Complexity: a Review of Complexity Theory

Steven M. Manson

[https://doi.org/10.1016/S0016-7185\(00\)00035-X](https://doi.org/10.1016/S0016-7185(00)00035-X)

Theory in Biology: Figure 1 or Figure 7?

Rob Phillips

<https://doi.org/10.1016/j.tcb.2015.10.007>

1.2 Collective dynamics of oscillations: synchronization and entrainment

In 1665, Christiaan Huygens serendipitously observed two pendulums, hanging on the same wooden beam, swing with the same rhythm (Figure 1.2), an observation he immediately shared in a letter to his father (*Œuvres complètes de Christiaan Huygens*). Then, he described this phenomenon "an odd kind of sympathy." Now, we call it "synchronization." Synchronization is the adjustment of the rhythms of two or more oscillating objects to establish a stable phase relationship between their cycles (Pikovsky et al., 2003). It is everywhere in nature, an emergent property of interacting oscillations, regardless if the oscillatory entities are a group of living things (e.g. fireflies), of nonliving things (e.g. pendulums), or of both (e.g. the day-night cycle and our circadian rhythm).

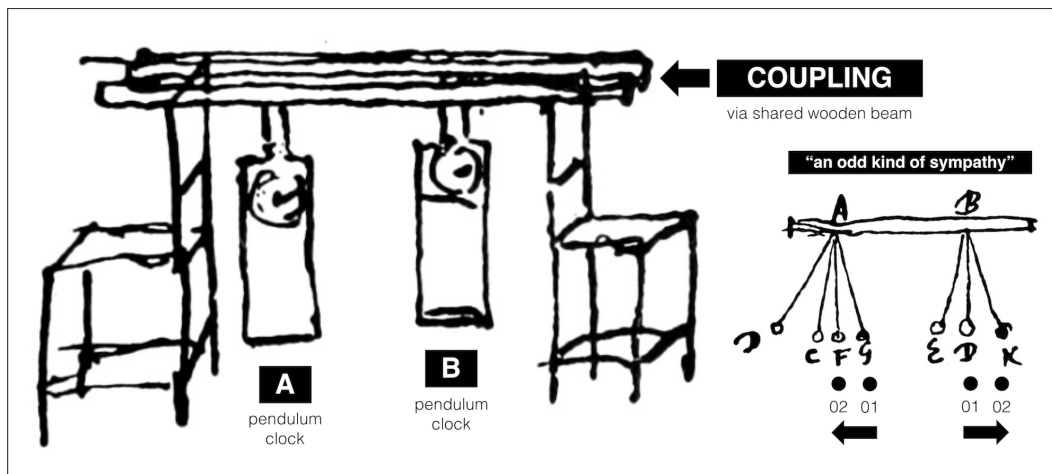


Figure 1.2 First known documentation of synchronization, an odd kind of sympathy. Drawings by Christiaan Huygens, accounting synchronization of two pendulums hanging on the same wooden beam, which he described as "an odd kind of sympathy." Huygens noted that the pendulums swing with the same rhythm, though at opposite directions. Annotations are added here to indicate the two oscillatory entities (i.e. pendulums A and B) and their coupling (i.e. via a shared support). Adapted and modified from *Œuvres complètes de Christiaan Huygens*.

A universal principle in synchronization is entrainment, whereby an autonomous oscillation is driven to cycle with another oscillation (Pikovsky et al., 2003; Balanov et al., 2008). While phase denotes the location of an oscillating object along its orbit, frequency denotes the time it takes to complete one revolution. An autonomous, endogenous oscillation will cycle on its own with a free-running frequency (its natural frequency, ω_o). During entrainment, the instantaneous frequency of the autonomous oscillation (ω) is locked to the frequency of an external oscillation (Ω), such that the difference in their frequencies becomes equal to zero (Figure 1.3A). Concomitantly, entrainment is easily achieved when the mismatch between ω_o and Ω (i.e. the natural frequency of the endogenous oscillation and the frequency

of the external oscillation, respectively) is not significant. Notably, increasing the strength of the external oscillation (entrainment strength, ε) results in a broader entrainment range, allowing synchronization of oscillations spanning a larger range of ω_o (Figure 1.3B). To give a general analogy, this is similar to the effect of periodic pushing (i.e. external oscillation) on a kid who is actively swinging on a swing set (i.e. endogenous oscillation). If the frequency of the kid's swinging matches the frequency of the pushing, the two will synchronize quickly. To synchronize swinging that has a different frequency, more force has to be exerted through the periodic pushing.

Entrainment behavior can be summarized as a plot of the entrainment strength of the external oscillation (ε) versus the instantaneous frequency of the endogenous oscillation (ω). Such a representation is more commonly known as an Arnold tongue (Figure 1.3C), named after Vladimir Igorevich Arnold (Arnol'd and Avez, 1968). Accordingly, Arnold tongues map finite regions of synchronization between the driven and the driving oscillations. Instead of experimentally analyzing changes in frequency, the period of the oscillations can be monitored instead: an oscillation with a high period has a low frequency (i.e. it cycles slowly), and vice versa. Arnold tongues can then alternatively be represented as a plot of entrainment strength versus detuning ($\tau_o - \mathcal{T}$), the period mismatch between the natural period of the endogenous oscillation (τ_o) and the period of the external oscillation (\mathcal{T}).

In addition to cases where the rhythm of the endogenous oscillation locks precisely to the rhythm of the external oscillation (i.e. 1:1 entrainment), there exists narrower synchronization regimes where entrainment occurs in a higher order (Figure 1.3D). More generally, in n:m entrainment, m cycles of the endogenous oscillation lock to n cycles of the external oscillation (Pikovsky et al., 2003; Balanov et al., 2008).

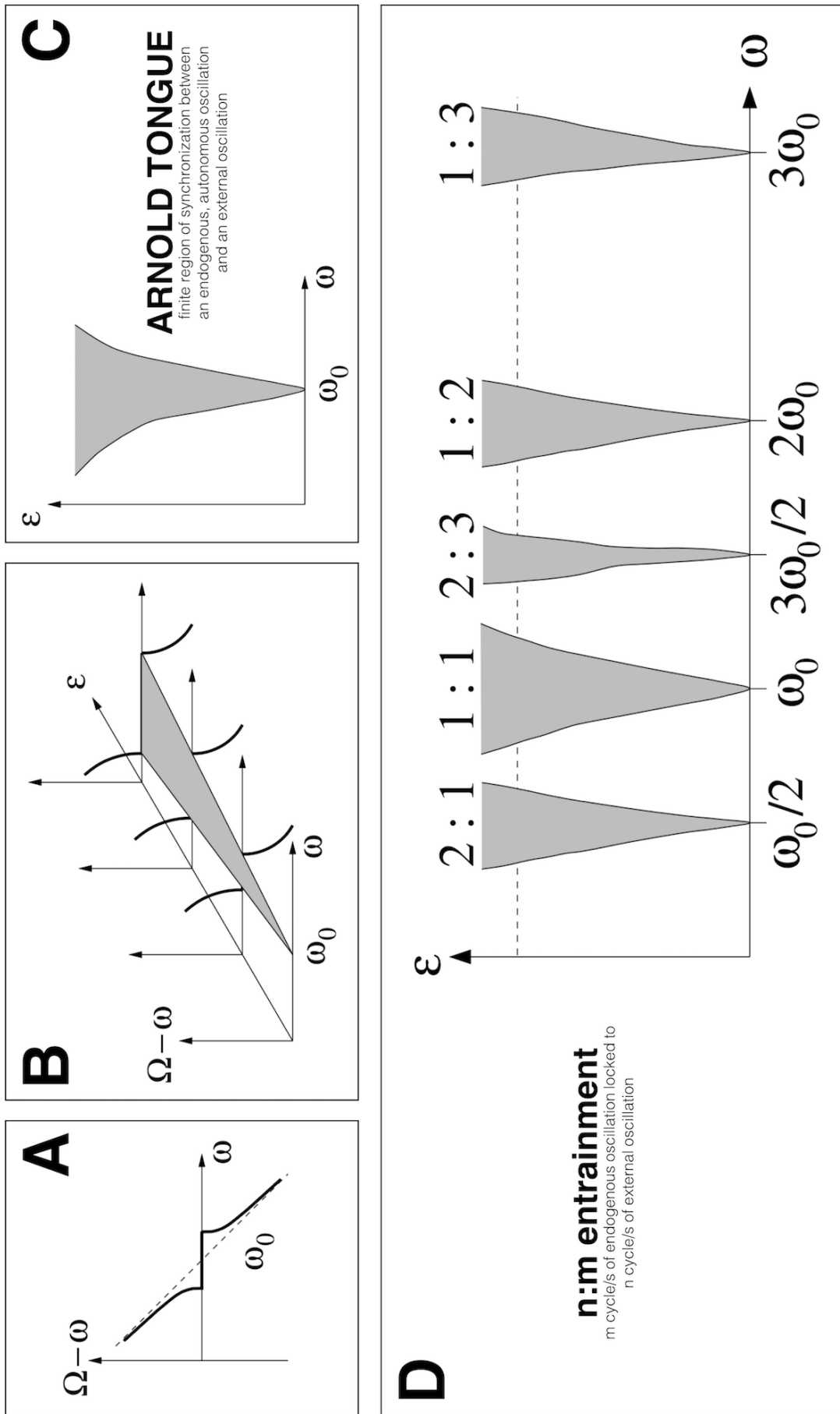


Figure 1.3 Entrainment is the synchronization of an autonomous, endogenous oscillation to an external oscillation. (A) During entrainment, the instantaneous frequency of the endogenous oscillation (ω) becomes equal to the frequency of the external oscillation (Ω). (B) Increasing the strength (ε) of the external oscillation results in entrainment of oscillations from a broader range of natural frequencies (ω_0). The shaded region, where the endogenous oscillation and the external oscillation are synchronized, is more commonly known as an Arnold tongue (C). (D) More generally, in n:m entrainment, m cycles of the endogenous oscillation lock to n cycles of the external oscillation. Adapted and modified from Figure 3.7 and Figure 3.19 of Pikovsky et al., 2003.

1.3 Entrainment of electrical circuits, of chemical reactions, and of biological systems

As a fundamental principle in synchronization, entrainment has been investigated in a wide variety of oscillatory systems. In this section, some of these investigations are cited.

1.3.1 Entrainment of electrical circuits

A circuit consisting of a nonlinear element with negative resistance connected to a module with an inductor (L) and a capacitor (C) generates self-sustaining electromagnetic oscillations (Balanov et al., 2008). Such LC-oscillator was used by Balanov et al., 2008 to experimentally investigate how an oscillatory system responds to periodic perturbation. In their experiments, the oscillator was periodically perturbed through application of an oscillating voltage to the circuit, and the oscillations were recorded using an oscilloscope. They modulated the perturbation strength and detuning by modulating the amplitude and the frequency of the applied voltage, respectively. Through such experimental strategy, the authors experimentally verified that a periodic orbit could be synchronized to a periodic perturbation via frequency-locking and phase-locking (i.e. entrainment) (Figure 1.4). In addition, they noted that oscillations are instead synchronized via suppression of natural dynamics when the perturbation strength is notably high (Balanov et al., 2008), marking transition to synchronized chaos (Postnov et al., 2001).

1.3.2 Entrainment of chemical reactions

The Belousov-Zhabotinsky (BZ) reaction is a thoroughly studied chemical reaction known to produce nonlinear chemical oscillations (Belousov, 1959; Zhabotinsky, 1964; Pechenkin, 2009). In the late 1960s and early 1970s, Ilya Prigogine, René Lefever, and John Nicolis worked together in developing a model of such self-sustaining oscillatory chemical reaction (Prigogine and Nicolis, 1967; Prigogine and Lefever, 1968; Lefever, 1968; Lefever and Nicolis, 1971). The model is as follows: (1) $A \rightarrow X$, (2) $B + X \rightarrow D + Y$, (3) $2X + Y \rightarrow 3X$, (4) $X \rightarrow E$. This model is more commonly known as Brusselator (Tyson, 1973), coined by John J. Tyson after the institutional affiliation of Prigogine, Lefever, and Nicolis. Entrainment of the Brusselator has been studied both analytically (Itō, 1979) and numerically (Kai and Tomita, 1979), with high congruence between the two approaches. The entrainment of the BZ reaction has also been investigated experimentally, for instance, in a reaction vessel (Buchholz et al., 1985) and in beads (Makki et al., 2014).

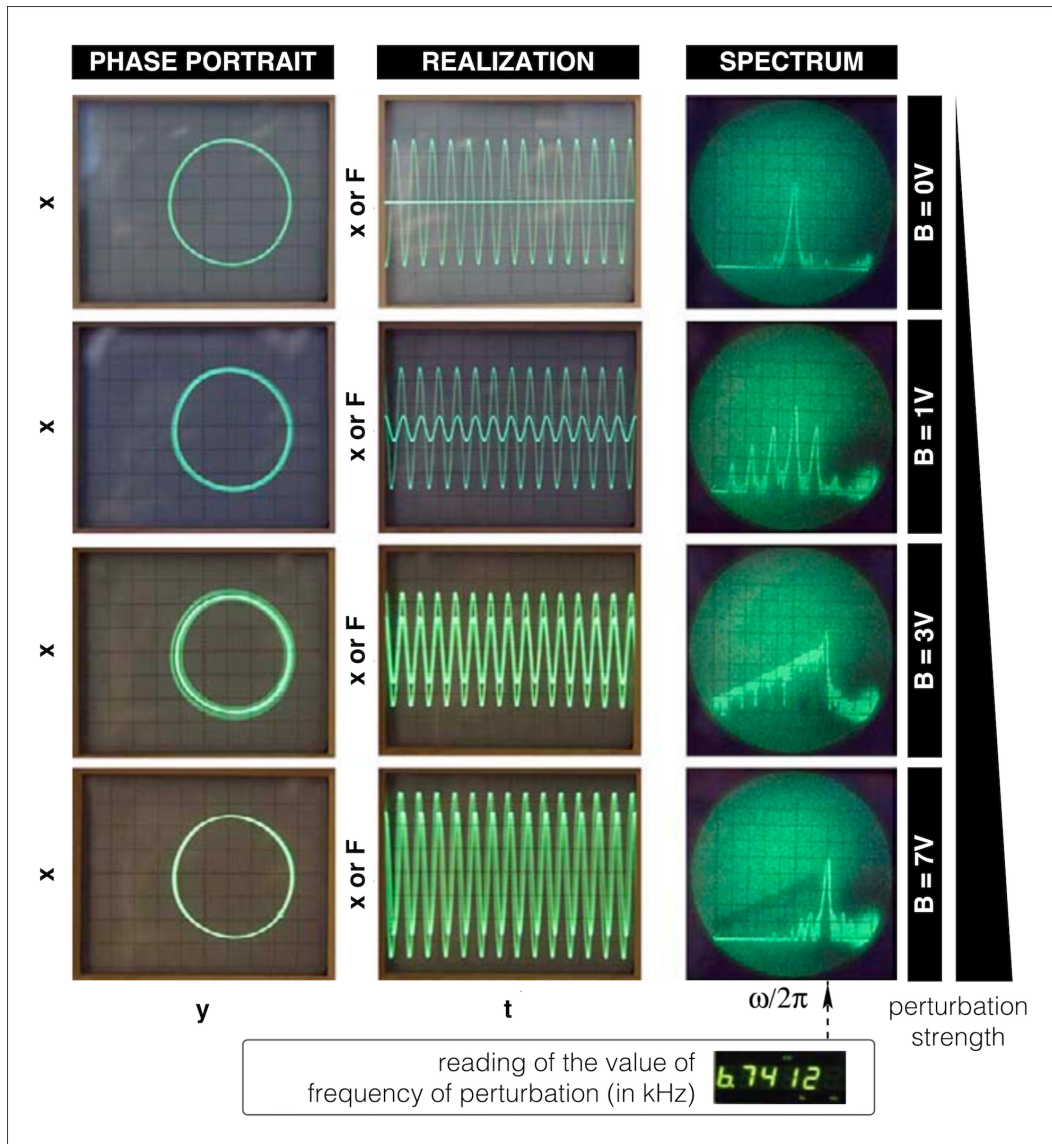


Figure 1.4 Entrainment of an electrical circuit (i.e. LC oscillator) to periodically oscillating voltage. An electrical circuit autonomously generating electromagnetic oscillations (i.e. LC oscillator), with free-running frequency of 6.62 kHz, was subjected to periodically oscillating voltage (frequency = 6.7412 kHz) at different amplitudes (i.e. different entrainment strengths). Shown are the phase portraits, the realizations of the voltage in the circuit (x) and the perturbation (F), and the spectra. Also indicated are the amplitudes (B) and the frequency reading of the applied perturbation. Here, the LC oscillator is frequency- and phase-locked to the perturbation at B = 7 V. Adapted and modified from Figure 3.14 of Balanov et al., 2008.

1.3.3 Entrainment of biological systems

Entrainment of circadian rhythms

A more widely known example of entrainment is that of a biological system – the synchronization of the circadian clock (autonomous, endogenous oscillation) to the day-night cycle (external oscillation) (Pittendrigh and Bruce, 1957; Pittendrigh, 1961). Circadian rhythms are ubiquitous, and its entrainment has been documented in nitrogen fixation of cyanobacteria (Huang and Grobbelaar, 1995), in zonation in fungi (Pittendrigh et al., 1959), in diurnal color changes in crabs (Brown Jr et al., 1955) and in stick insects (Gillis and Gillis, 2020), in the activity of cockroaches (Harker, 1956), in the leaf movements of plants (Cumming and Wagner, 1968), and in the sleep-wake (or rest-activity) cycle of humans (Roenneberg et al., 2015), among many others.

Motivated by the ubiquity of circadian rhythms and what is common between such rhythms in different living systems (i.e. capturing the phenomenology), Colin Pittendrigh and colleagues advocated for applications of synchronization theory in elucidating entrainment of the circadian clock (Pittendrigh and Bruce, 1957; Pittendrigh, 1961; Pittendrigh and Minis, 1964). More specifically, in 1957, Pittendrigh and Victor Bruce described an oscillator model for the circadian clock in living systems (Pittendrigh and Bruce, 1957). They argued for a shift in the idea of such temporal organization in biological systems from merely descriptive (i.e. a "rhythm") to something that has functional connotation (i.e. a "clock"). In introducing the oscillator model, Pittendrigh and Bruce elaborated that:

The generalization we are concerned with [in this model] is that most organisms, perhaps all, can measure time; that they possess clocks as part of their total adaptive organization. This generalization is based on fairly recent developments in spite of the fact that much of the pertinent evidence is comparatively old. This anomaly is itself interesting – a reminder of how a change in viewpoint can transform a problem. Thus the generalization – as such – leans heavily on the fact that an older literature reveals persistent daily and lunar rhythms to be extremely widespread phenomena; but it had to await recognition of such rhythms as manifestations of an underlying time measurement. It is this point of view that is of relatively recent origin.

This paradigm shift towards theory-driven research has inspired numerous investigations on entrainment of the circadian clock. A study from the group of Hanspeter Herzel (Institute for Theoretical Biology, Humboldt University of Berlin) looked into isophases in Arnold tongues (Bordyugov et al., 2015), which are regions in

the entrainment regime that share the same entrainment phase (i.e. the stable phase relationship between the endogenous oscillation and the external, entraining oscillation referred to as zeitgeber). In the said research, Bordyugov et al., 2015 numerically investigated how the entrainment phase is tuned depending on changes in detuning and the strength of the zeitgeber. This supported earlier empirical evidence in vertebrates, insects, and plants and unicellular organisms (Aschoff and Pohl, 1978). Notably, the numerical observations presented in the study also had high congruence with more recent experimental data. This was verified by analysing the effect of changes in detuning and/or the zeitgeber strength on the phase of entrainment in *Neurospora crassa* (Rémi et al., 2010) and in slices of the suprachiasmatic nucleus (SCN), the circadian pacemaker in mammals (Bordyugov et al., 2015).

That detuning affects entrainment phase echoes earlier descriptions of Pittendrigh and Bruce as they wrote in *An Oscillator Model for Biological Clocks* (Pittendrigh and Bruce, 1957):

Entrainment by the environmental cycle of light establishes the phase of the clock in addition to controlling its period; entrainment generally involves a unique phase relationship between the oscillator and its controlling periodicity.

Such dependence of the phase of entrainment on detuning has been attributed to occurrence of different human chronotypes (e.g. morning larks and night owls). In another study, numerical experiments revealed that, within the entrainment range, the entrainment phase varies with detuning over a range of 180° or π (Granada et al., 2013). This 180° rule appeared to be a feature of entrainment, and was consistently noted regardless if the analyses and numerical experiments were done using a phase response curve, a Kuramoto phase equation, or a periodically-driven damped oscillation. An insightful discussion in the aforementioned study is the visual description of the phase of entrainment based on phase response curves (Granada et al., 2013). A phase response curve (PRC) summarizes the response of an oscillation (i.e. shift in phase) to a perturbation (Johnson, 1999; Pikovsky et al., 2003; Izhikevich, 2007; Granada et al., 2013). This can alternatively be illustrated as a phase transition curve (PTC), which map the response in a plot of the phase after the perturbation (i.e. new phase) versus the phase before the perturbation (i.e. old phase). In this perspective, periodic perturbation can then be interpreted as iterative traversal along the PTC. Entrainment is henceforth achieved when the PTC intersects with the diagonal, where the new phase is equal to the old phase (i.e. a stable phase relationship is established between the endogenous oscillation and the periodic perturbation, equivalent to the entrainment phase) (Glass and

Mackey, 1988). In this visual representation, changing detuning, while keeping other things constant, can be generally regarded as shifting the same PTC in the phase space, either upwards or downwards the diagonal, as evidenced by numerical experiments and shown in Figure 1.5 (Granada et al., 2013). Such shifting results in a different intersection between the PTC and the diagonal, again where the new phase is equal to the old phase, and thus a different entrainment phase. For cases where the natural period of the endogenous circadian rhythm is more than the period of the day-night cycle (i.e. $\tau_o - \mathcal{T} > 0$), the PTC is shifted below the diagonal, implying most phases are delayed compared to the zeitgeber. On the other hand, for cases where the natural period of the endogenous circadian rhythm is less than the period of the day-night cycle (i.e. $\tau_o - \mathcal{T} < 0$), the PTC is shifted above the diagonal, implying most phases are advanced compared to the zeitgeber. Such curves in fact represent human chronotypes, where the former describes night owls (i.e. they are phase-delayed, waking up later and sleeping later) and the latter describes morning larks (i.e. they are phase-advanced, waking up earlier and sleeping earlier).

Studies on oscillator models of the circadian clock also revealed parameters that affect the transient to entrainment. For instance, two otherwise identical oscillations could have different times to achieve entrainment depending on their initial phases upon perturbation. Generally, an oscillation takes a longer time to get entrained if its initial phase is farther from the entrainment phase (Bagheri et al., 2008; Granada and Herzl, 2009). In addition to this and the properties of the entraining signal, transient time to entrainment is seen to be a feature inherent in the nature of oscillator. In particular, it was noted that the time for an oscillation to be entrained depends primarily on its radial relaxation time and the phase velocity distribution around the limit cycle (Granada and Herzl, 2009). Through numerical experiments with a generic limit cycle model, it was recorded that a low radial relaxation rate and an equal distribution of phases around the limit cycle (i.e. a sinusoidal waveform) results in longest transient times to entrainment (Granada and Herzl, 2009). Based on this, Granada and Herzl, 2009 propositioned that the fast entrainment of the circadian pacemaker in mammals (i.e. the suprachiasmatic nucleus, SCN) could be attributed to either of the following scenarios: (1) a sinusoidal oscillator with high radial relaxation rate, (2) a spike-like oscillator, which has uneven distribution of phase velocities around its limit cycle, with low radial relaxation rate, or (3) a spike-like oscillator with high radial relaxation rate. As there are numerous indications that the circadian oscillator has a sinusoidal waveform (Yamaguchi et al., 2003; Liu et al., 2007), it was suggested that the clock must have a short relaxation time. Combined theoretical and experimental considerations of the circadian clock moreover elucidated how coupling affects its entrainment, specifically by narrowing down its entrainment regime (Abraham et al., 2010).

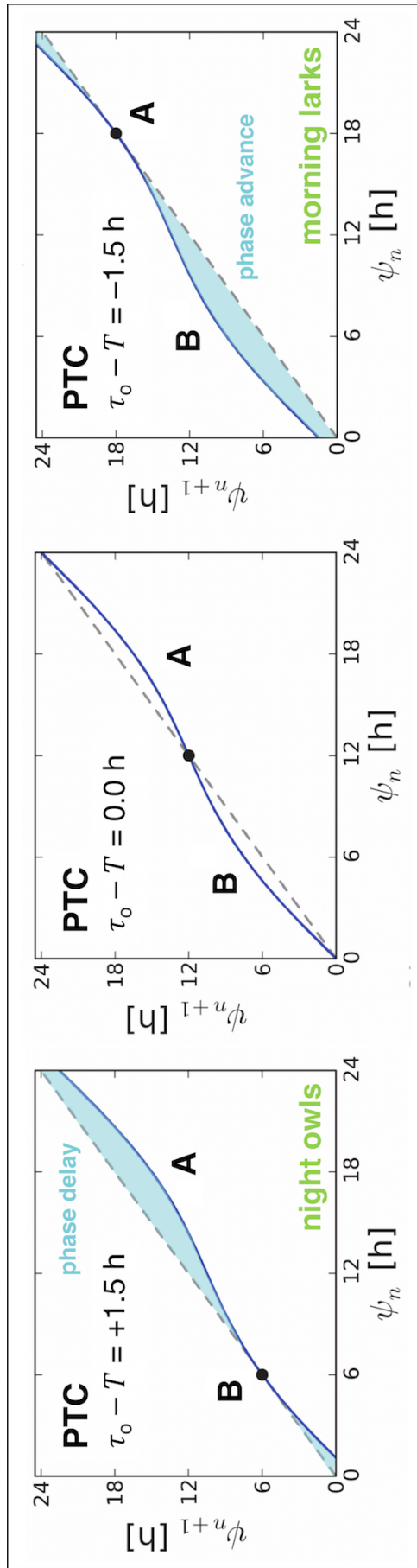


Figure 1.5 On detuning, entrainment phase, and human chronotypes. Numerically-determined phase transition curves at different detuning between endogenous circadian clock (τ_0) and the day-night cycle (i.e. zeitgeber, \mathcal{T}). Intersection of a curve with the diagonal, where the new phase is equal to the old phase, marks the entrainment phase at that detuning. Left-most and right-most plots depict phase delay in night owls and phase advance in morning larks, respectively. Adapted and modified from Granada et al., 2013.

Entrainment of infradian and ultradian rhythms

While circadian rhythms have a periodicity of 24 hours, there are other biological rhythms which have a periodicity longer or shorter than the day-night cycle on Earth (i.e. 24 hours). In fact, entrainment has also been recorded and studied in these other biological rhythms.

Entrainment has been noted between periodic stimuli and infradian rhythms, which have a period longer than 24 hours. For instance, it was found that the endogenous spawning cycle of *Platynereis dumerilii*, a marine annelid, is in synchrony with the lunar cycle and can be experimentally entrained in the laboratory with light (Zantke et al., 2013).

Entrainment of ultradian rhythms, which have a period less than 24 hours, has similarly been documented. In one research, oscillations of a transcription factor in myoblast cells (i.e. Hes1 oscillations, natural period = around 2-3 hours) were experimentally synchronized to periodic Dll1, a Notch ligand, via optogenetics (Isomura et al., 2017). Experimental entrainment has also been studied in other ultradian rhythms, like a synthetic genetic oscillator in bacteria (Mondragón-Palomino et al., 2011) and rhythmic nuclear translocation of a ligand in immune signaling (Kellogg and Tay, 2015; Heltberg et al., 2016). One elaborate ultradian rhythm is that involved in segmented tissue patterning in vertebrate embryos (i.e. somitogenesis), more commonly known as the segmentation clock (Hubaud and Pourquié, 2014; Oates et al., 2012). The segmentation clock during somitogenesis, a complex biological oscillatory system, is described in the next section, and its entrainment is the topic of this current research.

1.4 Somitogenesis, a complex spatially-extended biological system of coupled and phase-shifted signaling oscillations

1.4.1 Segmented tissue patterning in vertebrate embryos

Segmentation is a recurrent pattern in the animal kingdom (Tautz, 2004), and it has been documented in annelids (segmented worms), arthropods (e.g. insects and crustaceans), and chordates (e.g. vertebrates) (Davis and Patel, 1999; Tautz, 2004; Hannibal and Patel, 2013). In addition to visible reiterated partitioning of the body axis, each segment is more strictly defined by presence of some sort of anteroposterior polarity (Hannibal and Patel, 2013). A segment could be a single cell, like in the notochord of a sea squirt (i.e. *Ciona savignyi*, Jiang et al., 2005) and in the trunk of a crustacean (i.e. *Parhyale hawaiiensis*, Scholtz and Dohle, 1996; Browne et al., 2005), or a group of cells, like the somites in vertebrate embryos.

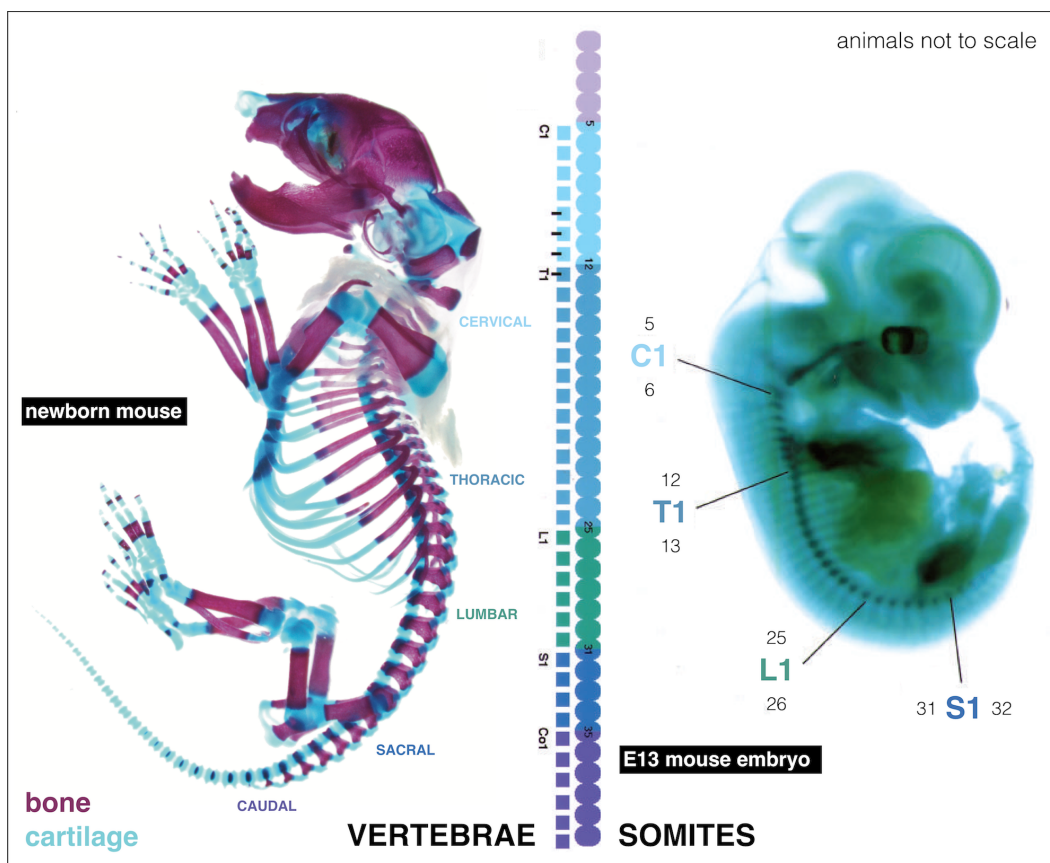


Figure 1.6 Somites lay out the segmented body plan of the mouse, a vertebrate. The segmented body plan in mouse, and other vertebrates, is laid out in embryonic development during somitogenesis, i.e. the formation of somites, the precursors of vertebrae. Skeletal staining of newborn mouse was done by Philipp Stachel-Braum in the lab of Bernhard Herrmann (Max Planck Institute for Molecular Genetics). Mouse embryo and scheme adapted and modified from Burke et al., 1995.

In vertebrate embryos, the segmented body plan is laid out in an event more commonly known as somitogenesis. During somitogenesis, the unsegmented mesoderm periodically forms somites, which upon resegmentation (i.e. "Neugliederung" according to Remak, 1855) will eventually give rise to the vertebrae (Remak, 1855; Ward et al., 2017; Criswell and Gillis, 2020) (Figure 1.6).

Somitogenesis has captivated many for a long time. For instance, in the early 1900s, the formation of somites in chick (Williams, 1910), and in rat (Butcher, 1929) were systematically described (Figure 1.7). Several investigations have revealed that the segmented patterning arising during somitogenesis even sketch out a prepattern for later development, like that in the development of brachial nerves in salamanders (Detwiler, 1934; Detwiler, SR, 1935) and that in the development of patterned plumage at the back of partridges and quails (Haupaix et al., 2018).

The periodic formation of somites, during somitogenesis, is tightly regulated both in time and in space. In a species, a somite forms at a particular tempo (e.g. an ultradian rhythm forming one left-right pair for every 2 hours in mice, Tam, 1981), and its total number is conserved, remarkably even for experimentally size-reduced embryos (Cooke, 1975; Tam, 1981; Ishimatsu et al., 2018). Such precise integration of both temporal and spatial information in tissue patterning during embryonic development has made somitogenesis an attractive system for both experimental and theoretical studies.

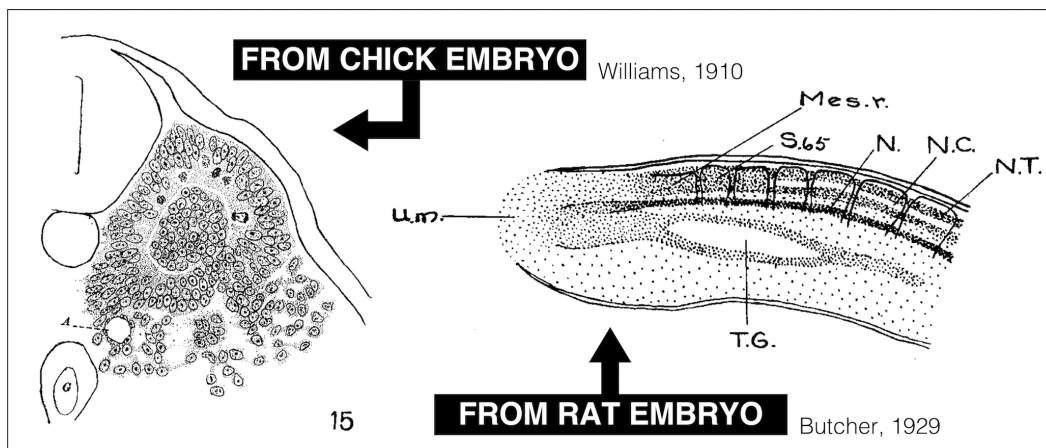


Figure 1.7 Early descriptions of somites in chick and rat embryos. **Left:** Transverse section through the middle of the last somite in a 44-somite chick embryo. A: aorta. G: [endoderm]. **Right:** Sagittal reconstruction of the tip of tail of rat embryo near the end of somitogenesis. u.m.: undifferentiated material. Mes.r.: mesodermal remnant. T.G.: tail gut. S.65: 65th somite. N: notochord. N.C.: neural canal. N.T.: neural tube. Figures adapted and modified from Williams, 1910 (i.e. Series 98, Section 287, for the chick embryo) and Butcher, 1929 (i.e. Series 180, Section 73, for the rat embryo).

1.4.2 Theoretical models of tissue patterning

Clock and wavefront model by Jonathan Cooke and Erik Christopher Zeeman

In 1975, Jonathan Cooke reported that the number of somites are similar, though proportionally smaller, in size-reduced frog embryos than controls (Cooke, 1975). A year later, Cooke and Erik Christopher Zeeman proposed a model to explain the observation (Cooke and Zeeman, 1976). In describing the model (Figure 1.8), Cooke and Zeeman wrote:

The model involves an interacting “clock” and “wavefront”. The clock is a smooth cellular oscillator, for which cells throughout the embryo are assumed to be phase-linked. The wavefront is a front of rapid cell change moving slowly down the long axis of the embryo... At the phenomenological level, cells in early embryos characteristically behave “smoothly” and stably with little overt change for considerable periods, interspersed with relatively rapid overt changes of behaviour and state of determination... the large unit time we propose as that occupied by transit of the wavefront must be partitioned by a regular series of much shorter time intervals... We propose that the latter are provided by an oscillator.

Classical interpretation of the clock and wavefront model argues that the somite size is a product of the velocity of regression of a posteriorly-moving molecular gradient (i.e. wavefront) and the period of the segmentation clock.

Phase-shift model by Brian C. Goodwin and Morrel H. Cohen

Meanwhile, Brian C. Goodwin and Morrel H. Cohen proposed that oscillatory dynamics in a tissue could encode both temporal and spatial information (Goodwin and Cohen, 1969). More precisely, Goodwin and Cohen asserted that:

...the map arises from wave-like propagation of activity from localized clocks or pacemakers. Individual cells are supposed temporally organized in the sense that biochemical events essential for the control of development recur periodically. This temporal organization of an individual cell is converted by functional coupling between cells into a spatial ordering of the temporal organization.

In this model (Figure 1.8), relative position along an axis is mapped based on the phase difference between one oscillation and a reference oscillation.

CLOCK AND WAVEFRONT MODEL

PHASE-SHIFT MODEL

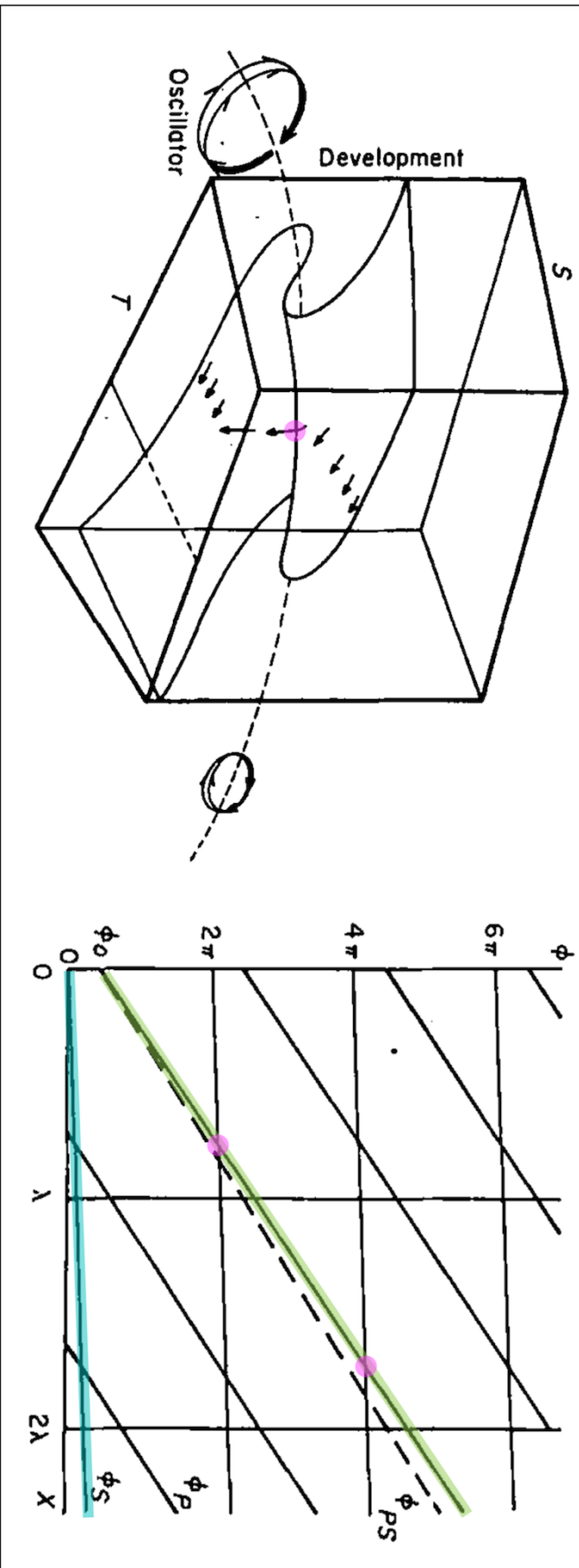


Figure 1.8 Theoretical models for periodic tissue patterning during somitogenesis. Clock and wavefront model: A smooth interval of time, through the passing of a posteriorly moving wavefront, is partitioned into smaller discrete units by the ticking of a clock. Classical interpretations of the model imply that the wavefront is determined by a molecular/morphogen gradient, that is independent of the segmentation clock. S denotes real space along the anteroposterior axis, while T denotes real developmental time. Point of "catastrophic instability", where a group of cells in a region of the presomitic mesoderm differentiates into a somite, is marked with a magenta circle. Adapted and modified from Figure 3 of Cooke and Zeeman, 1976. **Phase-shift model:** Positional information is encoded in the difference (ϕ_{PS} , dashed line) between the phase of one oscillation (ϕ_S , cyan line) and the phase of another oscillation (ϕ_P , green line). Without bounds to the increase of unwrapped ϕ_{PS} along the spatial axis, the spatial information is periodic (i.e. here, with spatial periodicity of λ). Regions where P and S are in-phase (i.e. their phase difference is equal to $0, 2\pi$, or 4π) are marked with magenta circles. Adapted and modified from Figure 2 of Goodwin and Cohen, 1969.

1.4.3 Signaling oscillations in the PSM: the segmentation clock

Signaling oscillations play a key role in the segmented patterning of the main body axis (i.e. the anterior-posterior axis, AP) of vertebrate embryos (Palmeirim et al., 1997). Cells of the presomitic mesoderm (PSM) elicit autonomous, intracellular signaling oscillations that are synchronized intercellularly. Synchronization of these oscillations mediates the periodic formation of somites, the precursors of the vertebrae. This is precisely regulated by the segmentation clock, an intricate genetic network consisting of FGF, Wnt, and Notch signaling (Dequéant and Pourquié, 2008; Hubaud and Pourquié, 2014; Aulehla et al., 2003; Dequéant et al., 2006; Aulehla et al., 2007). FGF and Wnt establish signaling gradients along the AP axis, while Notch is linked to the intercellular coupling and synchronization of signaling oscillations between PSM cells (Lewis, 2003; Aulehla and Pourquié, 2008; Aulehla and Pourquié, 2010; Herrgen et al., 2010; Niwa et al., 2011). Cross-talk between signaling oscillations in these three signaling pathways have been studied before, for instance by Niwa et al., 2011 on Notch and FGF and by Sonnen et al., 2018 on Notch and Wnt. YAP signaling has also been shown to be integrated in the segmentation clock, suggesting a feedback between tissue mechanics and oscillatory dynamics (Hubaud et al., 2017; Diaz-Cuadros et al., 2020). Transcriptome study of an *in vitro* system derived from stem cells has revealed a wide array of oscillating transcripts in human and mouse PSM, including genes involved in the maintenance of the circadian rhythm (Matsuda et al., 2020). Certainly, the segmentation clock is an elaborately complex system of multiple molecular key players (Figure 1.9).

1.4.4 Notch signaling and intercellular coupling of intracellular signaling oscillations in the mouse PSM

Elaborating on the work of Brian C. Goodwin regarding temporal organization in cells, Conrad H. Waddington proposed that if information could indeed be encoded "talandically" (i.e. via oscillations, Goodwin et al., 1963), then cells in tissues would do so by intercellular contact (Waddington, 1965). In the PSM, such contact is now attributed to Notch signaling. Live imaging of Notch signaling reporters has revealed that oscillations between cells in the PSM are not completely in-phase, but are slightly phase-shifted (Aulehla et al., 2007; Masamizu et al., 2006). The phase-shifted oscillations give an impression of a spatiotemporal wave pattern that traverses the AP axis of the PSM, similar to a stadium wave. This wave-like Notch signaling expression domain propagates from posterior PSM to anterior PSM, an example of collective dynamics emerging from a complex system at high levels of organization (Figure 1.10).

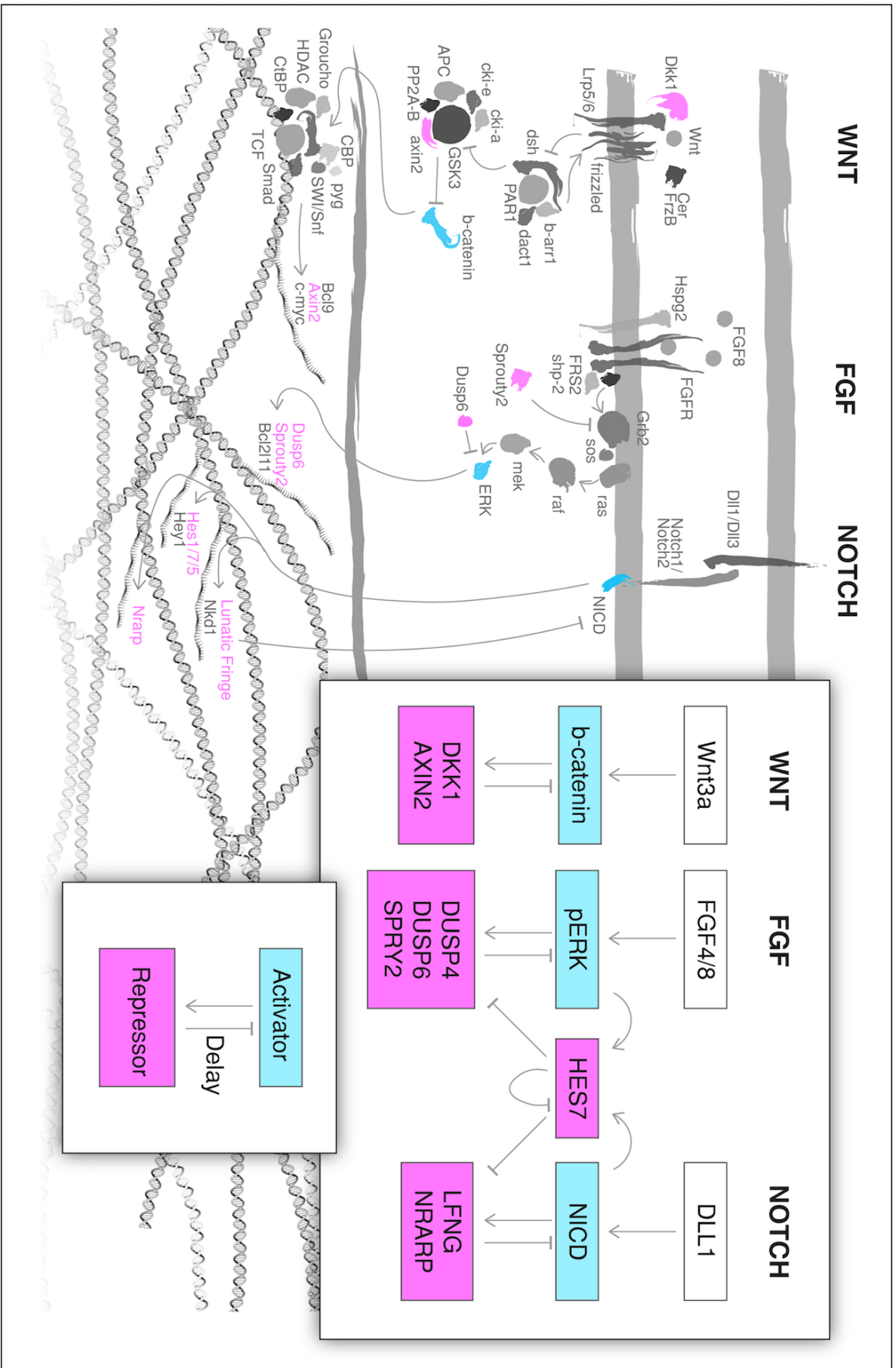


Figure 1.9 The segmentation clock is an elaborate molecular network of oscillatory signaling pathways. Illustrated are three key oscillatory signaling pathways in mouse somitogenesis: Wnt signaling, FGF signaling, and Notch signaling. Also shown is the topology of a delayed negative feedback loop, known to generate biological oscillations. Illustration by Stefano Vianello. Adapted and modified from Dequeant et al., 2006 and Hubaud and Pourquie, 2014.

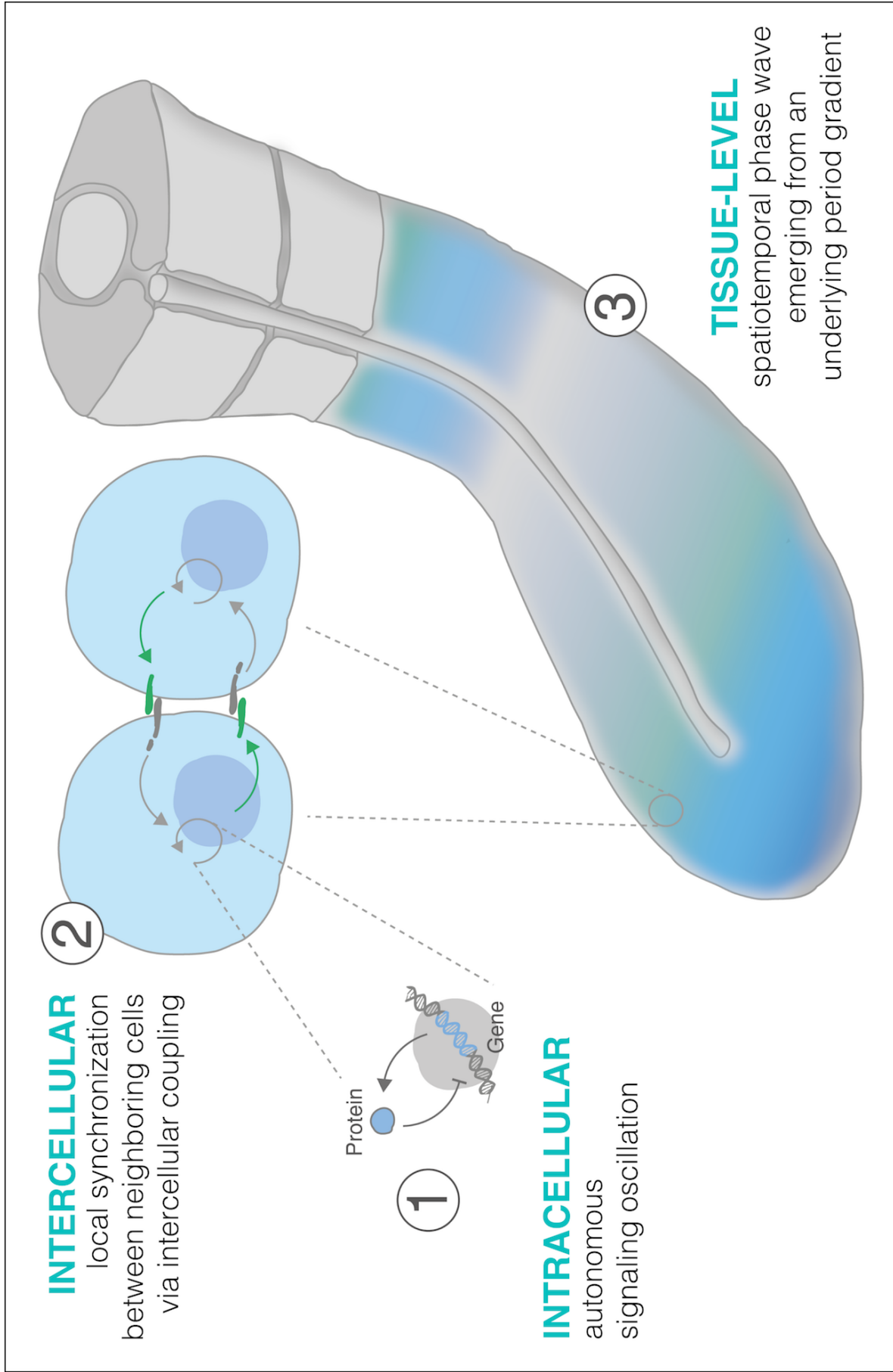


Figure 1.10 Levels of organization in the presomitic mesoderm (PSM). Autonomous intracellular signaling oscillations in the PSM, generated via an elaborate molecular network of signaling pathways (Figure 1.9), are coordinated between neighboring cells via intercellular coupling. These oscillations are phase-shifted along the AP axis of the tissue, resulting in an impression of a spatiotemporal wave pattern sweeping the tissue from posterior to anterior. Arrest of the wave at the anterior PSM coincides with somite formation. Illustration by Stefano Vianello. Adapted and modified from Oates et al., 2012.

Waddington, 1965 further described that:

A system in periodic motion frequently has a property analogous to inertia – the oscillation tends to continue, unless some definite influence occurs to produce damping, or some other more powerful controlling system is superposed on it and suppresses it... It is therefore one of the candidates for the "carriers of more or less stable cellular differentiation", the identification of which is one of the major problems of present-day theoretical biology.

Interestingly, the observed phase wave of Notch signaling in the PSM in fact emerges from an underlying gradient in periods of intracellular oscillations along the tissue's AP axis (Falk, 2019). In mouse embryos, Notch signaling oscillations gradually slow down from around 1 oscillation every 130 mins in the posterior PSM to around 1 oscillation every 170 mins in the anterior (Tsiairis and Aulehla, 2016). In the anteriormost PSM, arrest of signaling oscillations coincides with the formation of a new somite. Remarkably, while somitogenesis takes place in the anterior PSM, its period (around 2 hours in mouse embryos) matches the period of the oscillations in the posterior PSM (the fastest ones), rather than that in the anterior (slowest) (Soza-Ried et al., 2014; Tsiairis and Aulehla, 2016). Elucidation of whether the underlying period gradient is the "carrier" or a readout of "stable cellular differentiation" in the PSM has not been fully addressed.

Notch signaling is noted to mediate the collective temporal dynamics in the PSM, generally controlling the period of segmentation (Soza-Ried et al., 2014; Herrgen et al., 2010; Liao and Oates, 2017). In addition to mediating collective temporal dynamics during somitogenesis (i.e. when somites form), Notch signaling oscillations have also been reported to encode spatial information in the said embryonic tissue (i.e. where somites form) (Sonnen et al., 2018; Lauschke et al., 2012). Moreover, Notch signaling is shown to facilitate intercellular coupling and coupling delay during somitogenesis (Morelli et al., 2009; Herrgen et al., 2010; Yoshioka-Kobayashi et al., 2020; Oates, 2020).

In a recent study, intercellular coupling via Notch signaling was documented to account for synchronization of intracellular signaling oscillations in the mouse PSM. In mouse embryos lacking functional *Lfng*, a glycosyltransferase involved in Notch signaling (Evrard et al., 1998), intracellular signaling oscillations in the PSM are preserved but are asynchronous (Yoshioka-Kobayashi et al., 2020). Furthermore, *Lfng* was found to be involved in delays in intercellular coupling in mouse PSM cells, lengthening the transmission of Notch signaling from the cell sending the signal (i.e. Delta1, a Notch ligand).

1.4.5 Some recent advances in studying signaling oscillations in the mouse PSM

Spreadout, an *ex vivo* primary tissue culture assay for studying somitogenesis

Our lab developed a 2D-system (herein referred to as spreadout) that recapitulates key features of somitogenesis (Lauschke et al., 2012). This has enabled us to study signaling oscillations in a system that is more amenable to experimental perturbation than the living embryo. To generate spreadouts, we cut the posteriormost tip of the PSM (i.e. the tailbud) and culture it on fibronectin-coated glass. Spreadouts show signaling oscillations and spatiotemporal wave patterns that are reminiscent of an intact PSM (Figure 1.11). The wave-like expression domain propagates from center to periphery, comparable to the posterior-to-anterior PSM signaling dynamics. Accordingly, and mimicking the anterior-to-posterior formation of somites *in vivo*, segments form from the periphery of the spreadout to its center.

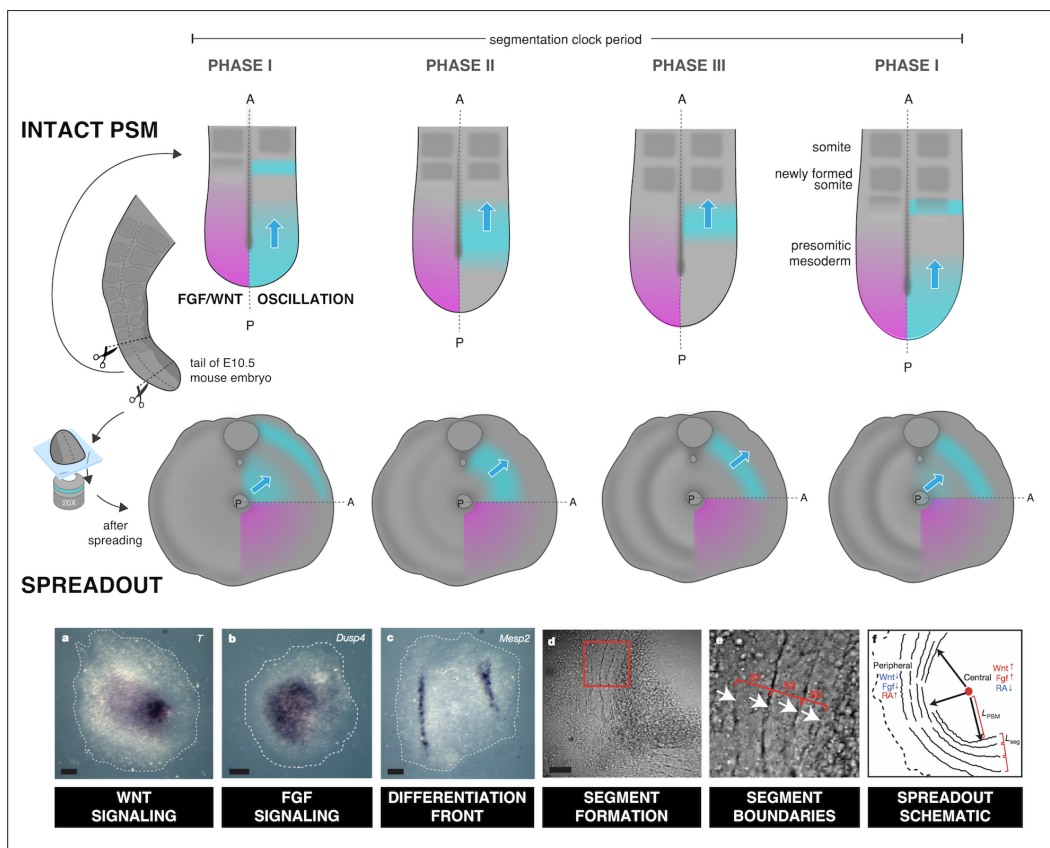


Figure 1.11 Spreadouts recapitulate key features of mouse somitogenesis. Schematic representation of the morphogen gradient and the segmentation clock in intact PSM and in a spreadout. The anteroposterior (AP) axis in the two experimental systems is specified. The center of a spreadout corresponds to posterior PSM, while its periphery corresponds to anterior. Illustration by Stefano Vianello. Bottom row: figures adapted and modified from Lauschke et al., 2012 which show: gradient of Wnt and FGF signaling visualized using *in situ* hybridization of spreadouts with probes against downstream targets, i.e. T for Wnt signaling (a) and *Dusp4* for FGF signaling (b); onset of differentiation at the periphery of spreadouts visualized using probes against *Mesp2* (c); and physical segment boundaries forming from periphery towards the center (d and e). Videos of oscillatory dynamics in intact PSM and in a spreadout are available at <https://youtu.be/T-fa1gYfwJk> and <https://youtu.be/EBLRLXUcsGk>, respectively.

Other experimental systems

In addition to spreadouts, various other experimental systems have been used to study somitogenesis in vertebrates. In 1976, for instance, PSM (i.e. *mésoderm somitique*) of frog and toad embryos was surgically isolated from its adjacent tissues (i.e. notochord, neural tube, ectoderm, and endoderm) and cultured in physiological buffer. This revealed that the PSM can autodifferentiate into somites and eventually develop into muscle (Brustis, 1976). A few years later, PSM of a snapping turtle was successfully explanted onto agar medium (Packard, 1980). Similar to the earlier study, somites formed irrespective of whether the PSM was cultured by itself or with the neural tube and/or the notochord. In an experimental protocol now more commonly known as a Keller explant, Raymond Keller (now with the Department of Biology, University of Virginia) and colleagues optimized explantation of the frog mesoderm. Using Keller explants, convergent extension in the frog PSM during somitogenesis was directly observed and examined (Keller et al., 1985; Wilson et al., 1989). Cells of the PSM have also been studied either with other dissociated cells or in isolation (Maroto et al., 2005; Masamizu et al., 2006; Webb et al., 2016; Tsiairis and Aulehla, 2016; Hubaud et al., 2017; Ho, 2020; Yoshioka-Kobayashi et al., 2020). More recently, stem cell-derived experimental systems have been developed to study signaling oscillations during somitogenesis (Chal et al., 2015; Hubaud et al., 2017; Matsumiya et al., 2018; Chu et al., 2019a; Diaz-Cuadros et al., 2020). These include gastruloids, self-organizing *in vitro* models exhibiting axial elongation and segmentation (van den Brink et al., 2020).

Dynamic readout

To monitor signaling oscillations in the mouse PSM, our lab has generated mouse lines expressing reporters of some of the cyclic genes of the segmentation clock (Sonnen et al., 2018; Dequéant et al., 2006; Aulehla et al., 2007). To visualize Notch signaling oscillations, we use LuVeLu, a mouse line expressing a destabilized reporter (i.e. Venus, Nagai et al., 2002) driven from the *Lfng* promoter, a downstream target of Notch (Aulehla et al., 2007). Meanwhile, to visualize Wnt signaling oscillations, we previously used a knock-in line expressing a reporter inserted into the *Axin2* locus, a downstream target of Wnt, separated by a T2A self-cleaving site (Sonnen et al., 2018). Recently, we use a mouse line expressing *Axin2* fused to a fast-maturing version of YFP (i.e. Achilles, Yoshioka-Kobayashi et al., 2020).

Dynamic perturbation

In addition to a dynamic readout, dynamic perturbation is important to dissect the role of signaling dynamics in the PSM (Sonnen and Aulehla, 2014). In this relation, our lab has optimized a microfluidics-based experimental platform to simultaneously culture, image, and subject spreadouts to pulses of signaling modulators (Figure 1.12) (Sonnen et al., 2018).

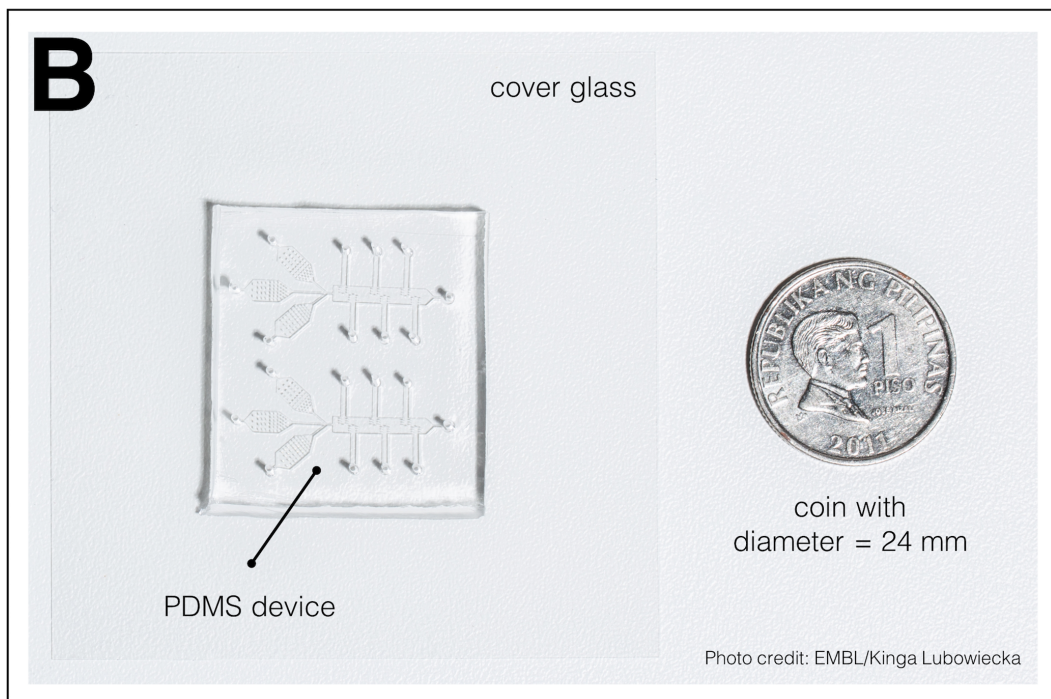
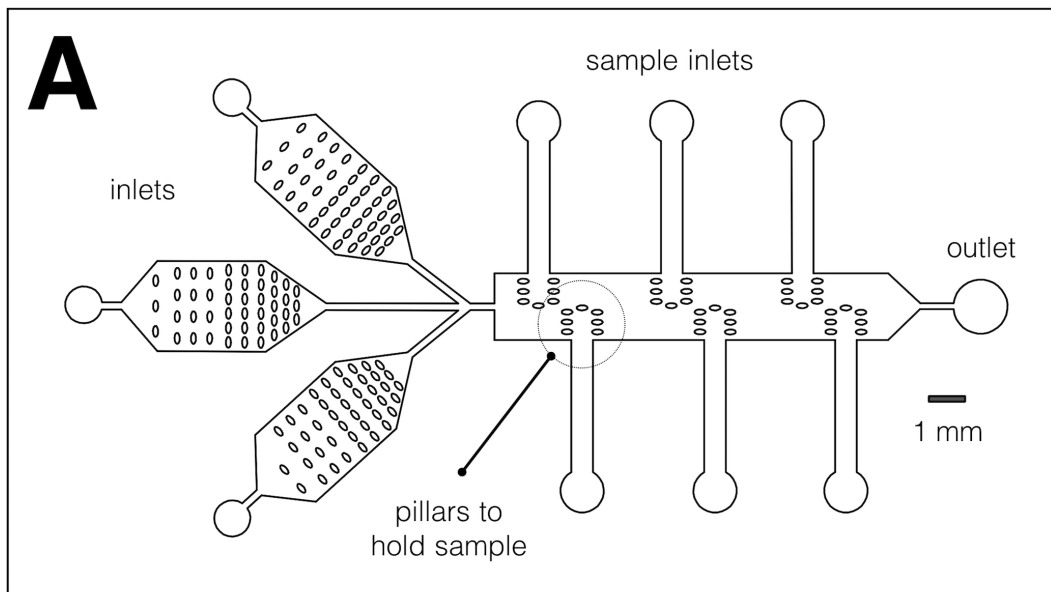


Figure 1.12 A microfluidics PDMS chip for culture, imaging, and entrainment of an *ex vivo* model of somitogenesis. (A) Design of the microfluidics chip, showing inlets for medium and drug, inlets for the samples, pillars to hold each sample, and an outlet. (B) Photo of the chip bonded to cover glass and a coin (diameter: 24 mm) for scale. The split layout separating the upper and lower channel systems allows simultaneous delivery of drug and DMSO control to samples on opposite sides of the same device. Photo credit: EMBL/Kinga Lubowiecka.

1.4.6 Some findings from our lab regarding signaling oscillations during somitogenesis

Collective oscillatory dynamics self-organize

In mouse embryos, we found that the spatiotemporal wave pattern of Notch signaling, a phase wave, emerges from an underlying period gradient along the AP axis (Falk, 2019). In spreadouts, an *ex vivo* model of somitogenesis which start out as a population of relatively homogeneous cells from the posteriormost tip of the mouse embryo tail (i.e. tailbud), with narrow period and phase distribution, we documented too that a period gradient emerges preceding propagation of a phase wave and segmentation of the tissue (Lauschke et al., 2012). Strikingly, we also noted emergence of the period gradient, organized from multiple foci, in a population of dissociated PSM cells (Tsiairis and Aulehla, 2016; Ho, 2020). These indicate that the period gradient is an emergent property of a population of PSM cells, each eliciting intracellular signaling oscillations.

Oscillatory dynamics also encode spatial information

Experiments in spreadouts, which undergo segmentation in the absence of axial elongation, reveal that the slope of the phase gradient, emerging from coupled oscillations in the PSM, is predictive of segment size (Lauschke et al., 2012). This implies that the positional information for segmentation as well is encoded in the collective dynamics of the oscillations. Recently, we also noted that the phase difference between LuVeLu oscillations (i.e. Notch reporter) and Axin2 oscillations (i.e. Wnt reporter) vary intracellularly across the PSM (Sonnen et al., 2018). In particular, in cells in the posterior PSM, the LuVeLu oscillations are out-of-phase to the Axin2 oscillations. The magnitude of this phase difference decreases towards the anterior, where the LuVeLu oscillations in cells become in-phase to the Axin2 oscillations. To further investigate this phenomenon, we developed a microfluidics-based platform that has allowed us to subject spreadouts to periodic pulses of signaling modulators (Sonnen et al., 2018). LuVeLu oscillations and Axin2 oscillations synchronize to 130-min periodic pulses of DAPT (i.e. a γ -secretase inhibitor, which inhibits Notch signaling) and Chiron (i.e. a GSK3 β inhibitor, which mimics downstream consequences of Wnt signaling activation), respectively. By modulating the timing of DAPT and Chiron pulses, we managed to tune the phase difference between the two oscillations. We reported that segments formed only when LuVeLu and Axin2 oscillations in PSM cells were in-phase (Sonnen et al., 2018), demonstrating the utility of entrainment in uncovering the nature and mechanism of synchronized signaling oscillations during somitogenesis. These findings further reveal that positional information is more specifically encoded in the phase-shift between intracellular signaling oscillations.

Aims of the study

” *I certainly have a feeling that I am discovering something that existed before me.*

— **Vladimir Igorevich Arnold**

Oscillations govern rhythms in biology, and entrainment behavior has been studied in various biological systems (Buck and Buck, 1968; Abraham et al., 2010; Soza-Ried et al., 2014; Bordyugov et al., 2015; Kellogg and Tay, 2015; Isomura et al., 2017; Sonnen et al., 2018). As fundamental concepts and principles in entrainment should extend to all oscillations, regardless of their nuances, entrainment can be used as both (a) a conceptual approach to deepen understanding of the nature of biological oscillations, and (b) an experimental tool to dynamically perturb their rhythms.

Through such principles-based top-down approach, using microfluidics-based experimental entrainment, this current research aims to delineate entrainment behavior of the segmentation clock in the presomitic mesoderm (PSM), a complex biological system of coupled and phase-shifted signaling oscillations. In particular, we intend to elucidate whether or not the segmentation clock follows general entrainment behavior, as noted in other less complex oscillatory systems. Moreover, we set to use entrainment to precisely control its period and phase, while remaining agnostic of what happens at the molecular level. More specifically, in the next chapters, we aim to address the following key questions:

CHAPTER 3

Does the segmentation clock obey unifying physical principles in synchronization?

CHAPTER 4

Is an emergent period gradient important for segmentation of the PSM?

CHAPTER 5

Does modulating the segmentation clock affect somitogenesis according to the classical clock and wavefront model?

Does the segmentation clock obey unifying physical principles in synchronization?

” *At the heart of the universe is a steady, insistent beat: the sound of cycles in sync.*

— Steven Strogatz

The universality of the principles governing synchronization in non-biological systems suggests that conceptual and experimental strategies used to understand such phenomena might similarly be leveraged to deepen our understanding of biological oscillatory systems. Oscillations are indeed integral to many biological processes, one of these being that of somitogenesis. In vertebrate embryos, signaling oscillations govern the periodic segmentation of the presomitic mesoderm (PSM, the unsegmented tissue at the posterior of the embryo) to form somites, the precursors of the vertebrae. Yet, while studies delving into the molecular network underlying somitogenesis (i.e. the segmentation clock) are abundant, investigations on the extent to which the behavior of signaling oscillations in the PSM follows universal principles in synchronization remain limited. Recently, we reported that microfluidics-based entrainment could allow the synchronization of signaling oscillations of an *ex vivo* somitogenesis model (Lauschke et al., 2012) (i.e. a spreadout) to periodic pulses of external signaling modulators (Sonnen et al., 2018). Here we elaborate on such entrainment behavior, and describe how it obeys principles of dynamical systems theory, despite the expected complexity of an embryonic tissue such as the mouse PSM. This has allowed us to systematically control both the period and the phase of the segmentation clock. We also report a unique entrainment behavior characterising the mouse PSM, which comes to be interpreted as a spatially-extended system of coupled and phase-shifted oscillations. As oscillating entities are expected to generally obey fundamental entrainment principles, we are certain that such an approach could then be further leveraged to probe the nature and mechanism of synchronization in a complex biological system.

3.1 Results

3.1.1 A microfluidics-based experimental platform enables entrainment of the segmentation clock to periodic pulses of DAPT

Studying dynamic signaling, like the oscillations in the PSM, necessitates both (a) a dynamic readout of the signaling state of the system under investigation and (b) a way to dynamically perturb such an endogenous rhythm and systematically alter its behavior (Sonnen and Aulehla, 2014). In this study, we focused on an *ex vivo* model of somitogenesis (more commonly known as a spreadout) recapitulating key features of somitogenesis in quasi-2D (Lauschke et al., 2012), and we visualized the signaling oscillations of Notch in this model using tissue from LuVeLu reporter mouse embryos (Aulehla et al., 2007). To perturb such oscillations, we developed a microfluidics device made of polydimethylsiloxane (PDMS) bonded to cover glass (Figure 1.12) where we could culture multiple tissue samples (Sonnen et al., 2018). Accordingly, this experimental setup allowed us not only to subject these samples to periodic pulses of external signaling modulators, but also to simultaneously visualize the effect of such perturbation on the oscillatory dynamics and patterning of the tissue (Figure 3.1A).

We approximated the signaling oscillations in the PSM based on the tissue-level dynamics of *Lfng*, visualized using LuVeLu, which coincides with the periodic segmentation of the tissue (i.e. the segmentation clock). This systems-level oscillation corresponds to the spatiotemporal wave pattern of *Lfng* traveling along the AP axis (from center to periphery of a spreadout), and the cyclic expression of a bright *Lfng* stripe in the anterior PSM (in the periphery of a spreadout), which marks the prospective somite (Cole et al., 2002; Morales et al., 2002). During PSM segmentation, the elevated *Lfng* in the stripe expression domain significantly contributes to the global intensity of LuVeLu, coinciding with the arrival of the spatiotemporal wave at the anterior PSM (periphery of a spreadout), as exemplified in Figure 8.1. By following the mean intensity value of the entire field of view during timelapse imaging, we thus acquire the timeseries corresponding to the rhythmic ticking of the segmentation clock (Figure 3.1A-B).

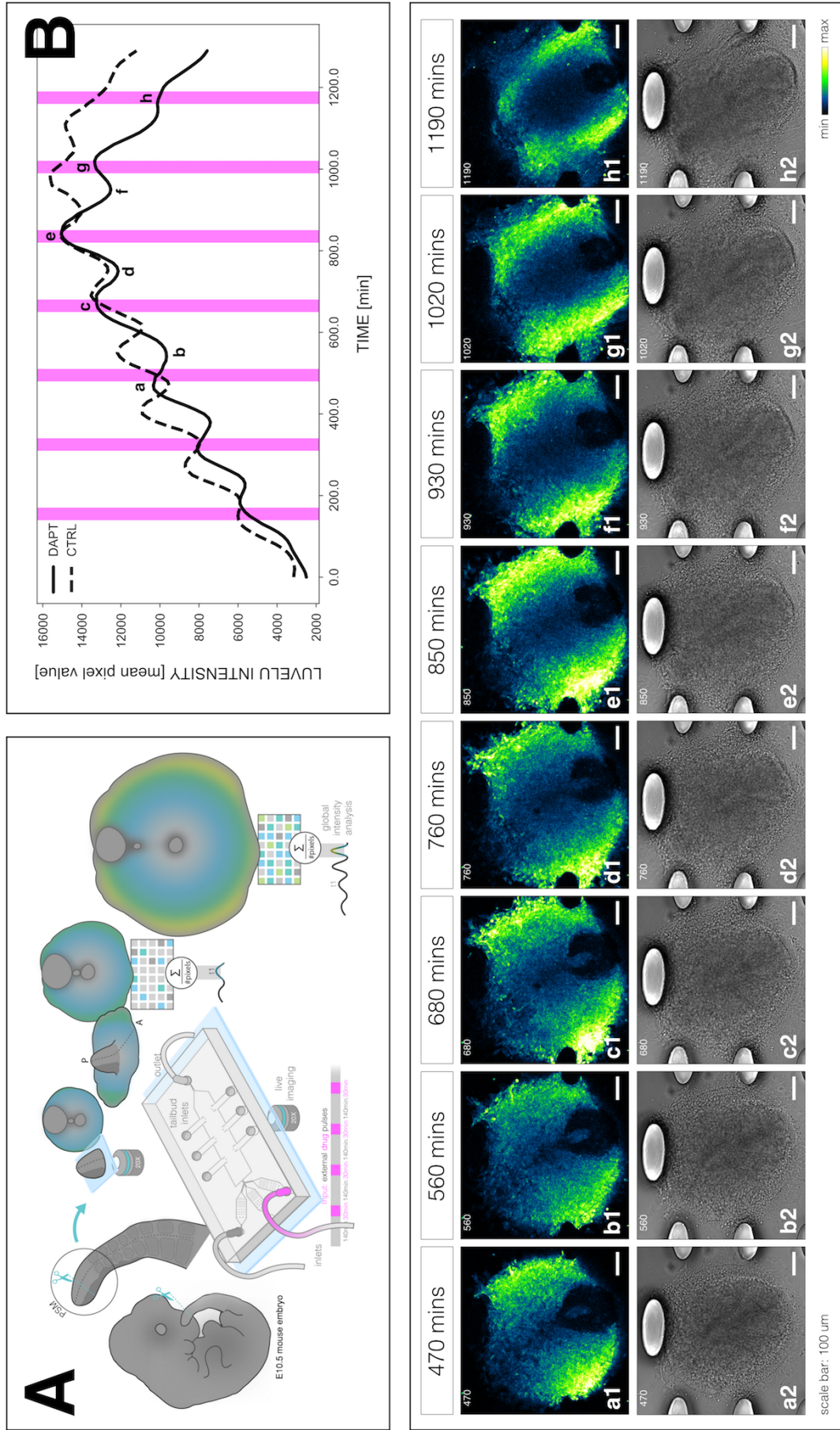


Figure 3.1 A microfluidics-based experimental platform enables simultaneous visualization and entrainment of signaling oscillations in a spread-out, an ex vivo model of somitogenesis. (A) Schematic of the microfluidics-based experimental platform where a spread-out is simultaneously imaged and subjected to periodic pulses of a drug. Relying on the tissue-level dynamics of *Lfng*, visualized by LuVeLu, global intensity analysis is used to recover systems-level signaling oscillations corresponding to the ticking of the segmentation clock. In particular, intensity profile (timeseries) is obtained by following the mean value of all the pixels in the 512 pixel x 512 pixel field of view across time. Illustration by Stefano Vianello. (B) Raw timeseries of segmentation clock subjected to 170-min periodic pulses of 2 μ M DAPT (or DMSO for control). The timeseries of the entrained sample and the control are marked with a solid line and a dashed line, respectively. Periodic pulses are indicated as magenta bars. Snapshots of LuVeLu (1) and brightfield (2) imaging of the DAPT-entrained sample at different timepoints (a-h) are specified.

3.1.2 Entrainment to periodic pulses of DAPT allows control over the period of the segmentation clock

An unperturbed autonomous oscillation will cycle on its own free-running, natural period. During entrainment, the instantaneous period of the autonomous oscillation comes to be locked to the period of an external periodic perturbation, such that the difference in their periods eventually becomes equal to zero (Pikovsky et al., 2003). Concomitantly, entrainment is more easily achieved when the detuning between the two oscillations (i.e. the mismatch between the natural period of the endogenous oscillation and the period of the perturbation) is low. Using our microfluidics-based experimental platform, we were able to control the period of the endogenous segmentation clock, coinciding with segmentation of the embryonic tissue, by entraining it to periodic pulses of 2 μ M DAPT. As each sample actively synchronized to the DAPT pulses during entrainment, independent samples became synchronous and more coherent (Figure 3.2A). While controls subjected to periodic pulses of DMSO cycled close to the free-running period of approximately 140 mins, entrained samples cycled with a period matching the period of the DAPT pulses (Figure 3.2B-C).

By modulating the interval between the DAPT pulses, thus changing the period of the perturbation, we could change the period of the segmentation clock (Figure 3.2D, 8.2-8.3), and as such the tempo when segments would form. As shown in Figure 3.2D, we were able to both speed up and slow down the segmentation clock. Notably, period-locking was less precise (i.e. higher standard deviation and standard error of the mean as shown in Table 3.1) in 120-min and 180-min periodic pulses of 2 μ M DAPT, which were also the perturbation periods that were the farthest from the free-running period of the endogenous oscillation (i.e. those with the highest detuning).

Guided by synchronization theory, changing entrainment strength, by changing the concentration of DAPT, predictably affected ease of entrainment of the segmentation clock as exemplified in Figure 3.3 (for 170-min periodic DAPT pulses) and Figure 8.4 (for 130-min periodic DAPT pulses). Locking to period of DAPT pulses was faster in samples entrained with a higher drug concentration (Figure 3.3B, 8.4A). Independent samples were also more coherent at higher concentrations as evidenced by higher first Kuramoto order parameter (Figure 3.3C-D, 8.4B).

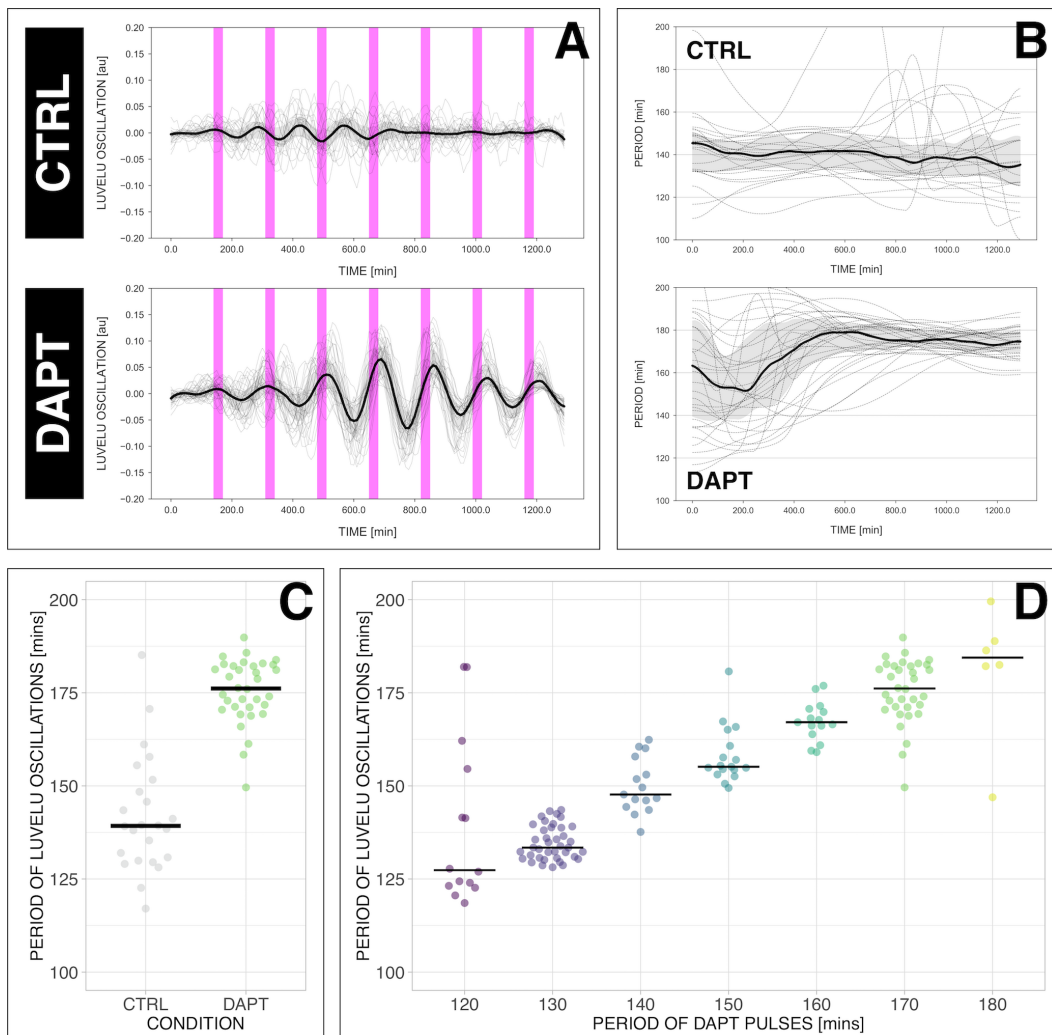


Figure 3.2 Entrainment to periodic pulses of DAPT allows control of the period of the segmentation clock (A) Detrended timeseries of the segmentation clock in spreadouts subjected to 170-min periodic pulses of 2 μ M DAPT (or DMSO for controls). Periodic pulses are indicated as magenta bars and the timeseries of each sample (for CTRL: $n = 24$ and $N = 7$, for DAPT: $n = 34$ and $N = 8$) is marked with a dashed line. The median of the oscillations is represented here as a solid line, while the gray shaded area denotes the interquartile range. (B) Period evolution during entrainment, obtained from wavelet analysis. The period evolution for each sample and the median of the periods are represented here as a dashed line and a solid line, respectively. The gray shaded area corresponds to the interquartile range. (C) Mean period from 650 to 850 mins after start of the experiment of samples subjected to 170-min periodic pulses of 2 μ M DAPT (or DMSO for controls). Each sample is represented as a dot, while the median of all samples is denoted as a solid horizontal line. (D) Mean period from 650 to 850 mins after start of the experiment of samples entrained to periodic pulses of 2 μ M DAPT. Each sample is represented as a dot, while the median of all samples is denoted as a solid horizontal line. The period of the DAPT pulses is specified (for 120-min: $n = 14$ and $N = 3$, for 130-min: $n = 39$ and $N = 10$, for 140-min: $n = 15$ and $N = 3$, for 150-min: $n = 17$ and $N = 4$, for 160-min: $n = 15$ and $N = 3$, for 170-min: $n = 34$ and $N = 8$, for 180-min: $n = 6$ and $N = 1$). Data are visualized using PlotsOfData (Postma and Goedhart, 2019), and a summary of these data is provided in Table 3.1. A similar plot including each condition's respective control is in Figure 8.2. The analysis of period and wavelet power across time is summarized in Figure 8.3.

Table 3.1. Summary statistics on period-locking of the segmentation clock in E10.5 spreadouts to periodic pulses of 2 μ M DAPT. This table summarizes the median, 95% confidence interval (CI) of the median, mean, standard deviation (SD), standard error of the mean (SEM), and 95% CI of the mean period (in mins) of the segmentation clock in spreadouts subjected to periodic pulses of 2 μ M DAPT. These summary statistics were determined using PlotsOfData (Postma and Goedhart, 2019). A plot of these data is shown in Figure 3.2D.

Pulse Period	n	N	Median, mins	95% CI of Median, mins	Mean, mins	SD, mins	SEM, mins
120 mins	14	3	127.36	123.16 – 148.03	139.39	22.28	6.18
130 mins	39	10	133.44	132.21 – 135.97	134.75	4.56	0.74
140 mins	15	3	147.68	146.10 – 153.02	150.00	7.42	1.98
150 mins	17	4	155.14	154.33 – 160.74	158.18	7.77	1.94
160 mins	15	3	167.09	166.16 – 169.84	167.33	5.28	1.41
170 mins	34	8	176.14	173.06 – 181.20	175.56	8.52	1.48
180 mins	6	1	184.43	164.54 – 194.21	181.06	17.88	8.00

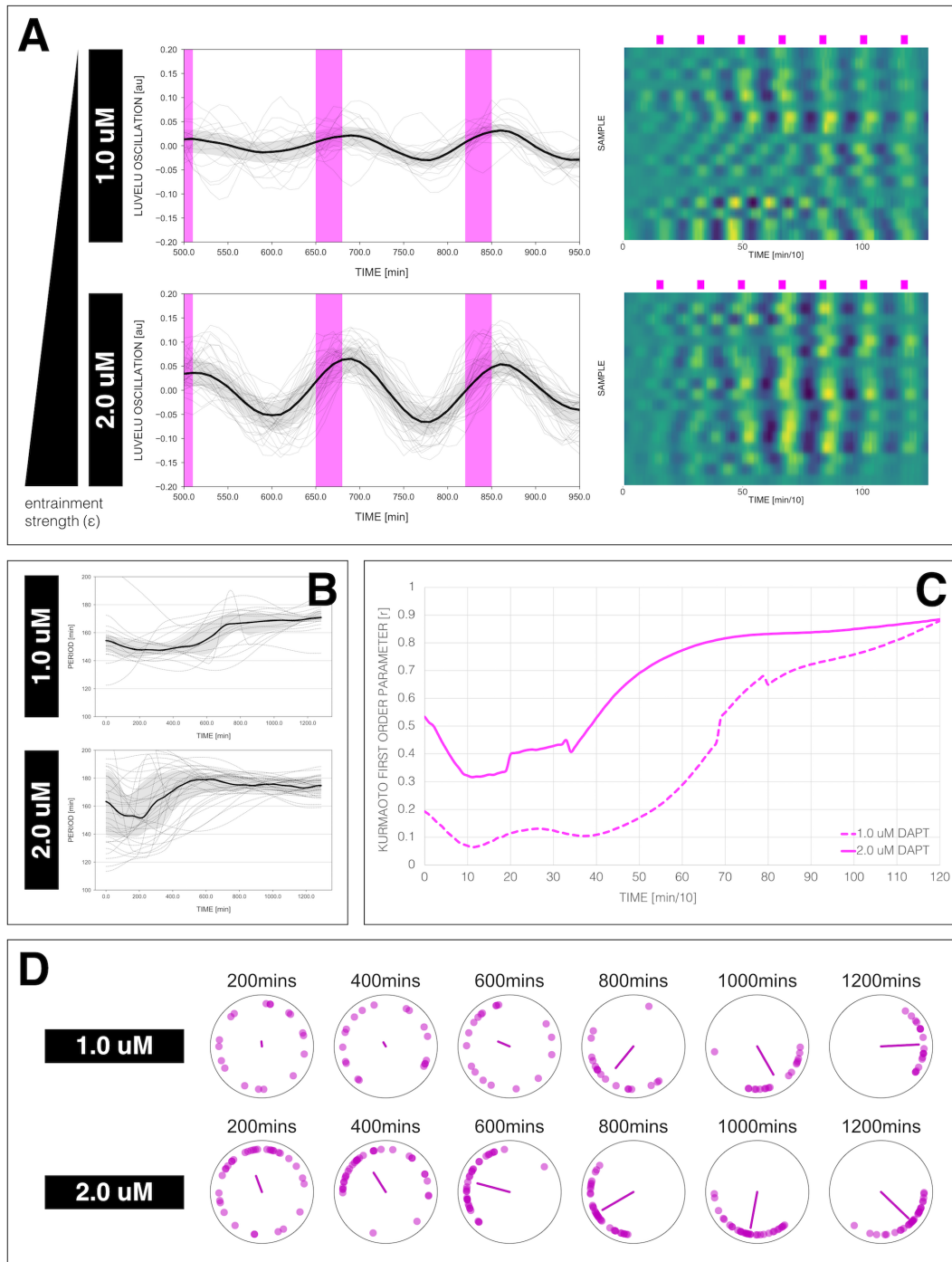


Figure 3.3 Changing the concentration of DAPT, equivalent to changing entrainment strength, affects entrainment of the segmentation clock to periodic DAPT pulses. (A) Left: Detrended timeseries of the segmentation clock in spreadouts entrained to 170-min periodic pulses of either 1.0 μM or 2.0 μM DAPT, zoomed in from 500 mins to 950 mins. Periodic pulses are indicated as magenta bars and the timeseries of each sample (for 1.0 μM : $n = 18$ and $N = 5$, for 2.0 μM : $n = 34$ and $N = 8$) is marked with a dashed line. The median of the oscillations is represented here as a solid line, while the gray shaded area denotes the interquartile range. The full detrended timeseries for the 2.0 μM DAPT condition can be seen in Figure 3.2A. Right: Detrended timeseries of the segmentation clock in spreadouts entrained to 170-min periodic pulses of either 1.0 μM ($n = 18$ and $N = 5$) or 2.0 μM ($n = 18$ and $N = 8$) DAPT represented as heatmaps. Periodic pulses are indicated as magenta bars. Each row corresponds to a sample. (B) Period evolution during entrainment, obtained from wavelet analysis. The period evolution for each sample and the median of the periods are represented here as a dashed line and a solid line, respectively. The gray shaded area corresponds to the interquartile range. (C) Evolution of first Kuramoto order parameter over time, showing change in coherence of multiple samples during the experiment. A first Kuramoto order parameter equal to 1.0 means that samples are in-phase. (D) Polar plots at different timepoints showing phase of each sample and their first Kuramoto order parameter, represented as a magenta dot along the circumference of a circle and a magenta line segment at the circle's center, respectively. A longer line segment corresponds to a higher first Kuramoto order parameter, and thus to more coherent samples. The direction of the line denotes the vectorial average of the sample phases.

3.1.3 The segmentation clock establishes a stable phase relationship with the periodic DAPT pulses via phase-locking

In addition to period-locking between the segmentation clock and the periodic DAPT pulses during entrainment, a stable phase relationship also becomes established between the two (i.e. they are phase-locked). To better understand the establishment of such phase relationship in our system, stroboscopic maps of the entrainment dynamics were plotted. Stroboscopic maps take a snapshot of the phase dynamics at regular intervals of time, specifically just before every pulse in a pulse train (Balanov et al., 2008; Isomura et al., 2017; Cross and Siggia, 2005; Izhikevich, 2007). To generate these maps for our entrainment experiments, the phase of the segmentation clock just before a DAPT pulse (old phase, at n th pulse, ϕ_n) was plotted against its phase just before the next DAPT pulse (new phase, at $n+1$ st pulse, ϕ_{n+1}) (Figure 3.4A). Each point in a stroboscopic map, thus, denotes a stepwise change in phase of the segmentation clock as it undergoes entrainment to the periodic DAPT pulses. Upon entrainment, if and when the segmentation clock ends up phase-locked to the periodic DAPT pulses, the new phase will be equal to the old phase. Successive iterations following phase-locking will thus keep registering the same phase value, then marking the same point in the phase space. This phase, which lies along the diagonal of the stroboscopic map, is the entrainment phase.

According to dynamical systems theory, the entrainment phase behaves as an attractor, i.e. it is a stable fixed point (Cross and Siggia, 2005; Izhikevich, 2007). Indeed, during entrainment of the segmentation clock to periodic pulses of DAPT, the phase dynamics converged to a region that lies along the diagonal of the stroboscopic map (Figure 3.4B). Such convergence is further highlighted by looking at the trajectories of individual samples within such maps (Figure 3.4C). It can thus be predicted that at same entrainment strength and detuning, faster (or slower) entrainment will be achieved when the initial phase of the endogenous oscillation is closer (or farther) to the entrainment phase (Granada et al., 2009). Certainly, this was observed in the entrainment experiments, as exemplified in Figure 3.4C.

To further verify whether or not the segmentation clock is entrained to the periodic DAPT pulses, we monitored its behavior after release from periodic perturbation. An entrained oscillation keeps the period of entrainment (and, accordingly, its stable phase relationship with the periodic pulses) for at least another cycle after the stop of perturbation, before it gradually returns to its free-running period (Kalmus, 1940; Pittendrigh and Bruce, 1957; Bordyugov et al., 2015; Abraham et al., 2010). Meanwhile, a forced/masked oscillation will almost automatically drift and return to its free-running period after release from periodic pulsing. To investigate this, we

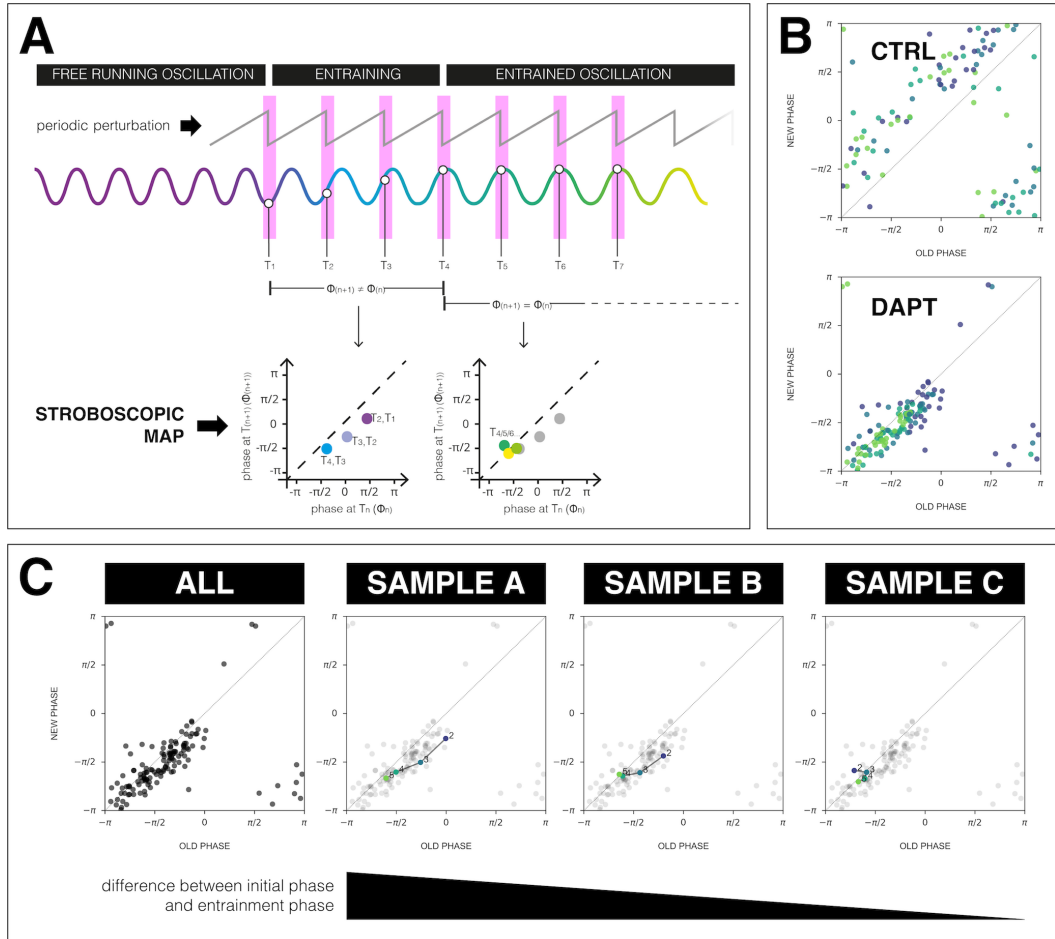


Figure 3.4 The segmentation clock is phase-locked to the periodic DAPT pulses. (A) Schematic of how to generate a stroboscopic map, where the phase of the segmentation clock just before a DAPT pulse (old phase, ϕ_n) is iteratively plotted against its phase just before the next pulse (new phase, ϕ_{n+1}). Illustration by Stefano Vianello. (B) Stroboscopic map of samples subjected to 170-min periodic pulses of 2 μ M DAPT (or DMSO for controls). Colors mark progression in time, from purple to yellow. (C) Stroboscopic maps of the segmentation clock entrained to 170-min periodic pulses of 2 μ M DAPT ($n = 34$ and $N = 8$), for all samples (ALL) and for three individual samples (SAMPLE A, SAMPLE B, SAMPLE C). The numbers and colors (from purple to yellow) denote progression in time.

subjected the segmentation clock to periodic pulses of 2 μM DAPT and assess how its rhythm changes during pulsing and after release (Figure 8.5). Ideally, one would subject oscillations to several rounds of periodic perturbation until they are effectively entrained, and continuously observe them for a long time after release. However, spreadouts allow for only a limited time prior to complete tissue segmentation and full oscillation arrest, thus limiting the total number of pulses we could use and the total number of oscillations we could observe. Because of this, we chose a period of 170 mins to push the segmentation clock (with natural period of around 140 mins) to a state with considerable detuning. This allowed us to note remarkable changes in rhythm if the samples were entrained. More specifically, we subjected spreadouts expressing LuVeLu to three 170-min pulses of DAPT and then switched to 170-min periodic pulses of DMSO. By evaluating the detrended timeseries, we recorded that independent samples were coherent and were adjusted to the rhythm of the pulses even a few cycles after release (i.e. switch to DMSO pulses) (Figure 8.5B). Analysis of period evolution using wavelet analysis also showed (a) change in period of the segmentation clock to match the entrainment period during the pulsing with DAPT, and (b) subsequent and gradual return to free-running period upon switching to pulsing with DMSO (Figure 8.5B). Concomitantly, we documented that samples subjected to DAPT pulses established a stable phase difference with the periodic pulses (i.e. they are phase-locked), and that they kept such constant phase difference for a few more cycles after switching to DMSO pulses before eventually drifting away (Figure 8.5C). These results strongly suggest that, in our experiments, the segmentation clock is indeed entrained, and not masked, to the periodic DAPT pulses.

3.1.4 Detuning between the free-running segmentation clock and the periodic pulses of DAPT affects the entrainment phase

One fundamental principle of entrainment is that the phase established upon entrainment will vary based on the magnitude and direction of detuning (Bordyugov et al., 2015; Granada et al., 2013). As described above, in addition to locking to the period of DAPT pulses, the segmentation clock was phase-locked with the periodic perturbation (Figure 3.4). Here, we provide evidence for such tuning of the entrainment phase upon entrainment of the segmentation clock to the periodic DAPT pulses. As shown in Figure 3.5, the entrainment phase systematically changed with the degree of detuning, thus obeying here too general entrainment principles (Bordyugov et al., 2015). For instance, at 130-min periodic pulses of 2 μM DAPT, the drug pulse coincided with the trough of the LuVeLu oscillations (Figure 3.5A, B1). Conversely, it coincided with the peak of the LuVeLu oscillations when the period

of 2 μM DAPT pulses was set to 170 mins (Figure 3.5A, B2). The localized region along the diagonal of the stroboscopic maps (Figure 3.5B-C, 8.6), corresponding to the entrainment phase, systematically shifts as one changes the period of the DAPT pulses. From 120-min to 180-min periodic DAPT pulses, the localized region gradually shifted from $\pi/2$ to $3\pi/2$ along the diagonal. The effect of detuning on the entrainment phase is in accordance with theoretical and experimental reports of entrainment in other oscillatory systems (Bordyugov et al., 2015; Granada et al., 2013).

3.1.5 The segmentation clock is amenable to higher-order entrainment

Up to this point, our investigation of entrainment behavior focused on 1:1 mode-locking between the segmentation clock and the periodic pulses of 2 μM DAPT, where the period of the segmentation clock matches the period of the DAPT pulses. During higher-order $n:m$ entrainment, the m cycles of the endogenous oscillation lock to n cycles of the periodic perturbation (Pikovsky et al., 2003; Balanov et al., 2008). It would be interesting to see if the oscillations in a complex biological system like the PSM can also be entrained to a higher-order. To investigate this, the concentration of DAPT was increased to enhance entrainment strength, as entrainment is much less efficiently achieved in these higher-order regimes. Certainly, even with high concentrations of DAPT, when the detuning between the free-running segmentation clock (natural period of around 140 mins) and the periodic DAPT pulses (period of 350 mins) was significantly high, the segmentation clock could no longer match the rhythm of the perturbation (Figure 3.6). Nonetheless, remarkably at this condition (i.e. detuning and entrainment strength) and in spite of the system's biological complexity, independent samples still become coherent and are instead locked to a period that is half the period of the DAPT pulses (Figure 3.6A-B). Considering hypothetical pulses with period around half the actual period of the perturbation, we generated stroboscopic maps and verified that these samples were (a) phase-locked to these hypothetical pulses and were (b) indeed entrained (Figure 3.6C). More specifically, corroborating these results, we documented here that the segmentation clock can be tuned to 1:2 entrainment, where the frequency of the endogenous oscillation is double the frequency of the periodic perturbation.

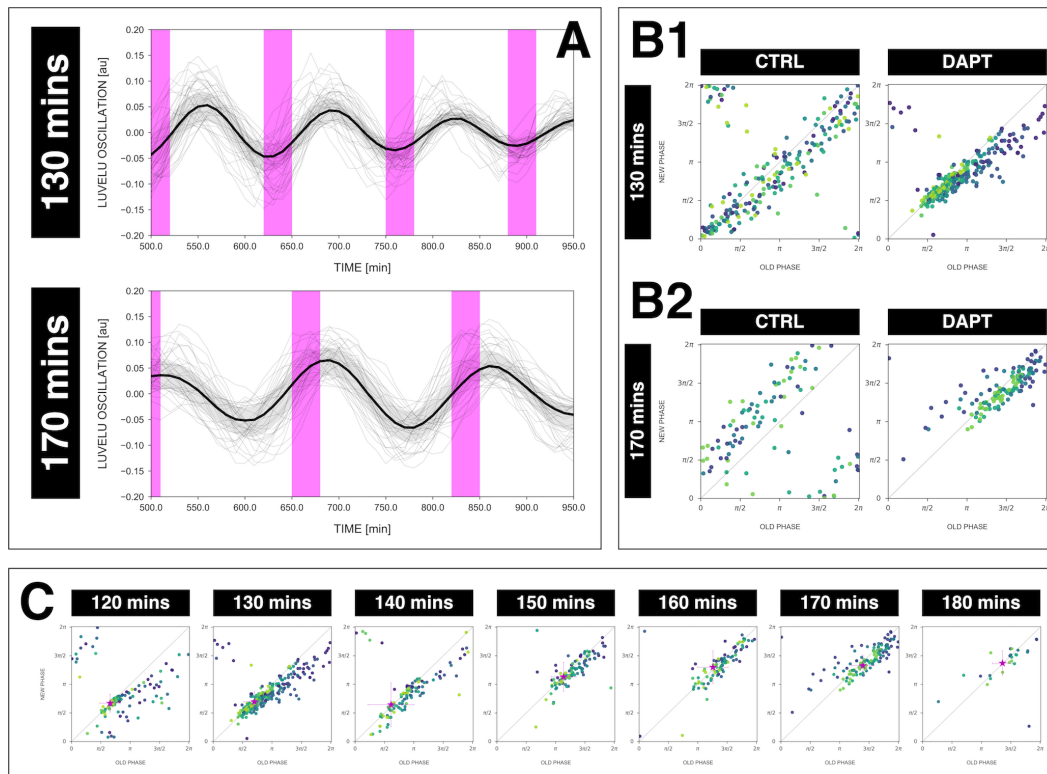


Figure 3.5 The entrainment phase varies according to the detuning between the free-running segmentation clock and the periodic DAPT pulses. (A) Detrended timeseries of the segmentation clock in spreadsheets entrained to either 130-min or 170-min periodic pulses of 2 uM DAPT, zoomed in from 500 mins to 950 mins. Periodic pulses are indicated as magenta bars and the timeseries of each sample (for 130-min: $n = 39$ and $N = 10$, for 170-min: $n = 34$ and $N = 8$) is marked with a dashed line. The median of the oscillations is represented here as a solid line, while the gray shaded area denotes the interquartile range. The full detrended timeseries for the 170-min condition can be seen in Figure 3.2A. (B) Stroboscopic maps of samples entrained to either 130-min (B1) or 170-min (B2) periodic pulses of 2 uM DAPT, with their respective controls (subjected to periodic pulses of DMSO). Colors mark progression in time, from purple to yellow. The maps in B2 are the same as those in Figure 3.4B. (C) Stroboscopic maps for different detuning values placed next to each other. The localized region close to the diagonal in each map marks the entrainment phase for that detuning. This is highlighted with a magenta star, which corresponds to the centroid of the said region. The centroid (x_c, y_c) was calculated from the vectorial average of the phases of all samples at the end of the experiment, where $x_c =$ vectorial average of old phase, $y_c =$ vectorial average of new phase. The spread of the points in the region is reported in terms of the circular standard deviation $(\sqrt{-2 \ln R})$, where R is the first Kuramoto order parameter). The period of the pulses of 2 uM DAPT is indicated above the maps. Colors mark progression in time, from purple to yellow. Stroboscopic maps of the entrained samples and their respective controls are shown in Figure 8.6.

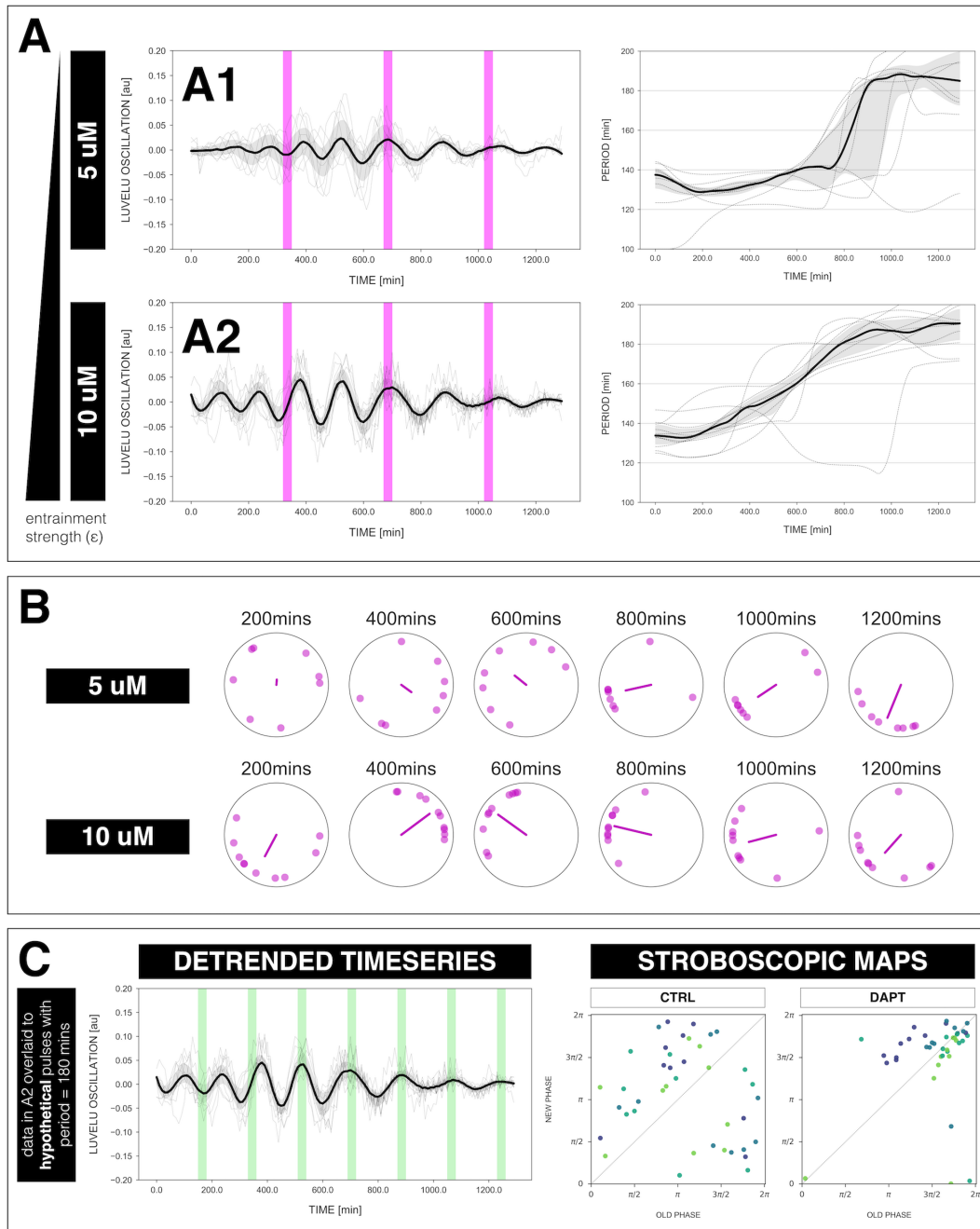


Figure 3.6 The segmentation clock can be entrained to a higher order. (A) Left: Detrended timeseries of the segmentation clock in spreadouts subjected to 350-min periodic pulses of either 5 uM DAPT (A1) or 10 uM DAPT (A2). Periodic pulses are indicated as magenta bars and the timeseries of each sample (for 5 uM DAPT: $n = 8$ and $N = 2$, for 10 uM DAPT: $n = 10$ and $N = 2$) is marked with a dashed line. The median of the oscillations is represented here as a solid line, while the gray shaded area denotes the interquartile range. Right: Period evolution during entrainment, obtained from wavelet analysis. The period evolution for each sample and the median of the periods are represented here as a dashed line and a solid line, respectively. The gray shaded area corresponds to the interquartile range. (B) Polar plots at different timepoints showing phase of each sample and their first Kuramoto order parameter, represented as a magenta dot along the circumference of a circle and a magenta line segment at the circle's center, respectively. A longer line segment corresponds to a higher first Kuramoto order parameter, and thus to more coherent samples. The direction of the line denotes the vectorial average of the sample phases. Time is indicated as mins elapsed from the start of the experiment. (C) Left: Detrended timeseries of the segmentation clock in spreadouts subjected to 350-min periodic pulses of 10 uM DAPT (A2). Hypothetical 180-min periodic pulses are indicated as green bars and the timeseries of each sample ($n = 10$ and $N = 2$) is marked with a dashed line. The median of the oscillations is represented here as a solid line, while the gray shaded area denotes the interquartile range. Right: Stroboscopic maps of samples subjected to 350-min periodic pulses of 10 uM DAPT (or DMSO for controls), considering perceived entrainment to hypothetical 180-min periodic pulses. Colors mark progression in time, from purple to yellow.

3.1.6 Entrainment results in the emergence of an altered period gradient along the AP axis

As mentioned earlier in the text, a period gradient naturally exists along the AP axis of the PSM. The fastest oscillations occur at the posterior of the PSM (corresponding to the center of spreadouts), where cells cycle approximately every 140 mins (Lauschke et al., 2012). This slows down to around 170 mins at the anterior PSM (corresponding to the periphery of spreadouts). The intracellular oscillations are coupled and the period gradient results in a slight shift in their phases. This phase shift gives an impression of a spatiotemporal wave pattern propagating from posterior to anterior PSM (or center to periphery in a spreadout) (Aulehla et al., 2007; Masamizu et al., 2006; Lauschke et al., 2012).

Growing evidence has emphasized the importance of the period gradient of Notch signaling in regulating somitogenesis (Sonnen and Aulehla, 2014; Lauschke et al., 2012). To visualize the effect of entrainment on the period gradient, entrainment dynamics were evaluated across the entire sample to keep its spatial information. Rather than focusing on the systems-level LuVeLu oscillations corresponding to the segmentation clock from the mean global intensity of each sample, wavelet analysis was performed for the timeseries of each pixel of the timelapse movies (Figure 3.7A). The generated wavelet movies would thus show both period and phase dynamics in time (across the duration of entrainment) and in space (across the tissue).

In controls, subjected to periodic pulses of DMSO, we observed a period gradient reminiscent of such gradient *in vivo* (Figure 3.7B, 3.7D-E, 8.7). While one may expect to achieve a uniform response upon entrainment, for instance, entrainment of the segmentation clock to 170-min periodic pulses of 2 μ M DAPT also resulted in the emergence of a period gradient, from 177.52 ± 13.25 mins ($n = 9$ and $N = 6$) at the center to 195.04 ± 13.55 mins ($n = 9$ and $N = 6$) near the periphery at 850 mins after the start of the experiment (Figure 3.7C-E, 8.7). This period gradient is different from what is present *in vivo* (i.e. from around 140 mins to 170 mins, Falk, 2019). An altered period gradient was similarly observed for samples subjected to 130-min periodic pulses of 2 μ M DAPT (Figure 8.8). For both conditions (Figure 3.8), the period of the fastest oscillations at the center, comprising of posterior PSM cells, adjusted to the entrainment period, which also was the period of the segmentation clock in these samples (Figure 3.2D). The period of the oscillations gradually increased towards the periphery, comprising of anterior PSM cells, to a much slower value, which could even exceed the slowest period observed *in vivo* (e.g. 195.04 ± 13.55 mins near the periphery in samples subjected to 170-min periodic DAPT pulses).

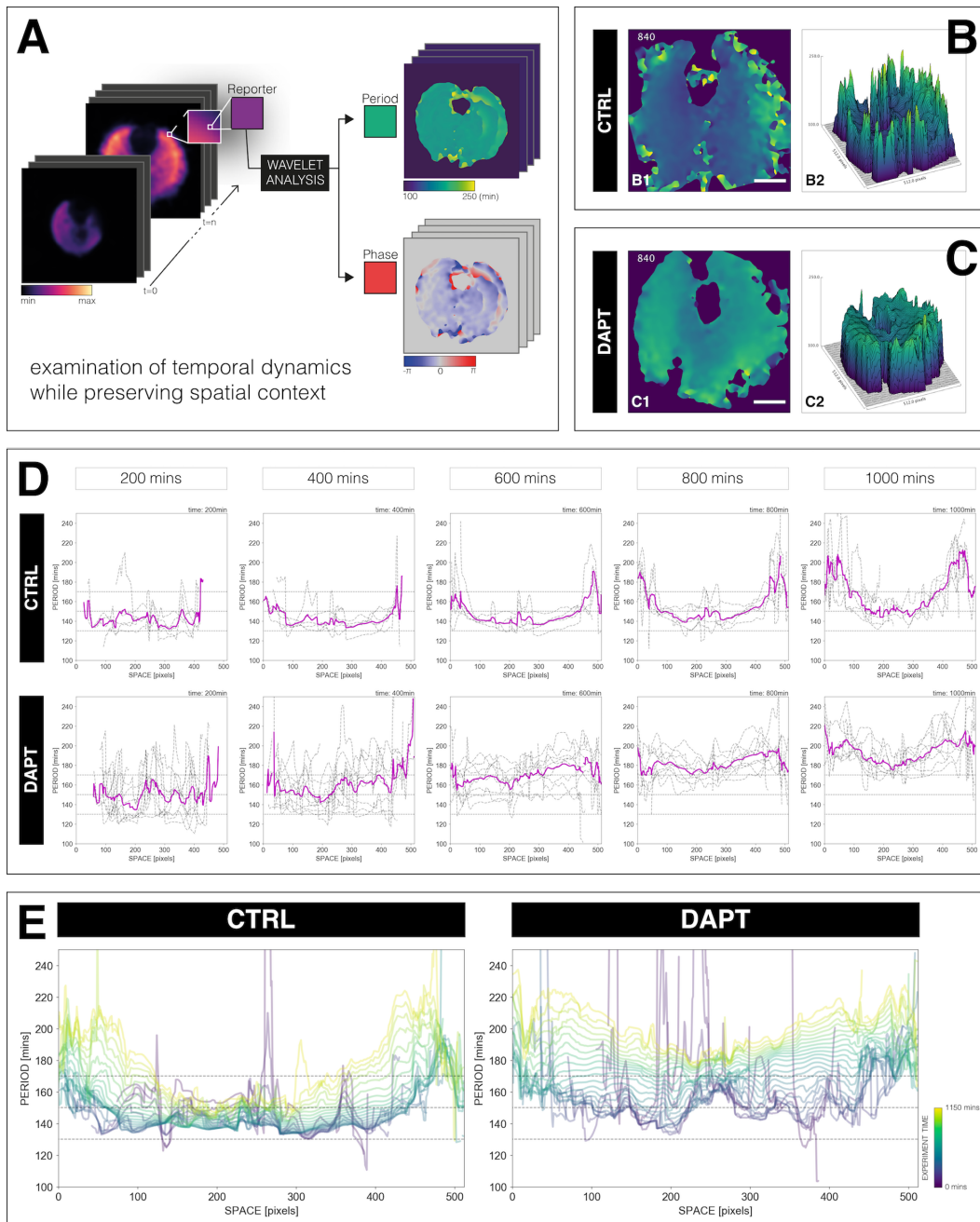


Figure 3.7 An altered period gradient emerges upon entrainment of the segmentation clock to a slower period. (A) Schematic of pipeline developed by Gregor Mönke to generate period and phase wavelet movies from wavelet analysis of each pixel of a timelapse movie. Illustration by Stefano Vianello. (B) Snapshot of period wavelet movie of a sample subjected to 170-min periodic pulses of DMSO, taken at 840 mins after the start of experiment (B1). Sample is rotated so that the dorsal side is up. Period of the sample at the specified timepoint represented as a surface plot (B2). (C) Snapshot of period wavelet movie of a sample entrained to 170-min periodic pulses of 2 μ M DAPT, taken at 840 mins after the start of experiment (C1). Sample is rotated so that the dorsal side is up. Period of the sample at the specified timepoint represented as a surface plot (C2). Snapshots of the period wavelet movie from 640 mins to 940 mins after start of the experiment are shown in Figure 8.7. (D) Average period gradient along the periphery-center-periphery axis of spreadouts subjected to 170-min periodic pulses of 2 μ M DAPT (or DMSO for controls) at different timepoints. Period gradient tracing average period over 50 pixels at different positions along the periphery-center-periphery axis at the equator (i.e. perpendicular to the dorsal-ventral axis) of the sample is marked with a dashed black line. The average of this period gradient across multiple samples (for CTRL: $n = 5$ and $N = 4$, for DAPT: $n = 9$ and $N = 6$) is marked with a solid magenta line. Periods equal to 130 mins, 150 mins, and 170 mins are highlighted, and time is indicated as mins elapsed from the start of the experiment. Pixel size is 1.38 μ m and cells have a diameter of around 10 μ m. (E) Temporal evolution of the period gradient as an overlay of the average period gradient across multiple timepoints. Periods equal to 130 mins, 150 mins, and 170 mins are highlighted. Colors mark progression in time, from purple to yellow. Pixel size is 1.38 μ m and cells have a diameter of around 10 μ m.

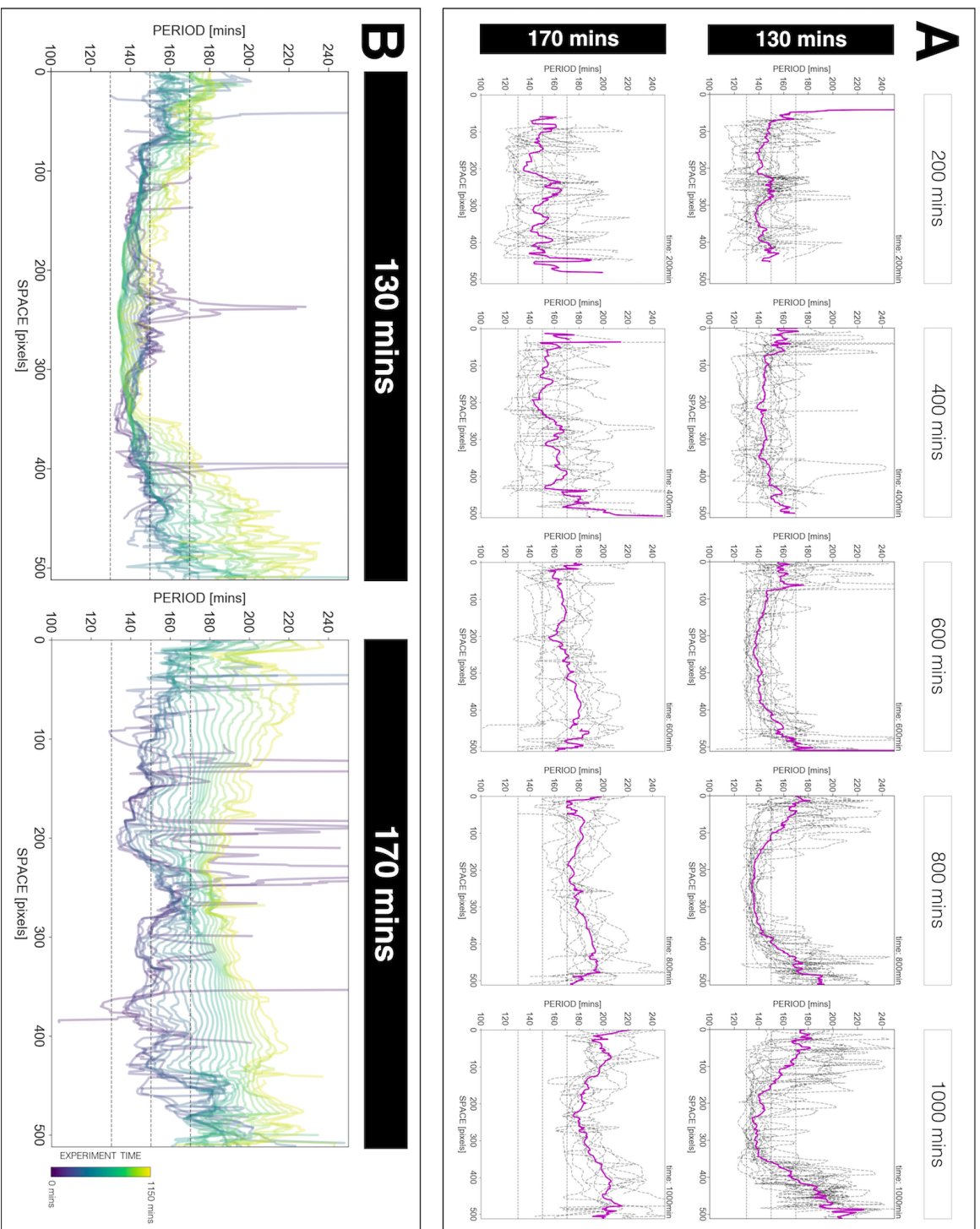


Figure 3.8 A period gradient emerges even upon entrainment of the segmentation clock to periodic pulses of 2 μM DAPT. (A) Average period gradient along the periphery-center-periphery axis of spreadouts subjected to either 130-min or 170-min periodic pulses of 2 μM DAPT at different timepoints. Period gradient tracing average period over 50 pixels at different positions along the periphery-center-periphery axis at the equator (i.e. perpendicular to the dorsal-ventral axis) of the sample is marked with a dashed black line. The average of this period gradient across multiple samples (for 130-min: $n = 15$ and $N = 7$, for 170-min: $n = 9$ and $N = 6$) is marked with a solid magenta line. Periods equal to 130 mins, 150 mins, and 170 mins are highlighted, and time is indicated as mins elapsed from the start of the experiment. Pixel size is 1.38 μm and cells have a diameter of around 10 μm . (B) Temporal evolution of the period gradient as an overlay of the average period gradient across multiple samples at different timepoints. Periods equal to 130 mins, 150 mins, and 170 mins are highlighted. Colors mark progression in time, from purple to yellow. Pixel size is 1.38 μm and cells have a diameter of around 10 μm .

3.2 Discussion

Spatiotemporal regulation via oscillations in the patterning of the PSM provides an attractive system to study dynamics from both theoretical and experimental perspectives. Here, we aimed to elucidate whether or not signaling oscillations during somitogenesis experimentally follow known theoretical principles of entrainment. Previously, periodic perturbation of Notch signaling via heat shock-driven expression of a Delta ligand was used to modulate the segmentation of PSM in zebrafish (Soza-Ried et al., 2014). In the cited study, the readout to assess the effect of the periodic perturbation was static, mostly relying on the somite size and morphology. While this gave important insight on how periodic segmentation of the PSM responds to periodic perturbation, experimental investigation on the underlying signaling dynamics was lacking.

In this chapter, we used a microfluidics-based experimental platform to subject an *ex vivo* model of somitogenesis (i.e. spreadout) expressing a dynamic Notch signaling reporter (LuVeLu, a dynamic readout) to periodic pulses of a signaling modulator (pulses of DAPT, a dynamic perturbation). Using this platform, we were able to study the entrainment of the segmentation clock to periodic pulses of DAPT. We noted that the period of the clock locked to the period of the DAPT pulses (Figure 3.2, 8.2-8.3). While treatment with DAPT, an inhibitor of Notch signaling, could naturally lengthen the period of the oscillations at least in the zebrafish PSM (Liao et al., 2016; Herrgen et al., 2010; Morelli et al., 2009), inhibition of Notch signaling *per se* would not explain the coherence between independent samples during entrainment. Slowing down (or speeding up) initially asynchronous oscillations would not result in their eventual coherence. However, as samples in our system were entrained and synchronized to the periodic DAPT pulses, they became synchronous and more coherent. Moreover, if the effect of DAPT was merely to slow down oscillations, this effect would be more pronounced at shorter periods of DAPT pulses, where they are closer to each other. Instead, at shorter periods (i.e. 120-min and 130-min periodic pulses of 2 μ M DAPT), the segmentation clock was sped up, locking to the period of the perturbation. Even if DAPT has a different effect in the mouse PSM, for instance by speeding up the oscillations through disruption of coupling between mouse PSM cells via Notch signaling (Morelli et al., 2009; Yoshioka-Kobayashi et al., 2020), the pharmacological inhibition of intercellular coupling could by itself not explain how we are able to both speed up and slow down the segmentation clock to a precise period matching our pre-defined period of DAPT pulsing. This hints to how different phases of oscillations respond differently to the same perturbation (Granada et al., 2013), uncovering another rich concept in dynamical systems theory (i.e. phase response curves) which will not be thoroughly covered in this text. More

generally, this highlights the power of dynamic perturbation of oscillatory systems via entrainment.

Building on the above discussion, in addition to period-locking, the segmentation clock was phase-locked to the periodic pulses of DAPT. The segmentation clock established a stable phase relationship with the periodic perturbation, marked by the phase of entrainment (Figure 3.4-3.5). As we were focusing on the entrainment of the segmentation clock with free-running period of around 140 mins, controlling the period of the DAPT pulses allowed us to modulate detuning and see its effect on the entrainment phase. Though the entrainment phase is theoretically expected to systematically change with detuning (Bordyugov et al., 2015; Granada et al., 2013), we were excited to experimentally observe this in the entrainment of periodic segmentation in a tissue of a developing mouse embryo (Figure 3.5, 8.6), a complex biological system comprising of rather heterogeneous intracellular signaling oscillations. Because of this observed behavior, which follow universal principles, we could fairly predict the entrainment phase for a certain detuning with just the entrainment phases for the other conditions.

We noted that the segmentation clock could maintain its adjusted rhythm even after release from the entraining signal (Figure 8.5), strongly suggesting that what we observed here are not due to masking (Bordyugov et al., 2015; Roenneberg et al., 2005; Mrosovsky, 1999). Remarkably, we also recorded that the segmentation clock is amenable to higher-order entrainment (Figure 3.6). The 1:2 entrainment of the segmentation clock shown in this chapter is particularly opposite in direction to subharmonic response in periodically-driven systems, most notably documented by Faraday, 1831 in liquids on a horizontal surface subjected to vertical oscillations.

For bulk of the data presented in this chapter, we restricted our analyses to systems-level oscillations of LuVeLu, corresponding to the segmentation clock, obtained from global intensity analysis of the timelapse fluorescence imaging. This relied on the tissue-level dynamics of LuVeLu, a dynamic reporter of Lfng, in the PSM. During somitogenesis, formation of a segment coincides with complete propagation of a Lfng wave along the AP axis and concurrent expression of a bright Lfng stripe at the anterior PSM (Cole et al., 2002; Morales et al., 2002; Aulehla et al., 2007). We highlighted the entrainment behavior of the PSM based mostly on a periodic phenomenon that is a global and tissue-level property of the system. While this tissue-level perspective was appropriate for most of the analyses presented here, this inhibited us from making interpretations on entrainment behavior at the cellular level. The PSM is in fact a spatially-extended system of coupled and phase-shifted intracellular signaling oscillations (Maroto et al., 2005; Masamizu et al., 2006; Webb et al., 2016; Herrgen et al., 2010; Gomez et al., 2008; Oates et al., 2012; Tsiairis and Aulehla, 2016). To address this, we performed wavelet analysis for each pixel of

the timelapse movies (Figure 3.7A). This allowed us to extract the period and phase of oscillations in the tissue, while preserving their spatial information.

Through wavelet movies, we confirmed that spreadouts subjected to periodic pulses of DMSO (control) preserved the period gradient along the AP axis that is present in vivo (from around 140 mins to around 170 mins) (Figure 3.7B, D and 8.8). Strikingly, while the segmentation clock entrained to the period of the DAPT pulses (Figure 3.2, 8.2), the wavelet movies revealed that not all intracellular signaling oscillations locked to the period of the perturbation. In fact, we noted a period gradient as well, though altered than the control (Figure 3.7C-E, 3.8, 8.7, 8.8). More interestingly, the period of LuVeLu oscillations in the center of the spreadout, corresponding to the fast-oscillating posterior PSM cells, were the ones that were closest to the period of DAPT pulses. This was most remarkable for spreadouts subjected to 170-min periodic pulses of DAPT, as the oscillations in the center locked to the period of entrainment despite supposedly having the most significant detuning. The segmentation clock and the intracellular signaling oscillations in the center of the ex vivo model had approximately the same period, which are locked to the period of the DAPT pulses. This is reminiscent of how the period of somitogenesis matches the period of intracellular signaling oscillations in the posterior PSM in unperturbed conditions (Soza-Ried et al., 2014; Tsiairis and Aulehla, 2016). Definitely, how the period gradient emerges in spreadouts during entrainment will have to be assessed more thoroughly. This could provide deeper understanding into the nature of the coupled and phase-shifted oscillations in the PSM. At a more biological point of view, the above observations could imply the importance of the period gradient, and consequent phase gradient, in regulating tissue patterning during somitogenesis. We hope to more thoroughly address these points in the next chapter.

Furthermore, in light of results presented here, one could envision that, during entrainment, the coupling of intracellular signaling oscillations to the periodic perturbation acts on top of the inherent intercellular coupling between PSM cells. Indeed, the role of coupling was previously seen to govern the behavior of oscillations during entrainment (Abraham et al., 2010). Certainly, investigating the link between coupling and entrainment behavior of intracellular signaling oscillations in the PSM would be an exciting topic for future studies.

3.3 Conclusion

In this chapter, we investigated whether or not the segmentation clock follows universal entrainment principles that have been thoroughly studied theoretically and experimentally in other oscillatory systems. In the recent years, our lab has developed an *ex vivo* model of somitogenesis (Lauschke et al., 2012), more commonly known as a spreadout, using tissue from mouse embryos expressing a dynamic reporter of the underlying segmentation clock in the PSM (Aulehla et al., 2007) that could now be subjected to periodic pulses of signaling modulators using microfluidics (Sonnen et al., 2018). Given these technological advancements, we show here that the principles of entrainment can be extended to the precise control of the segmentation clock in the developing mouse embryo. We describe here that the period and phase of these oscillations lock to those of a periodic perturbation. We also report that, even for a spatially-extended system of coupled and phase-shifted oscillations, the entrainment phase accordingly change with the detuning between tissue-level oscillations of Notch signaling (i.e. the segmentation clock) and periodic pulses of a Notch inhibitor. We also document that the segmentation clock can be entrained to a higher-order (i.e. 1:2 entrainment). Delving into the behavior of the intracellular oscillations in their spatial context, we also make here interesting biological insights into the emergence and maintenance of period gradient in the PSM during somitogenesis. The period gradient appears to be an emergent property of the system, as it was observed even when the oscillations were influenced to artificial periods upon entrainment. That such a network of oscillations in the PSM can be simplified in some contexts to systems-level oscillations is inspiring. As we have noted that the segmentation clock in the mouse embryo behaves predictably based on fundamental principles, we now have an experimental handle to control its period and phase. This would allow further elucidation of spatiotemporal information encoded in oscillatory signaling during somitogenesis. Moreover, this will enable uncovering of the nature and mechanism of these oscillations and their synchronization during patterning of the PSM in developing vertebrate embryos. With some customization, the experimental approach presented here could be extended to more physiologically relevant systems like intact tail/PSM of mouse embryos, or whole medaka or zebrafish embryos. To enhance experimental control, microfluidics-based entrainment can also be coupled with other techniques like optogenetics (Isomura et al., 2017; Izquierdo et al., 2018; Krueger et al., 2019) or auxin-inducible degron system (Nishimura et al., 2009). More generally, we highlight in this chapter the universality of entrainment principles and cite its promise as an experimental tool to probe complex biological oscillatory systems.

3.4 Outlook

Delineation of the range of 1:1 mode-locking

Here, we have controlled the period of the segmentation clock from 120 mins to 180 mins by locking them to the period of pulses of 2 μM DAPT (1:1 mode-locking). It appears that we are close to the edge of the entrainment range as evidenced by less efficient entrainment at high detuning (120-min and 180-min) (Figure 3.2D) and the entrainment phase spreads over the range of around π within the detuning values considered (Figure 3.5C) (Granada et al., 2013). While this is a broad range and already sufficient to describe the entrainment behavior in our system, it would be interesting to see how much we could push the period of the segmentation clock even further. However, we noticed that subjecting the samples to periods shorter than 120 mins already has an effect on the signaling dynamics. As the DAPT pulses were much closer to each other at shorter periods of perturbation, the signal becomes very dim and the oscillations are abolished. While there were some indications of 2:1 higher-order entrainment at 90-min periodic DAPT pulses, suggesting the 1:1 mode-locking at 2 μM DAPT does not go beyond period of 90 mins, we could not yet be certain if this observation was because of entrainment or due to DAPT already significantly affecting Notch signaling. To proceed in probing the 1:1 entrainment range at 2 μM DAPT, it is thus advised that one would instead focus on periods longer than 180 mins, but shorter than 350 mins where mode-locking already goes to the 1:2 higher-order regime (Figure 3.6).

Simulation of segmentation clock entrainment using a phenomenological model

Simulating entrainment of the segmentation clock would alternatively allow mapping of Arnold tongues (1:1 and potentially even the higher-order entrainment regimes). It would be powerful to eventually come up with a phenomenological model of entrainment in our system, capturing observations and incorporating experimental data presented in this text, which already span quite several conditions in entrainment parameter space. Numerical experiments could then be done with this model without necessitating numerous additional experiments, with different detuning and entrainment strength, using embryonic tissues. Coarse-grained modeling of segmentation at the level of dynamical modules (i.e. timers, oscillators, and switches) has been recently presented (Clark, 2020), and could guide such simulation of entrainment in the PSM.

Elucidation of the effect of detuning on entrainment phase to navigate oscillatory nature of the segmentation clock

One plausible way to guide in phenomenological modeling of entrainment of the segmentation clock is by thorough investigation of the effect of detuning on entrainment phase. We document here that the phase of entrainment accordingly changes

with the period mismatch between the free-running segmentation clock and the DAPT pulses. More specifically, we note that the entrainment phase changed from around $\pi/2$ to around $3\pi/2$ at 120-min and at 180-min periodic pulses of 2 μM DAPT, respectively. For these conditions spanning the entrainment range at the given concentration of DAPT (i.e. entrainment strength), the range of entrainment phase was around π , which is in accord with the 180° rule described in Granada et al., 2013. The 180° rule is a feature of entrainment and has been numerically shown via different approaches: either through phase response curves, a Kuramoto phase equation, or a periodically-driven damped oscillator (Granada et al., 2013). While each of these resulted in the entrainment phase spanning a range of π within the entrainment range (i.e. the 180° rule), it would be informative to precisely know how the phase of entrainment changes with detuning between these different approaches. By corroborating this with how detuning affects the phase of entrainment in our experiments (Figure 8.9), one could hopefully determine which of the aforementioned strategies is most applicable to better model the oscillatory nature of the mouse segmentation clock and its entrainment.

Perturbation with single drug pulse to map the phase response curve

As entrainment works as a periodic iteration of single perturbations, knowing how an oscillation responds to a single perturbation would provide a more holistic insight into the series of periodic phase changes during (and leading to) entrainment. To address this, it is hence valuable to map the phase response curve (PRC), which summarizes how the phase of an oscillation changes (i.e. shifts its phase) after being perturbed (Johnson, 1999; Pikovsky et al., 2003; Izhikevich, 2007; Granada et al., 2013). More specifically, a PRC specifies how response to a perturbation could be different depending on which phase of the oscillation the perturbation happened. Phase response curves can alternatively be mapped as phase transition curves (PTC), which follow the oscillation's change in phase by plotting its new phase (because of the perturbation) versus its old phase (unperturbed or a cycle before the perturbation). In this chapter, the phase dynamics of the segmentation clock when subjected to periodic perturbations (i.e. periodic DAPT pulses) is illustrated using stroboscopic maps, which are in principle similar to mapping PTCs. This strategy was in fact used to study entrainment of the cell cycle and cell-to-cell communication in myoblast cells (Isomura et al., 2017; Cross and Siggia, 2005). To refine delineation of PRC and PTC in our system, one could do single perturbation experiments (i.e. single pulse of DAPT) and note phase (and period) changes, if any, such perturbation causes to the oscillation. Some experiments towards this direction were already started in the lab in collaboration with Gregor Mönke. While this strategy could be experimentally tedious, a highly resolved PTC can then be used to theoretically determine the entrainment phase at different detuning and specify the entrainment

range at different entrainment strengths, thus enabling more precise mapping of finite regions of entrainment (i.e. Arnold tongues).

Entrainment with periodic pulses of a drug that activates Notch signaling

In this chapter, we highlight how subjecting the segmentation clock to periodic pulses of DAPT, a γ -secretase inhibitor affecting Notch signaling (Geling et al., 2002), obeys principles of entrainment and follows synchronization theory. To exemplify universality of entrainment principles in our system, one could subject samples to periodic pulses of a drug that instead activates Notch signaling. In addition to whether or not one could entrain the segmentation clock using this drug, it would be most curious how the entrainment phase would change by inverting the "direction" of the perturbation, which is more or less theoretically equivalent to inverting the PRC. To minimize experimental conditions, one could focus on entrainment with 130-min and 170-min pulses, and note period- and phase-locking in these conditions. If our intuition is true, for a magnitude of entrainment strength equivalent to that using 2 uM DAPT, the entrainment phases will be opposite those observed in our experiments (e.g. for 130-min: pulse of drug would instead correspond to peak of LuVeLu, while for 170-min: pulse of drug would instead correspond to trough of LuVeLu). To address this, we have done some preliminary experiments using 4 uM MLN4924 (Figure 8.10-8.11), which stabilizes Notch signaling by inhibiting ubiquitin/proteasomal degradation (Seymour et al., 2019; Carrieri et al., 2019; Nawrocki et al., 2012). We recorded that the segmentation clock adjusted to the rhythm of the periodic perturbation and that its period locked to the period of the MLN4924 pulses (Figure 8.10A-B). While we noted that the entrainment phase at 130-min periodic MLN4924 pulses inverted (vs 130-min periodic DAPT pulses), the entrainment phase at 170-min periodic MLN4924 pulses did not change (vs 170-min periodic DAPT pulses) (Figure 8.11). In fact, with periodic pulses of 4 uM MLN4924, the entrainment phases between the two said detuning were equal. It would now be interesting to investigate if we could use MLN4924 for entrainment but the concentration we used so far was too high (i.e. too high entrainment strength not equivalent to that with 2 uM DAPT), or if what we have observed is no longer entrainment but is forcing/masking instead. Notably, while DAPT acts within the feedback loop that results in Notch signaling oscillations, MLN4924 does not (Figure 8.10C). It would be interesting to elucidate whether or not this explains our preliminary observations. More generally, it would be very exciting if entrainment behavior (e.g. entrainment phase for a given detuning and entrainment strength) could give one insight into the mode of action of a molecule in signaling pathways that result in oscillations.

Investigation of oscillatory dynamics at the edge of the synchronization regime

Entrainment of oscillatory systems is a rich topic in dynamical systems theory. In addition to things presented here, which focus on behaviors of an oscillatory system within the entrainment range, principles underlying oscillatory dynamics at the edge of the synchronization regime (i.e. Arnold tongues) are also abundant. For instance, depending on the shape of the Arnold tongue, the strength of the perturbation, and the detuning, an endogenous oscillation could be synchronized to a periodic perturbation through entrainment (i.e. period- and phase-locking) or through suppression of natural dynamics (Balanov et al., 2008), with the latter occurring at notably high perturbation strengths and marking the transition to synchronized chaos (Postnov et al., 2001). Enriched by recent discussions with Adrián Granada (Charité Comprehensive Cancer Center), one could get an impression of where in the entrainment parameter space (i.e. entrainment strength versus detuning) a condition lies by recording the timeseries of a sample subjected to pulses of drug of given period and known concentration, and then by looking at its corresponding power spectral density. The spectra should be able to differentiate between the two aforementioned scenarios (Balanov et al., 2008), especially at conditions closest to the edge of Arnold tongues. This offers an approach to document transition to synchronized chaos, if present, in our system.

Microfluidics-based entrainment in culture conditions that enable persistent signaling oscillations

As mentioned earlier in this text, one limitation of our system is that PSM cells arrest their oscillations as they differentiate, hence limiting the number of oscillations we could observe before the tissue fully segments. While this was not a restriction in the interpretation of experiments specified here (as evidenced by stable period- and phase-locking, among others), it would be interesting to see if entrainment dynamics of oscillations in the PSM change or persist for longer timepoints. This would be most useful for pulse-and-release experiments (discussed in Section 3.1.3 and illustrated in Figure 8.5) and for conditions (i.e. period of DAPT pulses and concentration of DAPT) beyond those considered in this chapter. To tackle this, one could consider using primary or stem cell-derived PSM cells (Hubaud et al., 2017; Matsumiya et al., 2018; Chu et al., 2019b; Diaz-Cuadros et al., 2020; Matsuda et al., 2020) cultured in conditions that would keep them in posterior PSM identity (Hubaud et al., 2017), hence impeding their differentiation, and thus sustaining their oscillations. While such system would not fully recapitulate the tissue-level organization of intracellular oscillations in the PSM and the periodic segmentation of the embryonic tissue, it would allow monitoring of entrainment of oscillations in a rather homogenous fraction of PSM cells for a much longer period of time.

Is an emergent period gradient important for segmentation of the presomitic mesoderm?

“*..we can see how the whole becomes not only more than but very different from the sum of its parts.*

— Philip Warren Anderson

In Chapter 3, we highlighted how the segmentation clock follows synchronization principles. We further illustrated how this has allowed us to experimentally modulate the clock's period and phase with high precision, ultimately allowing us to control the ticking of the segmentation of the presomitic mesoderm (PSM). Remarkably, while such tissue-level oscillatory phenomenon in the PSM is entrained to our periodic perturbation, we noted that only a select population of intracellular signaling oscillations is locked to the periodic drug pulses. More specifically, while the segmentation clock, even as a spatially-extended system of coupled and phase-shifted signaling oscillations, generally obeys entrainment theory, we documented a curious behavior of emergence of a period gradient along the AP axis of the embryonic tissue. Such self-organization in the PSM (Figure 3.7C-E, 3.8, 8.7, 8.8), even in artificial periods of the oscillations upon entrainment, could hint to the importance of emergence and maintenance of a period gradient, and thus its consequent phase wave, in tissue patterning. As this period gradient is globally manifested as an apparent wave of Notch signaling that propagates along the AP axis of the PSM, we are interested in uncovering if it confers spatiotemporal cues during somitogenesis.

In this chapter, we present observations on entrainment dynamics across entire spreadouts. In particular, we elaborate on the observed emergence of a frequency gradient and the modulation of the phase gradient upon entrainment. Furthermore, we report evidence on the effect of modulating the wave of Notch signaling to tissue patterning. We believe these could unravel key insight into the underlying intercellular coupling of signaling oscillations, which act on top of each intracellular oscillation's coupling with the periodic perturbation during entrainment, and its role in spatiotemporal information processing.

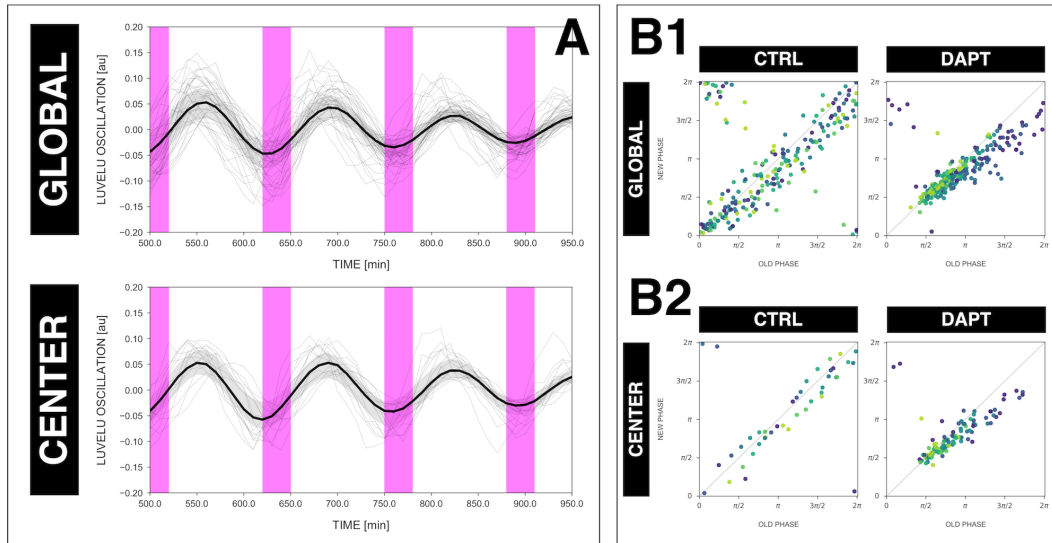
4.1 Results

4.1.1 The rhythm of the segmentation clock matches the rhythm of oscillations in the posterior PSM (i.e. the center of spreadouts) regardless whether the clock is sped up or slowed down

As elaborated earlier in the text, intracellular signaling oscillations slow down from posterior to anterior PSM (i.e. center to periphery of spreadouts), ultimately arresting in the anterior PSM just before tissue segmentation. Strikingly, the period of tissue segmentation matches the period of the fastest oscillations localized in the posterior PSM (i.e. center of spreadouts) (Tsiairis and Aulehla, 2016; Soza-Ried et al., 2014). Considering this and the observations we documented for samples whose segmentation clock entrained to the periodic DAPT pulses, we were curious whether or not the rhythm of the segmentation clock in these samples also matches the rhythm of the oscillations in their posterior PSM (i.e. center of spreadouts), even with their faster/slower segmentation clock (Figure 3.2, 8.2, 8.3) and with their altered period gradient (Figure 3.7C-E, 3.8, 8.8).

To study this, we compared the timeseries acquired from (a) the mean global intensity of the entire field of view (Figure 3.1A) and from (b) a circular ROI at the center of the spreadouts (radius: 25 pixels, 1 pixel = 1.38 μm) (for details, please refer to Section 6.5.1), corresponding to the segmentation clock and the oscillations in the posterior PSM, respectively. Upon comparison, we noted that the oscillations at the center of spreadouts adjusted its rhythm to the periodic DAPT pulses similarly as the segmentation clock (Figure 4.1), regardless whether the clock was sped up (Figure 4.1A) or slowed down (Figure 4.1C). Moreover, the phase locking between the periodic DAPT pulses and either the segmentation clock or the oscillations at the center of the samples are similar (Figure 4.1B1-B2, D1-D2, 4.2). Concomitantly, for oscillations in the center of spreadouts (i.e. the posterior PSM), the entrainment phase at 130-min periodic pulses of DAPT is different to the entrainment phase at 170-min periodic pulses of DAPT (Figure 4.2B), here too exemplifying the effect of detuning on the phase of entrainment.

130 mins – FASTER SEGMENTATION CLOCK



170 mins – SLOWER SEGMENTATION CLOCK

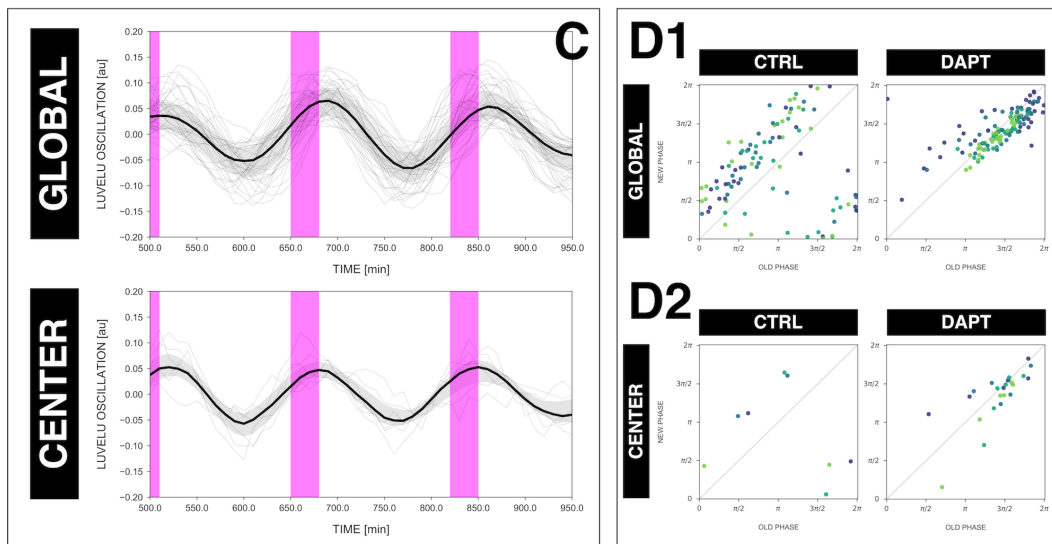


Figure 4.1 The rhythm of the segmentation clock matches the rhythm of oscillations in the posterior PSM (i.e. the center of spreadouts) regardless whether the clock is sped up or slowed down. (A) Detrended timeseries of either the segmentation clock (GLOBAL) or oscillations in the center of spreadouts (CENTER) entrained to 130-min periodic pulses of 2 μ M DAPT, zoomed in from 500 mins to 950 mins. Periodic pulses are indicated as magenta bars and the timeseries of each sample (for GLOBAL: $n = 39$ and $N = 10$, for CENTER: $n = 15$ and $N = 7$) is marked with a dashed line. The median of the oscillations is represented here as a solid line, while the gray shaded area denotes the interquartile range. The plot for GLOBAL is the same as that for the 130-min condition in Figure 3.5A. (B) Stroboscopic maps of either the segmentation clock (GLOBAL, B1) or oscillations in the center of spreadouts (CENTER, B2) subjected to 130-min periodic pulses of 2 μ M DAPT, with their respective controls (subjected to periodic pulses of DMSO). Colors mark progression in time, from purple to yellow. The maps in B1 are the same as those in Figure 3.5B1. (C) Detrended timeseries of either the segmentation clock (GLOBAL) or oscillations in the center of spreadouts (CENTER) entrained to 170-min periodic pulses of 2 μ M DAPT, zoomed in from 500 mins to 950 mins. Periodic pulses are indicated as magenta bars and the timeseries of each sample (for GLOBAL: $n = 34$ and $N = 8$, for CENTER: $n = 6$ and $N = 5$) is marked with a dashed line. The median of the oscillations is represented here as a solid line, while the gray shaded area denotes the interquartile range. The plot for GLOBAL is the same as that for the 170-min condition in Figure 3.5A. (D) Stroboscopic maps of either the segmentation clock (GLOBAL, D1) or oscillations in the center of spreadouts (CENTER, D2) subjected to 170-min periodic pulses of 2 μ M DAPT, with their respective controls (subjected to periodic pulses of DMSO). Colors mark progression in time, from purple to yellow. The maps in D1 are the same as those in Figure 3.5B2.

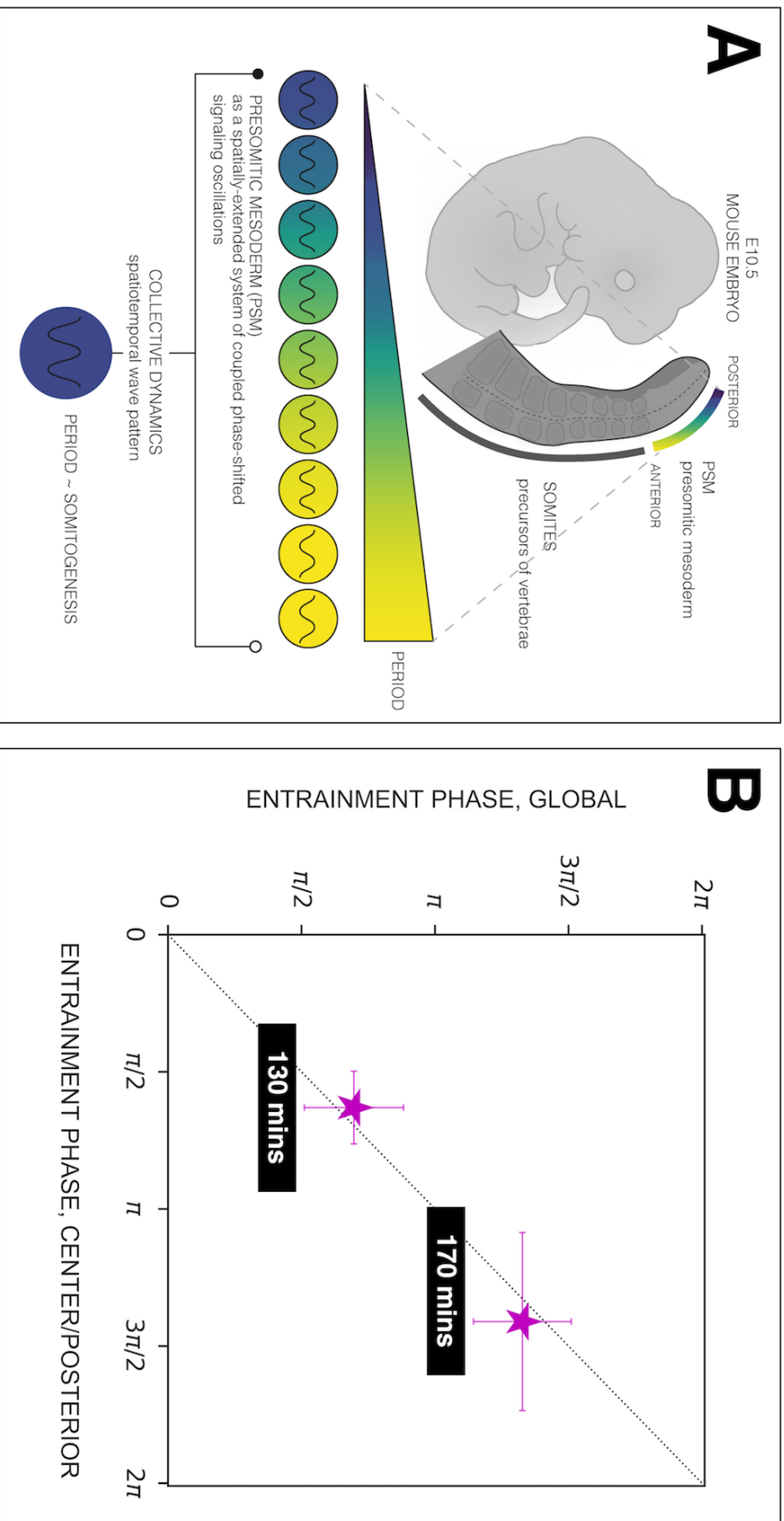


Figure 4.2 The phase of oscillations in the posterior PSM (i.e. the center of spreadouts) matches the phase of the segmentation clock. (A) Scheme of the phase-shifted oscillations along the AP axis of the PSM and its correlation to the segmentation clock. Illustration by Stefano Vanello. (B) Comparison of the phase relationship between the periodic DAPT pulses and either the segmentation clock (GLOBAL) or the center of spreadouts (equivalent to posterior PSM, CENTER/POSTERIOR). The entrainment phase was calculated from the vectorial average of the phases of all samples at the time corresponding to the last DAPT pulse considered. The spread of sample phases is reported in terms of the circular standard deviation ($\sqrt{-2/nR}$, where R is the first Kuramoto order parameter). 130-min: (GLOBAL: $n = 39$ and $N = 10$) and (CENTER: $n = 15$ and $N = 7$), 170-min: (GLOBAL: $n = 34$ and $N = 8$) and (CENTER: $n = 6$ and $N = 5$).

4.1.2 A higher (or lower) period gradient correlates with a higher (or lower) amplitude gradient

We earlier noted an altered period gradient along the AP axis in spreadouts upon entrainment of their segmentation clock to periodic pulses of 2 μ M DAPT. In particular, we recorded a generally lower period gradient when the segmentation clock was sped up (Figure 3.8, 8.8), and a generally higher period gradient when the segmentation clock was slowed down (Figure 3.7, 3.8). In nonlinear dynamics, a primary source of nonlinearity in oscillatory systems is the interdependence between an oscillation's frequency/period and its amplitude (Arnol'd and Avez, 1968). Given the experimentally-modulated artificial period gradients in our samples upon entrainment of their segmentation clock to periodic DAPT pulses, we wondered if we could see a correlation between the period gradient and the amplitude gradient, and between the underlying period/frequency of intracellular signaling oscillations and their amplitude.

To evaluate the amplitude gradient, we first generated amplitude wavelet movies corresponding to the timelapse intensity movies, using an approach similar to generating period and phase wavelet movies illustrated in Figure 3.7A (for details, please refer to Section 6.5.3). Comparing the temporal evolution of the amplitude gradient with the temporal evolution of the period gradient revealed that a higher (or lower) period gradient correlated with a higher (or lower) amplitude gradient (Figure 4.3). More specifically, the amplitude gradient in samples with a faster segmentation clock (i.e. 130 mins), which correspondingly have a lower period gradient (Figure 4.3A), is lower (Figure 4.3B) than the amplitude gradient in samples with slower segmentation clock (i.e. 170 mins), which correspondingly have a higher period gradient (Figure 4.3A).

Furthermore, in addition to a higher (or lower) tissue-level period gradient correlating with a higher (or lower) tissue-level amplitude gradient, the fastest intracellular signaling oscillations (i.e. with the shortest period) in each sample, localized in the center of spreadouts (i.e. equivalent to the posterior PSM), have the lowest amplitude for both the 130-min (Figure 4.4, 8.12) and 170-min conditions (Figure 4.4, 8.13). These observations exemplify interdependence between the frequency/period and the amplitude of the signaling oscillations at both the tissue and cellular levels.

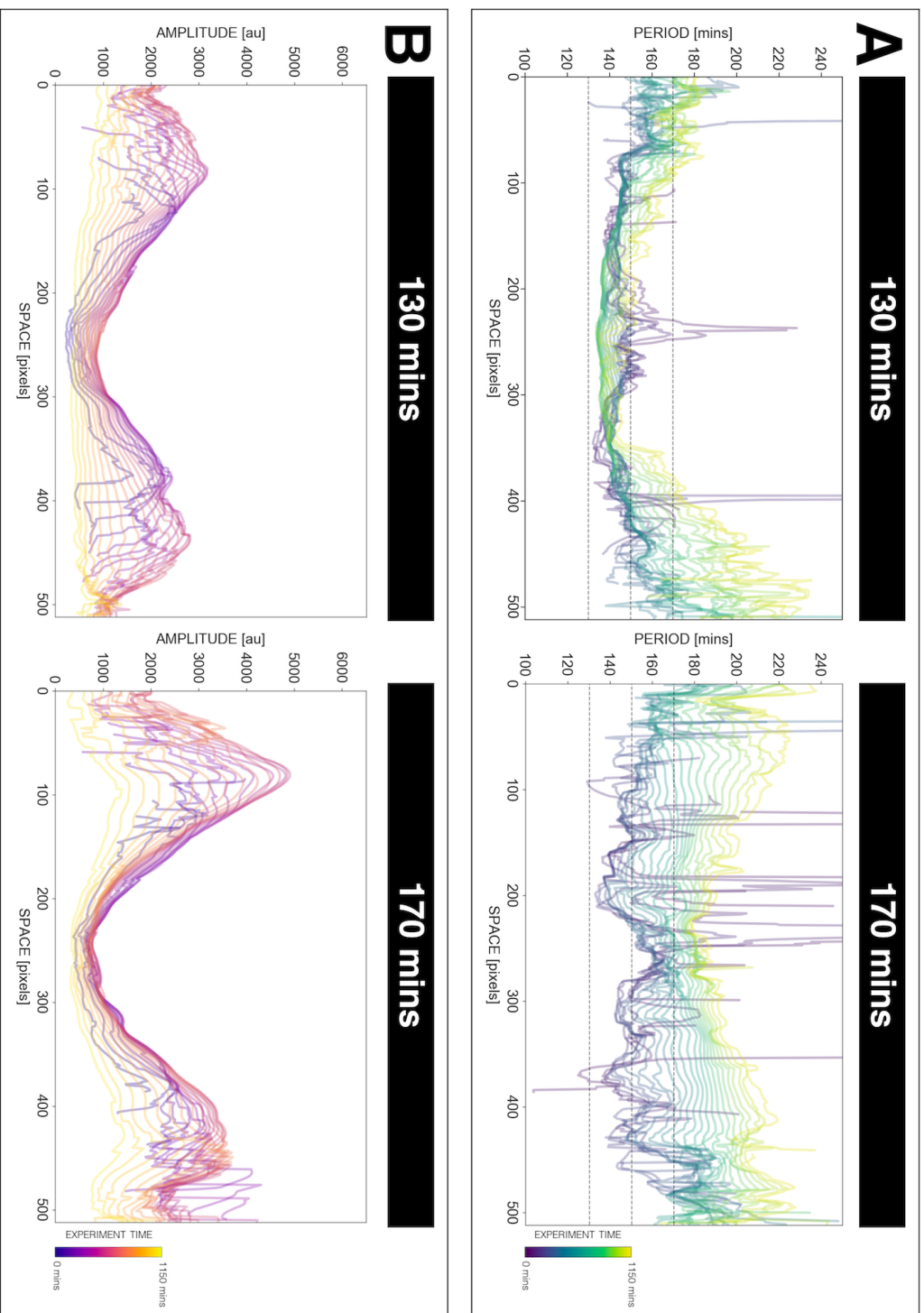


Figure 4.3 A higher (or lower) period gradient correlates with a higher (or lower) amplitude gradient. (A) Temporal evolution of the period gradient as an overlay of the average period gradient across multiple samples (for 130-min: $n = 15$ and $N = 7$, for 170-min: $n = 9$ and $N = 6$) at different timepoints. Periods are equal to 130 mins, 150 mins, and 170 mins are highlighted. Colors mark progression in time, from purple to yellow. Pixel size is 1.38 μm and cells have a diameter of around 10 μm . Plots are the same as those in Figure 3.8B. (B) Temporal evolution of the amplitude gradient as an overlay of the average amplitude gradient across multiple samples at different timepoints. Colors mark progression in time, from purple to yellow. Pixel size is 1.38 μm and cells have a diameter of around 10 μm .

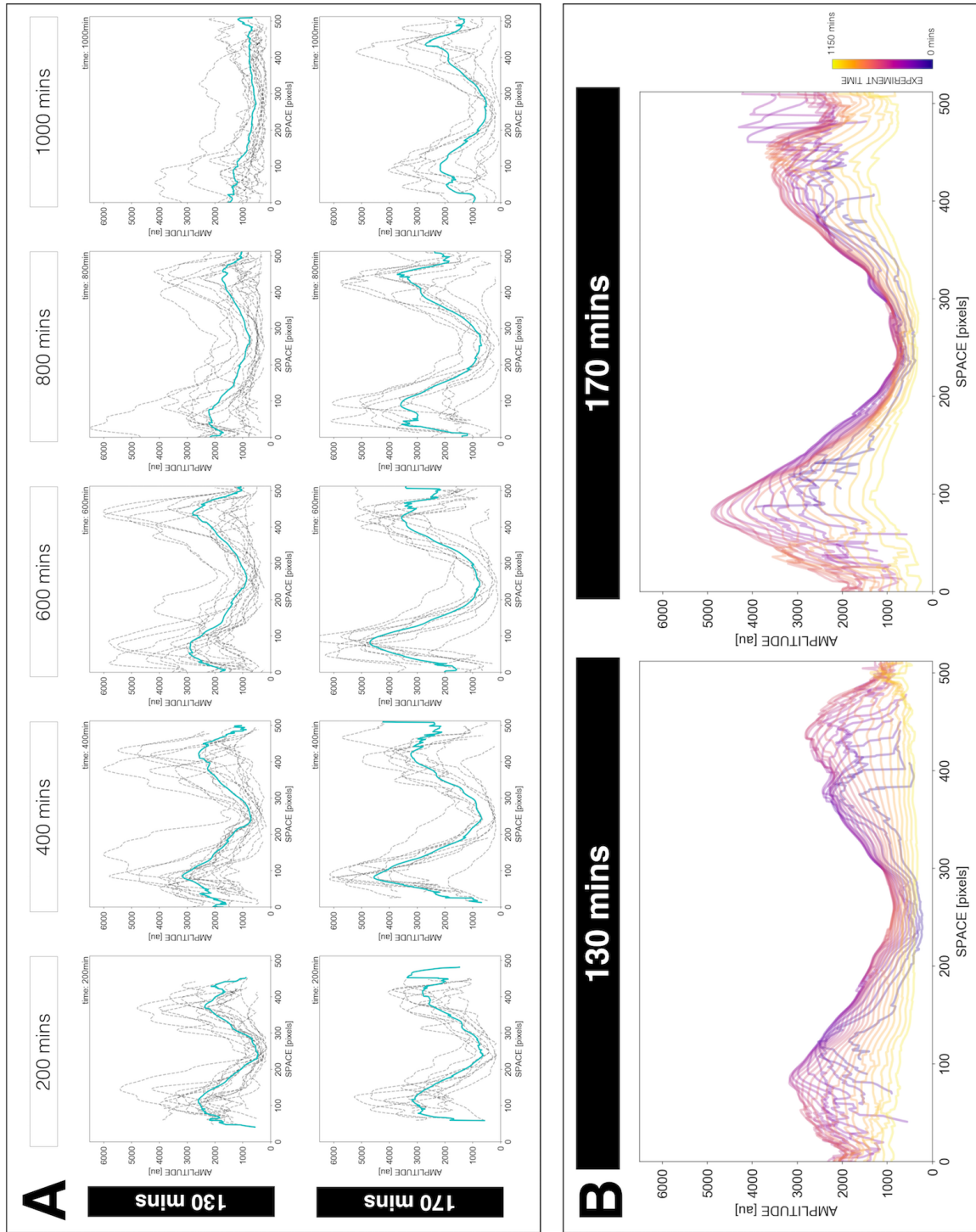


Figure 4.4 Oscillations at the posterior PSM (i.e. the center of spreadouts) have the lowest amplitude regardless whether the segmentation clock is sped up or slowed down. (A) Average amplitude gradient along the periphery-center-periphery axis of spreadouts subjected to either 130-min or 170-min periodic pulses of 2 μ M DAPT at different timepoints. Amplitude gradient tracing average amplitude over 50 pixels at different positions along the periphery-center-periphery axis at the equator (i.e. perpendicular to the dorsal-ventral axis) of the sample is marked with a dashed black line. The average of this amplitude gradient across multiple samples (for 130-min: $n = 15$ and $N = 7$, for 170-min: $n = 9$ and $N = 6$) is marked with a solid cyan line. Time is indicated as mins elapsed from the start of the experiment. Pixel size is 1.38 μ m and cells have a diameter of around 10 μ m. (B) Temporal evolution of the amplitude gradient as an overlay of the average amplitude gradient across multiple samples at different timepoints. Colors mark progression in time, from purple to yellow. Pixel size is 1.38 μ m and cells have a diameter of around 10 μ m. Plots are the same as those in Figure 4.3B.

4.1.3 The frequency gradient precedes the phase gradient in samples subjected to periodic pulses of DAPT

After interesting observations on emergence of altered period gradient upon entrainment of the segmentation clock to periodic DAPT pulses, we carried out a more thorough analysis of the frequency gradient and the phase gradient in spreadouts subjected to the periodic perturbation (for details, please refer to Section 6.5.4). Detailed investigation of the temporal evolution of both the frequency gradient and the phase gradient revealed that the former precedes the latter. Spreadouts subjected to periodic pulses of DAPT start with a rather flat frequency gradient (Figure 3.7C-E, 4.5, 8.8, 8.14). While spreadouts generally start as a narrow population of cells in the PSM (i.e. the tailbud) whose intracellular signaling oscillations share almost equivalent frequencies (Lauschke et al., 2012), it seemed that, a little while after the start of the experiment, almost all cells in these samples instead adjust their period/frequency to a value close to that of the DAPT pulses, i.e. to either 130 mins (0.048 rad/min) (Figure 4.5) or 170 mins (0.037 rad/min) (Figure 8.14). Eventually, in these samples, a frequency gradient emerges with the fastest oscillations (locked to the frequency of the DAPT pulses) localized in the center and the slower oscillations localized towards the periphery (Figure 8.15). Meanwhile, the phase gradient also starts flat but only builds up after emergence of a frequency gradient (Figure 4.5, 8.14, 8.15). That the frequency gradient precedes the phase gradient is also evident when we plotted the slope of the phase gradient versus the corresponding slope of the frequency gradient at different timepoints (Figure 4.7A), as elaborated later in Section 4.1.5.

4.1.4 Entrainment of the segmentation clock results in a less steep phase gradient

We next monitored the slope of the spatial gradients of frequency and phase in spreadouts subjected to periodic pulses of 2 μ M DAPT, and compared them to their controls. We recorded a remarkable trend in the evolution of the slope of the frequency gradient in spreadouts that is correlated to the period of their segmentation clock (Figure 4.6A). Samples with the fastest segmentation clock (i.e. those subjected to 130-min periodic pulses of 2 μ M DAPT) have the steepest frequency gradient (Figure 4.6A, C). In contrast, samples with the slowest segmentation clock (i.e. those subjected to 170-min periodic pulses of 2 μ M DAPT) have the flattest frequency gradient (Figure 4.6A, D). Meanwhile, their respective controls (i.e. those subjected to either 130-min or 170-min periodic pulses of DMSO), with intermediate period of free-running segmentation clock at around 140 mins, both have intermediate slopes of frequency gradient. Despite differences in slopes of the frequency gradient,

samples subjected to periodic DAPT pulses, regardless whether they have a faster or a slower segmentation clock, have a flatter phase gradient than controls (Figure 4.6B-D). Temporal derivative of the slope of frequency gradient and slope of phase gradient is summarized in Table 4.1.

4.1.5 When the segmentation clock is entrained to periodic DAPT pulses, a change in slope of the frequency gradient translates less to a corresponding change in slope of the phase gradient

Earlier in this chapter, we reported clear evidence that the frequency gradient precedes phase gradient even in samples whose segmentation clock were entrained to periodic DAPT pulses (Section 4.1.3). In spite of differences in the spatial profile of the frequency gradient which correlate well with the period of the segmentation clock (Figure 4.6A), we documented that the phase gradient in entrained samples was consistently flatter than controls (Figure 4.6B). To gain better insight into this, we compared the slope of the frequency gradient to the corresponding slope of the phase gradient across different timepoints. Figure 4.7A further illustrates the precedence of emergence of the frequency gradient to the emergence of the phase gradient in samples subjected to periodic pulses of DAPT. This is best exemplified by points that have a nonzero slope of frequency gradient, but have a zero slope of phase gradient. In contrast to controls, we noted that a change in slope of the frequency gradient translates less to a corresponding change in the slope of the phase gradient when the segmentation clock is entrained to periodic DAPT pulses. We quantified this by defining a quantity (alpha, α), which is the ratio between the slope of the frequency gradient and the slope of the phase gradient. Compared to their respective controls, we consistently documented a higher α for those subjected to periodic DAPT pulses (Table 4.1, Figure 4.7B). The magnitude of α was exceptionally highest in samples with a slower segmentation clock (i.e. those subjected to 130-min periodic pulses of 2 μ M DAPT).

Table 4.1 Temporal derivative of slope of frequency gradient and of slope of phase gradient in spreadouts subjected to periodic pulses of 2 μ M DAPT (or DMSO for controls). Temporal derivative of slope of frequency gradient and of slope of phase gradient are in [rad/(min-pixel)]/min and (rad/pixel)/min, respectively. Alpha is calculated here as the ratio between the temporal derivative of the slope of the frequency gradient and the temporal derivative of the slope of the phase gradient. Pixel size is 1.38 μ m and cells have a diameter of around 10 μ m.

Period of Pulses	Condition	n	N	Frequency Gradient	Phase Gradient	Alpha in min ⁻¹
130 mins	CTRL	6	5	-6.48E-08	-1.66E-05	3.90E-03
130 mins	DAPT	15	7	-1.04E-07	5.38E-06	-1.93E-02
170 mins	CTRL	5	4	-4.32E-08	-3.65E-05	1.18E-03
170 mins	DAPT	9	6	-4.53E-08	-2.02E-05	2.25E-03

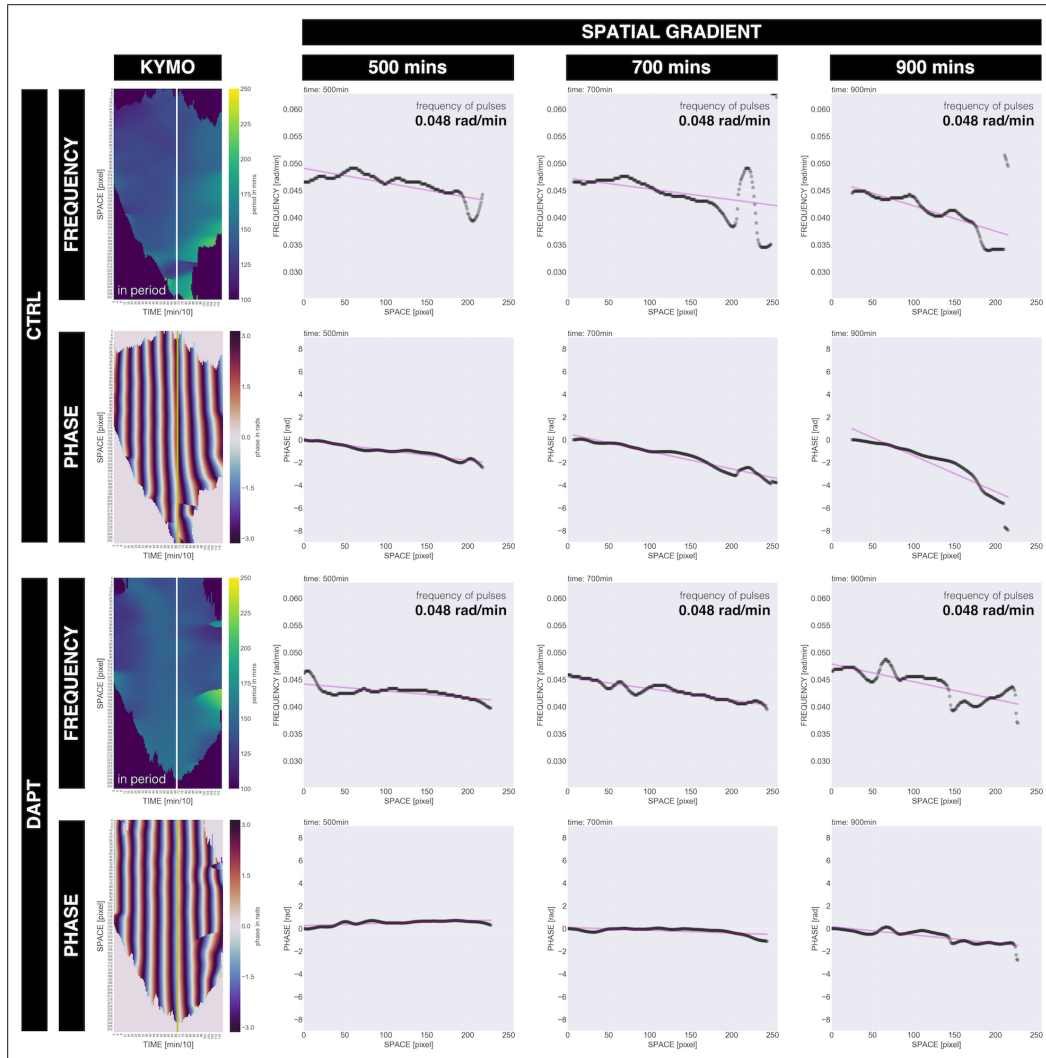


Figure 4.5 The frequency gradient precedes the phase gradient in samples entrained to 130-min periodic pulses of 2 μM DAPT. Spatial gradient in spreadout subjected to 130-min periodic pulses of 2 μM DAPT (or DMSO for control). Left: Kymographs plotting either the period or phase in space (y-axis) over time (x-axis). Center to periphery axis is from pixel 0 to pixel 256, from top to bottom of the kymograph. Kymographs include a line at time = 700 mins after the start of the experiment. Right: Spatial frequency gradient and spatial phase gradient at different timepoints. Center to periphery axis is from pixel 0 to pixel 256, from left to right of the spatial gradient plots. The faint magenta line denotes the linear fit to the experimental spatial gradient. Frequency of the DAPT (or DMSO) pulses is specified, and time is indicated as mins elapsed from the start of the experiment. Pixel size is 1.38 μm and cells have a diameter of around 10 μm .

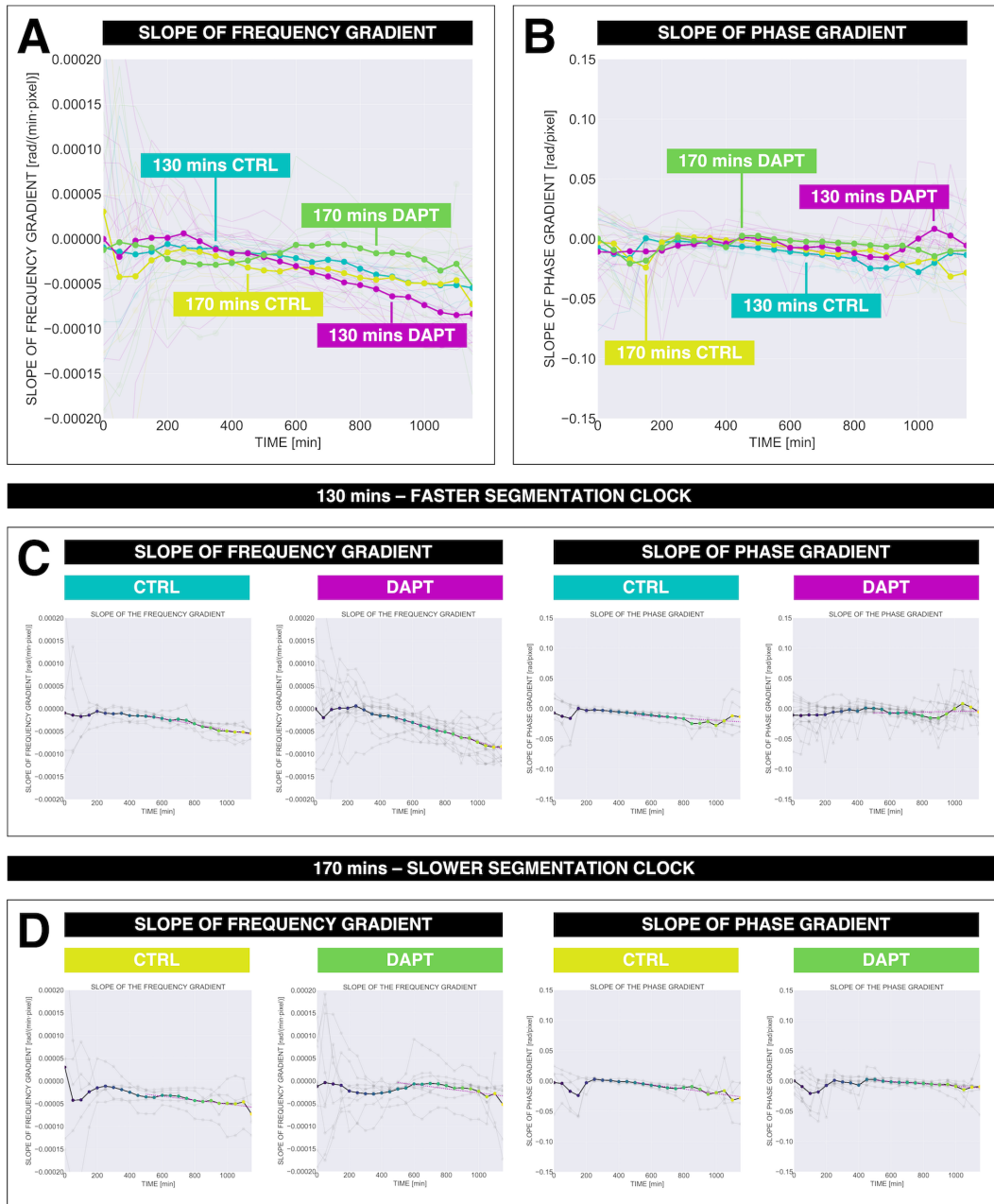


Figure 4.6 Entrainment of the segmentation clock results in a less steep phase gradient. (A) Temporal evolution of slope of frequency gradient in spreadouts subjected to either 130-min or 170-min periodic pulses of 2 μM DAPT (or DMSO for controls). Data for individual samples (for 130-DAPT: $n = 15$ and $N = 7$, for 130-CTRL: $n = 6$ and $N = 5$, for 170-DAPT: $n = 9$ and $N = 6$, for 170-CTRL: $n = 5$ and $N = 4$) are marked with thin solid lines, while their mean is marked with a thick solid line. Different conditions are denoted with different colors. Pixel size is 1.38 μm and cells have a diameter of around 10 μm . (B) Temporal evolution of slope of phase gradient in spreadouts subjected to either 130-min or 170-min periodic pulses of 2 μM DAPT (or DMSO for controls). Data for individual samples (for 130-DAPT: $n = 15$ and $N = 7$, for 130-CTRL: $n = 6$ and $N = 5$, for 170-DAPT: $n = 9$ and $N = 6$, for 170-CTRL: $n = 5$ and $N = 4$) are marked with thin solid lines, while their mean is marked with a thick solid line. Different conditions are denoted with different colors. Pixel size is 1.38 μm and cells have a diameter of around 10 μm . (C) Temporal evolution of slope of frequency gradient and slope of phase gradient in spreadouts subjected to 130-min periodic pulses of 2 μM DAPT (or DMSO for controls). Data for individual samples (for DAPT: $n = 15$ and $N = 7$, for CTRL: $n = 6$ and $N = 5$) are marked with faint lines, while their mean is marked with a thick solid line. Colors in data points mark progression in time, from purple to yellow. Magenta dashed line denotes linear fit to experimental data for determination of the temporal derivative of the slope from 500 mins after the start of the experiment. Pixel size is 1.38 μm and cells have a diameter of around 10 μm . (D) Temporal evolution of slope of frequency gradient and slope of phase gradient in spreadouts subjected to 170-min periodic pulses of 2 μM DAPT (or DMSO for controls). Data for individual samples (for DAPT: $n = 9$ and $N = 6$, for CTRL: $n = 5$ and $N = 4$) are marked with faint lines, while their mean is marked with a thick solid line. Colors in data points mark progression in time, from purple to yellow. Magenta dashed line denotes linear fit to experimental data for determination of the temporal derivative of the slope from 500 mins after the start of the experiment. Pixel size is 1.38 μm and cells have a diameter of around 10 μm .

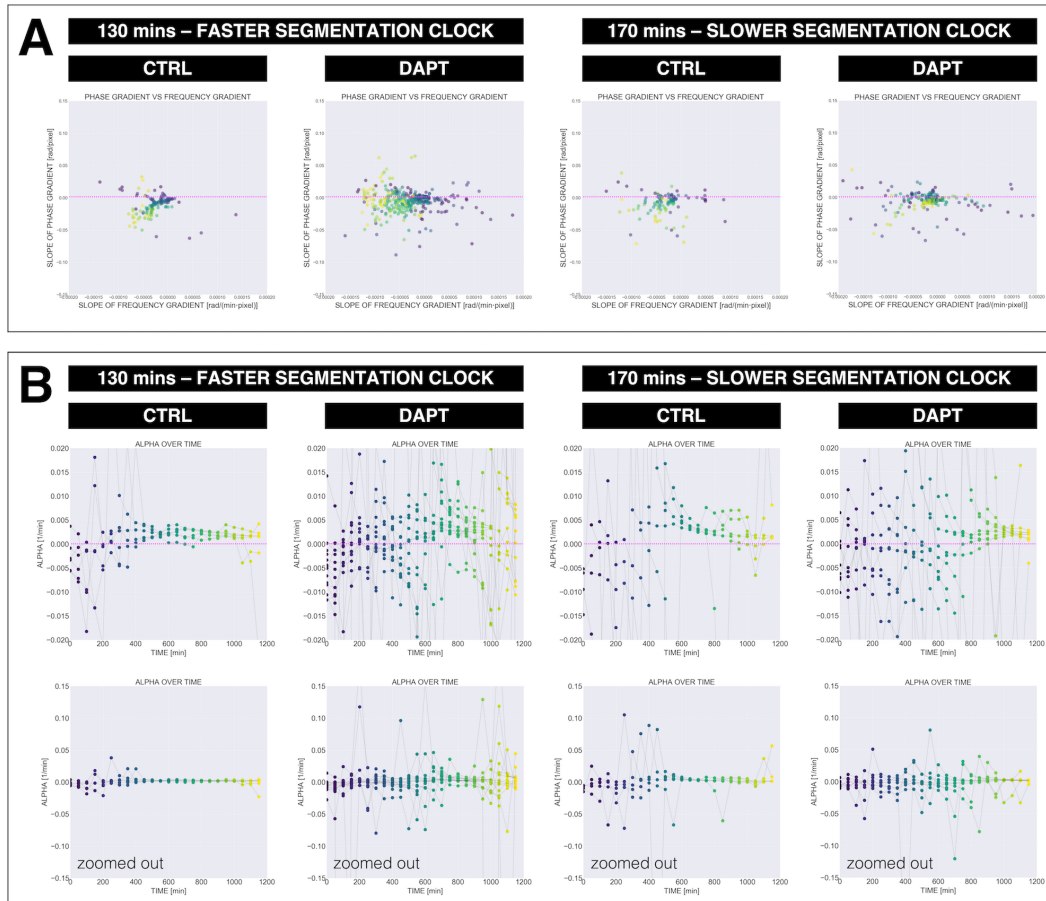


Figure 4.7 A change in slope of the frequency gradient translates less to a corresponding change in slope of the phase gradient when the segmentation clock is entrained to periodic DAPT pulses. (A) Plot of the slope of phase gradient versus the slope of the frequency gradient for spreadouts subjected to either 130-min or 170-min periodic pulses of 2 μ M DAPT (or DMSO for controls). Colors mark progression in time, from purple to yellow. Slope of phase gradient = 0 is highlighted with a magenta dashed line. Pixel size is 1.38 μ m and cells have a diameter of around 10 μ m. 130-min: (CTRL: $n = 6$ and $N = 5$) and (DAPT: $n = 15$ and $N = 7$), 170-min: (CTRL: $n = 5$ and $N = 4$) and (DAPT: $n = 9$ and $N = 6$). (B) Alpha across time calculated from ratio between slope of frequency gradient and slope of phase gradient at each timepoint. Colors mark progression in time, from purple to yellow. Alpha = 0 is highlighted with a magenta dashed line. Plots in the bottom row are zoomed out versions of plots in the top row.

4.1.6 Entrained samples undergo segmentation despite having a flatter phase gradient than controls

We summarized our results on the slopes of frequency and phase gradients in a 3D plot, as illustrated in Figures 4.8A and 8.16. Considering the observations we have documented thus far, where we recorded an altered frequency gradient and a flatter phase gradient (Table 4.1-4.2) in entrained samples compared to their respective controls, we were eager to verify whether or not samples subjected to periodic DAPT pulses really segment.

As mentioned earlier, spreadouts start as a rather homogeneous population of intracellular signaling oscillations. To make them, tailbuds of mouse embryos are cut away from the rest of the PSM and are cultured on fibronectin-coated glass (Lauschke et al., 2012). These primary tissue spread until they re-establish an AP axis (i.e. center-to-periphery axis), when the oscillatory field is largest. Afterwards, spreadouts start to segment. Because segmented tissue does not longer oscillate, the oscillatory field regresses step-wise, coinciding every segmentation. The spread and regression of the oscillatory domain were evident in our timelapse movies, already suggesting successful re-establishment of the AP axis and segmentation even in spreadouts subjected to periodic DAPT pulses. By integrating information from timelapse movies of spreadouts expressing LuVeLu, their timeseries acquired from global intensity analyses, and their corresponding kymographs, we approximated the time of the re-establishment of the AP axis and the time corresponding to the formation of the first segment. We defined the time to re-establishing the AP axis as the time a complete wave of LuVeLu arrives at the farthest periphery of spreadouts (i.e. its maximum oscillatory domain), just before regression of oscillatory field. We then defined the time to form the first segment as the time a wave arriving in the periphery results in the first regression. As illustrated in Figure 4.8B, all samples, regardless whether their segmentation clock was sped up or slowed down, re-established their AP axis at similar times. Concomitantly, samples with a faster segmentation clock (i.e. those subjected to 130-min periodic pulses of 2 μ M DAPT) segmented first than those with a slower segmentation clock (i.e. those subjected to 170-min periodic pulses of 2 μ M DAPT). Interestingly, the time to formation of the first segment overlaps with the time the phase gradient has just started to build up (i.e. slope of the phase gradient deviates from 0) (Figure 4.6B).

In addition to signaling dynamics of *Lfng* (visualized using LuVeLu), which are indicative of segment formation (i.e. arrival of the wave at the periphery of spreadouts, turning on of the *Lfng* stripe expression domain also at the periphery of spreadouts, and regression of the oscillatory domain), the formation of segments was verified from brightfield channel of timelapse movies recording actual formation of

physical segment boundaries. Using tissues from embryos expressing reporters for *Axin2* and *Mesp2*, which naturally show polarized expression of the said genes in newly-formed/presumptive somites (Aulehla et al., 2003; Morimoto et al., 2005), we further confirmed that segmentation properly occurs in our entrained samples. Indeed, even in samples subjected to periodic pulses of 2 μ M DAPT, *Axin2* is correctly localized in the caudal (i.e. posterior or towards the center of spreadouts) half of newly-formed segments (Figure 4.10C), while *Mesp2* is correctly localized in the rostral (i.e. anterior or towards the periphery of spreadouts) half (Figure 8.17).

4.1.7 Increasing entrainment strength abolishes the period gradient and its consequent phase wave

We attributed the re-emergence of the period gradient, even upon entrainment of the segmentation clock, to the inherent intercellular coupling between intracellular signaling oscillations in the embryonic tissue. We thought one way to bypass this, and hence abolish the period gradient, is by increasing the entrainment strength in our experiments (in collaboration with Katharina Sonnen). By increasing the concentration of DAPT, and hence increasing the strength of entrainment, we could potentially flatten the period gradient, equivalent to making all oscillations in the tissue lock to the periodic perturbation. As period/frequency gradient precedes phase gradient (Section 4.1.3), abolishing the period/frequency gradient (i.e. by adjusting the rhythm of all oscillations in the PSM to cycle with the same period using high entrainment strength) would be correlated to abolishing the spatiotemporal phase wave traversing the tissue, instead inducing Notch signaling pulses. Indeed, abolishment of the phase wave is evident in kymographs (i.e. space versus time plots) of spreadouts subjected to periodic pulses of high concentrations of DAPT. In these samples, almost the entire AP axis (i.e. space) has one phase value at a given time (Figure 4.9A), implying occurrence of pulses instead. This is better quantified upon determination of the slope of the spatial phase gradient (i.e. $\Delta\text{phase}/\Delta\text{space}$). Certainly, subjecting spreadouts to periodic perturbation with high entrainment strength (i.e. 130-min periodic pulses of 5 μ M DAPT) resulted in a flat spatial phase gradient (Figure 4.9B, Table 4.3). Such abolishment of the phase gradient is well correlated with the loss of the underlying period gradient, as shown in Figure 4.9C. No physical segment boundaries were seen in these samples ($n = 4$ and $N = 1$) upon inspection of the brightfield channel during timelapse imaging. If segments really do not form in these samples, and if this is due to abolishment of the period gradient and not because of the effect of DAPT, then this observation corroborates strongly with the earlier observation that segments do not form until a spatial phase gradient, resulting from precedent emergence of an underlying spatial frequency gradient (Section 4.1.3), builds up in the embryonic tissue (Section 4.1.6).

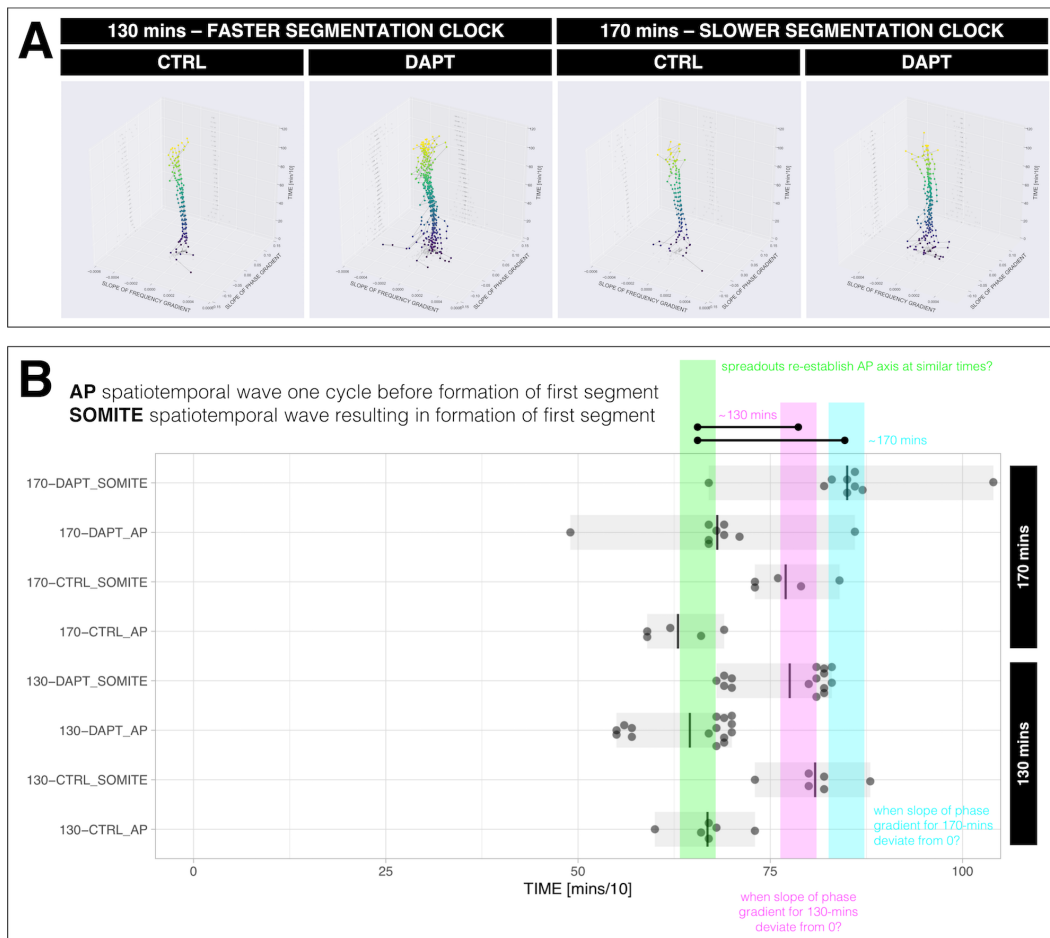


Figure 4.8 Entrained spreadouts undergo segmentation even with a flatter phase gradient than respective controls, with samples with slower segmentation clock starting to segment later. (A) 3D plot of the slope of frequency gradient, the slope of phase gradient, and time for spreadouts subjected to either 130-min or 170-min periodic pulses of 2 μ M DAPT (or DMSO for controls). Plots include projections of (a) slope of frequency gradient versus time, (b) slope of phase gradient versus time, and (c) slope of frequency gradient versus slope of phase gradient. Colors mark progression in time, from purple to yellow. Pixel size is 1.38 μ m and cells have a diameter of around 10 μ m. A bigger version is illustrated in Figure 8.16. 130-min: (CTRL: $n = 6$ and $N = 5$) and (DAPT: $n = 15$ and $N = 7$), 170-min: (CTRL: $n = 5$ and $N = 4$) and (DAPT: $n = 9$ and $N = 6$). (B) Approximate time to re-establish AP axis and to form the first segment in spreadouts subjected to either 130-min or 170-min periodic pulses of 2 μ M DAPT (or DMSO for controls). Time is approximated from timelapse movies, their timeseries acquired from global intensity analyses, and their corresponding kymographs. As segmented tissue does not oscillate, the time to re-establish the AP axis ($_AP$) is defined as the time for arrival of wave at the periphery of spreadouts one cycle before regression of oscillatory field. Meanwhile, the time to form the first segment ($_SOMITE$) is defined as the time for arrival of wave at the periphery of spreadouts resulting in the first regression. Black dots mark individual samples (for 130-DAPT: $n = 15$ and $N = 7$, for 130-CTRL: $n = 6$ and $N = 5$, for 170-DAPT: $n = 9$ and $N = 6$, for 170-CTRL: $n = 5$ and $N = 4$), while a black line marks their mean. The gray shaded area denotes the range. Approximate times corresponding to re-establishment of AP axis, first segmentation of samples with a faster segmentation clock (i.e. 130-DAPT), and first segmentation of samples with a slower segmentation clock (i.e. 170-DAPT) are highlighted.

Table 4.2. Slope of phase gradient in spreadouts subjected to periodic pulses of 2 μ M DAPT (or DMSO for controls). The number of samples (n) and number of independent experiments (N) are enumerated, along with the period of 2 μ M DAPT pulses (or DMSO for controls, CTRL). The mean slope of the phase gradient at 850 mins after the start of experiment is specified, including the standard deviation (SD), the standard error of the mean (SEM), and the 95% confidence interval (CI) of the mean. These summary statistics are in (rad/pixel)/min and were determined using PlotsOfData (Postma and Goedhart, 2019). Pixel size is 1.38 μ m and cells have a diameter of around 10 μ m. The temporal evolution of the slope of phase gradient is illustrated in Figure 4.6, while its temporal derivative is specified in Table 4.1.

Period of Pulses	Condition	n	N	Mean, (rad/pixel)/min	SD, (rad/pixel)/min	SEM, (rad/pixel)/min	95% CI of Mean
130 mins	CTRL	6	5	-2.47E-02	1.50E-02	6.71-E-03	-4.19E-02 -- -7.42E-03
130 mins	DAPT	15	7	-1.52E-02	1.37E-02	3.65E-03	-2.30E-02 -- -7.33E-03
170 mins	CTRL	5	4	-9.13E-03	5.58E-03	2.79E-03	-1.69E-02 -- -1.39E-03
170 mins	DAPT	9	6	-5.26E-03	3.75E-03	1.33E-03	-8.32E-02 -- -2.21E-03

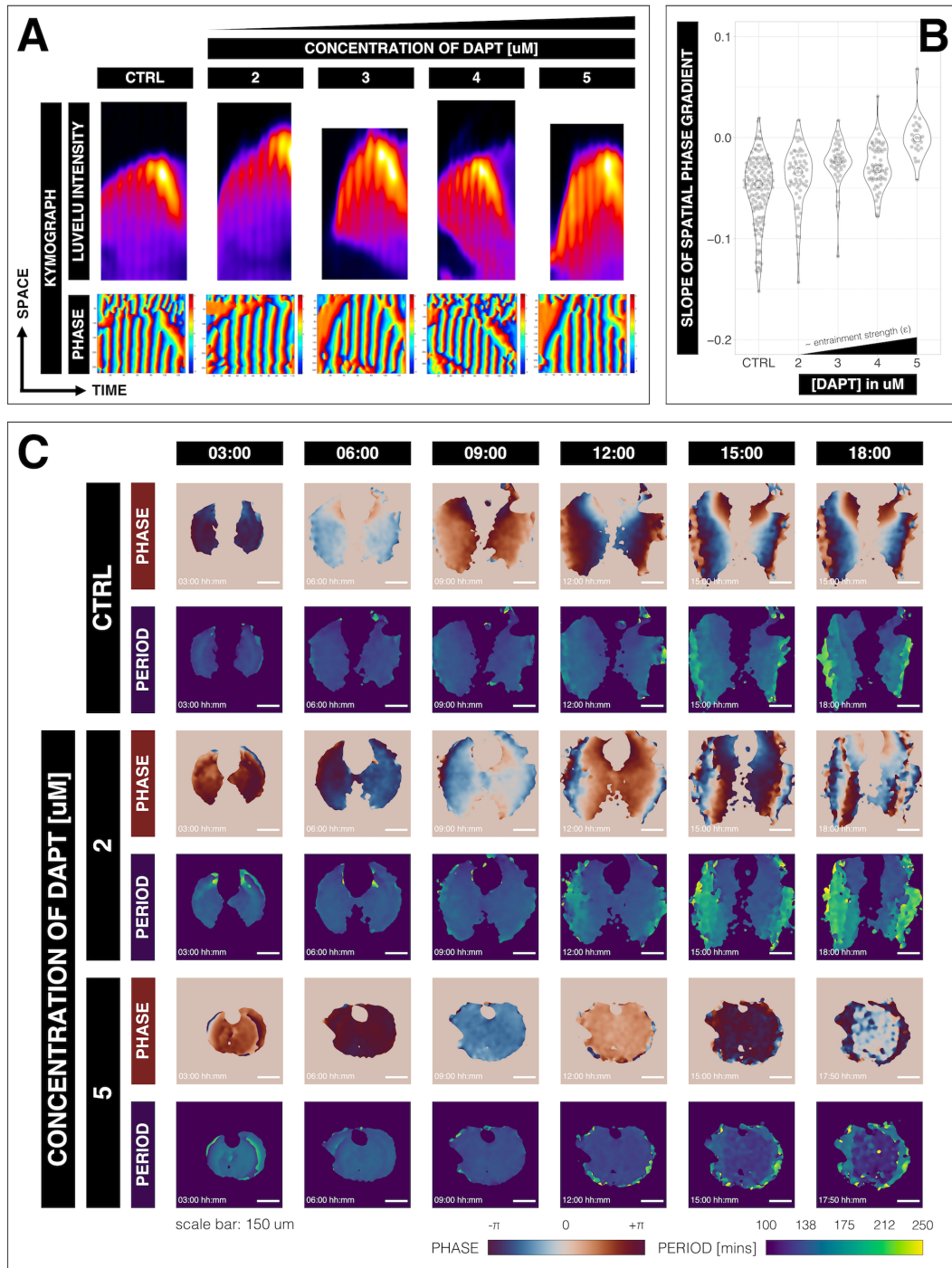


Figure 4.9 Increasing entrainment strength abolishes the period gradient and its consequent phase wave. (A) Intensity and phase kymographs of spreadouts subjected to 130-min periodic pulses of DAPT (or DMSO for control). Concentrations of DAPT are indicated above the kymographs. Intensities of LuVeLu are represented using the Fire lookup table (LUT), from dark purple to bright yellow. Phases are represented from $-\pi$ to $+\pi$, from blue to red. Experiments were done and data were analyzed by Katharina Sonnen. (B) Slope of spatial phase gradient ($\Delta\text{phase}/\Delta\text{space}$) corresponding to waves/pulses of LuVeLu in spreadouts subjected to 130-min periodic pulses of DAPT (or DMSO for controls), represented as violin plots with a circle on the median. Concentrations of DAPT are indicated. The number of samples (n) and number of independent experiments (N) are: $n = 23$ and $N = 8$ for CTRL, $n = 10$ and $N = 3$ for 2 μM DAPT, $n = 6$ and $N = 2$ for 3 μM DAPT, $n = 7$ and $N = 2$ for 4 μM DAPT, and $n = 4$ and $N = 1$ for 5 μM DAPT. For each sample, multiple timepoints corresponding to a wave/pulse of LuVeLu were considered. Slope of spatial gradient at each of these timepoints is represented as a dot. Experiments were done and data were analyzed by Katharina Sonnen. Data are visualized using PlotsOfData (Postma and Goedhart, 2019), and a summary of these data is provided in Table 4.3. (C) Snapshots of phase and period wavelet movies of spreadouts subjected to 130-min periodic pulses of either 2 μM or 5 μM DAPT (or DMSO for control) at different timepoints. Time is indicated as hh:mm elapsed from the start of the experiment. Samples are rotated so that dorsal side is up. Experiment using 5 μM DAPT was carried out by Katharina Sonnen.

Table 4.3 Slope of the spatial phase gradient corresponding to waves/pulses of LuVeLu in spreadouts subjected to 130-min periodic pulses of DAPT (or DMSO for controls). Concentrations of DAPT are indicated. The number of samples (n) and number of independent experiments (N) are enumerated, along with the total number of waves/pulses of LuVeLu considered. The mean slope of the spatial phase gradient is specified, including the standard deviation (SD) and the 95% confidence interval (CI) of the mean. These summary statistics were determined using PlotsOfData (Postma and Goedhart, 2019). A plot of these data is shown in Figure 4.9B.

Condition	Number of Waves/Pulses Considered	n	N	Mean	SD	95% CI of Mean
CTRL	141	23	8	-0.05	0.03	-0.06 – -0.05
2 μ M DAPT	59	10	3	-0.04	0.03	-0.05 – -0.03
3 μ M DAPT	43	6	2	-0.02	0.02	-0.03 – -0.02
4 μ M DAPT	61	7	2	-0.03	0.02	-0.03 – -0.02
5 μ M DAPT	25	4	1	0	0.02	-0.01 – 0.01

4.1.8 Oscillations of Wnt signaling are also entrained to periodic pulses of DAPT and are phase-shifted to entrained oscillations of Notch signaling

Leveraging unifying principles in synchronization has allowed us to predictably control the period and phase of the segmentation clock using microfluidics-based entrainment, even while being agnostic of the underlying molecular events happening in the PSM. While we did achieve to capitalize on the phenomenology of the segmentation clock (i.e. its oscillatory nature) to control it in our experiments, it remains as an actually intricate genetic network comprising of crosstalk between the Wnt signaling pathway, FGF signaling pathway, and Notch signaling pathway (Dequéant and Pourquié, 2008; Hubaud and Pourquié, 2014; Aulehla et al., 2003; Dequéant et al., 2006; Aulehla et al., 2007). Considering this, we wondered how far we could use our top-down principles-based approach to control signaling oscillations in the said genetic network. If there exists a crosstalk between oscillatory signaling pathways in the segmentation clock, we hypothesized that we could control signaling oscillations in one pathway via periodic perturbation of another pathway, regardless of the underlying molecular complexity in their interactions. For instance, we could look into the effect of periodic pulses of DAPT, a modulator of Notch signaling, to signaling oscillations of Wnt target genes. This is most appealing as we have recently documented how the intracellular phase shift in oscillations of Notch and Wnt is instructive to formation of segments in the presomitic mesoderm (Sonnen et al., 2018), which greatly relies on a spatial frequency gradient (i.e. a frequency gradient along the AP axis) in at least one of these oscillations. Our lab has previously shown that oscillations of Axin2, a downstream target of Wnt signaling that oscillates in the PSM (Aulehla et al., 2003), can be entrained to DAPT pulses with a period close to the free-running period of the segmentation clock (Sonnen et al., 2018). Here, we were curious if we would still observe similar entrainment at a more significant detuning.

In this study, we used a mouse line (i.e. Axin2-GSAGS-Achilles) recently generated in our lab by Nobuko Tsuchida-Straeten, in collaboration with Yvonne Petersen of the EMBL Transgenic Service, using Achilles plasmid kindly shared by the lab of Ryoichiro Kageyama (Institute for Integrated Cell-Material Sciences, Kyoto University). This mouse line expresses a fusion protein consisting of Axin2 and of a fast-maturing version of YFP (i.e. Achilles) (Yoshioka-Kobayashi et al., 2020). We recovered tissues from embryos of these mice and subjected them to pulses of 2 μ M DAPT with a period (i.e. 170 mins) significantly different from the free-running period of the segmentation clock (i.e. around 140 mins). We acquired the timeseries corresponding to tissue-level oscillations of Axin2 via global intensity analysis as illustrated in Figure 3.1A.

We noted that the oscillations of Axin2 are indeed also entrained to the periodic pulses of a Notch signaling modulator (i.e. DAPT) (Figure 4.10A-B), even at a more significant detuning. We then proceeded to compare the entrainment behavior of Wnt signaling oscillations to Notch signaling oscillations. While it would be most ideal to do simultaneous imaging of these oscillations in the same tissue, we banked on the power of entrainment to synchronize independent samples and use pulses of drug (or time from start of the experiment) as temporal landmarks for the comparison. Using this strategy, we documented that, while oscillations of Axin2 are entrained to periodic DAPT pulses, these oscillations are phase-shifted to entrained oscillations of LuVeLu (Figure 4.10A-B). Moreover, Axin2 oscillations entrain to periodic DAPT pulses at least a cycle later compared to LuVeLu (Figure 8.18). While LuVeLu locked to the periodic perturbation at around the third DAPT pulse (i.e. at around 500 mins after start of experiment), Axin2 became locked just after the fourth DAPT pulse (i.e. at around 700 mins after start of experiment). That Axin2 is entrained to DAPT pulses later than LuVeLu is also true for 130-min periodic pulses as we had previously documented using another Axin2 reporter (Sonnen et al., 2018). Furthermore, imaging with Axin2-GSAGS-Achilles also enabled us to score tissue segmentation in our experiments. In particular, we found that Axin2 is properly polarized in physical segments of spreadouts subjected to 170-min periodic pulses of 2 μ M DAPT (Figure 4.10C).

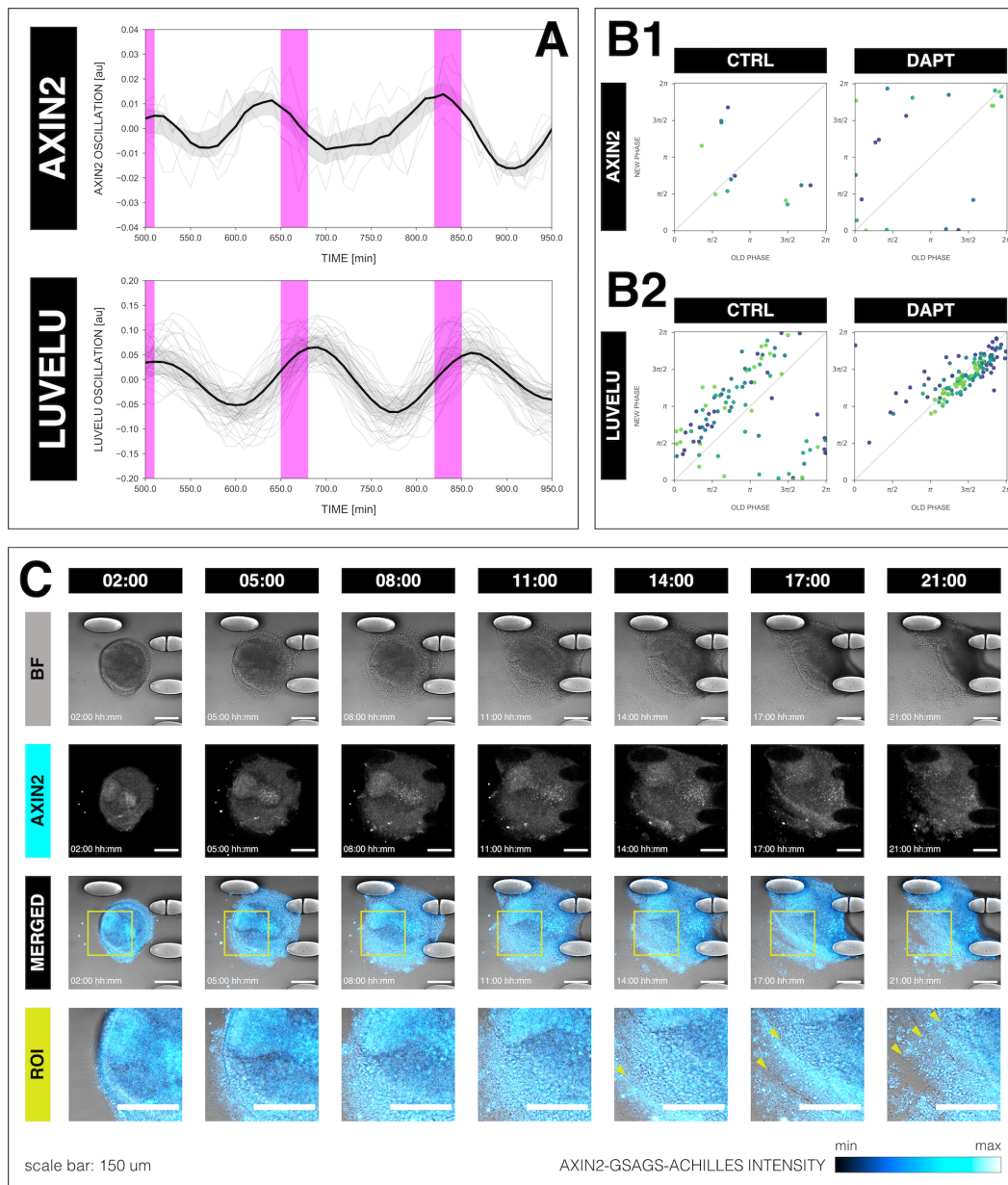


Figure 4.10 Tissue-level oscillations of Wnt signaling are also entrained to periodic pulses of DAPT and are phase-shifted to entrained tissue-level oscillations of Notch signaling. (A) Detrended timeseries of tissue-level oscillations in spreadouts expressing either Axin2-GSAGS-Achilles or LuVeLu entrained to 170-min periodic pulses of 2 μ M DAPT, zoomed in from 500 mins to 950 mins. Periodic pulses are indicated as magenta bars and the timeseries of each sample (for AXIN2: $n = 5$ and $N = 1$, for LUVELU: $n = 34$ and $N = 8$) is marked with a dashed line. The median of the oscillations is represented here as a solid line, while the gray shaded area denotes the interquartile range. The full detrended timeseries can be seen in Figure 8.18A. The plot for LuVeLu is the same as that for the 2 μ M DAPT condition in Figure 3.3A. (B) Stroboscopic maps of samples expressing either Axin2-GSAGS-Achilles (B1) or LuVeLu (B2) entrained to 170-min periodic pulses of 2 μ M DAPT, with their respective controls (subjected to periodic pulses of DMSO). Colors mark progression in time, from purple to yellow. The maps in B2 are the same as those in Figure 3.4B. (C) Snapshots of timelapse imaging of spreadout subjected to 170-min periodic pulses of 2 μ M DAPT. Shown are the brightfield channel, the Axin2-GSAGS-Achilles channel, and their merge. Also shown is a ROI in the merge of the two channels, with green arrowheads marking segment boundaries. Time is indicated as hh:mm elapsed from the start of the experiment.

4.2 Discussion

In the previous chapter, we focused on unifying principles in synchronization to entrain the segmentation clock. In this chapter, we enumerated several behaviors characteristic of the PSM as a biologically-complex, spatially-extended system of coupled and phase-shifted intracellular signaling oscillations. In particular, we here carried out more thorough analyses of the emergent period gradient, investigated how it relates to the consequent phase wave, and looked into how this could be affecting tissue segmentation.

Growing evidence has emphasized the importance of the spatiotemporal wave-like pattern of Notch signaling in regulating somitogenesis. This propagating phase wave arises from the phase shift in signaling oscillations between individual PSM cells, and the underlying phase dynamics has been noted to encode both temporal and spatial information (i.e. both when and where the somites will form) (Sonnen et al., 2018; Lauschke et al., 2012). Phase-shifted oscillations can result either from (a) differences in timing of oscillations with the same period or from (b) oscillations cycling with different periods. In the presomitic mesoderm, the spatiotemporal phase wave is specifically caused by a period gradient along the AP axis of the tissue (Aulehla et al., 2007; Masamizu et al., 2006; Lauschke et al., 2012; Tsiairis and Aulehla, 2016). The establishment and maintenance of such period gradient is attributed to intercellular coupling of the signaling oscillations (Herrgen et al., 2010; Liao and Oates, 2017; Morelli et al., 2009; Yoshioka-Kobayashi et al., 2020).

Here, we noted that oscillations in the center of spreadouts, corresponding to posterior PSM, acquire a rhythm similar to the rhythm of the segmentation clock upon periodic perturbation with pulses of DAPT (Figure 4.1, 4.2), similar to controls and *in vivo* (Tsiairis and Aulehla, 2016; Soza-Ried et al., 2014). More strikingly, such phenomenology is preserved regardless whether the segmentation clock is sped up or slowed down, highlighting an underlying mechanism for information processing where the segmentation clock robustly matches the fast oscillations in the center of spreadouts (i.e. posterior PSM). In moderate concentration of DAPT (i.e. 2 μM), this observation was not because all oscillations throughout the PSM acquired the same period. In fact, to reiterate, in entrained samples, the period of intracellular oscillations also slowed down from the center (i.e. posterior PSM) towards the periphery (i.e. anterior PSM). That we could alter the absolute value of periods, while somehow keep their relative difference along the AP axis of the tissue and also preserve the correspondence between rhythms of the posterior PSM and the segmentation clock, strongly suggests that the period gradient is a robust and emergent property of the system.

One characteristic of a nonlinear oscillation is the interdependence between its frequency and its amplitude (Arnol'd and Avez, 1968). In this chapter, we documented a similar interdependence between the frequency/period and amplitude of Notch signaling oscillations at both the cellular and tissue levels (Figure 4.4). At a cellular level, fast oscillations in the center of spreadouts (i.e. posterior PSM) correlated with lower amplitudes. The amplitude increased towards the periphery (i.e. anterior PSM) where the oscillations are slower. At a tissue level, when comparing samples that have either a faster (i.e. 130 mins) or slower (i.e. 170 mins) segmentation clock, a generally higher period gradient across the tissue correlated with a higher amplitude gradient. Samples subjected to 130-min periodic pulses of DAPT, which have a faster segmentation clock, generally have a lower amplitude than their corresponding controls (Figure 8.12). Interestingly, on the other hand, despite having a markedly higher period gradient (Figure 3.7C-E), samples subjected to 170-min periodic DAPT pulses, which have a slower segmentation clock, have an amplitude gradient that is not too different than respective controls (Figure 8.13). Whether or not this implies a threshold in maximum attainable amplitude in our system, and if this is restricted by the underlying molecular machinery in PSM cells are exciting prospects for future studies.

We further investigated the emergence of the phase wave from its underlying period/frequency gradient. We documented clear evidence that the frequency gradient precedes the phase gradient in our samples (Section 4.1.3, Figure 8.15). This is reminiscent of what happens in vivo, where a gradient in frequencies precedes the first spatiotemporal wave of Notch signaling in gastrulating mouse embryos (Falk, 2019). These support the argument that the phase shift in our system, and hence the spatiotemporal phase wave, results from the gradient in periods of intracellular signaling oscillations.

While we noted presence of phase waves in entrained spreadouts, we recorded that these samples have a less steep phase gradient (i.e. the phase waves are more pulse-like) compared to controls (Figure 4.6). In spite of a consistently flatter spatial phase gradient in entrained samples, we documented that the spatial frequency gradient actually seemed to correlate well with the period of the segmentation clock. More specifically, samples with the fastest (or slowest) segmentation clock have the steepest (or flattest) spatial frequency gradient (Figure 4.6A). It therefore seems that a high temporal derivative of slope of spatial frequency/period gradient is reflective of fast segmentation of the tissue. Spreadouts keep the range of periods in the period gradient constant during segmentation (Lauschke et al., 2012). As the tissue segments, in the absence of axial elongation, less space is left for this period gradient. Concomitantly, the slope of the period gradient increases with time. However, a slower segmentation clock would not necessarily result in a lower temporal derivative of the slope of the period gradient. In fact, based on the classical

clock and wavefront model (Cooke and Zeeman, 1976), where the size of segmented tissue is proportional to the period of the segmentation clock, the temporal derivative of the slope of the period gradient in samples that segment slower would overlap that in samples that segment faster. This is true if the range of periods in their period gradient is the same and remains stable, regardless of the absolute period values. This is illustrated in Figure 4.11. If the range of the period/frequency gradient is a constant in our experiments, then a lower temporal derivative of the slope of the frequency gradient (Figure 4.6A, Table 4.1) hence suggests that while our samples with slower segmentation clock (i.e. 170 mins) do segment slower, they do not form proportionally bigger segments, which contradicts the classical clock and wavefront model.

One striking finding relates to translating the frequency gradient into a phase gradient. To describe this, we defined a quantity (i.e. alpha, α), which is the ratio between the slope of the spatial frequency gradient and the slope of the spatial phase gradient. Calculating this quantity from the temporal derivative of the slopes, as shown in Table 4.1, assumes that α is constant. Calculating α for each timepoint, as shown in Figure 4.7B, instead shows that it is actually rather dynamic. Indeed, alpha is at first erratic but then becomes stable, even tending to converge towards a single value. Regardless of approach, we nonetheless noted that samples subjected to periodic pulses of DAPT have higher alpha than controls. This jive well with the observation that samples subjected to fast periodic pulses of 2 μ M DAPT (i.e. 130 mins) has a steep frequency gradient correlated with a rather flat phase gradient (Figure 4.6A-C, Table 4.1). Remarkably, the quantification also implies that samples subjected to slow periodic pulses of 2 μ M DAPT (i.e. 170 mins) actively translates its already flat frequency gradient to an even flatter phase gradient compared to respective controls (Figure 4.6A-B, D, Table 4.1). More generally, when the segmentation clock is entrained to periodic DAPT pulses, regardless whether it is sped up or slowed down, a change in slope of the frequency gradient translates less to a corresponding change in slope of the phase gradient.

We summarized our observations as 3D plots, which merge (a) the temporal evolution of the slope of the frequency gradient, (b) the temporal evolution of the slope of the phase gradient, and (c) the relationship between these two slopes (Figure 4.8A, 8.16). We noted samples subjected to periodic pulses of 2 μ M DAPT properly segmented, even with an altered frequency gradient and its rather flat but still apparent consequent phase gradient. Proper segmentation of the tissue was scored here based on morphology of physical segment boundaries, Lfng dynamics visualized using LuVeLu, and the polarized (and entrained) expression of Axin2 and Mesp2 in segments (Section 4.1.6). We found that spreadouts with slower segmentation clock (i.e. 170 mins) segmented later, which appears to correlate well with later time for the frequency gradient and phase gradient to build up in these samples. That the

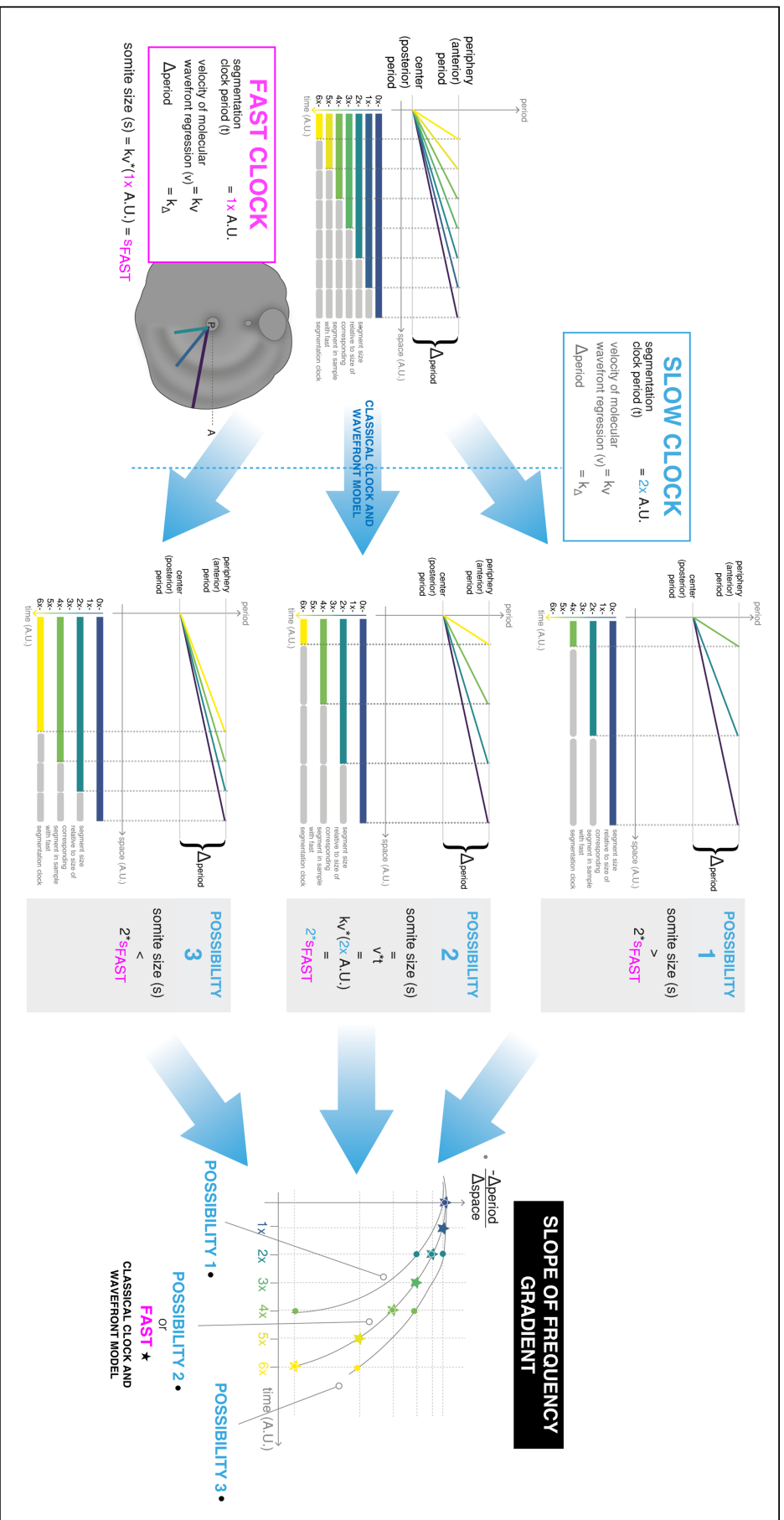


Figure 4.11 Possible outcomes of the change in the slope of the period/frequency gradient in a sample with slow segmentation clock (compared to a sample with fast segmentation clock) during tissue segmentation in the absence of axial elongation (e.g. in spreadouts). Depicted are the changes in the slope of the period gradient in a sample with fast segmentation clock (period = 1x A.U.), and possible outcomes in another sample with slow segmentation clock (period = 2x A.U.). Here, the velocity of wavefront regression, pertaining to a molecular gradient as in the classical clock and wavefront model, is constant ($v = k_{\omega}$) between the two samples. The range of periods in the period gradient along the unsegmented tissue is also constant (Δ period = $k\lambda$), albeit the absolute values of the periods are higher in the slower sample. The slope of the frequency gradient is illustrated as the negative of the slope of the period/frequency gradient. Segment sizes are shown relative to corresponding segment size in the fast sample. If the classical interpretation of the clock and wavefront holds here, the slopes of the period/frequency gradient of the fast and slow samples overlap throughout. Illustration by Stefano Vianello.

time to form the first segment seems to overlap with build up of phase gradient might indicate necessity of a phase gradient, even a slight one, for segmentation to occur. Another way to interpret this observation is that the tissue does not segment while it has no phase gradient (i.e. the slope of its phase gradient is equal to 0).

The observation that spreadouts subjected to periodic pulses of moderate DAPT (i.e. 2 μM) consistently exhibit an already flatter spatial phase gradient than controls could be attributed to the tendency of oscillations in these samples to adjust to the rhythm of the perturbation. During entrainment, signaling oscillations in each cell of the PSM are coupled to the external periodic perturbation. However, this PSM-scale coupling happens on top of intrinsic coupling between the cell and its neighbors, mediated by the reciprocal engagement of membrane receptors and ligands belonging to the Notch signaling pathway (Herrgen et al., 2010; Liao and Oates, 2017; Morelli et al., 2009; Yoshioka-Kobayashi et al., 2020). Such intercellular coupling could be ascribed to the emergence of a period gradient, even during entrainment of the segmentation clock, and hence propagation of a still apparent phase wave. Indeed, a balance between intercellular coupling of intracellular signaling oscillations and their coupling to the periodic perturbation appears to be a feature of our experimental system. Hence, to abolish the period gradient, locking most oscillations to the drug pulses, the balance must be tipped in favor of the latter (i.e. coupling to the periodic perturbation). This could be achieved either by decreasing intercellular coupling (e.g. using mouse lacking *Lfng* as in Yoshioka-Kobayashi et al., 2020) or by increasing entrainment strength (i.e. by increasing the concentration of DAPT as in Figure 3.3, 8.4). In this study, we capitalized on microfluidics-based entrainment to experimentally tune the period gradient and its consequent phase wave. By increasing entrainment strength (i.e. using 5 μM DAPT), we locked all oscillations in the tissue to the periodic pulsing, bypassing the underlying intercellular coupling. This resulted in abolishment of both the period gradient and the phase gradient (Figure 4.9). Instead of a spatiotemporal wave, we noted induction of Notch signaling pulses. Preliminary evidence suggests absence of physical segment boundaries in these samples ($n = 4$ and $N = 1$), which would have to be proven more thoroughly (e.g. by using live reporters of segment boundary formation). If such observation is confirmed, this would support the argument that the phase wave of Notch signaling is necessary for tissue patterning. In the future, it would be crucial to more strongly verify that the loss of segmentation is indeed due to the absence of the phase wave and not because of the inhibiting effect of the drug. While this is yet to be addressed, it is important to note that the highest drug concentration used in this part of the study (i.e. 5 μM) is still low compared to drug concentrations more commonly used to inhibit Notch signaling (e.g. 25 μM as in Hubaud et al., 2017).

It is very interesting to distinguish whether the period/frequency gradient or the phase gradient, or both, confers the information for tissue patterning in the PSM. Phase waves could emerge even between oscillations with same frequencies. However, as already discussed, in our experiments, phase waves in the tissue emerge naturally from a precedent self-organized frequency gradient, which we could control via microfluidics-based entrainment. Based on these, it would thus seem sound to argue that the instructions for segmentation is more precisely encoded in the frequency gradient, and that the phase wave is a readout of the differences in frequencies of oscillations in the embryonic tissue. Such gradient in frequencies of signaling oscillations is in fact vital in modulating the intracellular phase shift between Notch and Wnt oscillations during somitogenesis. As reported in Sonnen et al., 2018, modulation of phase shift between these two oscillations allows encoding of not only temporal information but also intracellular spatial information along the AP axis of the mouse PSM, jiving well with the phase-shift model of tissue patterning (Goodwin and Cohen, 1969). In this framework, reciprocal entrainment of Wnt oscillations in spreadouts subjected to periodic pulses of DAPT would then be a requirement to preserve the differential phase shift between Wnt and Notch across the tissue and for proper segmentation to occur. Our evidence for periodic formation of physical segment boundaries in these samples already imply that the modulation of phase-shift between Wnt and Notch is functional even upon entrainment of the segmentation clock. Certainly, by using tissues from embryos expressing a dynamic reporter (i.e. Achilles) fused to Axin2, a downstream target of Wnt signaling, we noted that oscillations of Wnt signaling are also entrained to the periodic pulses of the Notch signaling modulator (i.e. DAPT). Notably, these oscillations are phase-shifted to entrained oscillations of Notch signaling (Figure 4.10) and entrain at a later timepoint (Figure 8.18).

That we could lock the segmentation clock to the periodic perturbation while entraining just a population of its constituent intracellular signaling oscillations was remarkable. We thought this could be reflective of how these oscillations are interacting during tissue patterning and how this could be related to gradients of morphogens in the tissue. Growing evidence has indeed shown that the concentration of FGF is instructive of the behavior of signaling oscillations (Diaz-Cuadros et al., 2020; also Volker Lauschke and Takehito Tomita in our lab), which then collectively manifest as a period gradient of Notch signaling oscillations along the AP axis of the tissue. A notable observation we presented here is that the fastest oscillations are consistently localized in the center of spreadouts (i.e. posterior PSM), which happens to be the region with the highest concentration of FGF (Lauschke et al., 2012). In addition, the period of these oscillations also happen to consistently lock to the period of the periodic perturbation (Figure 8.19A, B, Section 3.1.6, 4.1.1), suggesting that FGF concentration could be correlated with local entrainment. That we could experimentally define this period via entrainment would also imply that

FGF concentration does not define the absolute period of oscillations in the PSM. Instead, a gradient in concentration of FGF would seem more instructive of the relative differences in period of intracellular signaling oscillations in the embryonic tissue, with oscillations slowing down from region of high to low FGF signaling. Indeed, preliminary experiments, in collaboration with Takehito Tomita, revealed that embedding spreadouts with a bead coated with high concentrations of FGF8b (i.e. 0.8 ug/uL) and subjecting them to periodic DAPT pulses (Figure 8.19B) resulted in an ectopic "center" in the samples (n = 5 and N = 1), a localized region situated in the position of the bead that is locked to the periodic perturbation and from which oscillations appear to gradually slow down (Figure 8.19C). It was previously noted that a coupling gradient across a tissue could result in a period gradient (Ermentrout et al., 1998). Whether or not the period gradient in the PSM is similarly a readout of an underlying coupling gradient is still unclear. It would then be important to assess how periodic perturbation affects the FGF gradient, if at all, in our system, and to evaluate if this morphogen gradient is translated to a gradient in intercellular coupling. It would also be worthwhile to investigate if the emergence of a period gradient, even upon periodic perturbation, results from the emergence of an FGF gradient (i.e. symmetry-breaking) in spreadouts, which start as a rather homogeneous population of signaling oscillations (Lauschke et al., 2012). Nonetheless, it is exciting to think that the PSM as a spatially-extended system seems capable of globally scanning itself for region of highest morphogen concentration, and is able to do so robustly, especially when challenged with a periodic perturbation. Definitely, how entrainment of intracellular oscillations in such a narrow distribution of cells in the PSM is translated to entrainment of the segmentation clock, potentially via the emergent period/frequency gradient, would be an inspiring perspective for more thorough investigations.

4.3 Conclusion

While the segmentation clock can be abstracted to a generic oscillation following unifying principles in entrainment, we presented in this chapter noteworthy observations on behavior of its constituent intracellular signaling oscillations that reflect the system's underlying biology. Specifically, we elaborate on the emergence of a period gradient, even upon entrainment of the segmentation clock to periodic pulses of moderate entrainment strength. We argue that such gradient is a self-organized property of the PSM as a spatially-extended system of coupled, phase-shifted intracellular signaling oscillations. We also report that the emergence of such period gradient precedes the emergence of a phase gradient, which is manifested as an apparent spatiotemporal wave of Notch signaling. By modulating the period gradient via microfluidics-based entrainment, and hence tuning its consequent phase wave, we reveal here that entrained samples still segment, despite having a much flatter phase gradient. We also highlight the utility of entrainment to abolish the spatiotemporal wave of Notch signaling (i.e. by locking intracellular oscillations to periodic perturbation with high entrainment strength), offering an experimental strategy to investigate its necessity, and especially the underlying period gradient, for proper tissue patterning. In addition, we note that Wnt oscillations are similarly entrained to periodic pulses of a modulator of Notch signaling, and we present preliminary evidence suggesting that fast intracellular oscillations locked to the periodic perturbation are localized in the region with high FGF concentration. More generally, if the period gradient is a readout of intercellular coupling between intracellular signaling oscillations, the results we discuss in this chapter appear to enrich our insight into how precisely and robustly such coupling affects collective tissue-level dynamics (i.e. periodic tissue segmentation) during somitogenesis. As coupling governs entrainment phenomena (Abraham et al., 2010), study of the entrainment behavior of signaling oscillations across the PSM, as elaborated here, offers an alternative top-down approach to shed light into the intercellular coupling during somitogenesis, supplementing earlier studies on the subject matter (Herrgen et al., 2010; Morelli et al., 2009; Yoshioka-Kobayashi et al., 2020).

4.4 Outlook

Microfluidics-based entrainment of spreadouts after establishment of endogenous period gradient

In our experiments, spreadouts were subjected to periodic drug pulses from the start of culture and imaging, when the samples are still primarily a homogeneous population of oscillations with narrow period and phase distribution (i.e. taken from the posterior-most tip of the PSM, the tailbud). It would then be interesting to see how entrainment behavior would be different if the entraining signal is instead introduced when spreadouts have already spread and established its endogenous period gradient, just before the start of segmentation.

Development of optimal masking strategy to determine the oscillatory domain in timelapse movies

For investigations of the spatial gradients of period/frequency and phase, wavelet movies were masked based on a threshold in corresponding intensity timelapse movies to restrict analyses to the oscillatory domain. While this was sufficient to determine the slope of the said gradients, the masking strategy limited us from precisely determining the range of periods/frequencies and phases in the unsegmented PSM. Segmented tissue does not longer oscillate (Aulehla et al., 2007; Masamizu et al., 2006), but cells still have background fluorescence intensity that could sometimes be similar to low intensity signal at the center of spreadouts (i.e. posterior PSM). Masking via threshold intensity, therefore, is not most ideal to sharply distinguish the segmented tissue from the PSM. Hence, development of a more optimal masking strategy would enable us to measure the bounds of the period/frequency and phase spanning the unsegmented, oscillating tissue. One potential way to approach this is masking based instead on the amplitude of the oscillations. We found that amplitude increases from center to periphery (i.e. anterior PSM), matching the slowing down of oscillations along this AP axis (Figure 4.3). As segmentation coincides with arrest of oscillations, the amplitude drops from the periphery outwards. The peripheral edge, with the highest amplitude, could then be used to mark the boundary of the oscillatory domain.

Local entrainment or physical separation of the posterior PSM (i.e. center of spreadouts)

Here, we looked deeper into the emergence of an altered period gradient upon entrainment of the segmentation clock to periodic pulses of 2 μM DAPT. Notably, the fastest oscillations in posterior PSM cells (i.e. center of spreadouts) consistently locked to the entrainment period, while anterior PSM cells (i.e. periphery of spreadouts) oscillated at a slower pace. This is most remarkable for samples with a slower segmentation clock (i.e. 170 mins), where anterior PSM cells oscillate at a

period much slower than any oscillation in vivo. While we have evidence that FGF concentration determines relative period of oscillations in the tissue, it is still unclear if such an altered gradient in period was due to (a) the differential entrainment efficiency of cells at different regions of the AP axis, or to (b) active adjustment of an initially uniform period across all PSM cells, following global entrainment to the same period. To discriminate between these two possibilities, one could perform local entrainment of the posterior PSM. This could be carried out by using a laminar flow microfluidics setup or via optogenetics. An alternative approach is to physically separate the posterior PSM from the rest of the tissue using techniques like laser ablation. If oscillations in the anterior PSM are still slower even after physical separation, then the prompt to slow down (i.e. relative to the periodic perturbation) is autonomous in these oscillations. On the other hand, if all oscillations (including those in the anterior PSM) lock to the periodic perturbation after physical separation, then something in the posterior PSM actively influences more anterior oscillations to become slower.

Entrainment of signaling oscillations in Notch signaling mutant embryos

It would be very informative to study entrainment dynamics in Notch signaling mutant samples, which lack intercellular coupling and the spatiotemporal phase wave of Notch signaling. Specifically, one could subject tissues from embryos mutant for *Lfng*, which acts in the Notch signaling pathway by regulating the synchronization of Notch oscillations between neighboring cells (Aulehla and Johnson, 1999; Okubo et al., 2012; Yoshioka-Kobayashi et al., 2020), to periodic pulses of DAPT and visualize oscillatory dynamics using LuVeLu, a dynamic reporter driven from a *Lfng* promoter that is integrated outside the endogenous *Lfng* locus. *Lfng* mutants have been described in published literature. For instance, while intracellular signaling oscillations are preserved, embryos lacking *Lfng* show gross segmentation defects (Okubo et al., 2012; Evrard et al., 1998). Recently, *Lfng* mutants were used to delineate the importance of intercellular coupling and its delay to synchronize oscillations in the PSM (Yoshioka-Kobayashi et al., 2020). It is thus intriguing to see how these embryos would respond to entrainment, and whether or not synchronization to a periodic perturbation (i.e. via entrainment) would rescue the defective segmentation phenotype.

Entrainment of signaling oscillations in randomized PSM cells

Our lab recently developed a new technique that allows randomization of low input of PSM cells (RAFL: randomization assay for low input), uncovering the rules of synchronization between oscillations falling within a narrow distribution of periods and phases (Ho, 2020). In this system, cells that were randomized self-organize and form multiple foci of signaling oscillations, with each focus being reminiscent of an individual PSM. To complement the investigation of rules for intercellular coupling

during somitogenesis, one could implement an experimental setup for subjecting these randomized PSM cells to periodic pulses of signaling modulators. Moreover, close examination of entrainment dynamics in a single cell (a) in isolation and (b) coupled to other cell/s could be performed. This would certainly provide rich insight into intercellular coupling between intracellular signaling oscillations in cells of the PSM.

Does modulating the segmentation clock affect somitogenesis according to the classical clock and wavefront model?

“ *It is as though every cell has access to, and can read, a clock and a map.*

— **Brian C. Goodwin and Morrel H. Cohen**

Recently, substantial evidence has challenged the classical "clock and wavefront" model of somitogenesis (Sonnen et al., 2018; Lauschke et al., 2012). In these studies, the phase dynamics were seen to predict both the time and the location where somites will form, in accordance with what was proposed by another model of tissue patterning: the the phase-shift model (Goodwin and Cohen, 1969). This latter model emphasizes that the phase dynamics encode not only temporal but also spatial information, with a coordinate system organized around areas with the same phase relationship. In the classical clock and wavefront model, in contrast, a large time scale (i.e. regression of a wavefront) is thought to be simply partitioned into smaller time units (i.e. cycling of a clock) (Cooke and Zeeman, 1976). Based on this model, the size of a somite would thus be determined by the velocity of wavefront regression and the ticking of the segmentation clock. In this chapter, we will highlight the use of the microfluidics-based entrainment platform as an experimental tool to precisely modulate the rate at which segments are formed (i.e. the activity of the segmentation clock), while simultaneously scoring somitogenesis in intact PSM using live imaging. Ultimately, in this chapter, we aim to revisit the general interpretation of the clock and wavefront model of somitogenesis, to reinterpret it based on our recent observations, and attempt to reconcile it with the phase-shift model for tissue patterning.

5.1 Results

5.1.1 Intact PSM can be cultured within PDMS microfluidics chips for entrainment

As presented in the previous chapters, we are now able to control the period of the segmentation clock with high precision using microfluidics-based entrainment. To examine in a more physiologically relevant system if a slower (or faster) segmentation clock results in proportionally bigger (or smaller) somites, as predicted by the classical clock and wavefront model, we extended our experimental platform to culture, imaging, and entrainment of intact PSM. Accordingly, in collaboration with Katharina Sonnen (Hubrecht Institute), then a postdoctoral fellow in our lab, a new microfluidics device was fabricated that allowed for elongation of the embryonic tissue (Figure 5.1). Dissected tails of E10.5 mouse embryos were cultured within PDMS chips coated with PLL-PEG, which prevents cell attachment. These embryonic tissues were incubated at 37°C and under high oxygen conditions (i.e. 65% O₂). As shown in Figure 5.2, tails inside the PDMS chip grew well and elongated similar to *in vivo*. Moreover, the signaling oscillations and the spatiotemporal wave pattern were preserved, and segmentation was not disrupted.

5.1.2 Microfluidics-based entrainment enables precise adjustment of the segmentation clock in intact PSM

Upon optimization of the microfluidics setup for culture and imaging of intact PSM, we subjected the embryonic tissues to pulses of DAPT with a period (i.e. 170 mins) slower than the free-running period of the segmentation clock (i.e. 140 mins). Based on onset of *Lfng* stripe marking segment boundaries (i.e. visualized using LuVeLu) and actual segment morphology, we counted consistently less somites in samples subjected to the periodic perturbation compared to controls (Figure 5.3A). The segmentation clock in each intact PSM adjusted to the rhythm of the periodic DAPT pulses (Figure 5.3B), resulting in coherence of independent samples (Figure 5.3C). Using microfluidics-based entrainment, we successfully modulated the period of segmentation (Figure 5.3D), locking it to the period of the perturbation (i.e. 170 mins). As another hallmark of entrainment, the segmentation clock in intact PSM also established a stable phase relationship with the DAPT pulses (Figure 5.3E), with an entrainment phase remarkably similar to that when spreadouts (i.e. our *ex vivo* primary culture assay) were subjected to the same periodic perturbation (i.e. 170-min periodic pulses of 2 μ M DAPT) (Figure 3.5B2).

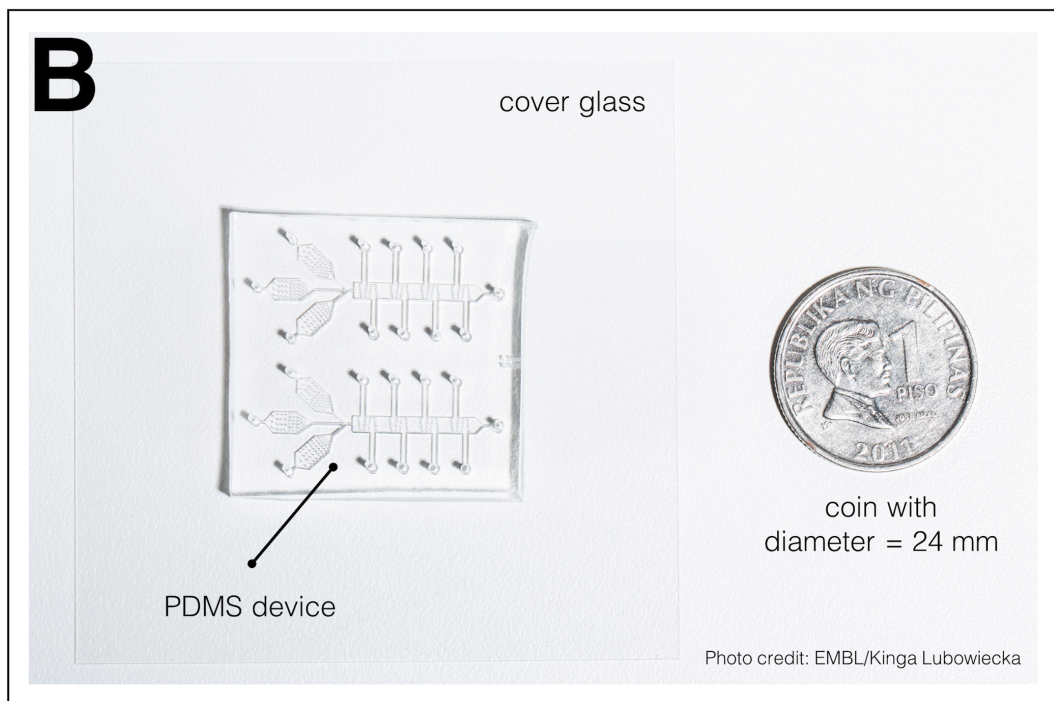
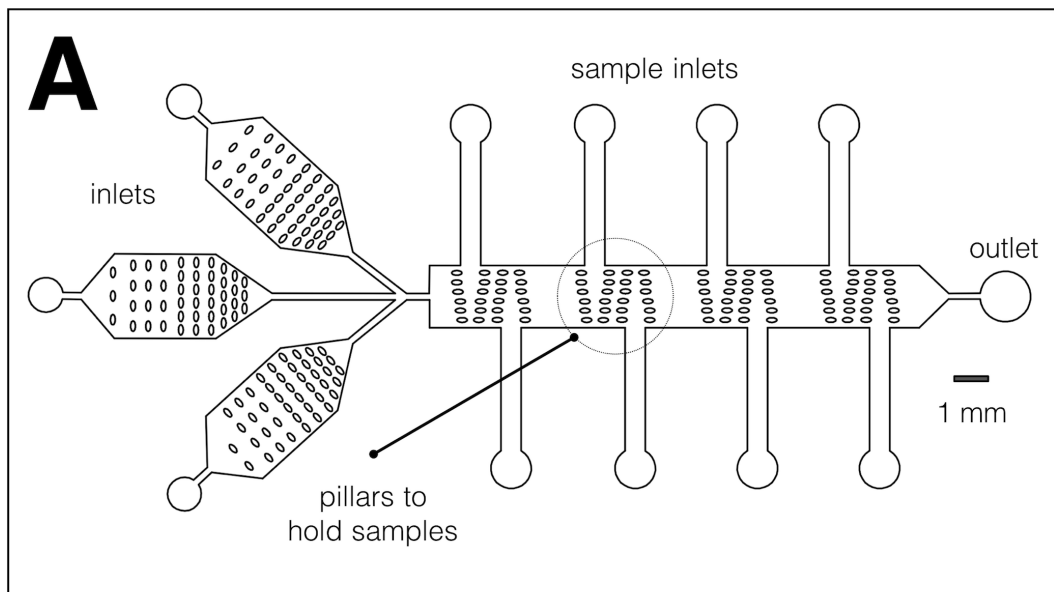


Figure 5.1 A microfluidics PDMS chip for culture, imaging, and entrainment of intact PSM. (A) Design of the microfluidics chip, showing inlets for medium and drug, inlets for the samples, pillars to hold each sample, and an outlet. (B) Photo of the chip bonded to cover glass and a coin (diameter: 24 mm) for scale. The split layout separating the upper and lower channel systems allows simultaneous delivery of drug and DMSO control to samples on opposite sides of the same device. Photo credit: EMBL/Kinga Lubowiecka.

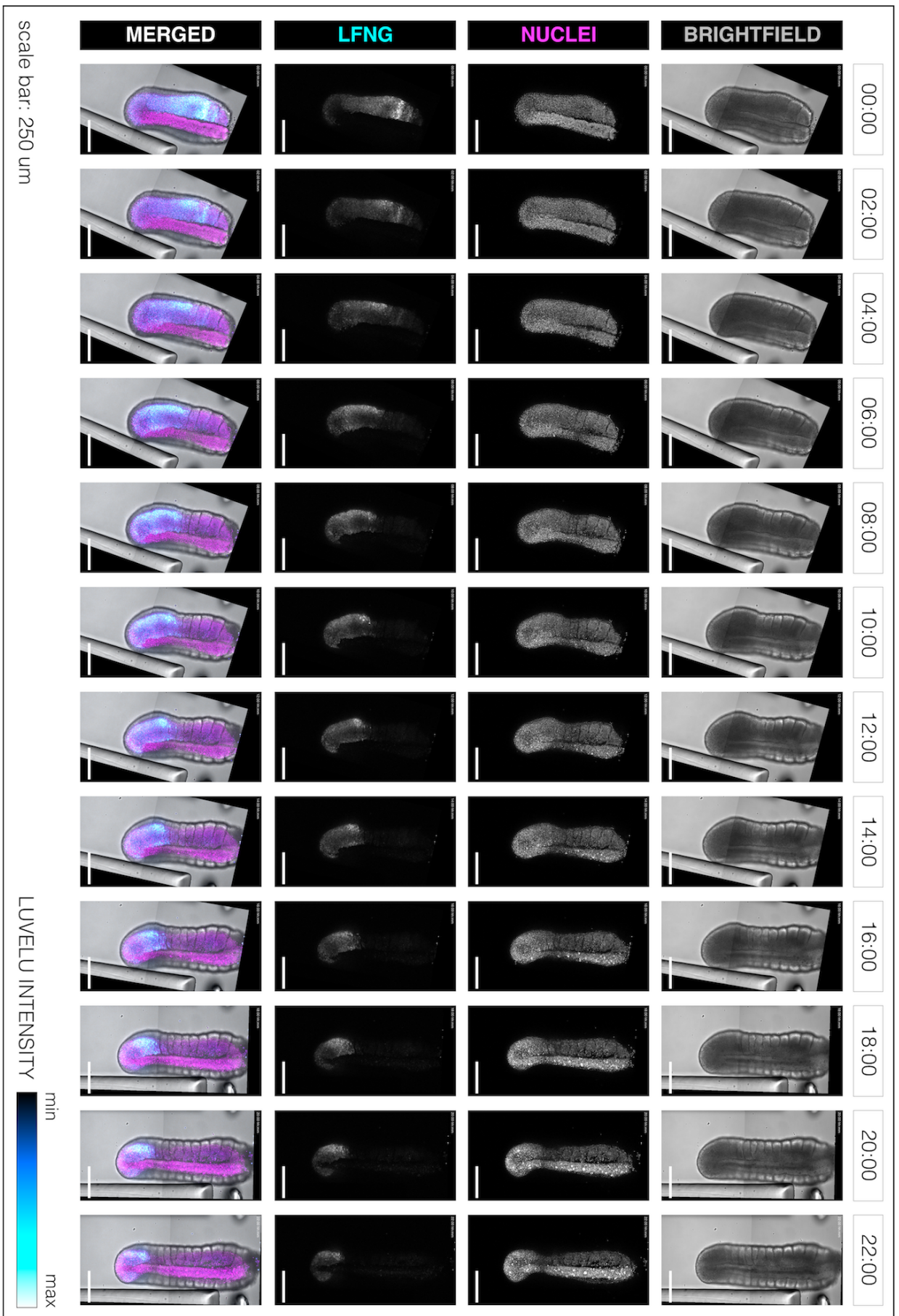


Figure 5.2 Intact PSM of mouse embryos can be cultured inside PDMS chip for microfluidics-based entrainment. Dissected tails of E10.5 mouse embryos were cultured in PLL-PEG coated PDMS chip at 37°C and under 65% O₂. Illustrated are stills from the live imaging of one such tails as somitogenesis proceeds. Shown are the brightfield channel, the H2B-mCherry channel (nuclear marker), the Luvellu channel (Lfhg dynamics), and their merge. Time is indicated as hh:mm elapsed from the start of imaging.

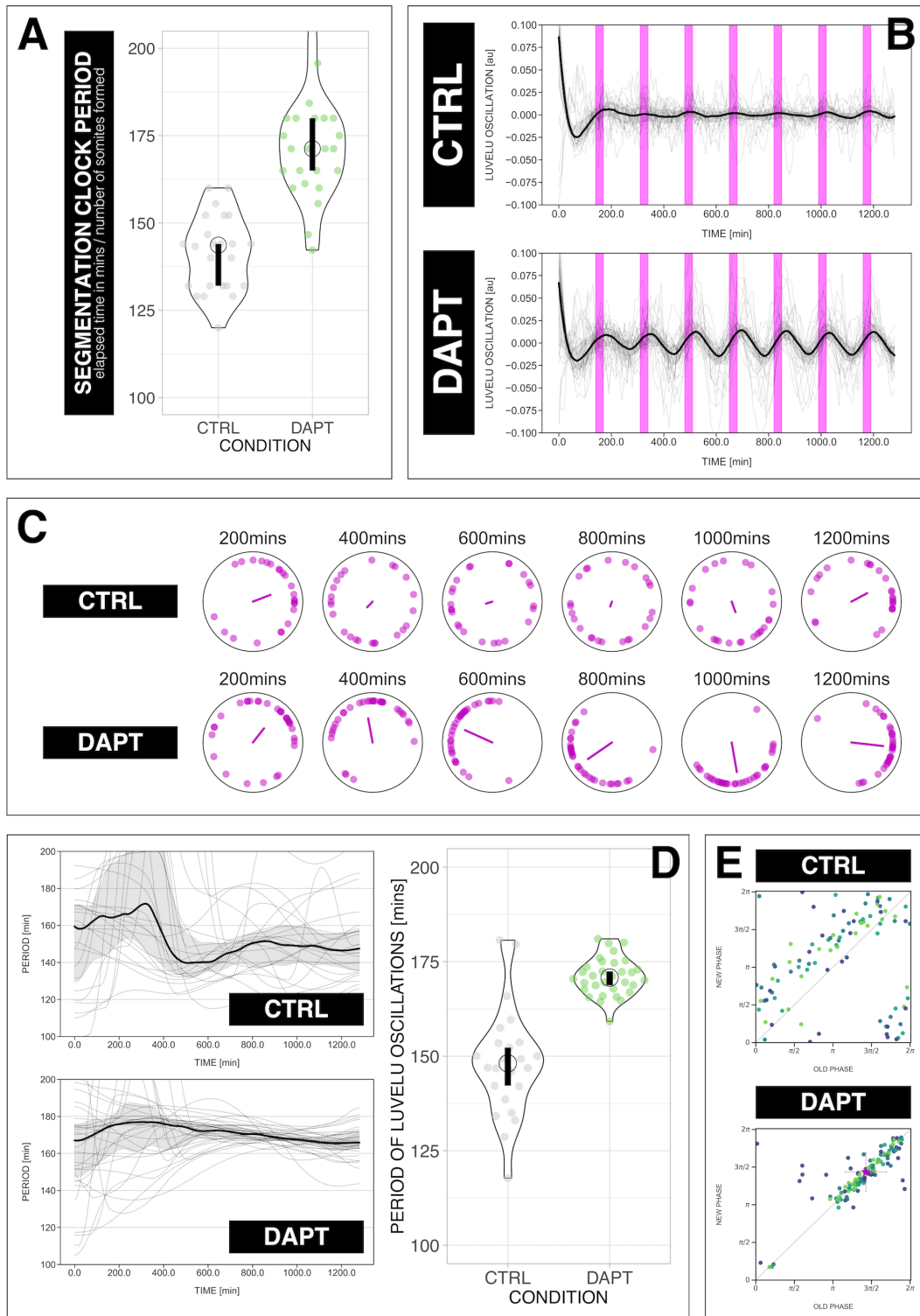


Figure 5.3 Segmentation clock in intact PSM is entrained to periodic DAPT pulses. (A) Segmentation period, determined from counting the number of somites formed and/or the number of LuVeLu waves that traversed the PSM within imaging time, of E10.5 mouse tails (i.e. PSM and 2 somites) subjected to 170-min periodic pulses of 2 μ M DAPT (or DMSO for controls), represented as a violin plot with a circle on the median. Segmentation period of each sample (for CTRL: $n = 24$ and $N = 6$, for DAPT: $n = 24$ and $N = 6$) is represented as a dot, while the 95% confidence interval (CI) of the median is represented as a solid vertical line. Median (95% CI) for CTRL and for DAPT are 143.67 mins (132-144 mins) and 171.25 mins (165-180 mins), respectively. Data are visualized and summary statistics are determined using PlotsOfData (Postma and Goedhart, 2019). (B) Detrended timeseries of the segmentation clock in intact PSM subjected to 170-min periodic pulses of 2 μ M DAPT (or DMSO for controls). Periodic pulses are indicated as magenta bars and the timeseries of each sample (for CTRL: $n = 24$ and $N = 8$, for DAPT: $n = 32$ and $N = 8$) is marked with a dashed line. The median of the oscillations is represented here as a solid line, while the gray shaded area denotes the interquartile range. Caption continued on the following page..

Figure 5.3 ..continued caption from previous page. (C) Polar plots at different timepoints showing phase of each sample and their first Kuramoto order parameter, represented as a magenta dot along the circumference of a circle and a magenta line segment at the circle's center, respectively. A longer line segment corresponds to a higher first Kuramoto order parameter, and thus to more coherent samples. The direction of the line denotes the vectorial average of the sample phases. (D) Left: Period evolution during entrainment, obtained from wavelet analysis. The period evolution for each sample and the median of the periods are represented here as a dashed line and a solid line, respectively. The gray shaded area corresponds to the interquartile range. Right: Mean period from 650 to 850 mins after start of the experiment of samples subjected to 170-min periodic pulses of 2 μM DAPT (or DMSO for controls), represented as a violin plot with a circle on the median. Each sample is represented as a dot, while the 95% confidence interval of the median is denoted as a solid vertical line. Median (95% CI) for CTRL and for DAPT are 148.13 mins (142.22-152.27 mins) and 170.81 mins (168.79-172.44 mins), respectively. Data are visualized and summary statistics are determined using PlotsOfData (Postma and Goedhart, 2019). (E) Stroboscopic maps of samples subjected to 170-min periodic pulses of 2 μM DAPT (or DMSO for controls). The localized region close to the diagonal in map for DAPT condition marks the entrainment phase. This is highlighted with a magenta star, which corresponds to the centroid of the said region. The centroid (x_c, y_c) was calculated from the vectorial average of the phases of all samples at the end of the experiment, where x_c = vectorial average of old phase, y_c = vectorial average of new phase. The spread of the points in the region is reported in terms of the circular standard deviation ($\sqrt{-2\ln R}$, where R is the first Kuramoto order parameter). Colors mark progression in time, from purple to yellow.

5.1.3 Segment polarity is preserved in somites formed from intact PSM subjected to microfluidics-based entrainment

Segments are not only identified based on the presence of periodic tissue boundaries, but are more strictly defined based on AP polarity (Hannibal and Patel, 2013). For instance, polarized expression of *Tbx18* and of *Uncx4.1* mark the rostral (i.e. anterior) and the caudal (i.e. posterior) halves of a somite, respectively (Kraus et al., 2001; Neidhardt et al., 1997). To check whether or not we preserve somite polarity in tissues subjected to periodic perturbation, we immediately recovered the samples after the experiment and hybridized them with probes against somite polarity markers. As shown in Figure 5.4, expression of *Uncx4.1* is preserved and restricted in caudal halves of somites when tissues were hybridized with digoxigenin (DIG) probes against the said transcript. In collaboration with Hidenobu Miyazawa, we also optimized hybridization chain reaction (HCR) for tails of mouse embryos and published the protocol in protocols.io: <https://dx.doi.org/10.17504/protocols.io.7pyhmpw>. Unlike conventional in situ hybridization protocols using DIG-conjugated probes, HCR enables multiplex in situ hybridization, is more quantitative, and has high sensitivity (Choi et al., 2016; Choi et al., 2018). Using HCR, we further verified that viable somites form in entrained samples, evidenced by expression of markers of somite polarity (i.e. both *Tbx18* and *Uncx4.1*) in the tissue complementing the morphological segments (Figure 8.20). In addition, we visualized expression of *Tbx6*, which marks the PSM (Chapman et al., 1996).



Figure 5.4 Segment polarity is preserved in somites formed from intact PSM subjected to microfluidics-based entrainment. Tails of E10.5 mouse embryos (i.e. PSM and 2 somites) were subjected to 170-min periodic pulses of 2 μ M DAPT (or DMSO for control). Samples were recovered after the experiment and were hybridized with DIG-conjugated probes against Uncx4.1 (marking the posterior boundary of each somite) and Shh (marking the notochord and the floor plate of the neural tube). White asterisks mark aberrant segments, while white arrowhead marks a notably bigger somite. Sample IDs and culture times are also indicated.

5.1.4 Left-right asymmetry is present in some samples adjusted to a slower segmentation clock with periodic DAPT pulses

While the morphology of somites in tails subjected to microfluidics-based entrainment generally look normal, we noted segmentation phenotypes that were present only in some ($n = 3/12$) of these samples (i.e. not in controls). In particular, we recorded more *Uncx4.1* positive stripes in one side of the the tissue compared to its contralateral counterpart. Some of the entrained tails showed mismatch between the number of left and right somites. For these samples, on the side with more *Uncx4.1* stripes, it seemed that an *Uncx4.1* domain split into two from medial to lateral (marked with white asterisk in Figure 5.4, 8.20). This resulted in left-right asymmetry and correlated well with a kink in the tissue. The timing of segmentation resulting in the mismatch (i.e. altered segment) coincided with the time the samples locked to the periodic perturbation (i.e. slowed down its segmentation clock), at around the 4th-5th DAPT pulse between 600-800 mins from the start of the experiment (Figure 5.3B-D).

5.1.5 A slower segmentation clock does not always result in a proportionally bigger somite

As exemplified throughout this text, microfluidics-based entrainment has enabled us to systematically modulate the period of segmentation, in spreadouts and now in intact PSM. Such modulation occurs without significant effect on regression of morphogen gradient (Sonnen et al., 2018). This then allows us to experimentally revisit the classical interpretation of the clock and wavefront model, and probe the effect of the period of the clock on somite size. If the general interpretation of the clock and wavefront model is true, slowing down the segmentation clock – for a constant velocity of wavefront regression – should result in proportionally bigger somites. Indeed, we noted that the slowing down of the segmentation clock, after the 4th-5th DAPT pulse, resulted in bigger somite size (marked with white arrowhead in Figure 5.4, 5.5, 8.20), in accordance to what would be predicted by the classical clock and wavefront model. In multiple instances ($n = 6$ and $N = 6$), however, it seemed that the size of the successive somites returned to a regular size, and did not appear significantly larger compared to the rest (Figure 5.4, 5.5), even though the period of segmentation remained slow (Figure 5.3D).

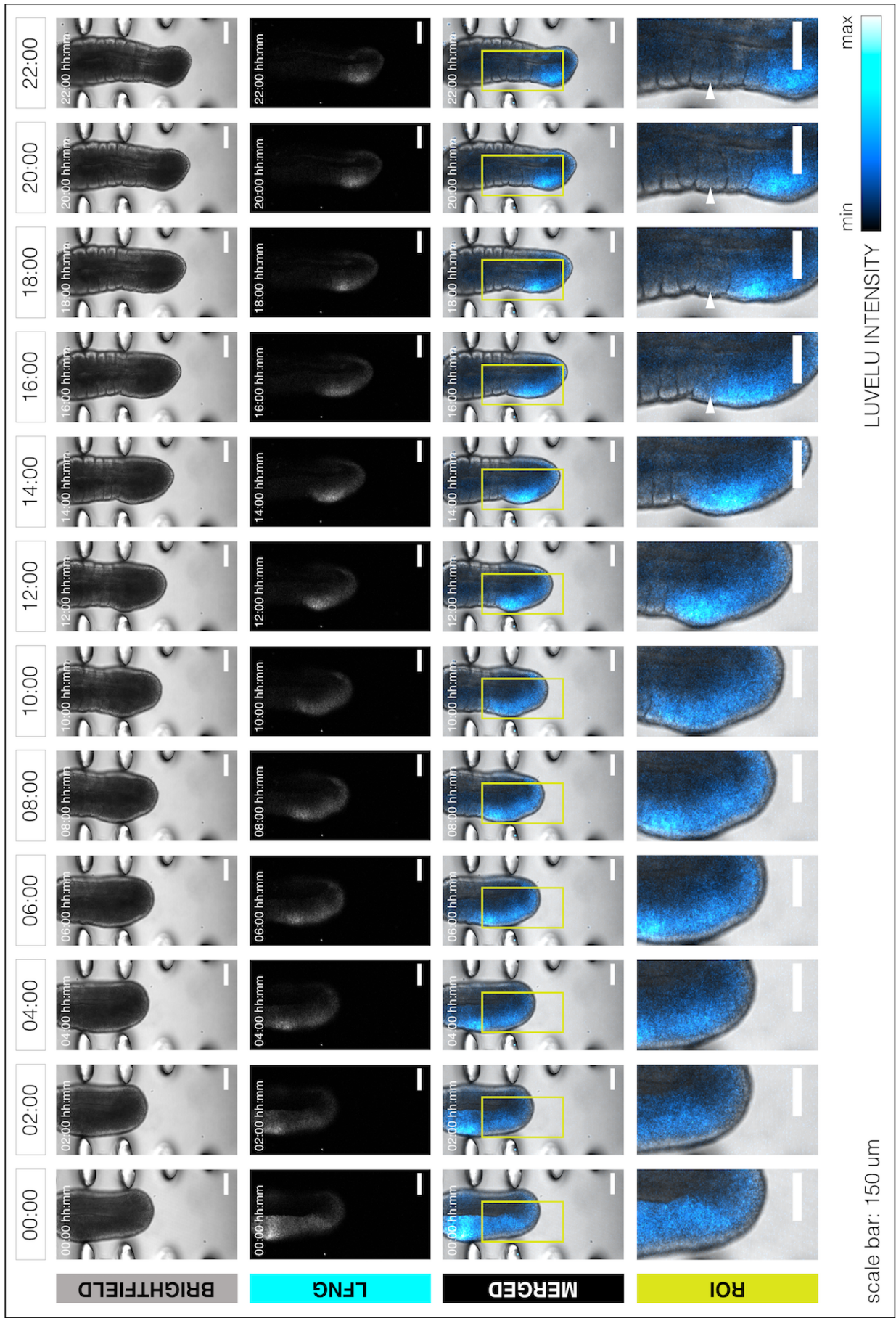


Figure 5.5 A slower segmentation clock does not always result in a proportionally bigger somite. Dissected tails of E10.5 mouse embryos were cultured in PLL-PEG coated PDMS chip at 37°C and under 65% O₂, and subjected to 170-min periodic pulses of 2 μM DAPT. Illustrated are stills from the live imaging of one such tails as somitogenesis proceeds, during the entrainment experiment. Shown are the brightfield channel, the LuVeLu channel (Lfng dynamics), and their merge. Also shown is a ROI in the merge of the two channels, with white arrowhead marking a remarkably bigger somite. Time is indicated as hh:mm elapsed from the start of imaging.

5.2 Discussion

To perform entrainment in a more physiologically-relevant system, the microfluidics-based experimental platform employed for entrainment of spreadouts was optimized for the culture of intact PSM. We presented here how we used such platform to simultaneously culture, image, and entrain said embryonic tissue (Figure 5.1, 5.2).

By tuning the period of the drug pulses, we demonstrated how we used microfluidics-based entrainment to control the period of the segmentation clock. Characteristic of successful entrainment, we noted that the segmentation clock in intact PSM was both period-locked and phase-locked to the periodic perturbation (Figure 5.3). More specifically, we managed to slow down the clock to around 170 mins, precisely matching the period of the DAPT pulses.

Remarkably, we documented that the entrainment phase when the segmentation clock in intact PSM was subjected to periodic pulses of DAPT is similar to that when the segmentation clock in spreadouts was subjected to the same perturbation (i.e. 170-min periodic pulses of 2 μ M DAPT). That detuning affected the entrainment phase similarly in these two experimental systems, which have very different multicellular geometries, is noteworthy. This very likely features the same underlying oscillatory machineries in spreadouts and in intact PSM (i.e. intracellular signaling oscillations in PSM cells), and highlights once more the power and flexibility of our top-down entrainment approach in controlling the segmentation clock in these systems.

Segment formation and establishment of segment polarity are key features of proper somitogenesis. Indeed, aberrant signaling dynamics in the PSM has been attributed to formation of the former, but not the latter (Feller et al., 2008; Oginuma et al., 2010). Certainly, in addition to partitioning the AP body axis into repetitive structures, segments in animals are more strictly defined by some sort of AP polarity (Hannibal and Patel, 2013). To assess polarity in segments formed from intact PSM subjected to periodic perturbation, we recovered the samples after the experiment and carried out in situ hybridization for somite polarity markers, either by using DIG probes or by hybridization chain reaction (HCR). We verified formation of bona fide somites in samples subjected to periodic DAPT pulses, evidenced by properly polarized expression of *Uncx4.1* and *Tbx18*, in addition to segment boundaries (Figure 5.4, 8.20). *Uncx4.1* correctly polarized in the caudal (i.e. posterior) half of somites (Neidhardt et al., 1997), while *Tbx18* correctly polarized in the rostral (i.e. anterior) half (Kraus et al., 2001). This strongly implies that normal somitogenesis is happening in these samples albeit having a slower segmentation clock.

While most somites indeed looked normal, we also recorded defects in segmentation in some samples ($n = 3/12$) that were entrained to the periodic DAPT pulses. More specifically, we noted left-right asymmetry, where one side had more segments than its contralateral counterpart. This correlated well with a kink in the tissue, reminiscent of congenital scoliosis in humans (Pourquié, 2011). Based on visualization of *Uncx4.1* expression, it seemed that for these altered segments, one segment had split into two (marked with white asterisk in Figure 5.4, 8.20). We hypothesize that the abnormal segment could reflect differential entrainment along the mediolateral axis, where the medial part of the PSM had already slowed down (i.e. resulting in one *Uncx4.1* stripe) while the lateral part had not (i.e. resulting in two *Uncx4.1* stripes). This and why the left and right sides in a sample did not respond similarly are worthwhile prospects for future research. Interestingly, the mismatch between contralateral sides in these tissues (around the 6th segment) happened at around the same time the samples locked to the periodic perturbation (around the 4th-5th DAPT pulse).

Different segmentation phenotypes (Figure 5.4) could imply different response to the periodic pulsing, especially during the transient to entrainment, depending on the phase of the segmentation clock at the time of perturbation (for more details, please refer to brief discussion on phase response curves in Chapter 3 Section 3.4). Nonetheless, we also present here a phenotype that could not be generally accounted for by the classical interpretation of the clock and wavefront model. In particular, in multiple instances, slowing down the segmentation clock did not simply result in proportionally bigger somites. As exemplified in this chapter, we documented samples ($n = 6$ and $N = 6$) where a notably bigger somite indeed formed when the segmentation clock effectively locked to a slower period. However, despite maintaining a slower segmentation clock, successive somites formed with a relatively regular size. As shown in Figures 5.4, 5.5, and 8.20 (marked with white arrowhead), only the 5th-6th newly-formed somite, coinciding with start of effective entrainment by the 4th-5th DAPT pulse (Figure 5.3B), are bigger than the other somites, even when the later ones formed with a similarly slower segmentation clock (i.e. 170 mins) (Figure 5.3D, Possibility 3 in Figure 5.6). Certainly, quantification of the somite size, possibly as a proportion of the PSM size, would allow making stronger arguments about this. Preferably, quantification would be done in 3D, during live imaging, and with minimal manual intervention (e.g. Naganathan et al., 2020). Nonetheless, this observation is clearly at odds with traditional interpretations of the clock and wavefront model, and we thus hypothesize that these observations could instead be clarified by taking into account the phase shift between Notch and Wnt oscillations in PSM cells as a spatiotemporal cue for segmentation (Sonnen et al., 2018).

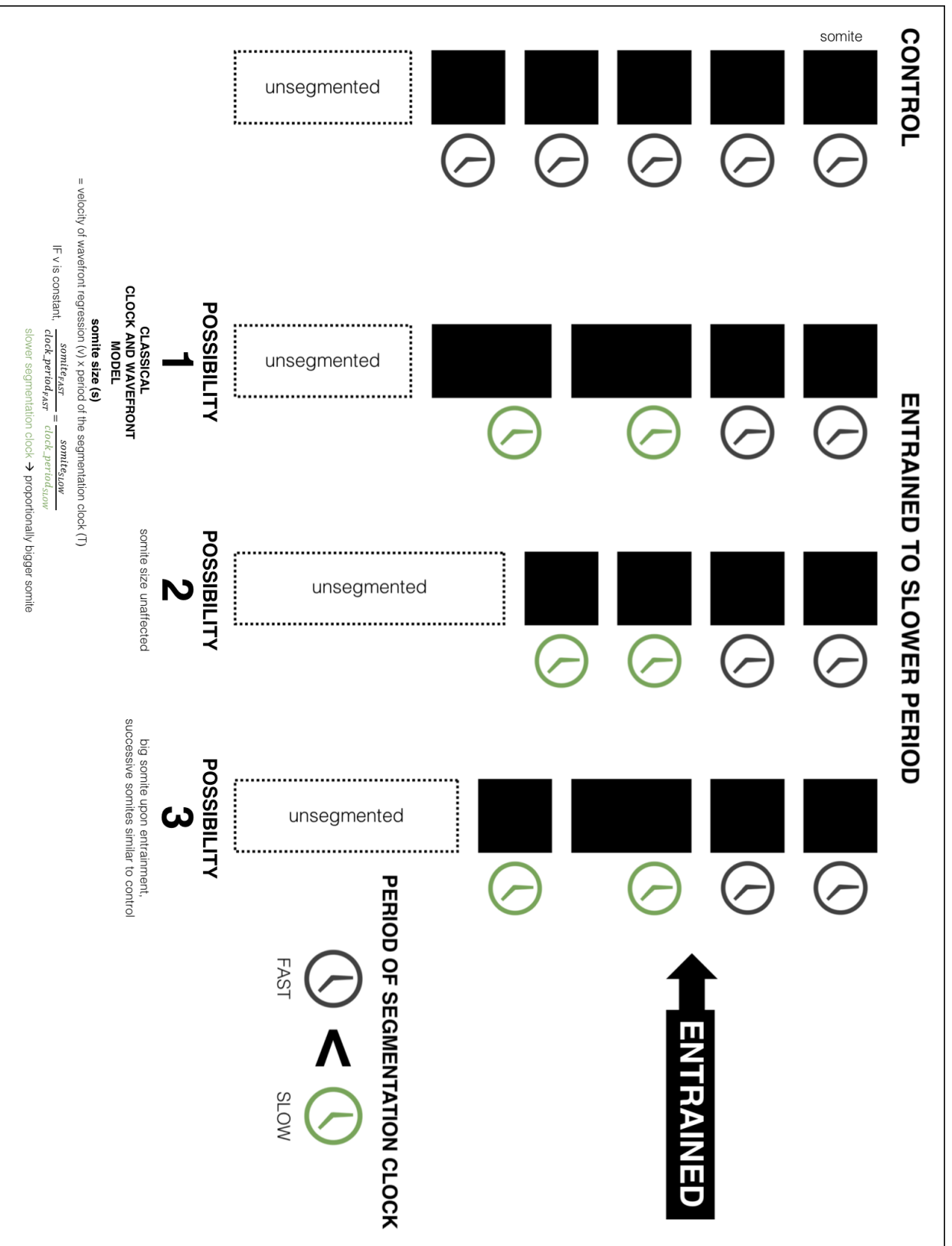


Figure 5.6 Possible effects of slowing down the segmentation clock on somite size. If the classical clock and wavefront model holds, at constant velocity of regression of a molecular wavefront, a slower segmentation clock would result in proportionally bigger somites (Possibility 1). Alternatively, it could be possible that slowing down the segmentation clock would not drastically change the somite size (Possibility 2) or would change the size of just 1-2 somites (Possibility 3).

We previously reported that the in-phase coincidence between intracellular Notch oscillations and intracellular Wnt oscillations marks the region of segment formation (Sonnen et al., 2018). Such region will lie at a precise location (X_a) along the AP axis of the unsegmented mesoderm (Sonnen et al., 2018; Lauschke et al., 2012). That segmentation phenotypes (i.e. an aberrant segment or a notably bigger somite), if any, consistently form at the time the samples are successfully locked to the periodic drug pulses already suggests that switching to a slower segmentation clock somehow alters instructive cues for proper somitogenesis (i.e. phase shift between Notch and Wnt), at least for one cycle. Upon entrainment of Notch oscillations to periodic DAPT pulses, it is likely that the aforementioned region for segmentation could shift to a different location (X_b) along the AP axis, then possibly corresponding to the big somite, seemingly following the classical clock and wavefront model. However, we noted that Wnt oscillations also become entrained to the periodic DAPT pulses a cycle later (as elaborated in Chapter 4 Section 4.1.8, and in Sonnen et al., 2018). If Wnt oscillations catch up to entrainment of Notch oscillations and their differential phase shift is properly restored along the AP axis in intact PSM, then the region where intracellular Notch and Wnt oscillations are in-phase could possibly return to X_a , explaining successive somites that formed with a more regular size.

While there are still exciting outlooks for future investigations, taking into account the results presented here, we believe that the classical interpretation of the clock and wavefront model is limited. Our observations support redefinition of the "wavefront" as something integrated in the dynamics of the segmentation clock, as earlier proposed by Aulehla, 2008 (i.e. The Appendix model) and by Murray et al., 2011. This agrees with a less widely known refinement of the classical clock and wavefront model, as propositioned by one of its proponents, Jonathan Cooke, after the discovery of a molecular segmentation clock in the late 1990s (Palmeirim et al., 1997). In a commentary (Cooke, 1998) regarding the work by Palmeirim et al., 1997, Cooke stated that:

The molecular observations suggest novel more integrated versions of clock and wavefront ideas, that make the required global measurement of developmental time within embryos dependent upon the same 'clock' oscillator both for repeated (segmentation) and slow smooth graded (wavefront) components.

Incorporating more recent studies (Sonnen et al., 2018; Lauschke et al., 2012), this "wavefront" is likely read out as intracellular phase-shift between signaling oscillations from different signaling pathways (i.e. Notch and Wnt), and is not just a static gradient of morphogen passively overlaying the PSM. This corroborates with previous findings that onset of stripes of *Lfng* expression in the anterior PSM,

marking presumptive segment boundaries, occurs in the tissue even in the absence of proper gradients of Wnt or FGF (Aulehla et al., 2007). Such integration between the phase-shift model (Goodwin and Cohen, 1969) and the clock and wavefront model (Cooke and Zeeman, 1976) certainly offers a more holistic view of tissue patterning during somitogenesis. In this framework, as the segmentation clock feeds back into this dynamic "wavefront", and vice versa, slowing down the clock would not simply result in a bigger somite. If in our experiments the oscillatory dynamics confers both temporal (i.e. clock) and spatial (i.e. wavefront) information, and if such information is encoded for instance in the period of the oscillations and in their differential intracellular phase-shift along the AP axis of the PSM (e.g. as in the phase-shift model; Sonnen et al., 2018), respectively, then changing the former while preserving the latter would change the timing but not necessarily the spacing of somite formation.

5.3 Conclusion

Here, we successfully control the segmentation clock in intact PSM via microfluidics-based entrainment. In particular, we are able to lock the phase of the segmentation clock in intact PSM to the periodic DAPT pulses, with an entrainment phase strikingly similar to experiments with spreadouts. Moreover, we are also able to tune the period of the segmentation clock in our samples. We achieve these without marked effects on viability of the tissue, as evidenced for example by proper segment polarity in somites formed during the experiments.

Remarkably, we note segmentation phenotypes that coincide with time when the samples were effectively locked to the periodic perturbation. For instance, we record an aberrant segment, which seemed to be split into two, on one side of the tail, resulting in left-right asymmetry and a kink in the tissue. While we have not addressed why the left and right sides of the tissue did not respond similarly to the perturbation, we think that the aberrant segment reflects differential entrainment along the mediolateral axis of the PSM.

In addition, we document a notably big somite when the segmentation clock successfully adjusted to a slower period. More strikingly, while the segmentation clock is kept slow henceforward, successive somites appear to have relatively regular sizes. This contradicts more traditional interpretations of the clock and wavefront model, where a slower segmentation clock results in a proportionally bigger somite if the velocity of regression of morphogen gradient (i.e. wavefront) is kept constant. Instead, we attribute this to a dynamic wavefront that is integrated into the dynamics of the segmentation clock. Specifically, we believe that our observations are better explained when alternatively taking into account the intracellular phase-shift between Wnt and Notch oscillations as instructive cues for timing and spacing of somitogenesis. This is yet to be tested and will be an inspiring topic for more thorough research.

On a rather pragmatic note, we show here how we could define the period of the segmentation clock a priori using entrainment, which had not been possible using genetics or pharmacological intervention. In addition, we also demonstrate how we could synchronize independent samples through active synchronization to the periodic perturbation, which would be very useful in some experiments (i.e. -omics). More generally, we present here microfluidics-based entrainment as a top-down approach to control oscillations, while grossly preserving proper patterning, in an intact embryonic tissue.

5.4 Outlook

3D imaging and development of automated workflow for tracking and measuring somite and PSM

Imaging in 3D could be considered to have a more holistic view on signaling dynamics and its effect on tissue patterning. This is most important for further investigations on left-right asymmetry and formation of a notably bigger somite. One could optimize an experimental system for simultaneous light-sheet microscopy (Falk, 2019) and entrainment, more possibly via optogenetics (Isomura et al., 2017). For quantification of effect of changing the period of the segmentation clock to tissue patterning, an automated workflow for tracking and measuring somite and PSM size, both in 2D and 3D, could be developed. Ideally, quantification is done with minimal manual intervention. This could be achieved using machine learning, potentially in collaboration with the lab of Anna Kreshuk (Cell Biology and Biophysics Unit, EMBL). Such workflow for analyzing somite size in intact tissue, in 3D, through time is recently reported by Naganathan et al., 2020.

Integrating Wnt and FGF signaling dynamics

The segmentation clock, which governs the precise spatiotemporal regulation of somitogenesis, is a genetic network built from the interaction of Fgf, Wnt, and Notch signaling (Dequéant and Pourquié, 2008; Hubaud and Pourquié, 2014; Aulehla et al., 2003; Dequéant et al., 2006; Aulehla et al., 2007). The crosstalk between these signaling pathways could be elucidated by experiments on embryos expressing reporters for multiple of said pathways. Live imaging of mouse embryos expressing reporters for both Notch and Wnt (e.g. Axin2) oscillations would be valuable to reconcile the phase shift between the two oscillations during entrainment, as presented here. Experiments could also be done with tissues from mouse embryos expressing reporters for Notch and FGF (e.g. Dusp4) oscillations. Tails derived from such embryos could be entrained to periodic DAPT pulses to assess how entrainment behavior of FGF oscillations relate to the Notch signaling dynamics. Alternatively, the samples could be entrained to periodic pulses of Chiron to evaluate how Notch and FGF oscillations respond to a periodic Wnt perturbation.

Entrainment of just one side (i.e. left or right) of intact PSM

Microfluidics setup could be modified to subject just either the left or the right side of the PSM to periodic drug pulses. For instance, a laminar flow system (e.g. Lucchetta et al., 2005) could be considered to pulse drug on one side of the tail while pulsing DMSO control on its contralateral counterpart. This could potentially allow different halves of the tail to have different periods of segmentation. With such system, effect of different periods of the segmentation clock to patterning (i.e. somite size) can be studied in the same tissue.

Entrainment of signaling oscillations in intact medaka embryos

Unlike mouse embryos, embryos of medaka (*Oryzias latipes*, Japanese rice fish) develop ex utero. These embryos could then be examined intact and studied in nearly physiological conditions. To provide a means to see conservation of key principles in synchronization across the animal kingdom, in an intact organism, and in a somitogenic context similar to that of the mouse, an entrainment platform, either via microfluidics and/or optogenetics, could be designed and optimized to allow entrainment of signaling oscillations in intact medaka embryos expressing a destabilized reporter fused to the *her7* gene (Vibe, 2021), noted to be the core oscillator during somitogenesis in fish (Lewis, 2003). Retrieval and culture of live medaka embryos after entrainment would also allow investigations on how alterations, if any, in patterning (i.e. timing and spacing) of somites affect later development (e.g. Hox expression domain, number of vertebrae, positioning of fins). Such experimental platform could also be used to precisely modulate the segmentation clock in other fish embryos, like zebrafish.

Dissection of molecular mechanisms underlying spatiotemporal information processing in the PSM via signaling oscillations

To elucidate the mechanism of how spatiotemporal information encoded in the wave-like pattern of Notch signaling is locally decoded by cells of the PSM to guide tissue patterning, samples could be recovered at specific timepoints during entrainment, as exemplified by post-entrainment in situ hybridization and HCR (Figure 5.4, 8.20), with a defined period and phase, and use them for molecular analyses like RNAseq and ATACseq. This would enable elucidation of how information, encoded in period and/or phase of signaling oscillations, is decoded during tissue patterning at a molecular level. As independent tissues actively synchronize to the same periodic perturbation during entrainment, multiple samples could be pooled for these molecular analyses, with the phase of the clock no longer being a confounding variable.

Precise modulation of segmentation via periodic perturbation of glycolytic flux

A recurring theme in this text is the power of our principles-based top-down approach to control an oscillatory system while being agnostic of the intricate details happening at the molecular level. We also elaborated how the system response could actually give us insight into these details, allowing us to generate testable hypotheses. One way of further emphasizing these points is exemplified here through precise modulation of the segmentation clock via periodic perturbation of the glycolytic flux.

Hidenobu Miyazawa and Marteinn Snabjornsson, both from our lab, have uncovered an instructive role of the glycolytic flux through phosphofructokinase (PFK) in proper somitogenesis. To study this, Marteinn Snabjornsson and Nobuko Tsuchida-Straeten developed a transgenic mouse line with a mutant form of PFKFB3, altering the cellular localization of the enzyme eventually enhancing the glycolytic flux through PFK (Yan et al., 2017). Recently, Hidenobu Miyazawa recorded that the period of LuVeLu oscillations in intact PSM responds to glucose concentration in the culture medium in a dose-dependent manner. In addition, at same glucose concentrations, the segmentation and underlying LuVeLu oscillations in PFKFB3 mutant mouse are slower than wild type control.

To test the link between glycolytic flux and oscillatory dynamics in the PSM, in collaboration with Hidenobu Miyazawa, we subjected intact PSM to periodic pulses of alternating concentrations of hydrolyzable glucose (e.g. 120-min period: 30-min 0.5 mM glucose pulses separated by 90-min intervals of culture in 2.0 mM glucose) via microfluidics-based entrainment (Figure 8.21A). Indeed, the segmentation clock in intact PSM adjusted to the rhythm of the periodic glucose pulses (Figure 8.21B). In particular, we were able to lock the period of the segmentation clock to the periodic perturbation (Figure 8.21C), and make independent samples more synchronous (Figure 8.21D). Strikingly, the difference in free-running period of wild type and mutant embryos, earlier noted by Hidenobu Miyazawa, was reflected in the entrainment behavior. As both tissues were subjected to the same period of glucose pulses, the inherent difference in period between the two genotypes manifested as different detuning values. First, likely because of the less significant detuning at 120-min periodic pulses, tissues from PFKFB3 wild type embryos were entrained much more effectively, locking more precisely to the period of the perturbation (Figure 8.21C). In addition to adjusting to the entrainment period (i.e. 120 mins), the period of the segmentation clock is faster in these experiments than when tissues are cultured in either just 0.5 mM glucose or just 2.0 mM glucose (data available from Hidenobu Miyazawa). Second, and more remarkably, the difference in detuning in the two conditions accordingly resulted in different phase of entrainment (i.e. comparing PFKFB3WT and PFKFB3 MUT subjected to alternating concentrations of hydrolyzable glucose in Figure 8.21B).

Experiments with wild type tissues revealed that we could both speed up and slow down the segmentation clock by tuning the period of the glucose pulses (Figure 8.22A). Notably, detuning affects entrainment phase in these experiments too (Figure 8.22B), further highlighting the universality and applicability of entrainment principles in controlling our system.

These preliminary results suggest that glycolytic flux, as modulated here by alternating concentrations of hydrolyzable glucose, is potentially integrated into the oscillatory signaling pathways underlying the segmentation clock. It would be interesting to see if one would note similar results using other metabolites in glycolysis. Strikingly, the entrainment phase at different detuning matches that for periodic perturbation of the segmentation clock in wild type tissues with pulses of DAPT (Figure 3.5C). Whether or not glycolytic flux has the same general effect to oscillatory signaling dynamics as DAPT, a γ -secretase inhibitor, is worthwhile to test. It would also be exciting to know how such perturbation of glycolysis affects Wnt signaling oscillations (e.g. Axin2), and would be very curious to investigate how tissues from embryos with aberrant Wnt signaling would respond to the entrainment.

Materials and methods

This chapter elaborates on materials and methods used in this research. These include information on used mouse lines, a protocol for making the microfluidics devices, and a detailed overview of the entrainment/imaging experiments.

6.1 Animals

6.1.1 Mouse lines

For most of the experiments in this study, we used a transgenic mouse line expressing a dynamic Notch signaling reporter driven from the *Lfng* promoter, more commonly known as LuVeLu. The generation of LuVeLu was previously described by Aulehla et al., 2007. Briefly, the expression of Venus, an improved version of YFP (Nagai et al., 2002), was driven from a 2-kb fragment of the *Lfng* promoter (Morales et al., 2002; Cole et al., 2002). The locus was flanked by *Lfng* 3'-UTR and a modified PEST domain (Rogers et al., 1986) to destabilize the reporter mRNA and protein, respectively. For experiments visualizing nuclei, we used the R26-H2B-mCherry mouse line which expresses H2B-mCherry ubiquitously via the ROSA26 locus transcriptional machinery (Abe et al., 2011). For experiments visualizing *Mesp2* during entrainment, we used the *Mesp2*-GFP mouse line generated by Morimoto et al., 2006.

Axin2-GSAGS-Achilles, a mouse line expressing Axin2 fused to Achilles, a fast-maturing variant of YFP (Yoshioka-Kobayashi et al., 2020), was generated in-house by Nobuko Tsuchida-Straeten. PFKFB3 Tg (K472/473A), a mouse line with impeded nuclear localization of PFKFB3 (Yan et al., 2017), was also generated in-house by Nobuko Tsuchida-Straeten and Marteinn Snaebjornsson. Generation of these mouse lines were done in collaboration with Yvonne Petersen of the EMBL Transgenic Service.

Mice were kept in an outbred background and were housed in the EMBL Laboratory Animal Resources (LAR). All animal experiments were conducted under veterinarian supervision and after project approval by European Molecular Biology Laboratory, following the guidelines of the European Commission, Directive 2010/63/EU and AVMA Guidelines 2007.

6.1.2 Genotyping

Tails of mice were clipped and put separately in 1.5 mL Eppendorf tubes. These were stored at 4°C until use for genotyping. To genotype, clipped tail was lysed in 300 uL of 50 mM NaOH at 95°C for around two hours. Lysed tail was cooled to room temperature and then neutralized with 30 uL of 1M Tris (pH 5) for 3 minutes. The resulting solution contained the tail DNA and could be stored at 4°C until further use. In a PCR tube, 1 uL of tail DNA was mixed with 0.4 uL of primer mix (containing 25 uM of each primer), 8.6 uL of distilled H₂O, and 10 uL of OneTaq Quick-Load 2x Master Mix with Standard Buffer (New England Biolabs, M0486S). The buffer already contained the DNA polymerases, dNTPs, MgCl₂, and loading/tracking dye for agarose gel electrophoresis. PCR mixture was subjected to 35 cycles of amplification using the PCR program specified in Table 6.1. Primers used and expected PCR products are summarized in Tables 6.2 and 6.3, respectively.

Table 6.1 PCR program for genotyping.

Step	Temperature	Time
Initial denaturation	95°C	2 minutes
Amplification (35 cycles)	94°C	30 seconds
	60°C	45 seconds
	68°C	45 seconds
	68°C	45 seconds
Final extension	68°C	5 minutes
Hold	4°C	–

Table 6.2 List of primers for genotyping mouse lines used in this study.

Target	Primer Number	Primer Description	Primer Sequence (5'→3')
Achilles	2121	Achilles reverse	CGGTGAACAGCTCCTCGCCC
	2126	Achilles forward	CCTTCCTGAGCAAAGACCCC
Axin2	708	Axin2 WT forward	GTCTCAACGAGCTTTCCTGTCT
	711	Axin2 WT reverse	CCTCCCTAGGCTTTGTCTTCTT
	910	Axin2 WT forward	GTTCTCCATTGGCGAGATGT
CAG promoter	1927	CAG reverse	CTCGACCATGGTAATAGCGA
	1930	CAG forward	GGCTTCTGGCGTGTGACCGG
LuVeLu	1551	Ala1 forward	TGCTGCTGCCCGACAACCACT
	1552	Ala3 reverse	TGAAGAACACGACTGCCACGC
PFKFB3	1932	PFKFB3 reverse	ACTCGGCTCTGCGTCAGTTC
Rosa locus	1916	Rosa WT forward	GAGCTGCAGTGGAGTAGGCG

Table 6.3 List of expected PCR products for genotyping mouse lines used in this study. For sequence of primers specified, please refer to Table 6.2.

Mouse Line	Primers	PCR Product	Description
Axin2-stop-GSAGS-Achilles	708 + 711	305 bp	WT allele
	910 + 2121	252 bp	mutant allele
	2126 + 711	310 bp	after Cre recombination
LuVeLu	1551 + 1552	461 bp	mutant allele
Rosa-floxed-PFKFB3(K472/473A)	1916 + 1927	580 bp	floxed allele
	1930 + 1932	340 bp	after Cre recombination

6.2 Working with mouse embryos

6.2.1 Media preparation

On the day of the experiment, dissection medium and culture medium were freshly prepared as indicated in Table 6.4. Culture medium was filter sterilized using a PVDF filter (pore size: 0.22 μm , Merck). Both dissection medium and culture medium were equilibrated to 37°C for at least 15 minutes, and were kept in a 37°C incubator under 5% CO_2 until use.

Table 6.4 Recipe for media preparation. Formulations specified here are for the preparation of approximately 50 mL of medium. Special DMEM/F12* used in these media does not contain glucose, L-glutamine, sodium pyruvate, and phenol red. Culture medium is filter sterilized after preparation.

Component	Dissection Medium	Culture Medium
BSA (Equitech-Bio, BAC62)	0.5 g	0.02 g
DMEM/F12* (Cell Culture Technologies)	50 mL	50 mL
1 M HEPES (Gibco, 15630-106)	1 mL	–
10000 U/mL PenStrep (Gibco, 15140-122)	–	500 μL
45% Glucose (Sigma, G8769)	44.4 μL	44.4 μL
200 mM L-Glutamine (Gibco, 25030-081)	500 μL	500 μL

6.2.2 Mouse dissection and embryo recovery

Female mice were sacrificed on 10.5 dpc (days post coitum) via cervical dislocation. The skin on their ventral side (belly area) was wiped with 70% ethanol, and an incision was made using a clean pair of surgical scissors. The uterine horns were harvested and were washed once with dissection medium. In dissection medium, under a stereo microscope (Leica M80), the deciduae were cut open using clean forceps and the embryos were recovered. The embryos were again washed with fresh dissection medium and their tails were clipped using forceps. Clipped tails were then transferred to a new dish with fresh dissection medium. The volume of dissection medium in the dish was kept to minimum to lessen autofluorescence, which could interfere with subsequent screening. The tails were then screened for presence of the reporter-of-interest (e.g. LuVeLu) using a stereo fluorescence microscope.

For experiments using intact PSM, the tails were cut with a scalpel, keeping the PSM and two somites. For experiments using spreadouts, only the tailbud was cut from the rest of the tail. The isolated embryonic tissues were immediately transferred to pre-equilibrated culture medium that was supplemented with HEPES (170 μL of 1 M HEPES in 10 mL culture medium). These tissues were then directly loaded in the microfluidics device (refer to Section 6.3.5).

6.2.3 In situ hybridization using digoxigenin-labeled probes

In situ hybridization was performed using protocol adapted from the lab of Bernhard Herrmann (Max Planck Institute for Molecular Genetics), which was based on Wilkinson and Nieto, 1993. A schematic of the protocol, from Day 1 to Day 4, including the time for each step and recipes for preparation of some of the solutions, is available at https://github.com/PGLSanchez/EMBL-files/blob/master/PROTOCOL/insitu_protocol_datasheet_A3.pdf.

Solutions

Solutions used in this protocol are summarized in Table 6.5.

Table 6.5 List of solutions for in situ hybridization.

Solution	Component	Amount
1x PBS	NaCl	0.8 g
	KCl	0.2 g
	Na ₂ PO ₄	1.15 g
	KH ₂ PO ₄	0.2 g
	distilled H ₂ O (dH ₂ O)	dilute to 1 L
2x Ca ²⁺ and Mg ²⁺	MgCl ₂ ·6H ₂ O	0.2 g
	CaCl ₂ ·2H ₂ O	0.264 g
	dH ₂ O	dilute to 1 L
Hybridization buffer	formamide	250 mL
	20x SSC (pH 5)	125 mL
	20% SDS	25 mL
	50 ug/uL yeast tRNA	500 uL
	50 ug/uL heparin	50 uL
	dH ₂ O	dilute to 1 L
	store at -20°C	
20x SSC (pH 5)	Na ₃ Citrate·2H ₂ O	88.23 g
	NaCl	175.32 g
	dH ₂ O	dilute to 1 L
Solution I (freshly prepared)	adjust to pH 5 with 1 M citric acid	
	formamide	25 mL
	20x SSC (pH 5)	12.5 mL
	20% SDS	2.5 mL
Solution III (freshly prepared)	dH ₂ O	dilute to 50 mL
	formamide	25 mL
	20x SSC (pH 5)	5 mL
	Tween20	50 uL
10x TBS (pH 7.5)	dH ₂ O	dilute to 50 mL
	NaCl	81.8 g
	KCl	2 g
	Tris-base	30.3 g
	dH ₂ O	dilute to 1 L
NTMT (freshly prepared)	adjust to pH 7.5 with 32% HCl	
	5 M NaCl	10 mL
	1 M Tris-HCl (pH 9.5)	50 mL
	1 M MgCl ₂	25 mL
	Tween20	500 uL
	dH ₂ O	dilute to 500 mL

Recovery, fixation, and dehydration of samples

Samples were recovered in and washed with ice-cold PBS (with Ca^{2+} and Mg^{2+}). For whole E10.5 embryos, amnion was removed and the forebrain was punctured to reduce trapping of reagents in the lumen. Then, the samples were fixed in 4% formaldehyde (1.08 mL 37% formaldehyde diluted to 10 mL with PBS + Ca^{2+} and Mg^{2+}) overnight at 4°C, with gentle shaking. After fixation, samples were washed twice with 0.1% Tween20 in 1x PBS (PBST), with each wash taking 5 mins. Samples were then dehydrated with a series of graded methanol:PBST washes (from 25% methanol to 100% methanol), each taking 5 mins. Samples were placed in fresh 100% methanol and incubated at -20°C at least overnight.

Synthesis of digoxigenin-labeled RNA probes

10 ug of plasmid containing probe template was linearized and the reaction was purified using a spin column (Qiagen PCR Purification Kit). Linearized plasmid was eluted in 50 uL elution buffer (Buffer EB, Qiagen 19086). Linearized plasmid was then used as template in in vitro transcription using Riboprobe Combination Systems (Promega). Components of the in vitro transcription mixture are listed in Table 6.6. Mixture was incubated in a 37°C water bath for two hours. After incubation, 1 uL was run on 1% agarose gel electrophoresis. To the rest of the mixture, 1 unit of RQ1 RNase-free DNase (Promega, M610A) was added. Solution was incubated at 37°C for 15 mins.

Table 6.6 Components of in vitro transcription mixture for synthesis of digoxigenin-labeled RNA probes.

Component	Volume
Linearized plasmid	8 uL
Distilled H ₂ O	3 uL
5x Transcription Optimized Buffer (Promega, P118C)	4 uL
100 mM Dithiothreitol (DTT, Promega, P117C)	1 uL
10x Digoxigenin (DIG) RNA Labeling Mix (Roche, 11277073910)	2 uL
40 U/mL Ribonuclease Inhibitor (RNasin) Plus (Promega, N261A)	1 uL
T7 (Promega, P207B) RNA Polymerase	1 uL

After DNase treatment, RNA probes were precipitated out of the mixture. 100 uL of Tris-EDTA (pH 8), 1 uL of 20 mg/mL glycogen (Roche, 10901393001), and 30 uL of 10 M ammonium acetate were mixed in the solution. Then, 400 uL of cold absolute ethanol was added and the solution was immediately centrifuged for 10 mins at 14000 rpm at 4°C. Supernatant was removed and the pellet was washed with 1 mL cold 70% ethanol. Suspension was centrifuged for 5 mins at 14000 rpm at 4°C. Afterwards, pellet was air-dried and subsequently redissolved in 50 uL of Tris-EDTA (pH 8). 50 uL of hybridization buffer was added in the solution, and the DIG-labeled probe was stored at -20°C until further use. Probes used in this study were those against Uncx4.1 (Mansouri et al., 1997), Shh (Echelard et al., 1993), and Dnm2. Primers used to clone Dnm2 probe into a TOPO vector

(Invitrogen) were: 5'-GGAGTGGACTTTGAGAAGCG-3' (1979_DNM2_ORF_fwd) and 5'-GGCAGGCACTTAACAGTGGT-3' (1982_DNM2_3UTR_rev).

Day 1: Sample rehydration, pre-hybridization and hybridization with probes

Samples were rehydrated with a series of graded methanol:PBST washes (from 75% methanol to 25% methanol), each taking 5 mins. Then, they were washed with PBST twice, with each wash taking 5 mins. Afterwards, samples were treated with 6% H₂O₂ for at most 5 mins. They were subsequently digested with 10 ug/mL proteinase K. Digestion with proteinase was done for 10 mins for tails and 12 mins for whole E10.5 embryos. After digestion, samples were quickly washed twice with PBST, with each wash taking 5 mins. Samples were then fixed in a solution of 4% formaldehyde and 0.05% glutaraldehyde in PBST for 30 mins. After post-fixation, samples were washed twice with PBST, with each wash taking 5 mins. All steps were carried out at room temperature.

Directly after washing, samples were incubated in hybridization buffer (equilibrated to 37°C) for 15 mins at room temperature. Then, samples were incubated in fresh hybridization buffer at 68°C for 1 hour. While waiting, 10 uL of DIG-labeled probe was prepared for every 1 mL of the hybridization solution in hybridization buffer. Probe solution was denatured at 80°C 10 mins before use.

After pre-hybridization, samples were incubated in probe solution at 68°C overnight.

Day 2: Post-hybridization washing, blocking, and antibody incubation

Hybridization buffer, and freshly prepared Solution I and Solution III were pre-warmed to 68°C. Samples were placed in fresh hybridization buffer at 68°C for 30 mins. Then, samples were incubated in fresh Solution I at 68°C twice, each taking 30 mins. Afterwards, samples were incubated in fresh Solution III at 68°C four times, with the first two each taking 30 mins and the latter two each taking 1 hour. Samples were then washed thrice with 0.1% Tween in 1x TBS (TBST) at room temperature, with each wash taking 15 mins. Subsequently, they were incubated in 10% sheep serum in TBST (blocking solution) at room temperature for 2 hours.

While waiting, anti-DIG antibody was pre-absorbed. 10 mg of embryo powder was mixed with 1.8 mL TBST in a 2 mL Eppendorf tube, and was vortexed for 1 min. Then, the mixture was heated at 70°C for 30 mins, vortexed, and then cooled in ice. Then, 18 uL of 100% sheep serum and 12.5 uL of 0.75 U/uL anti-DIG antibody conjugated to alkaline phosphatase (Roche, 11093274910) were added to the mixture. For gentle mixing, mixture was put in a rotation wheel at 4°C for 1 hour. Then, it was centrifuged for 15 mins at 14000 rpm at 4°C. Supernatant was

collected into a 50 mL Falcon tube, and the solution was diluted to 25 mL with 1% sheep serum in TBST.

After the 2-hour blocking, blocking solution was replaced with the antibody solution. Samples were incubated in the antibody solution with gentle shaking at 4°C overnight.

Day 3: Washing post-antibody incubation

Samples were washed several times with TBST, as summarized in Table 6.7.

Table 6.7 TBST washes post-incubation with anti-DIG antibody.

Wash Number	Solution	Duration	Temperature
Wash 01	TBST	15 mins	room temperature
Wash 02	TBST	15 mins	room temperature
Wash 03	TBST	30 mins	room temperature
Wash 04	TBST	30 mins	room temperature
Wash 05	TBST	30 mins	room temperature
Wash 06	TBST	30 mins	room temperature
Wash 07	TBST	30 mins	room temperature
Wash 08	TBST	1 hour	room temperature
Wash 09	TBST	1 hour	room temperature
Wash 10	TBST	2 hours	room temperature
Wash 11	TBST	overnight	4°C (in the cold room)

Day 4: Color development

Samples were incubated thrice in fresh NTMT at room temperature, each taking 15 mins. Afterwards, samples were treated with a solution of 170 ug/mL BCIP (Roche, 11383221001) and 340 ug/mL NBT (Roche, 11383213001) in NTMT at room temperature until color reaction was complete. After color development, samples were washed thrice with PBST at room temperature, with each wash taking 5 mins. They were then post-fixed in 4% formaldehyde in PBST, sealed, and kept at 4°C until ready for imaging. Examples of expected result after wholemount in situ hybridization are shown in Figure 6.1.

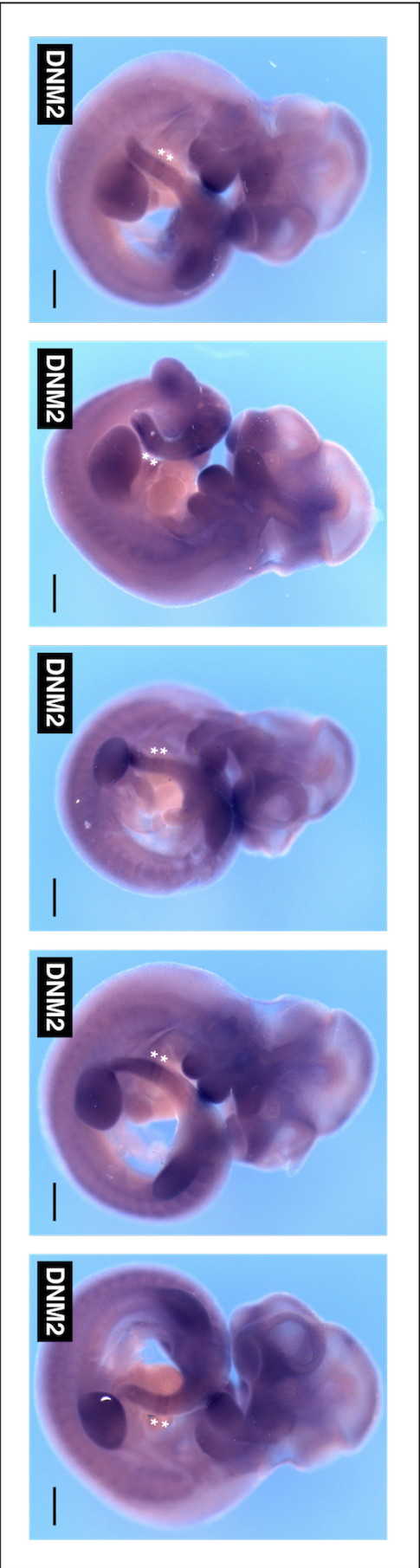


Figure 6.1 Wholemount in situ hybridization of E10.5 mouse embryos against *Dnm2*. E10.5 mouse embryos were hybridized with probes against *Dnm2*, which is involved in endocytosis of Delta ligands during Notch signaling. White asterisks mark two stripes of *Dnm2* expression at the anterior PSM. Scale bar: 0.5 mm.

6.2.4 Hybridization chain reaction of intact embryo tails

In situ hybridization chain reaction (HCR) of intact tails (somites and PSM) was carried out following previously described protocol (Choi et al., 2016; Choi et al., 2018). A full step-by-step guide, including modifications to the original protocol, is available at <https://dx.doi.org/10.17504/protocols.io.7pyhmpw>.

Day 1: Recovery and fixation of samples

Samples were recovered separately and placed in individual PCR tubes (capacity: around 200 μ L). They were washed quickly with cold PBS, and then fixed in 4% formaldehyde (1.08 mL 37% formaldehyde diluted to 10 mL with PBS + Ca^{2+} and Mg^{2+}). The samples were kept in formaldehyde overnight at 4°C, with gentle shaking.

Day 2: Dehydration of samples

After fixation, samples were washed twice with 0.1% Tween20 in 1x PBS (PBST), with each wash taking 5 mins. Samples were then dehydrated with a series of graded methanol:PBST washes (from 25% methanol to 100% methanol), each taking 5 mins. Samples were placed in fresh 100% methanol and incubated at -20°C at least overnight.

Day 3: Rehydration of samples and HCR detection

Samples were rehydrated with a series of graded methanol:PBST washes (from 100% methanol to 25% methanol), each taking 5 mins. Then, they were washed with PBST twice, with each wash taking 5 mins. Afterwards, samples were treated with 10 μ g/mL proteinase K (Merck, 39450-01-6) in PBST for 5 mins at room temperature. Samples were again washed twice with PBST. They were then fixed again in 4% formaldehyde for 20 mins at room temperature. Meanwhile, probe hybridization (PH) buffer (Molecular Instruments) was pre-warmed to 37°C for later use. Samples were then washed thrice with PBST and subsequently washed once with PH buffer. Samples were afterwards put in fresh PH buffer for 30 mins at 37°C.

While waiting, probe solution was prepared by adding 2 pmol (2 μ L of 1 μ M stock) of odd probe and 2 pmol of even probe mixture to every 500 μ L of pre-warmed PH buffer. After the 30-min incubation, PH buffer in the sample tubes was replaced with the probe solution. Samples were incubated in probe solution overnight at 37°C, with gentle shaking.

Probes used for HCR are summarized in Tables 6.8-6.10. These probes were designed using a script kindly provided by Tim Fulton and Ben Steventon (Department of Genetics, University of Cambridge). The .txt files containing the sequences are

Table 6.8 List of oligonucleotides used as probes against Tbx6 in HCR.

Oligonucleotide Name	Sequence (5'→3')
Tbx6_B2_O01	cctcgtaaatcctcatcaaaGGGGTGTCCCAGACGGTAGCCAGTC
Tbx6_B2_E01	TGGGAAGGTGGAGTCTGCCCCAGGCaaatcatccagtaaaccgcc
Tbx6_B2_O02	cctcgtaaatcctcatcaaaAGGGGCAAAGGAGCGGCTGCAGCCA
Tbx6_B2_E02	GTCTCGGGGCCAGAGCAGATGGGAaaatcatccagtaaaccgcc
Tbx6_B2_O03	cctcgtaaatcctcatcaaaCTGGGTCCAGGCCAGTGAAGTATAC
Tbx6_B2_E03	CATCCAGAAGAAACAAGTAGCGGGCaaatcatccagtaaaccgcc
Tbx6_B2_O04	cctcgtaaatcctcatcaaaTACGGGCTGCCGCATCCAGTGGGCA
Tbx6_B2_E04	GTTGGTGAGCTTAACACGATGGAAGaaatcatccagtaaaccgcc
Tbx6_B2_O05	cctcgtaaatcctcatcaaaATGAATGTGGTCTCAGGAAATCGGA
Tbx6_B2_E05	CTAGGGTTCTGGTAGGCTGTCACAGaaatcatccagtaaaccgcc
Tbx6_B2_O06	cctcgtaaatcctcatcaaaCACTCCCACAGGCCTCTGTGGCCAC
Tbx6_B2_E06	AGTCACAGGGACCCCCCTGGTGTATCaaatcatccagtaaaccgcc
Tbx6_B2_O07	cctcgtaaatcctcatcaaaCAGGGTGTAGAAGGTAGGCCTCAGC
Tbx6_B2_E07	GGTGACTGGGGGCGCCATGAAAAGCaaatcatccagtaaaccgcc
Tbx6_B2_O08	cctcgtaaatcctcatcaaaAAGGGACCCCCTTGGATGAAGTGTG
Tbx6_B2_E08	CCTCCAGGTCTGGGTACGGTAGAGaaatcatccagtaaaccgcc
Tbx6_B2_O09	cctcgtaaatcctcatcaaaGCCATTTGGTGGGGGGAGGGGGAT
Tbx6_B2_E09	TAAAGGGTGAAGAGAGGCCCAAGCaaatcatccagtaaaccgcc
Tbx6_B2_O10	cctcgtaaatcctcatcaaaGGCAGAGGCTCCCTCCATTTCGCACT
Tbx6_B2_E10	TACTGGGCTGGGAGCCCCATTTGGCaaatcatccagtaaaccgcc

available at <https://github.com/PGLSanchez/EMBL-files/tree/master/HCR-probes>.

Day 4: HCR amplification

Probe wash buffer (Molecular Instruments) was pre-warmed to 37°C, and amplification buffer (Molecular Instruments) was equilibrated to room temperature.

In separate tubes, for every 500 uL hairpin mixture, 30 pmol (10 uL of 3 uM stock, Molecular Instruments) of hairpin h1 (tube 1) and 30 pmol of hairpin h2 (tube 2) were prepared. Hairpins were snap-cooled by heating the tubes at 95°C for 1.5 mins and cooled to room temperature in the dark for at least 30 mins.

Samples were washed four times with probe wash buffer at 37°C, with each wash taking 15 mins. Afterwards, samples were washed twice with 5x SSCT (5x sodium chloride sodium citrate + 0.1% Tween20), and then washed with pre-equilibrated amplification buffer at room temperature.

Meanwhile, the hairpin mixture was prepared by mixing the snap-cooled hairpins h1 and h2 to amplification buffer at room temperature. The amplification buffer was then removed from the sample tubes, and the samples were incubated in the hairpin mixture overnight in the dark at room temperature. Hairpins (Molecular Instruments) used in this study consisted of the following amplifier sequences with their corresponding fluorophore: B2-Alexa546, B4-Alexa647, and B5-Alexa488.

Table 6.9 List of oligonucleotides used as probes against Tbx18 in HCR.

Oligonucleotide Name	Sequence (5'→3')
Tbx18_B4_O01	cctcaacctacctccaacaaAGGAACGCGGCCGCCAAGTTTCCTT
Tbx18_B4_E01	TTCTCTGGCGTTGGGATCCGAGGAAattctcaccatattcgcttc
Tbx18_B4_O02	cctcaacctacctccaacaaTCCGCTCCTTGACAGATCTACTCTCG
Tbx18_B4_E02	CCTATTTTCGTGAAAGCGCTTCCAGAattctcaccatattcgcttc
Tbx18_B4_O03	cctcaacctacctccaacaaAGTTTCAGCTTGTGCGAAGCTGATGA
Tbx18_B4_E03	CCTTGGTCATCCAGCTCATTGTTGGattctcaccatattcgcttc
Tbx18_B4_O04	cctcaacctacctccaacaaGCCCCAGATGGAAGGCAGGAGAGGA
Tbx18_B4_E04	CCAGACTACACAGCTGGCTGGTGTattctcaccatattcgcttc
Tbx18_B4_O05	cctcaacctacctccaacaaACTTGGTGAGGACCCCAAGAAACTT
Tbx18_B4_E05	CAACATCTGACGATCAGTCATGGTCattctcaccatattcgcttc
Tbx18_B4_O06	cctcaacctacctccaacaaCGTGGGCATTAGAAAAGTCTTTGGT
Tbx18_B4_E06	GCTGTAATAAACCCCATCACTTGGattctcaccatattcgcttc
Tbx18_B4_O07	cctcaacctacctccaacaaGGCTCACACCTTTAATCCAGTACT
Tbx18_B4_E07	AATAAACAGGAATGGCTGGGCGGTGattctcaccatattcgcttc
Tbx18_B4_O08	cctcaacctacctccaacaaCTAGGGAGTGCTTGACACIATTCCT
Tbx18_B4_E08	ATCTAAGAAAACCAAGCCACACAAGGattctcaccatattcgcttc
Tbx18_B4_O09	cctcaacctacctccaacaaGACGCATCCCTTCAGCTTCTCAGCC
Tbx18_B4_E09	ACATGAAATGCACGGAGCAGCTGGGattctcaccatattcgcttc
Tbx18_B4_O10	cctcaacctacctccaacaaGCCATCTTCCTTGATTAAGAAGTGC
Tbx18_B4_E10	CCATGGGATGCTGTCTCAGGATGAAattctcaccatattcgcttc

Day 5: Washing, nuclear staining, and imaging

Samples were washed with 5x SSCT. Nuclei were stained by washing the samples thrice with 1:1000 DAPI (10 ug/mL in 5x SSCT, Biotium 40043). Then, samples were again washed twice with 5x SSCT. Each washing was done in the dark at room temperature for 30 mins. Prior to imaging, the samples were cleared by incubating them in fructose-glycerol refractive index matching medium (Dekkers et al., 2019) in the dark at 4°C for at least 2 hours.

6.2.5 Correlative live imaging and immunofluorescence

Day 1: Fixation and primary antibody staining

Immediately after timelapse imaging, samples were quickly washed twice with 1x PBS at room temperature, with each wash taking 1 min. Then, they were fixed with 1:1 DMSO:methanol on ice for 1 min. After fixing the tissues, they were treated with H₂O₂ and NH₄Cl (1 mL 30% H₂O₂, 100 uL 1 M NH₄Cl, 900 uL 1x PBS), also on ice, for 15 minutes. Afterwards, samples were blocked with FCS (blocking buffer: 500 uL FCS diluted to 5 mL with 1% Triton X100 in PBS) at room temperature for one hour. Then, they were stained with primary antibodies, diluted in blocking buffer, at 4°C overnight.

Day 2: Washing and secondary antibody (and nuclear) staining

After primary antibody staining, samples were washed thrice with 1% Triton X100 in PBS at room temperature, with each wash taking around 45 mins. After washing,

Table 6.10 List of oligonucleotides used as probes against Uncx4.1 in HCR.

Oligonucleotide Name	Sequence (5'→3')
Uncx_B5_O01	ctcactcccaatctctataaTGAAGGGCTGGCTTTTCGCCGGCCAC
Uncx_B5_E01	TGTCTGGATCCCCCGAGTCTGCAAGaactaccctacaaatccaat
Uncx_B5_O02	ctcactcccaatctctataaTGCCAGCCGGTAAAGTTGGTGC
Uncx_B5_E02	TTGAACGCCTTCTCCAGCTCCTCCAaactaccctacaaatccaat
Uncx_B5_O03	ctcactcccaatctctataaGATTTTGGAAACCAGACCTGAACTCG
Uncx_B5_E03	TCTCCTTCTTTCTCCATTTGGCCCCGactaccctacaaatccaat
Uncx_B5_O04	ctcactcccaatctctataaGAGCAGTTTCTTCTCGTGTGCGT
Uncx_B5_E04	CGAGTGCAGGTGGCGGCTCTGACTCaactaccctacaaatccaat
Uncx_B5_O05	ctcactcccaatctctataaTAGCCTTAGGCAGGCCCGCAGTCGC
Uncx_B5_E05	ACAGCAGGCTCTCCACGCTGAACGGaactaccctacaaatccaat
Uncx_B5_O06	ctcactcccaatctctataaCCAATCAGGGTCCGAGGTGCACACG
Uncx_B5_E06	ATGGGGTAGAGCAAGAAGTGGCCCTaactaccctacaaatccaat
Uncx_B5_O07	ctcactcccaatctctataaTGGCCCCGGAGAGGCAACAACCTCA
Uncx_B5_E07	TAGGTCCCAGAAAGAAGCGGGAGCGaactaccctacaaatccaat
Uncx_B5_O08	ctcactcccaatctctataaGTCCATGTCCACCTCCTCGCCCTCG
Uncx_B5_E08	CATCTTCCAGCCGCGGTCCCCAGCTaactaccctacaaatccaat
Uncx_B5_O09	ctcactcccaatctctataaACCTCACCCAGGACCAGCAGCTGC
Uncx_B5_E09	GGTTTTTTGATCCCTCCGGAGGAGGactaccctacaaatccaat
Uncx_B5_O10	ctcactcccaatctctataaTGTGGGTTTTGTGTGTGTGTGTGTG
Uncx_B5_E10	GCATTTTACAAGGCTGAGGATTCTCaactaccctacaaatccaat

secondary antibodies and DAPI (1:1500 or 6.7 ug/mL, Biotium 40043), diluted in blocking buffer, were added to the samples. Samples were kept in the dark at 4°C overnight.

Day 3: Washing and imaging

After secondary antibody staining, samples were washed twice with 1% Triton X100 in PBS at room temperature, with each wash taking around 45 mins. Care was taken to minimize exposure of samples to light. After washing, fresh 1% Triton X100 in PBS was then added to the samples, and they were imaged immediately. Antibodies used in this study are listed in Table 6.11, and expected result of correlative live imaging and immunofluorescence is shown in Figure 6.2.

Table 6.11 List of antibodies used in this study.

Target Antigen	Host Species	Fluorophore	Supplier	Catalog#	Dilution
NICD	rabbit	–	Cell Signaling	4147S	1:200
GFP/Venus	mouse	–	Abcam	ab1218	1:500 (2 ug/mL)
Rabbit	goat	Alexa Fluor 647	Life Tech.	A21244	1:500 (4 ug/mL)
Mouse	goat	Alexa Fluor 488	Life Tech.	A11001	1:500 (4 ug/mL)

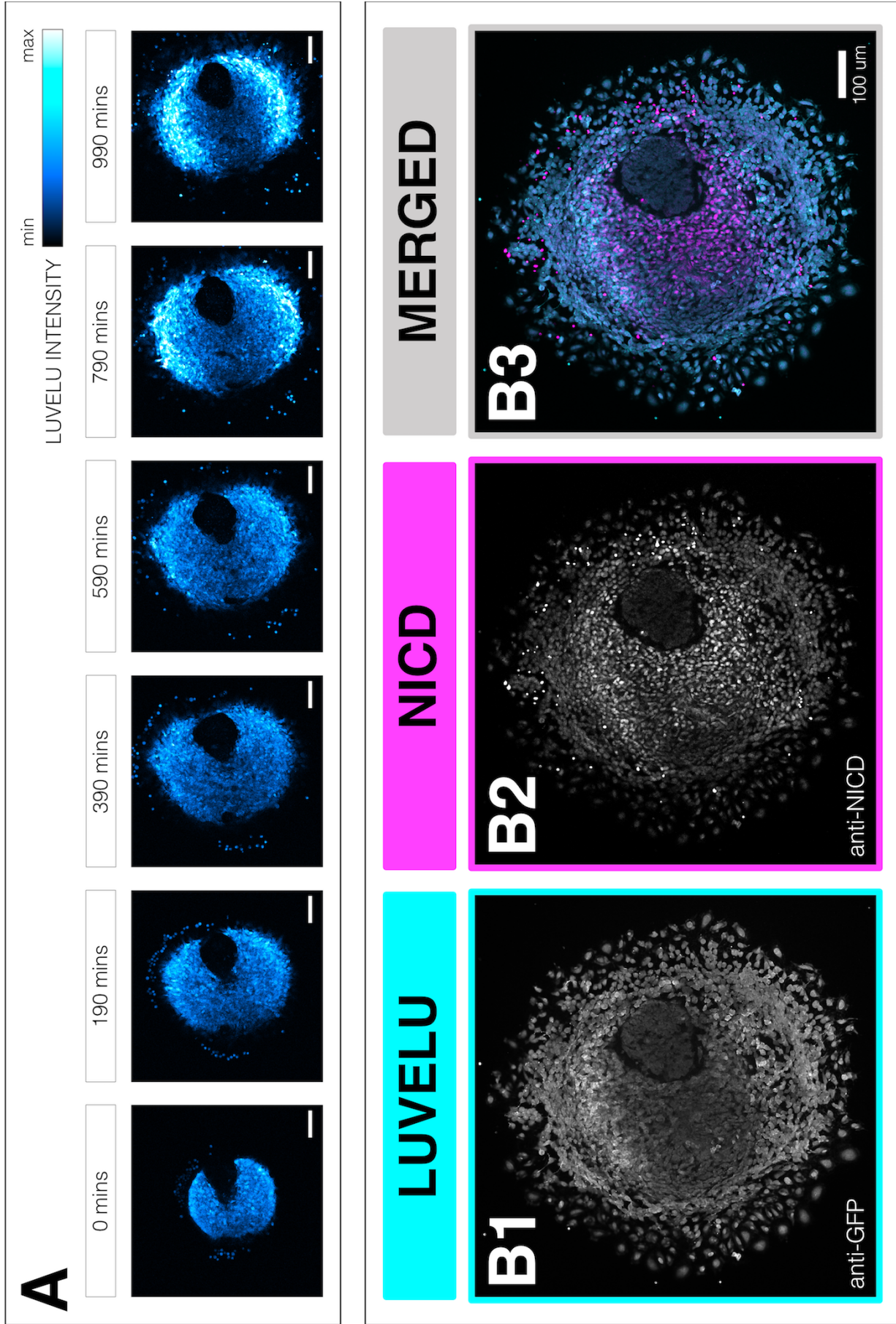


Figure 6.2 Correlative live imaging and immunofluorescence of spreadout. (A) Still frames from live imaging of a spreadout expressing LuVeLu. Time is indicated as mins elapsed from the start of the experiment. (B) Immunostaining of same spreadout, directly after live imaging, for LuVeLu (Venus stained with anti-GFP, Abcam ab1218) and NICD (anti-NICD, Cell Signaling 4147S). Scale bar: 100 μ m.

6.3 Microfluidics

6.3.1 Making of PDMS mold

Preparation of PDMS mold was carried out based on protocol from the lab of Christoph Merten (Genome Biology Unit, EMBL and Institute of Bioengineering, École Polytechnique Fédérale de Lausanne). The protocol with some modifications are summarized below. Most of the optimization here was done by Katharina Sonnen during her postdoctoral fellowship with the labs of Christoph Merten and Alexander Aulehla at EMBL in Heidelberg, Germany. All the steps were done in a clean room.

Instrument setup and wafer preparation

The mask aligner (Süss, MA-45) was set up using the following settings: 3-4 bar compressed air and 1 bar N₂. The vacuum, light power, and aligner power were all turned on, and the UV lamp was ignited (UV lamp has to be at working power of 350 W before use). Glass plate was cleaned carefully and fixed to the mask holder using vacuum. Mask holder was slid into its slot on the mask aligner, and was moved into position ready for use (by pressing the MASKHOLDER button).

Vacuum pump of spin coater (Laurell) was turned on and the lid was covered with aluminum foil to minimize spills. Desired time (in sec), speed (in rpm), and acceleration (in rpm/sec) were specified.

A 4-inch silicon wafer was heated at 140°C under a fume hood for 10-15 mins before use to evaporate any solvent on the surface.

Preparation of photoresist layers for UV exposure, exposure, and post-bake

Silicon wafer was coated with two layers of photoresists with different viscosities. For the first layer, silicon wafer was centered on the spin coater under a fume hood and was secured in position using vacuum. Enough SU-8 2025 photoresist (Microchem, now Kayaku Advanced Materials) was poured from the center of the wafer to cover the whole surface. Coating was done for 30 secs at 2000 rpm with acceleration of 408 rpm/sec. Coated wafer was soft baked under a fume hood at 65°C for 3 mins, then at 95°C for 7 mins. Wafer was then placed on the mask aligner (working energy of approximately 10 mJ/cm²/sec) and was exposed to UV for 45 secs (or 4.5 × 10 secs). Exposed wafer was post baked under a fume hood at 65°C for 3 mins, then at 95°C for 7 mins. After post-baking, wafer was cooled in air. Throughout the process, temperature was changed gradually to avoid the surface of the wafer from cracking.

For the second layer, cooled wafer was again centered on the spin coater under a fume hood and was secured in position using vacuum. Enough SU-8 2150 photoresist (Microchem, now Kayaku Advanced Materials), a more viscous photoresist, was poured from the center of the wafer to cover the whole surface. Coating was done for 35 secs at 1000 rpm with acceleration of 272 rpm/sec. Coated wafer was soft baked under a fume hood at 65°C for 10 mins, then at 95°C for 2 hours. Wafer was then placed on the mask aligner (working energy of approximately 10 mJ/cm²/sec). Negative photomask (Selba, Figures 6.3B-C) was placed directly on top of the wafer and was pressed gently onto the photoresist. The wafer with the photomask was exposed to UV for 90 secs (or 9.0 × 10 secs). Photomask was removed from the photoresist and the exposed wafer was post baked under a fume hood at 65°C for 10 mins, then at 95°C for 2 hours.

Development and silanization

Wafer was put in a glass plate on a shaker under a fume hood. mr-Dev 600 SU-8 photoresist developer (Micro Resist Technology, 108-65-6) was poured in the glass plate, and the wafer was incubated in the solution, with gentle shaking, for around 17 mins. This was repeated for 2-3 times with fresh developer every time. Quality of development was assessed by checking the structures under a microscope. Development was considered complete when structures were clearly visible and the edges were sharply defined. Developed wafer (i.e. PDMS mold) was placed on hot plate under a fume hood at room temperature. Hot plate was turned on and temperature was set to 140°C. The PDMS mold was incubated at 140°C for around 10 mins. Hot plate was turned off and the PDMS mold was gradually cooled down to room temperature (takes around 20 mins). Before its first use, the mold was silanized under a fume hood by incubating it with a drop of trichloro(1H,1H,2H,2H-perfluorooctyl)silane in a closed dish for at least 20 mins. The mold was then placed in a square plastic dish for subsequent use.

Shutting down the mask aligner

Mask holder was taken out of the aligner after pressing the MASKHOLDER button. Then, the vacuum was released and the glass plate was removed. Machine was turned off, and the gas was switched off only after the UV lamp had cooled down.

6.3.2 Making of microfluidics device from pre-existing mold

Preparation of PDMS microfluidics device from pre-existing PDMS mold was carried out based on protocol from the lab of Christoph Merten (Genome Biology Unit, EMBL and Institute of Bioengineering, École Polytechnique Fédérale de Lausanne). The protocol with some modifications are summarized below. Most of the optimization here was done by Katharina Sonnen during her postdoctoral fellowship with the labs of Christoph Merten and Alexander Aulehla at EMBL in Heidelberg, Germany. All the steps were done in a clean room.

PDMS preparation

Sylgard 184 silicone elastomer base (Dow) was mixed thoroughly with the curing agent (Dow) in a ratio of 9:1 (w/w). The PDMS mixture was degassed in a vacuum dessicator chamber for around 30 mins, and then poured onto the mold. Enough PDMS was poured to a height of around 5 mm, covering the structures completely. This was degassed again under vacuum for at least 1.5 hours. After degassing, the filled and degassed mold was placed in a 65°C incubator at least overnight before recovery of PDMS chip.

Recovery of PDMS chip

After solidifying the PDMS in a 65°C incubator, the boundaries of the PDMS chip were carefully cut away from the rest of the mold using a scalpel, and the chip was carefully peeled off. Holes for the inlets and outlets were bored into the PDMS using a 1 mm reusable biopsy punch (World Precision Instruments, 504646). Holes were punched with the patterned side up to prevent damage to the structures and the channel system. Dust on the surface was removed using a clear adhesive tape.

Plasma bonding

Cover glass (70 mm x 70 mm, 1.5H, Marienfeld 0107999 098) was cleaned with an air gun. The glass was then placed on a plasma oven tray with a clean PDMS chip (patterned side facing up). These were put under plasma (power = 2.5 in a Diener Femto plasma oven) for 1 minute. The PDMS chip was then immediately laid on the cover glass such that the patterned side directly presses against the glass. Equal pressure was applied on all sides of the chip to facilitate bonding. The device was then placed in a 65°C for around 1.5 hours. For storage, holes for inlets and outlets were sealed with a clear adhesive tape. PDMS devices were kept in room temperature until use. Images of PDMS devices for entrainment of signaling oscillations in spreadouts and in intact PSM are shown in Figure 6.3.

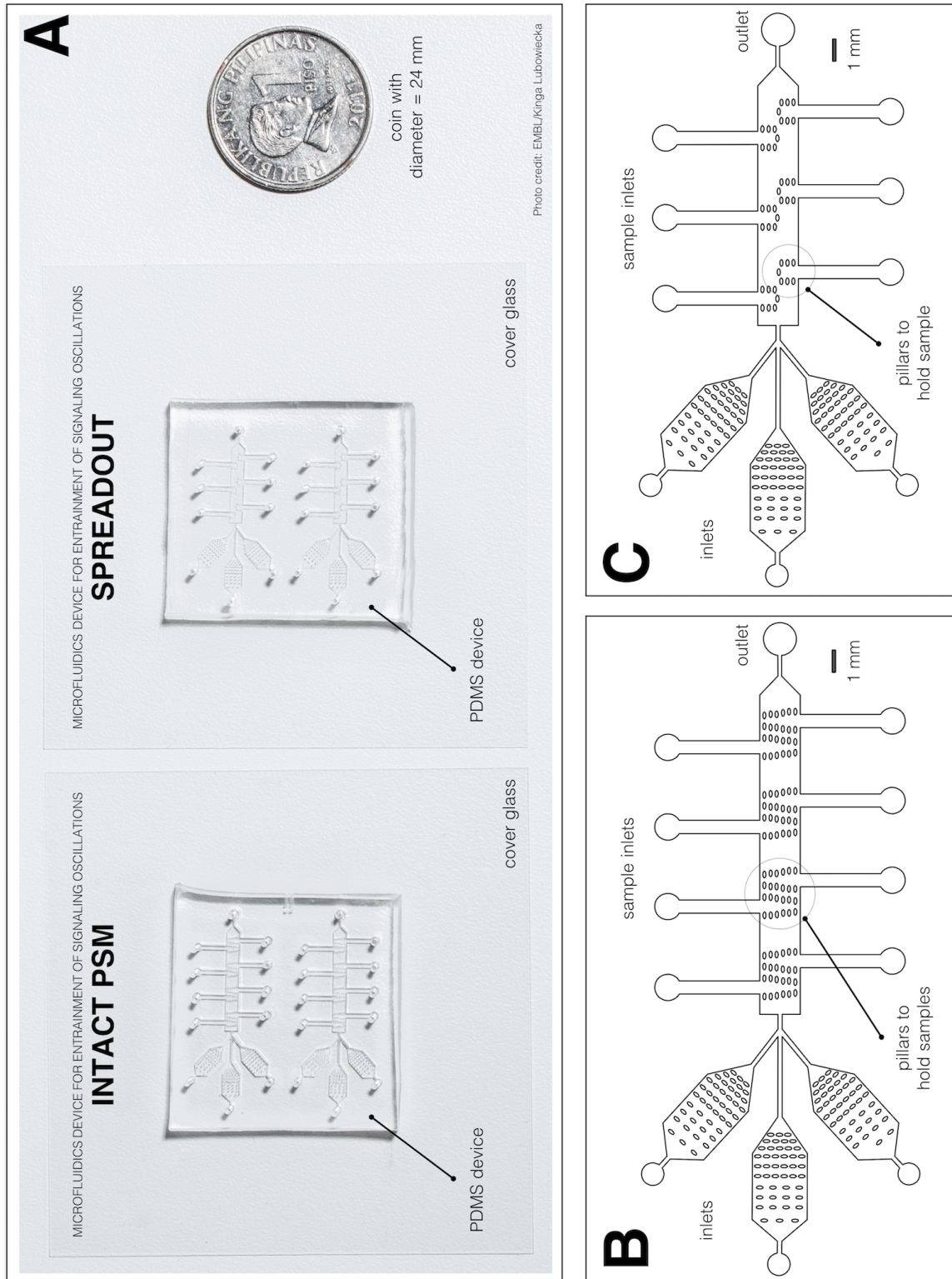


Figure 6.3 Microfluidics PDMS devices for culture, imaging, and entrapment of embryonic tissue samples. (A) Photo of the PDMS chips bonded to cover glass and a coin (diameter: 24 mm) for scale. The split layout separating the upper and lower channel systems allows simultaneous delivery of drug and DMSO control to samples on opposite sides of the same device. Photo credit: EMBL/Kinga Lubowiecka. (B) Design of the microfluidics chip for entrapment of intact PSM, showing inlets for medium and drug, inlets for each sample, pillars to hold each sample, and an outlet. (C) Design of the microfluidics chip for entrapment of spreadout, showing inlets for medium and drug, inlets for each sample, pillars to hold each sample, and an outlet.

6.3.3 Preparations for microfluidics-based entrainment of *ex vivo* model of somitogenesis (spreadout)

UV irradiation of PTFE tubing and PDMS device

PTFE tubing (inner diameter: 0.6 mm, APT AWG24T) and syringe needles (22G 1 1/4 - Nr. 12), as summarized in Table 6.12, were prepared a day prior to actual microfluidics-based entrainment experiment. In addition to 1 PDMS microfluidics device (Figures 1.12 and 6.3), each experiment required 4 3-meter PTFE tubing (each with syringe needle inserted in one end) for the drug/medium inlets, 2 1-meter PTFE tubing (each with syringe needle inserted in one end) for the outlets, and 24 1-centimeter plugs made from cut PDMS-filled PTFE tubing for the sample inlets and unused drug/medium inlets. These were all sterilized under UV for at least 20 minutes.

Table 6.12 List of PTFE tubing needed for a microfluidics-based entrainment experiment. For the first two items, a syringe needle is to be inserted inside one end of each tubing. Plugs are made from cut PDMS-filled PTFE tubing, and are used to seal inlets after sample loading. Controls are already taken into account in the specified quantities.

Item	With Needle?	Quantity	Use
3-meter PTFE tubing	Y	4	drug/medium inlet
1-meter PTFE tubing	Y	2	outlet
1-centimeter plug	N	24	sample inlet + unused drug/medium inlet

Fibronectin-coating of PDMS device and overnight soaking in buffer

While waiting, 5 mL of PenStrep (Gibco, 15140-122) was added to 495 mL of 1x PBS (PBS+PenStrep). 5.6 mL of the buffer was set aside to prepare fibronectin solution, while the rest was poured in a glass dish. After UV irradiation, the sterilized PDMS device was immersed in the PBS+PenStrep and bubbles were removed by flushing the channels with buffer. PDMS-filled PTFE plugs were also immersed in PBS+PenStrep. To prepare the fibronectin solution, 280 uL of fibronectin (Sigma-Aldrich, F1141) was added to the set aside 5.6 mL PBS+PenStrep. At least 2.5 mL of fibronectin solution was loaded into a 3 mL syringe (diameter: 8.66 mm, BD Luer-Lok REF 309658). A UV-irradiated needle, which was earlier inserted into a 1-meter PTFE tubing, was attached to the filled syringe. The tubing was then inserted into an outlet in the PDMS device, carefully avoiding introduction of bubbles. Fibronectin was flowed (flow rate: 50 uL/hr) into the PDMS device at room temperature overnight.

Preparation of syringes containing drug/medium

For a microfluidics-based experiment with periodic pulses of drug, four 10 mL syringes (diameter: 14.5 mm, BD Luer-Lok REF 300912) were filled with either the

drug, DMSO control, or culture medium (see Section 6.2.1). Components of solution in each of these syringes are specified in Table 6.13.

Table 6.13 List of syringe containing drug/medium for a microfluidics-based entrainment experiment. Formulations specified here are for any drug with final concentration X uM. For recipe to prepare culture medium, please refer to Table 6.4.

Component	Syringe A DRUG	Syringe B CONTROL	Syringe C MEDIUM	Syringe D MEDIUM
Drug (10 mM in DMSO)	X uL	–	–	–
DMSO (Sigma-Aldrich, D8418)	–	X uL	–	–
Cascade Blue (Invitrogen, C-3239)	2 uL	2 uL	–	–
Culture medium (see Table 6.4)	dilute to 10 mL	dilute to 10 mL	10 mL	10 mL

Drugs used in this study were DAPT (Sigma-Aldrich, D5942-5MG) and MLN4924 (Cayman, 15217). To prepare 10 mM stock of DAPT, 5 mg DAPT (MW = 432.46 g/mol) was dissolved in 1156.2 uL DMSO (Sigma-Aldrich, D8418). To prepare 10 mM stock of MLN4924, 1 mg MLN4924 (MW = 443.5 g/mol) was dissolved in 225.48 uL DMSO. These solutions were aliquoted and stored at -20°C until use.

Degassing drug/medium and PDMS device

After coating and overnight soaking, the PTFE tubing was cut away from the needle and was immediately immersed in the buffer. The dish containing immersed PDMS device, with attached tubing for the two outlets, and plugs were placed inside a vacuum desiccator chamber. The plunger of each syringe containing the drug/medium was pulled to maximum. The syringes were then also placed in the vacuum chamber, almost vertically, with the plunger resting on the desiccator. These were degassed under high pressure for at least 1.5 hours.

6.3.4 Preparations for microfluidics-based entrainment of intact PSM

Preparations for microfluidics-based entrainment experiments with intact PSM are similar to those with spreadouts in Section 6.3.3. However, instead of coating the PDMS device with fibronectin, the PDMS device was coated with PLL-PEG before overnight soaking in PBS+PenStrep buffer.

PLL-PEG-coating of PDMS device and overnight soaking in buffer

PLL-PEG solution was prepared by diluting 25 uL of 2 mg/mL PLL-PEG to 500 uL with 10 mM HEPES (pH 7). In the clean room, PDMS chip and cover glass (70 mm x 70 mm, 1.5H, Marienfeld 0107999 098) were put under plasma at maximum power (power = 9.9 in a Diener Femto plasma oven) for 1 minute. The PDMS chip was immediately bonded to the cover glass, with the patterned side directly pressing

against the glass. Directly after plasma bonding, the PDMS device (Figures 5.1 and 6.3) was filled with prepared PLL-PEG solution, carefully making sure there were no/minimal bubbles introduced into the microchannels. The PLL-PEG-filled PDMS device was let stand for 2 hours at room temperature.

After incubation, the PLL-PEG-filled PDMS device was flushed with PBS+PenStrep buffer (refer to Section 6.3.3). Flushed PLL-PEG was wiped off the surface of the PDMS device with a lint-free wipe (Kimberly-Clark). After flushing off the PLL-PEG, the PDMS device was immersed in PBS+PenStrep. Bubbles in the microchannels, if present, were removed by flushing in more buffer. At least 2.5 mL of PBS+PenStrep was loaded into a 3 mL syringe (diameter: 8.66 mm, BD Luer-Lok REF 309658). A UV-irradiated needle, which was earlier inserted into a 1-meter PTFE tubing, was attached to the filled syringe. The tubing was then inserted into an outlet in the PDMS device, carefully avoiding introduction of bubbles. Buffer was flowed (flow rate: 50 uL/hr) into the PDMS device at room temperature overnight.

6.3.5 Loading embryonic tissues in microfluidics device and mounting for live imaging

Before mouse dissection and recovery of mouse embryos, syringes containing the degassed drug/medium were each connected to a UV-irradiated 3-meter PTFE tubing via attached syringe needle, and were carefully mounted on programmable pumps (World Precision Instruments, AL-400) next to the microscope. Gas in the tubing was displaced with drug/medium by careful pushing of the syringes' plunger. Pumps were turned on and flow rate was set to 900 uL/hr. The microscope was then equilibrated to 37°C and 5% CO₂ (and 65% O₂ for experiments with intact PSM).

After recovery of embryonic tissues (refer to Section 6.2.2), using a pipette (i.e. P200 for spreadouts and P1000 for intact PSM), each sample was carefully loaded into the microfluidics device, which was already coated with either fibronectin (for spreadouts) or PLL-PEG (for intact PSM), immersed in a buffer of PBS and PenStrep, and degassed (refer to Sections 6.3.3 and 6.3.4). Each sample inlet was plugged with a PDMS-filled PTFE tubing immediately after sample loading. Unused inlets, if any, were also plugged.

Flow rate of drug/medium was set to 20 uL/hr and the tubings were carefully inserted into the drug/medium inlets in the PDMS device while it is immersed in buffer. The tubings connected to the syringes with medium were inserted first, and the tubing connected to the syringe with the drug was inserted last. A 15-min timer was started after insertion of the drug tubing. PDMS device was then removed from the buffer and excess liquid on the cover glass was removed carefully with

lint-free wipes (Kimberly-Clark). The PDMS device, with more than 1 m of attached tubings, was carefully placed inside a pre-equilibrated microfluidics holder (EMBL Mechanical Workshop, Figure 6.4) customized to fit the 70 mm x 70 mm cover glass (Marienfeld 0107999 098) and some PTFE tubing. Putting some of the tubing inside the microfluidics holder was necessary to equilibrate the drug/medium to desired environmental conditions before they are perfused into the microfluidics device. The cover glass was secured in place with grease and a U-shaped metal clamp. For experiments with intact PSM, a tube connected to a tank of 60% O₂ was attached to the microfluidics holder. The microfluidics holder was then carefully mounted on the stage of the microscope, and the end of the outlet tubings were placed in a beaker.

Fifteen minutes after insertion of the drug tubing in the PDMS device, each pump was tilted on its side and was equilibrated for another 15 mins. Afterwards, the pump mounting the syringes with the drug and DMSO control was turned off, and the pump mounting the syringes with the medium was set to flow rate of 60 uL/hr. Samples were equilibrated at these conditions for at least 30 mins before start of imaging/entrainment.

6.3.6 Setting up automated pumping

Entrainment via periodic pulses of drug was performed through alternate perfusion of medium and drug into the microfluidics device. Perfusion of drug/medium was done using syringes mounted on programmable syringe pumps (World Precision Instruments, AL-400). Diameter of syringe (14.5 mm for 10-mL syringe, BD Luer-Lok REF 300912) was accordingly set to match a defined flow rate and a specified volume of solution to be perfused with the duration of perfusion. Standard pumping programs of medium and drug/control are summarized in Tables 6.14 and 6.15, respectively, considering an entrainment experiment with period of drug pulses equal to 170 mins.

Table 6.14 Pumping program of medium for entrainment to 170-min periodic pulses of drug.

Phase	Function	Rate	Volume	Remark
PH:01	LP:ST			
PH:02	RATE	60 uL/hr	140 uL	perfuse medium for 140 mins
PH:03	LP:ST			
PH:04	PS:60			pause for 60 secs
PH:05	LP:30			loop PH:04 30 times (pause for 30 mins = 60 secs × 30)
PH:06	LP:30			loop PH:02 to PH:05 30 times (total: 30 periodic pulses)
PH:07	STOP			

Table 6.15 Pumping program of drug/control for entrainment to 170-min periodic pulses of drug.

Phase	Function	Rate	Volume	Remark
PH:01	LP:ST			
PH:02	LP:ST			
PH:03	LP:ST			
PH:04	PS:60			pause for 60 secs
PH:05	LP:70			loop PH:04 70 times (pause for 70 mins = 60 secs × 70)
PH:06	LP:02			loop PH:04 to PH:05 2x (pause 140 mins = 70 mins × 2)
PH:07	RATE	60 uL/hr	30 uL	perfuse drug/control for 30 mins
PH:08	LP:30			loop PH:02 to PH:07 30 times (total: 30 periodic pulses)
PH:09	STOP			

6.4 Confocal microscopy

For most of the experiments here, samples were imaged in an LSM 780 laser-scanning microscope (Carl Zeiss Microscopy) fitted with an incubation chamber (EMBL Mechanical Workshop). A Plan-Apochromat 20x air objective with a numerical aperture (NA) of 0.8 (Carl Zeiss Microscopy) was used for imaging, and the zoom was set to 0.6. Three z-stacks (spacing: 8 um) were scanned for each sample every 10 mins to acquire timelapse movies. Imaging of multiple samples in multiple locations was done with a motorized stage, controlled using Zen Black software (Carl Zeiss Microscopy), and automated using a VBA macro developed by Antonio Politi (Politi et al., 2018), which is available at <https://git.embl.de/grp-ellenberg/mypic>. The dimensions of the images were either 512 pixels x 512 pixels (for imaging of spreadouts) or 512 pixels x 1024 pixels (for imaging of intact PSM), with a pixel size of 1.38 um and bit depth of 16-bit. Detection of drug pulses, using Cascade Blue (excited with 405 nm) added to the solution, was also done every 10 mins with lower image resolution: 1 z-stack, 32 pixel x 32 pixel (pixel size = 22.14 um). Imaging and automated pumping of drug/medium through the microfluidics device were started simultaneously.

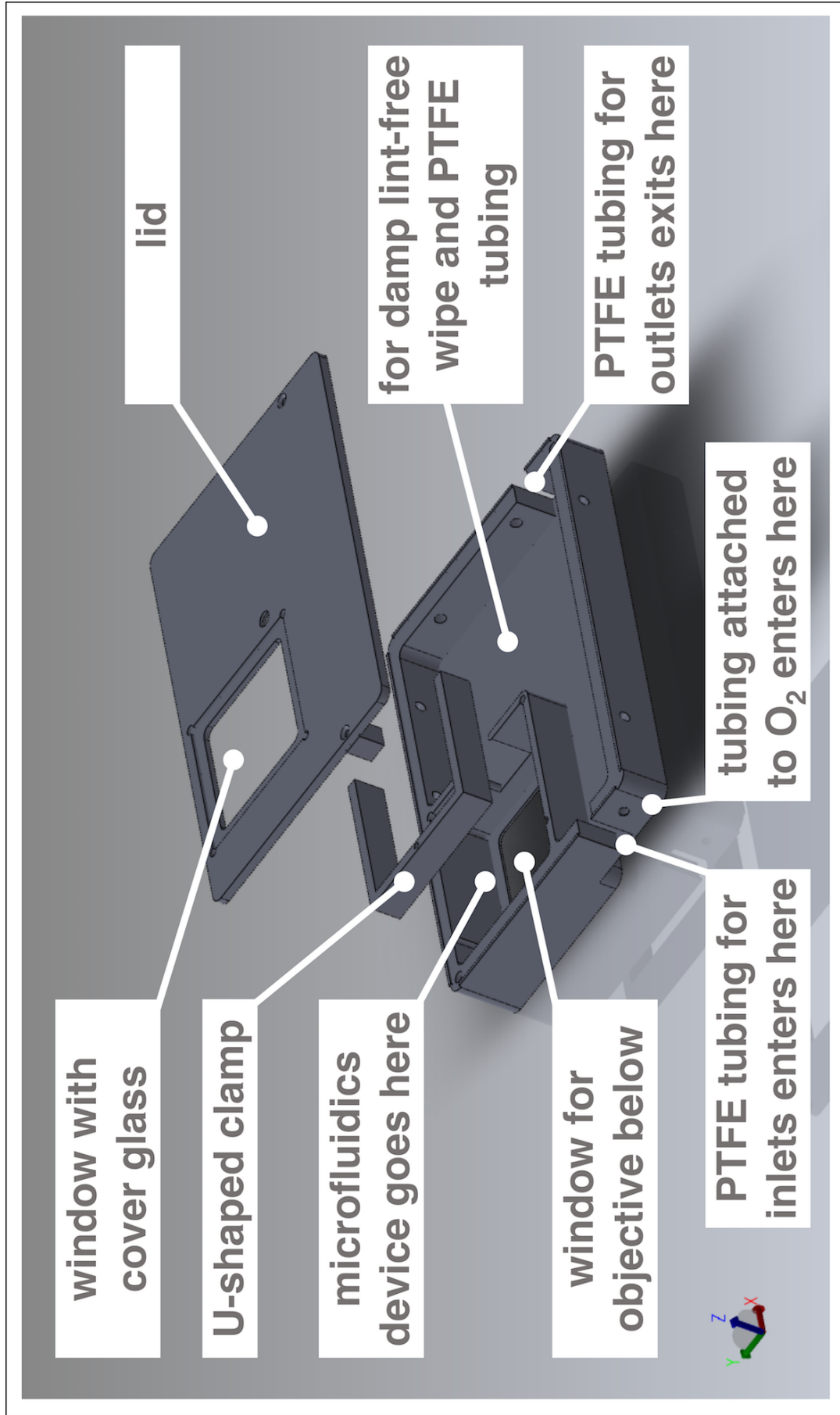


Figure 6.4 Customized box to mount microfluidics device on microscope for simultaneous culture, entrainment, and live imaging. Computer-aided design (CAD) of metal box customized to hold a microfluidics device bonded to a 70 mm x 70 mm cover glass. The box fits the stage of an LSM 780 laser-scanning microscope (Carl Zeiss Microscopy). Design by Katharina Sonnen, the EMBL Mechanical Design Office, and the EMBL Mechanical Workshop.

6.5 Data analysis

6.5.1 Extracting timeseries from global intensity and re-orientation of spreadouts for subsequent gradient analyses

To extract the timeseries corresponding to the segmentation clock (Figure 3.1), global intensity analysis of timelapse fluorescence imaging was done using Fiji (Schindelin et al., 2012). Z-stacks were first projected based on maximum intensity [in Fiji: Image > Stacks > Z Project]. Then, after maximum projection, the timeseries was obtained by plotting the z-axis profile [in Fiji: Image > Stacks > Plot Z-axis Profile]. Timeseries of replicate samples were compiled in a .txt file for subsequent analyses.

For analyses of period/frequency gradient and phase gradient, spreadouts that were centered in the field of view were considered. These samples were re-oriented so that the dorsal side (with the neural tube) is up. If necessary, these spreadouts were either flipped [in Fiji: Image > Transform > Flip], rotated 90° [in Fiji: Image > Transform > Rotate 90 Degrees], and/or rotated by a specified angle [in Fiji: Image > Transform > Rotate]. Specific conditions used to re-orient some of the samples are listed in Table 6.16 (for samples subjected to 130-min periodic pulses of DAPT/DMSO) and Table 6.17 (for samples subjected to 170-min periodic pulses of DAPT/DMSO). One sample that drastically drifted in x and y during overnight imaging (i.e. 20180422_LSM780_W09) was registered based on the brightfield channel (with pillars in the microfluidics device as reference landmarks) using MultiStackReg v1.45 (Brad Busse, available at <http://bradbusse.net/sciencedownloads.html>), prior to re-orientation.

To extract timeseries corresponding to signaling oscillations at the center of spreadouts (equivalent to posterior PSM), spreadouts that were centered in the field of view were considered. A 50 pixel x 50 pixel oval region of interest (ROI) was specified at the center (x = 256 and y = 256) of a re-oriented (and registered, if necessary) spreadout timelapse file [in Fiji: Edit > Selection > Specify]. Timeseries was extracted after specifying the center ROI [in Fiji: Image > Stacks > Plot Z-axis Profile]. Timeseries of replicate samples were compiled in a .txt file for subsequent analyses.

Table 6.16 Re-orientation of some spreadouts that were subjected to 130-min periodic pulses of 2 μ M DAPT (or DMSO control).

Sample ID	Condition	Flipped or Rotated 90°?	Angle of Rotation	Direction
20170616_W09	DAPT	flipped vertically	54°	+
20170616_W11	DAPT		10°	+
20180127_LSM780_W12	DAPT	flipped vertically		
20180324_W03	DMSO	rotated 90° right	10°	-
20180324_W05	DAPT	flipped vertically	14°	-
20180329_W09	DAPT		16°	+
20180402_W04	DMSO	rotated 90° right	16°	-
20180402_W09	DAPT	flipped vertically	56°	-
20180402_W10	DAPT	flipped vertically	16°	+
20180402_W13	DAPT	rotated 90° left		
20180402_W14	DAPT	flipped vertically	22°	+
20180403_W02	DMSO	flipped vertically		
20180403_W09	DAPT		30°	-
20180403_W13	DAPT		17°	-
20180413_W03	DMSO		15°	-
20180413_W04	DMSO	flipped vertically	41°	+
20180413_W05	DAPT	flipped vertically	46°	-
20180413_W09	DAPT		51°	+

Table 6.17 Re-orientation of some spreadouts that were subjected to 170-min periodic pulses of 2 μ M DAPT (or DMSO control).

Sample ID	Condition	Flipped or Rotated 90°?	Angle of Rotation	Direction
20170605_W10	DAPT	flipped vertically	35°	-
20180414_DB_W02	DMSO	flipped vertically	44°	-
20180414_DB_W06	DMSO	flipped vertically	31°	-
20180415_LSM780_W05	DMSO	rotated 90° right	10°	+
20180415_LSM780_W06	DAPT	flipped vertically	8°	-
20180415_LSM780_W07	DAPT	rotated 90° right	36°	+
20180421_DB_W02	DMSO		15°	-
20180421_DB_W09	DAPT	rotated 90° right	19°	+
20180421_DB_W12	DAPT		70°	+
20180421_NLO_W05	DAPT	flipped vertically	29°	-
20180421_NLO_W08	DAPT	flipped vertically	37°	-
20180422_LSM780_W09	DAPT		31°	+
20180429_DB_W02	DMSO		26°	-
20180429_DB_W08	DAPT	flipped vertically	32°	-

6.5.2 Monitoring period-locking and phase-locking

Entrainment was evaluated based on period-locking and phase-locking of the signaling oscillations to the periodic drug pulses. Oscillatory components were extracted from timeseries using a wavelet analysis workflow that was developed by Gregor Mönke, which was recently implemented as a Python-based standalone software (Mönke et al., 2020) available at <https://github.com/tensionhead/pyBOAT>. In this workflow, timeseries was first detrended using a sinc filter and then subjected to continuous wavelet transform. Time-resolved frequency analysis was done by cross-correlating the signal to wavelet functions of known frequencies, generating

a power spectrum. A high power score was assigned to wavelets that correlated well with the signal relative to white noise. Instantaneous period and phase were extracted upon evaluation of the power spectrum along a ridge tracing wavelet with maximum power for every timepoint.

Phase dynamics of signaling oscillations, upon subjecting them to periodic perturbation, were analyzed using stroboscopic maps (Balanov et al., 2008), based on protocol suggested by Paul François (Department of Physics, McGill University), and used in Cross and Siggia, 2005 and in Isomura et al., 2017. Briefly, the phase difference ($\Delta\phi$) was defined as:

$$\Delta\phi = \phi(t + T) - \phi(t)$$

where t is the time of perturbation and T is the period of the perturbation (i.e. one cycle after time = t). `old_phases` contains the $\phi(t)$, while `new_phases` contains the $\phi(t + T)$. The stroboscopic maps were then plotted as `new_phases` versus `old_phases` (for scheme, please refer to Figure 3.4A). The centroid was determined from the average phases of the final (`old_phase,new_phase`) pairs considered, and the circular standard deviation (`circSD`) was calculated using the formula:

$$\text{circSD} = \sqrt{-2\ln R}$$

where R is the first Kuramoto order parameter. As wavelets only partially overlap the signal at the edges of the timeseries, resulting in deviations from true phase values (Mönke et al., 2020), the first and last pulse pairs were not considered in the generation of stroboscopic maps. Polar plots were also generated summarizing the instantaneous phase of replicate samples and their first Kuramoto order parameter as shown in Figure 3.3D and Figure 8.4B. The Python code is available as a Jupyter notebook (.ipynb) at https://github.com/PGLSanchez/EMBL_OscillationsAnalysis/tree/master/EntrainmentAnalysis.

Detrended timeseries of replicate samples were in some part of the study represented as a heatmap using PlotTwist (Goedhart, 2020), as shown in Figure 3.3A. Average periods (from 650 mins to 850 mins after start of experiment) were meanwhile plotted using PlotsOfData (Postma and Goedhart, 2019), as shown in Figures 3.2C-D and Figure 8.2. These apps are available at <https://huygens.science.uva.nl/PlotTwist/> and at <https://huygens.science.uva.nl/PlotsOfData/>, respectively.

6.5.3 Generating wavelet movies

Period and phase wavelet movies were generated using the Wavelet Processing and Export workflow developed by Gregor Mönke, which runs on the EMBL cluster and is implemented in Galaxy with technical assistance from Jelle Scholtalbers (EMBL Genome Biology Computational Support). This workflow extracts timeseries of every pixel in a timelapse movie and subjects them to sinc filter-based detrending and subsequent continuous wavelet transform (Mönke et al., 2020). This results in extraction of instantaneous period and phase of each pixel, recovering period and phase wavelet movies corresponding to the input timelapse movie (for scheme, please refer to Figure 3.7A). Settings used to generate wavelet movies in this study were: sigma of 8.0, sample interval of 10 mins, period range from 100 to 250 mins, and number of periods analyzed of 151. For generating wavelet movies corresponding to timelapse movies of spreadouts subsequently used in Section 6.5.4, only timepoints 1 to 120 were considered. For generating wavelet movies corresponding to timelapse movies of intact PSM, prior to wavelet processing, samples were registered based on the fluorescence signal using MultiStackReg v1.45 (Brad Busse, available at <http://bradbuse.net/sciencedownloads.html>). Amplitude wavelet movies were generated in a similar manner.

6.5.4 Examining period/frequency gradient and phase gradient in spreadouts

Period/frequency gradient and phase gradient in spreadouts were analyzed in collaboration with Takehito Tomita and Paul François (Department of Physics, McGill University). Re-oriented spreadouts (dorsal side up) and their corresponding period and phase wavelet movies were used for the analyses.

Temporal evolution of the period gradient during the course of entrainment experiments was evaluated from the period wavelet movies of the spreadouts. As the period wavelet movies also contained wavelet transformations for pixels in the background, a binary mask was first created to differentiate pixels corresponding to signal. To create the mask, re-oriented (and registered, if necessary) timelapse movies of spreadouts were blurred using a Gaussian blur [in Fiji: Process > Filters > Gaussian Blur (sigma radius: 8, scaled units in microns)]. Then, signal was specified by thresholding [in Fiji: Image > Adjust > Threshold (Default method, dark background)]. After thresholding, pixels corresponding to the signal were assigned a value of 255, while those corresponding to the background were assigned a value of 0. If opposite, the values were inverted [in Fiji: Edit > Invert]. Then, the binary mask (signal = 1 and background = 0) was created by dividing all values by 255 [in

Fiji: Process > Math > Divide (value: 255)], and was used to mask the period wavelet movie. To analyze the period gradient, a 50 pixel-high rectangular ROI was defined at the equator of the spreadout, spanning the entire length of the frame (i.e. 512 pixels) and thus defining a periphery-center-periphery axis cutting across the dorsoventral axis of the sample. For each point along this axis, for a given timepoint, the average period across the 50 pixel width of the ROI was recorded. The mean period gradient for replicate samples was determined and monitored across time. The Python code used in the analysis is available as a Jupyter notebook (.ipynb) at https://github.com/PGLSanchez/EMBL_OscillationsAnalysis/tree/master/PeriodGradientAnalysis. Temporal evolution of the amplitude gradient during the course of entrainment experiments was evaluated from the amplitude wavelet movies of the spreadouts in a similar manner.

The slopes of the period/frequency and phase gradients were analyzed using another Python code, which is available as a Jupyter notebook (.ipynb) at https://github.com/PGLSanchez/EMBL_OscillationsAnalysis/tree/master/FrequencyPhase_GradientSlopeAnalysis. In the workflow, kymographs were generated from blurred intensity movies, period wavelet movies, and phase wavelet movies using a 1-pixel horizontal ROI at the equator of the spreadout and spanning half the length of the frame (i.e. 256 pixels), thus defining a center-periphery axis that is orthogonal to the dorsoventral axis. A binary mask was created from the intensity kymograph by considering a threshold normalized intensity (i.e. signal = normalized intensity > 0.15), and was used to mask the other kymographs. Frequency gradient at different timepoints was retrieved from the period kymograph. Meanwhile, the phase gradient at different timepoints was retrieved from the phase kymograph after unwrapping, and the phases were reported relative to the phase at the center of the spreadout. Linear regression was used to determine the slopes of the frequency gradient and the phase gradient. A quantity α was calculated from the ratio of the slope of the frequency gradient at a given timepoint to the slope of the phase gradient at the same timepoint.

Python codes in this study use Matplotlib (Hunter, 2007), NumPy (van der Walt et al., 2011; Harris et al., 2020), pandas (McKinney et al., 2010), scikit-image (van der Walt et al., 2014), SciPy (Virtanen et al., 2020), and seaborn (Waskom et al., 2014).

Abbreviations

AP	anteroposterior (or anterior-posterior), spreadouts: center-to-periphery
CTRL	control
DAPI	4',6-diamidino-2-phenylindole
DAPT	N-[N-(3,5-difluorophenacetyl)-L-alanyl]-S-phenylglycine t-butyl ester
DIG	digoxigenin
DMSO	dimethyl sulfoxide
dpc	days post coitum
E10.5	embryonic day 10.5
EMBL	European Molecular Biology Laboratory
GFP	green fluorescent protein
HCR	hybridization chain reaction
Lfng	Lunatic fringe
NICD	Notch receptor, intracellular domain
PBS	phosphate buffered saline
PCR	polymerase chain reaction
PDMS	polydimethylsiloxane
PLL-PEG	poly(L-lysine)-poly(ethylene glycol)
PSM	presomitic mesoderm
PTFE	polytetrafluoroethylene
PenStrep	penicillin streptomycin
ROI	region of interest
UV	ultraviolet
YFP	yellow fluorescent protein

Supplementary files and figures

8.1 Supplementary files

8.1.1 Codes and accompanying sample data

- Python script (as Jupyter notebook) for analysis of entrainment experiments and accompanying sample data, both available at https://github.com/PGLSanchez/EMBL_OscillationsAnalysis/tree/master/EntrainmentAnalysis
- Python script (as Jupyter notebook) for analysis of period gradient in spreadouts, available at https://github.com/PGLSanchez/EMBL_OscillationsAnalysis/tree/master/PeriodGradientAnalysis
- Python script (as Jupyter notebook) for analysis of slope of period/frequency gradient and phase gradient in spreadouts, available at https://github.com/PGLSanchez/EMBL_OscillationsAnalysis/tree/master/FrequencyPhase_GradientSlopeAnalysis
- Sample data to run script for analysis of period gradient in spreadouts: period wavelet movies of spreadouts subjected to 170-min periodic pulses of 2 μM DAPT, available at <https://doi.org/10.5281/zenodo.4017365>
- Sample data to run Python script for analysis of slope of period/frequency gradient and phase gradient in spreadouts, available at <https://doi.org/10.5281/zenodo.4017344>

8.1.2 Movies

- E10.5 spreadout, expressing LuVeLu, subjected to 130-min periodic pulses of DMSO control, with corresponding period and phase wavelet movies, available at https://github.com/PGLSanchez/EMBL-files/blob/master/MOVIES/SO_2.0D_130mins_CTRL.avi

- E10.5 spreadout, expressing LuVeLu, subjected to 130-min periodic pulses of 2 uM DAPT, with corresponding period and phase wavelet movies, available at https://github.com/PGLSanchez/EMBL-files/blob/master/MOVIES/SO_2.0D_130mins_DAPT.avi
- E10.5 spreadout, expressing LuVeLu, subjected to 170-min periodic pulses of DMSO control, with corresponding period and phase wavelet movies, available at https://github.com/PGLSanchez/EMBL-files/blob/master/MOVIES/SO_2.0D_170mins_CTRL.avi
- E10.5 spreadout, expressing LuVeLu, subjected to 170-min periodic pulses of 2 uM DAPT, with corresponding period and phase wavelet movies, available at https://github.com/PGLSanchez/EMBL-files/blob/master/MOVIES/SO_2.0D_170mins_DAPT.avi
- Intact E10.5 PSM, expressing LuVeLu and H2B-mCherry, cultured in PDMS microfluidics device and subjected to 170-min periodic pulses of DMSO control, available at https://github.com/PGLSanchez/EMBL-files/blob/master/MOVIES/intactPSM_inPDMSdevice.avi
- Intact E10.5 PSM, expressing LuVeLu, cultured in PDMS microfluidics device and subjected to 170-min periodic pulses of 2 uM DAPT, available at https://github.com/PGLSanchez/EMBL-files/blob/master/MOVIES/intactPSM_2.0D_170mins_DAPT.avi

8.1.3 Text files

- Text (.txt) files containing timeseries from microfluidics-based entrainment experiments, available at <https://github.com/PGLSanchez/EMBL-files/tree/master/ENTRAINMENT-timeseries>
- Text (.txt) files containing sequences of probes used for HCR (i.e. against Tbx6, Tbx18, and Uncx4.1), available at <https://github.com/PGLSanchez/EMBL-files/tree/master/HCR-probes>

8.2 Supplementary figures

The next pages contain figures supplementing results presented in the main text, i.e. from Chapter 3 to Chapter 5.

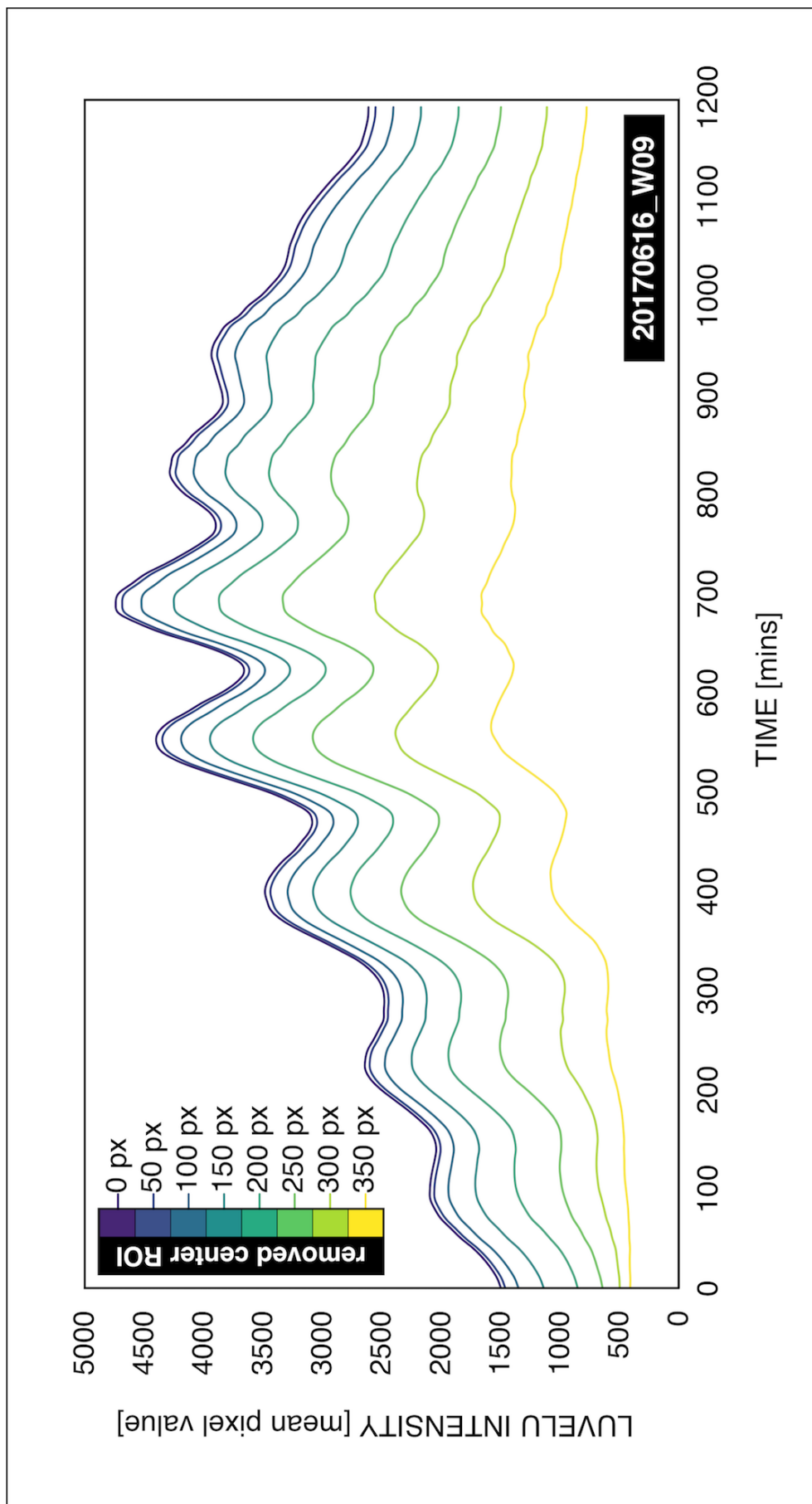


Figure 8.1 Timeseries acquired from global intensity analysis corresponds to the ticking of the segmentation clock. Global intensity analysis is used to recover the timeseries corresponding to the ticking of the segmentation clock. Oscillations at the center of a spreadout subjected to periodic pulses of 2 μ M DAPT were manually removed using oval ROIs of different pixel sizes (as specified in the figure and marked with different colors), verifying that the mean intensity value of the entire field of view is enriched by signal at the periphery of the sample. This corresponds to the arrival of the spatiotemporal wave at the anterior PSM, coinciding with periodic segmentation of the embryonic tissue (Figure 3.1).

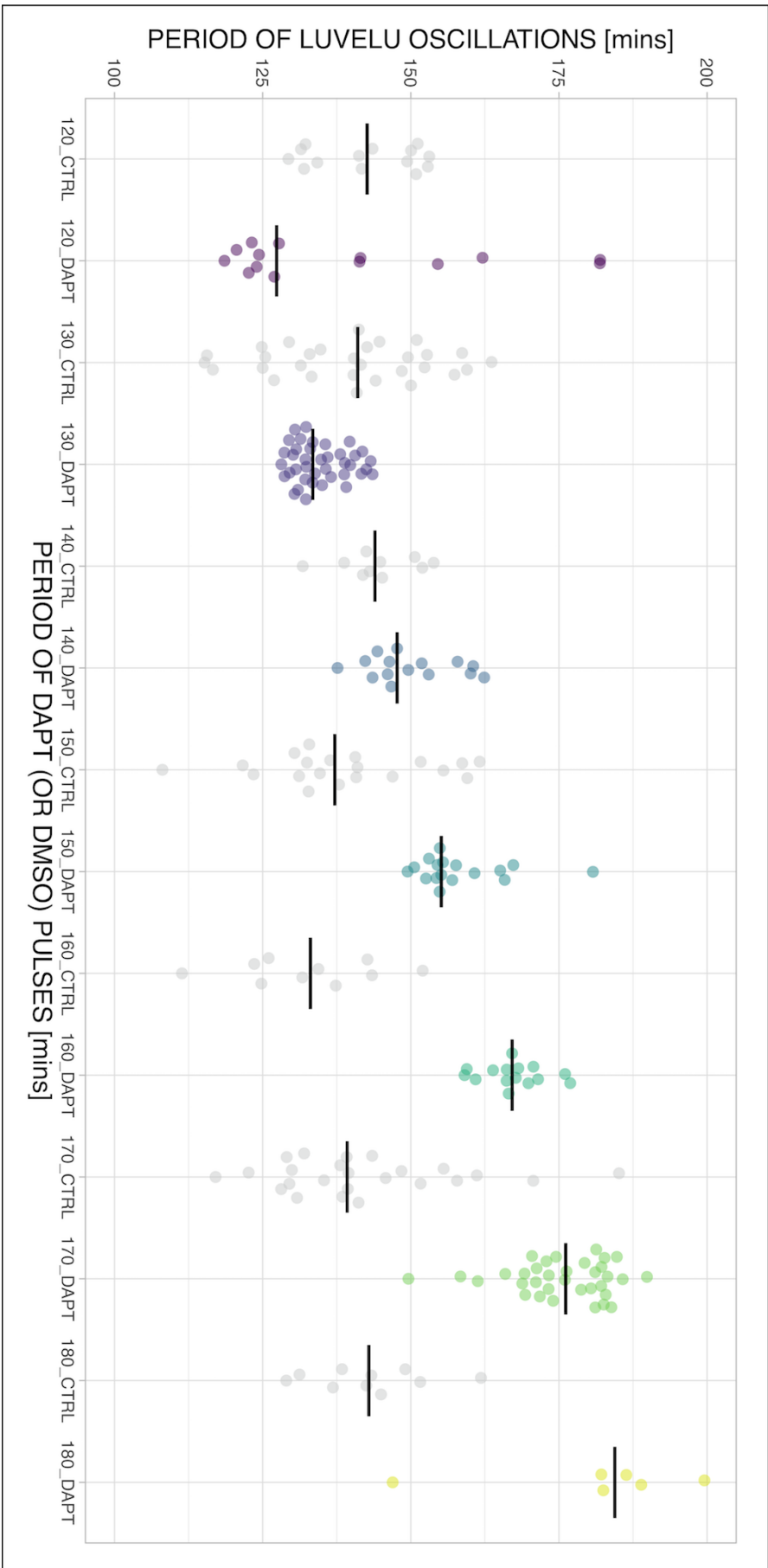


Figure 8.2 The period of the segmentation clock can both be sped up and slowed down by modulating the period of DAPT pulses. Mean period from 650 to 850 mins after start of the experiment of samples subjected to periodic pulses of 2 μ M DAPT (or DMSO for controls). Each sample is represented as a dot, while the median of all samples is denoted as a solid horizontal line. The period of the DAPT (or DMSO) pulses is specified. **120-min:** (CTRL: n = 14 and N = 3) and (DAPT: n = 14 and N = 3), **130-min:** (CTRL: n = 30 and N = 8) and (DAPT: n = 39 and N = 10), **140-min:** (CTRL: n = 10 and N = 3) and (DAPT: n = 15 and N = 3), **150-min:** (CTRL: n = 20 and N = 4) and (DAPT: n = 17 and N = 4), **160-min:** (CTRL: n = 10 and N = 3) and (DAPT: n = 15 and N = 3), **170-min:** (CTRL: n = 24 and N = 7) and (DAPT: n = 34 and N = 8), **180-min:** (CTRL: n = 10 and N = 2) and (DAPT: n = 6 and N = 1).

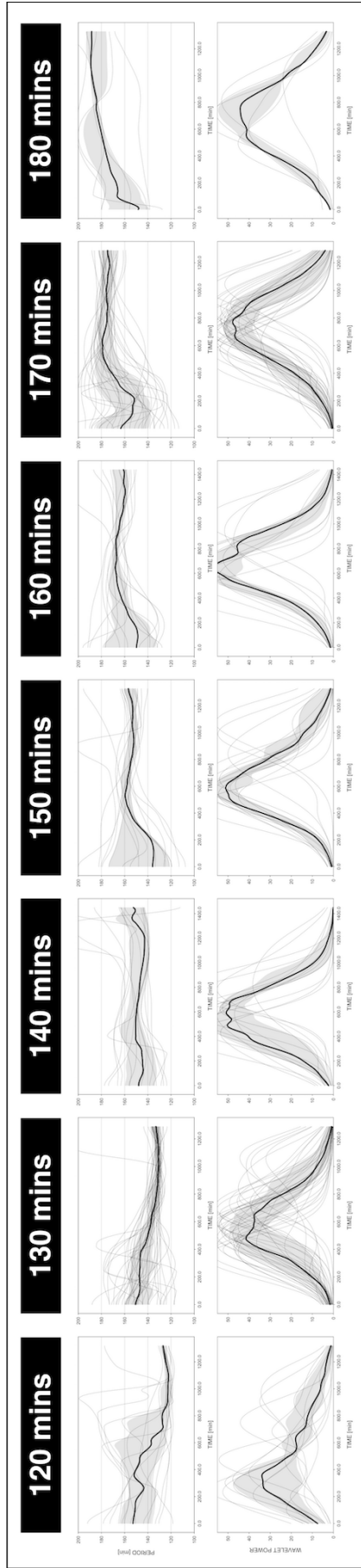


Figure 8.3 The period of the segmentation clock becomes locked to the period of the DAPT pulses. The period and wavelet power of the oscillations, obtained via wavelet analysis, are plotted across time. Each sample and their median are represented here as a dashed line and a solid line, respectively. The gray shaded area corresponds to the interquartile range. The period of the 2 μ M DAPT pulses is specified. **120-min:** $n = 14$ and $N = 3$, **130-min:** $n = 39$ and $N = 10$, **140-min:** $n = 15$ and $N = 3$, **150-min:** $n = 17$ and $N = 4$, **160-min:** $n = 15$ and $N = 3$, **170-min:** $n = 34$ and $N = 8$, **180-min:** $n = 6$ and $N = 1$.

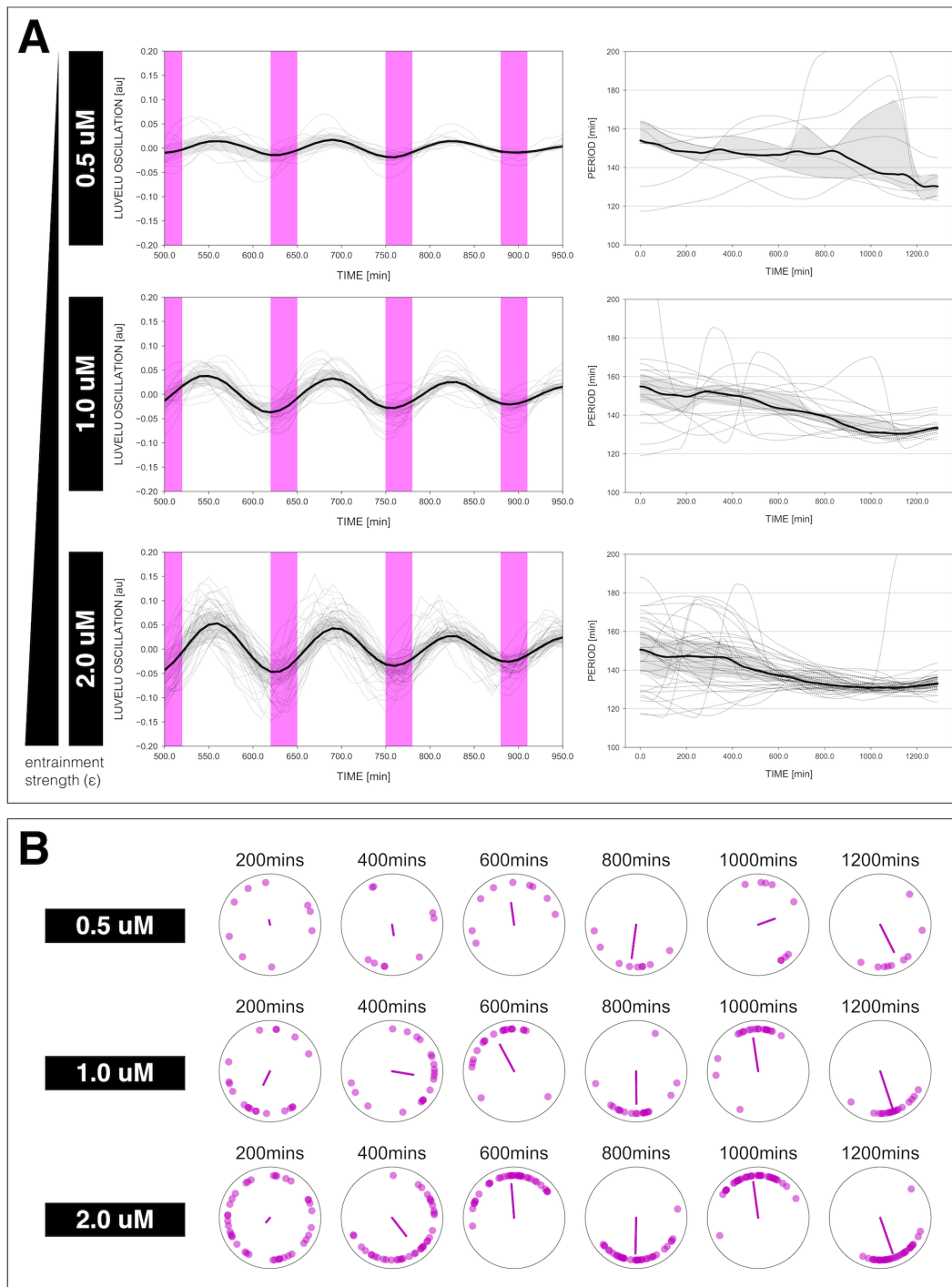


Figure 8.4 Changing the concentration of DAPT, equivalent to changing entrainment strength, affects entrainment of the segmentation clock to 130-min periodic DAPT pulses. **(A)** Left: Detrended timeseries of the segmentation clock in spreadouts entrained to 130-min periodic pulses of either 0.5 μM , 1 μM , or 2 μM DAPT, zoomed in from 500 mins to 950 mins. Periodic pulses are indicated as magenta bars and the timeseries of each sample (for 0.5 μM : $n = 9$ and $N = 2$, for 1 μM : $n = 20$ and $N = 4$, for 2 μM : $n = 39$ and $N = 10$) is marked with a dashed line. The median of the oscillations is represented here as a solid line, while the gray shaded area denotes the interquartile range. Right: Period evolution during entrainment, obtained from wavelet analysis. The period evolution for each sample and the median of the periods are represented here as a dashed line and a solid line, respectively. The gray shaded area corresponds to the interquartile range. **(B)** Polar plots at different timepoints showing phase of each sample and their first Kuramoto order parameter, represented as a magenta dot along the circumference of a circle and a magenta line segment at the circle's center, respectively. A longer line segment corresponds to a higher first Kuramoto order parameter, and thus to more coherent samples. The direction of the line denotes the vectorial average of the sample phases. Time is indicated as mins elapsed from the start of the experiment.

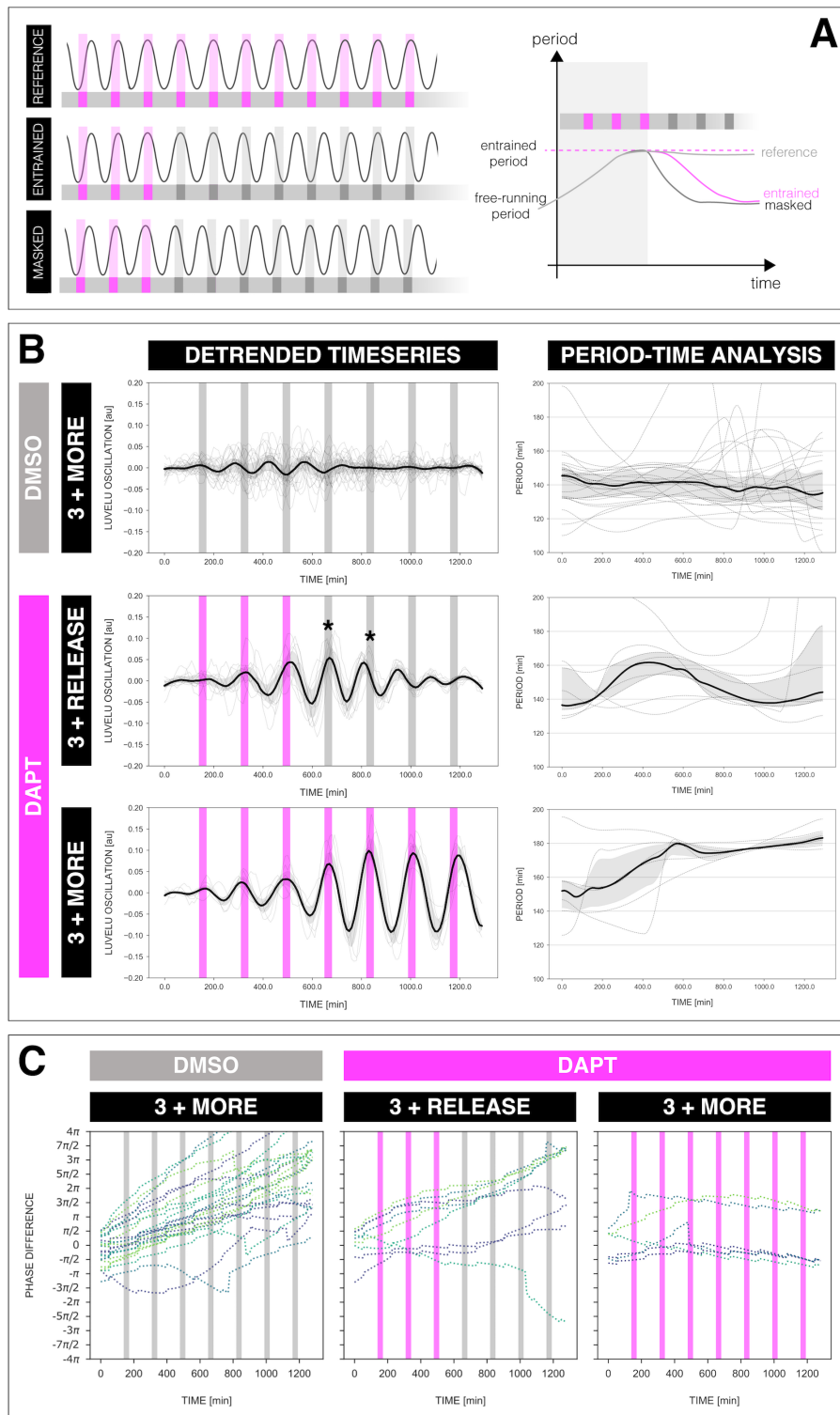


Figure 8.5 The segmentation clock keeps its adjusted rhythm even a few cycles after release from DAPT pulses. **(A)** Left: Scheme of pulse and release experiment where samples are subjected to three pulses of DAPT (magenta bars) and then to pulses of DMSO (gray bars), with expected timeseries for entrained and forced/masked sample. Right: Expected temporal evolution of period of the segmentation clock before and after release if it is entrained or forced/masked. Illustration by Stefano Vianello. **(B)** Left: Detrended timeseries of the segmentation clock in spreadouts subjected to 170-min periodic pulses of DMSO (gray bars) and/or 2 μ M DAPT (magenta bars). The timeseries of each sample (for continuous DMSO pulses: $n = 24$ and $N = 7$, for 3 DAPT pulses and then release: $n = 9$ and $N = 2$, for continuous DAPT pulses: $n = 6$ and $N = 2$) is marked with a dashed line. The median of the oscillations is represented here as a solid line, while the gray shaded area denotes the interquartile range. Right: Period evolution during entrainment, obtained from wavelet analysis. The period evolution for each sample and the median of the periods are represented here as a dashed line and a solid line, respectively. The gray shaded area corresponds to the interquartile range. Data for the continuous DMSO pulses are the same as the controls in Figure 3.2A-B. **(C)** Phase difference between the segmentation clock and the drug pulses. Note that a phase of $-\pi/2$ is equivalent to a phase of $3\pi/2$, and a phase of 0 is equivalent to a phase of 2π . Periodic pulses of DMSO and 2 μ M DAPT are indicated as gray bars and as magenta bars, respectively. Each sample within each condition is marked with different colors.

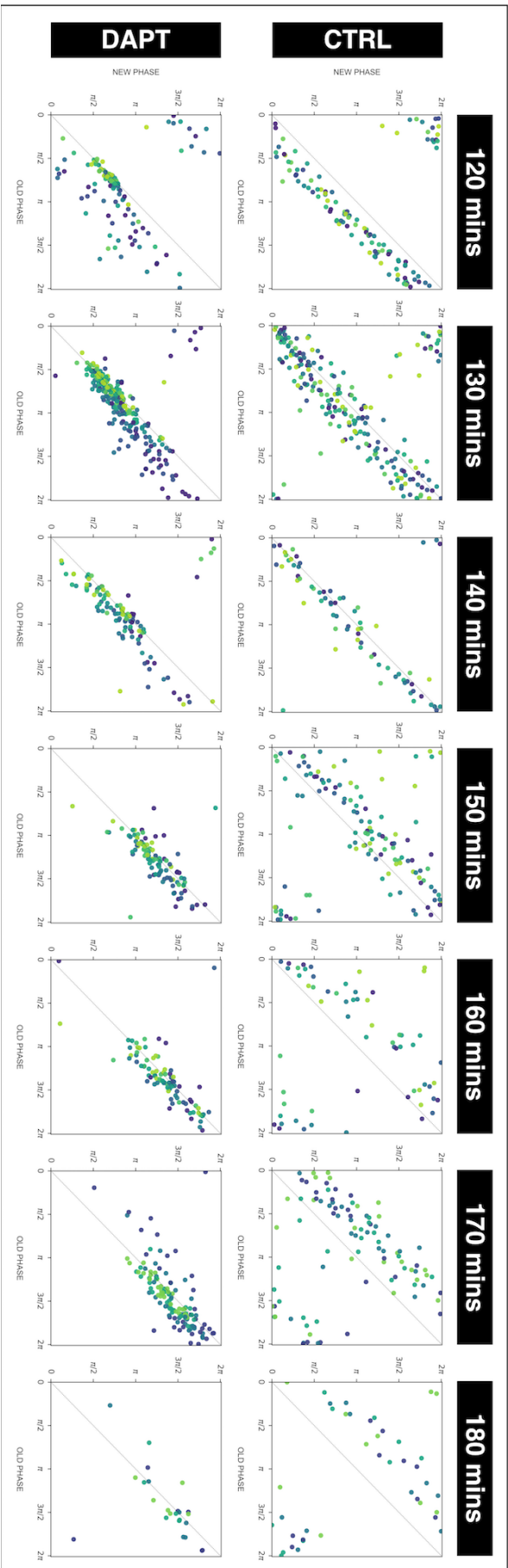


Figure 8.6 The segmentation clock establishes a stable phase relationship with the periodic DAPT pulses. Stroboscopic maps summarizing phase dynamics when the segmentation clock was subjected to periodic pulses of 2 μM DAPT (or DMSO for controls). The period of the DAPT (or DMSO) pulses is specified. Colors mark progression in time, from purple to yellow. **120-min:** (CTRL: $n = 14$ and $N = 3$) and (DAPT: $n = 14$ and $N = 3$), **130-min:** (CTRL: $n = 30$ and $N = 8$) and (DAPT: $n = 39$ and $N = 10$), **140-min:** (CTRL: $n = 10$ and $N = 3$) and (DAPT: $n = 15$ and $N = 3$), **150-min:** (CTRL: $n = 20$ and $N = 4$) and (DAPT: $n = 17$ and $N = 4$), **160-min:** (CTRL: $n = 10$ and $N = 3$) and (DAPT: $n = 15$ and $N = 3$), **170-min:** (CTRL: $n = 24$ and $N = 7$) and (DAPT: $n = 34$ and $N = 8$), **180-min:** (CTRL: $n = 10$ and $N = 2$) and (DAPT: $n = 6$ and $N = 1$).

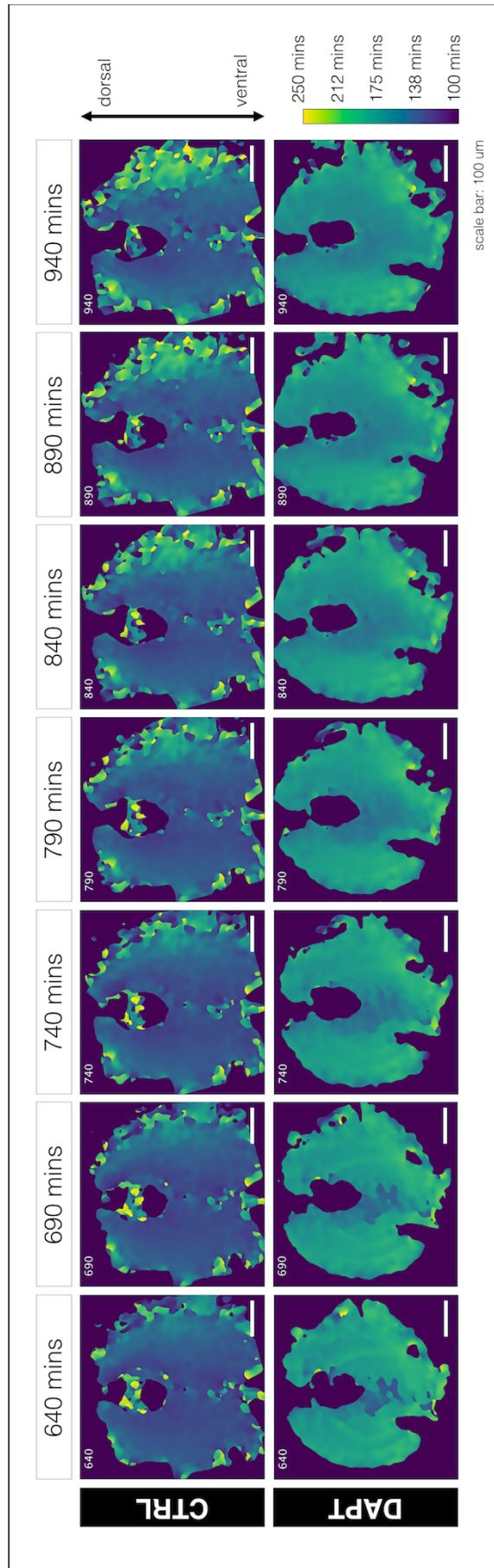


Figure 8.7 A period gradient emerges in the tissue even after globally slowing down the period of the LuVeLu oscillations. Snapshots of period wavelet movie of a sample subjected to 170-min periodic pulses of 2 μ M DAPT (or DMSO for control) at different time points. Time is indicated as mins elapsed from the start of the experiment. Sample is rotated so that the dorsal side is up.

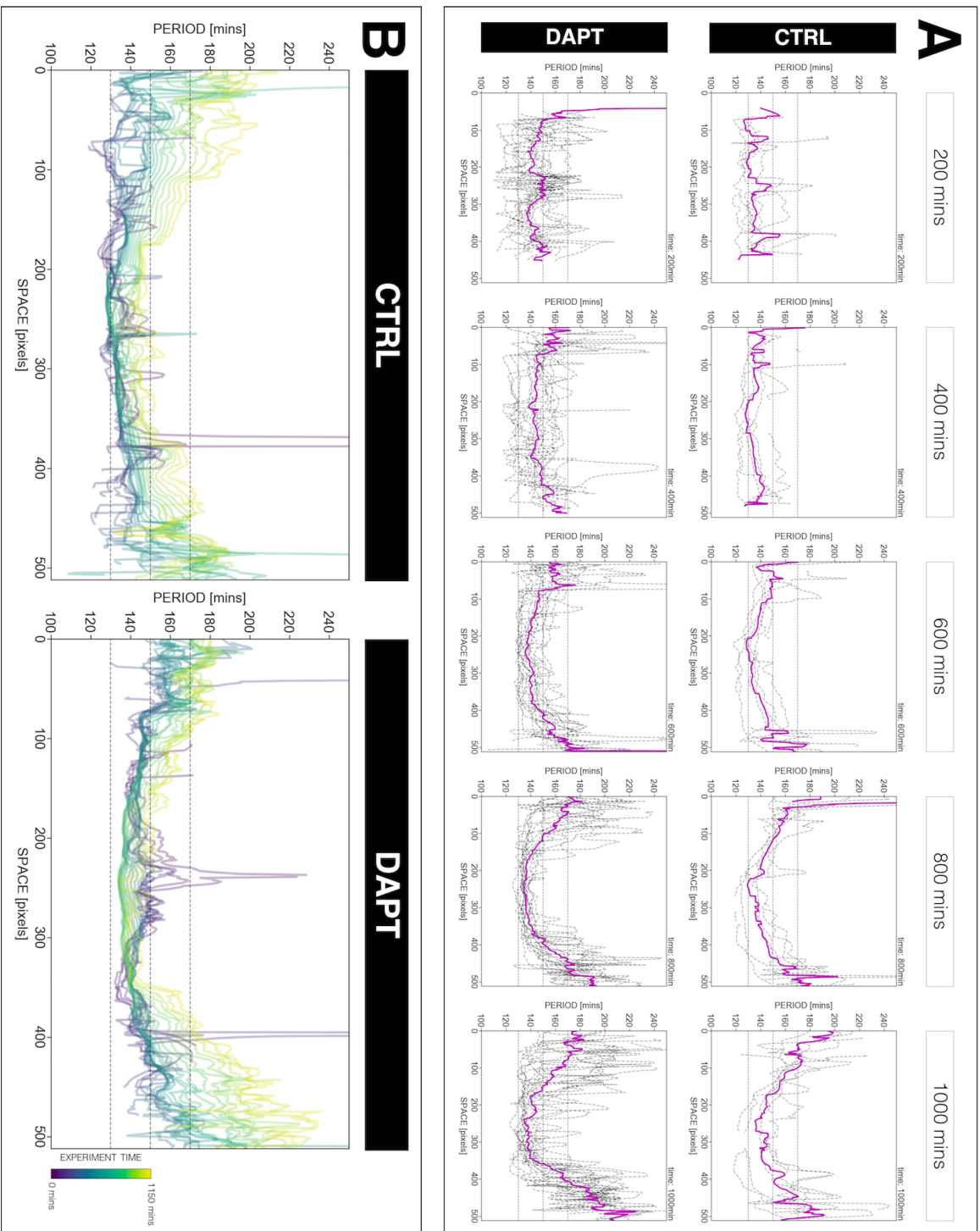


Figure 8.8 An altered period gradient emerges upon entrainment of the segmentation clock to a faster period. (A) Average period gradient tracing average period over 50 pixels at different positions along the periphery-center-periphery axis at the equator (i.e. perpendicular to the dorsal-ventral axis) of the sample is marked with a dashed black line. The average of this period gradient across multiple samples (for CTRL: $n = 6$ and $N = 5$, for DAPT: $n = 15$ and $N = 7$) is marked with a solid magenta line. Periods equal to 130 mins, 150 mins, and 170 mins are highlighted, and time is indicated as mins elapsed from the start of the experiment. Pixel size is 1.38 μm and cells have a diameter of around 10 μm . (B) Temporal evolution of the period gradient as an overlay of the average period gradient across multiple samples at different timepoints. Periods equal to 130 mins, 150 mins, and 170 mins are highlighted. Colors mark progression in time, from purple to yellow. Pixel size is 1.38 μm and cells have a diameter of around 10 μm .

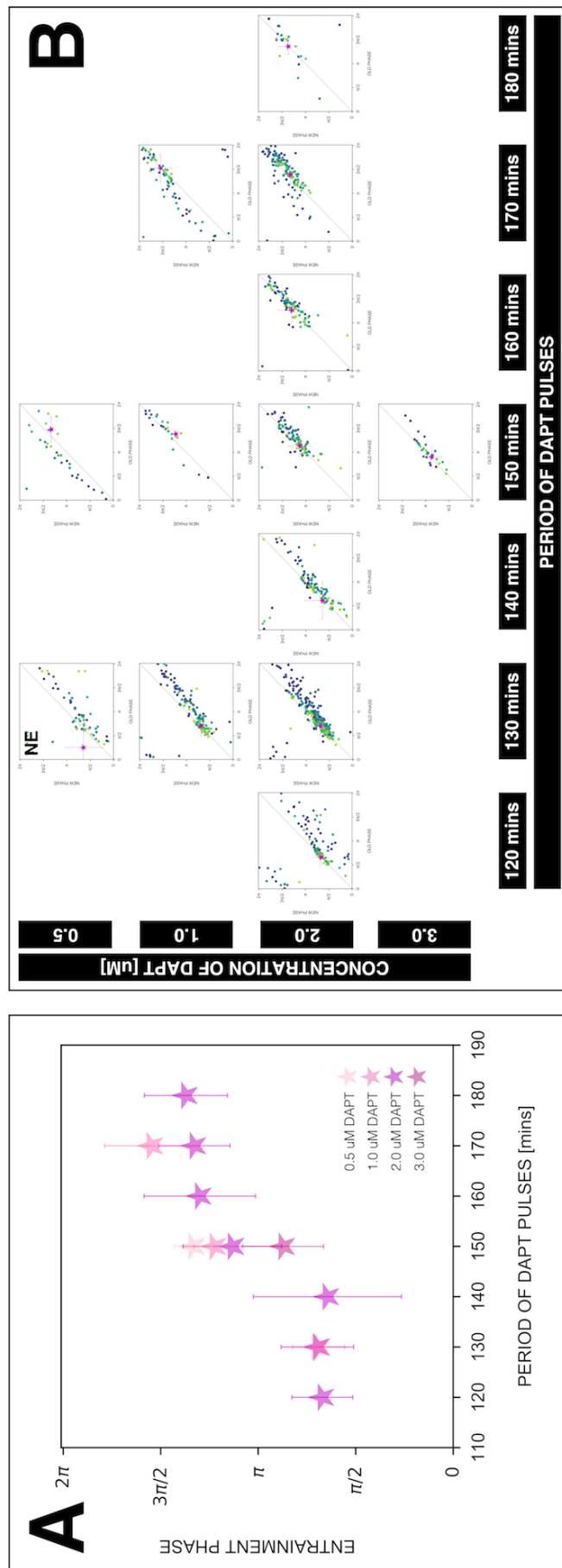


Figure 8.9 Detuning affects the entrainment phase of the segmentation clock. (A) Entrainment phase at different periods of DAPT pulses (i.e. detuning) and different drug concentrations (i.e. entrainment strength). Entrainment phase was calculated from the vectorial average of the phases of all samples at the time corresponding to last considered DAPT pulse. The spread of the entrainment phase between samples is reported in terms of the circular standard deviation ($\sqrt{-2/nR}$, where R is the first Kuramoto order parameter). Colors mark concentration of DAPT. (B) Stroboscopic maps for different values of detuning and entrainment strength placed next to each other. The localized region close to the diagonal in each map marks the entrainment phase for that detuning and entrainment strength. This is highlighted with a magenta star, which corresponds to the centroid of the said region. The centroid (x_c, y_c) was calculated from the vectorial average of the phases of all samples at the end of the experiment, where $x_c =$ vectorial average of old phase, $y_c =$ vectorial average of new phase. The spread of the points in the region is reported in terms of the circular standard deviation ($\sqrt{-2/nR}$, where R is the first Kuramoto order parameter). The period of the DAPT pulses and the concentration of DAPT are indicated. Colors mark progression in time, from purple to yellow. NE means not entrained. **120-min:** (2 μM : $n = 14$ and $N = 3$), **130-min:** (0.5 μM : $n = 9$ and $N = 2$), (1 μM : $n = 20$ and $N = 4$), (2 μM : $n = 39$ and $N = 10$), **140-min:** (2 μM : $n = 15$ and $N = 3$), **150-min:** (0.5 μM : $n = 6$ and $N = 1$), (1 μM : $n = 4$ and $N = 1$), (2 μM : $n = 17$ and $N = 4$), (3 μM : $n = 5$ and $N = 1$), **160-min:** (2 μM : $n = 15$ and $N = 3$), **170-min:** (1 μM : $n = 18$ and $N = 5$), (2 μM : $n = 6$ and $N = 1$), **180-min:** (2 μM : $n = 8$ and $N = 1$).

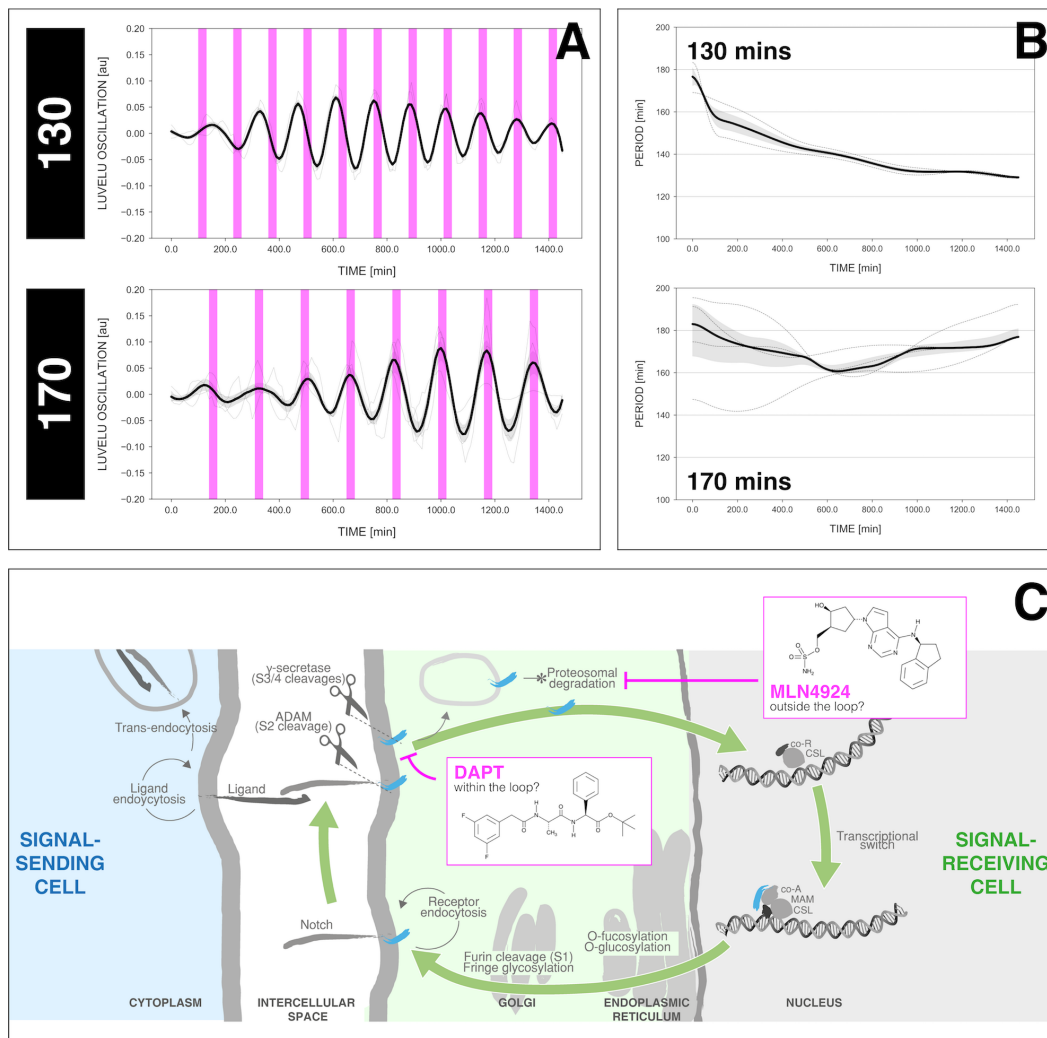


Figure 8.10 The segmentation clock adjusts its rhythm to periodic pulses of MLN4924, a Notch signaling activator. (A) Detrended timeseries of the segmentation clock in spreadouts entrained to either 130-min or 170-min periodic pulses of 4 μ M MLN4924. Periodic pulses are indicated as magenta bars and the timeseries of each sample (for 130-min: $n = 2$ and $N = 1$, for 170-min: $n = 4$ and $N = 1$) is marked with a dashed line. The median of the oscillations is represented here as a solid line, while the gray shaded area denotes the interquartile range. (B) Period evolution during entrainment, obtained from wavelet analysis. The period evolution for each sample and the median of the periods are represented here as a dashed line and a solid line, respectively. The gray shaded area corresponds to the interquartile range. (C) Schematic of the Notch signaling pathway (modified and adapted from Kopan and Ilagan, 2009) highlighting the targets of DAPT and MLN4924. Illustration by Stefano Vianello.

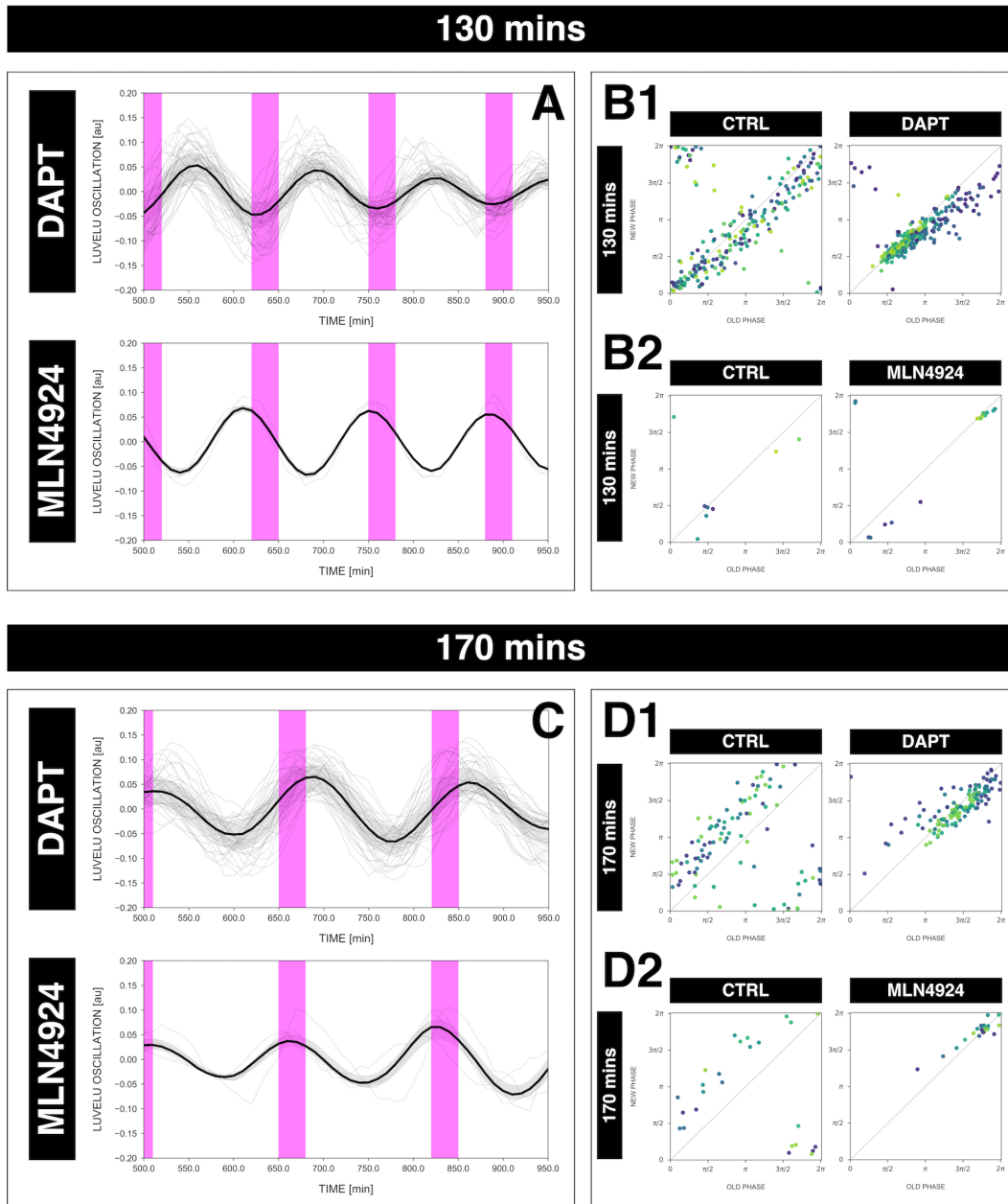


Figure 8.11 The segmentation clock is phase-locked to periodic pulses of MLN4924, a Notch signaling activator. (A) Detrended timeseries of the segmentation clock in spreadouts entrained to 130-min periodic pulses of either 2 μ M DAPT or 4 μ M MLN4924, zoomed in from 500 mins to 950 mins. Periodic pulses are indicated as magenta bars and the timeseries of each sample (for DAPT: $n = 39$ and $N = 10$, for MLN4924: $n = 2$ and $N = 1$) is marked with a dashed line. The median of the oscillations is represented here as a solid line, while the gray shaded area denotes the interquartile range. The plot for DAPT is the same as that for the 130-min condition in Figure 3.5A. (B) Stroboscopic maps of samples subjected to 130-min periodic pulses of either 2 μ M DAPT (B1) or 4 μ M MLN4924 (B2), with their respective controls (subjected to periodic pulses of DMSO). Colors mark progression in time, from purple to yellow. The maps in B1 are the same as those in Figure 3.5B1. (C) Detrended timeseries of the segmentation clock in spreadouts entrained to 170-min periodic pulses of either 2 μ M DAPT or 4 μ M MLN4924, zoomed in from 500 mins to 950 mins. Periodic pulses are indicated as magenta bars and the timeseries of each sample (for DAPT: $n = 34$ and $N = 8$, for MLN4924: $n = 4$ and $N = 1$) is marked with a dashed line. The median of the oscillations is represented here as a solid line, while the gray shaded area denotes the interquartile range. The plot for DAPT is the same as that for the 170-min condition in Figure 3.5A. (D) Stroboscopic maps of samples subjected to 170-min periodic pulses of either 2 μ M DAPT (D1) or 4 μ M MLN4924 (D2), with their respective controls (subjected to periodic pulses of DMSO). Colors mark progression in time, from purple to yellow. The maps in D1 are the same as those in Figure 3.5B2.

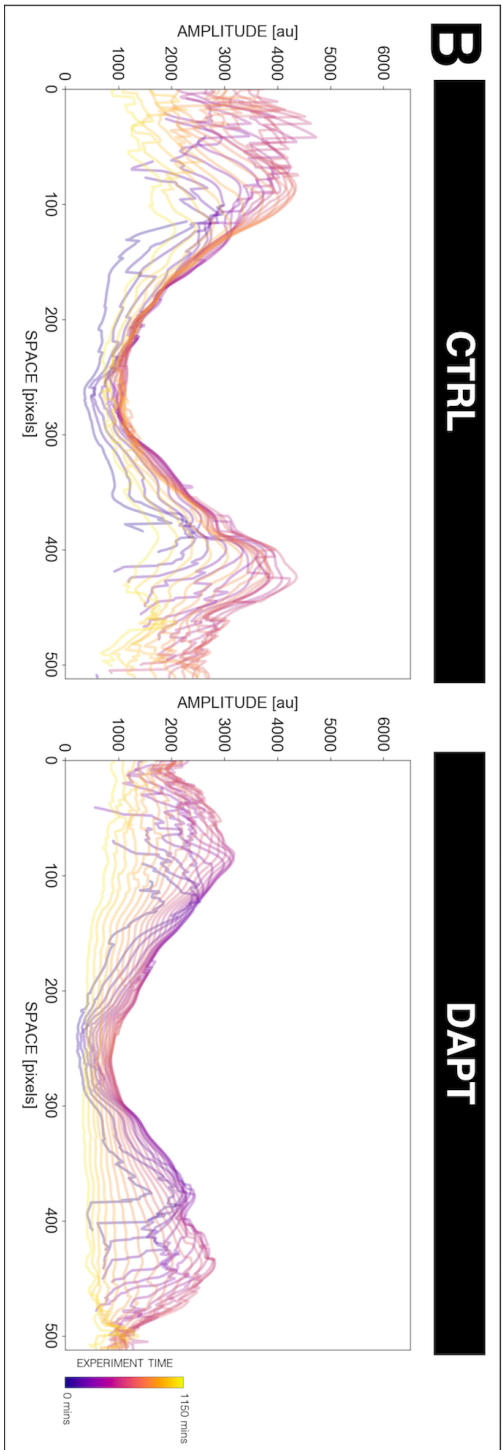
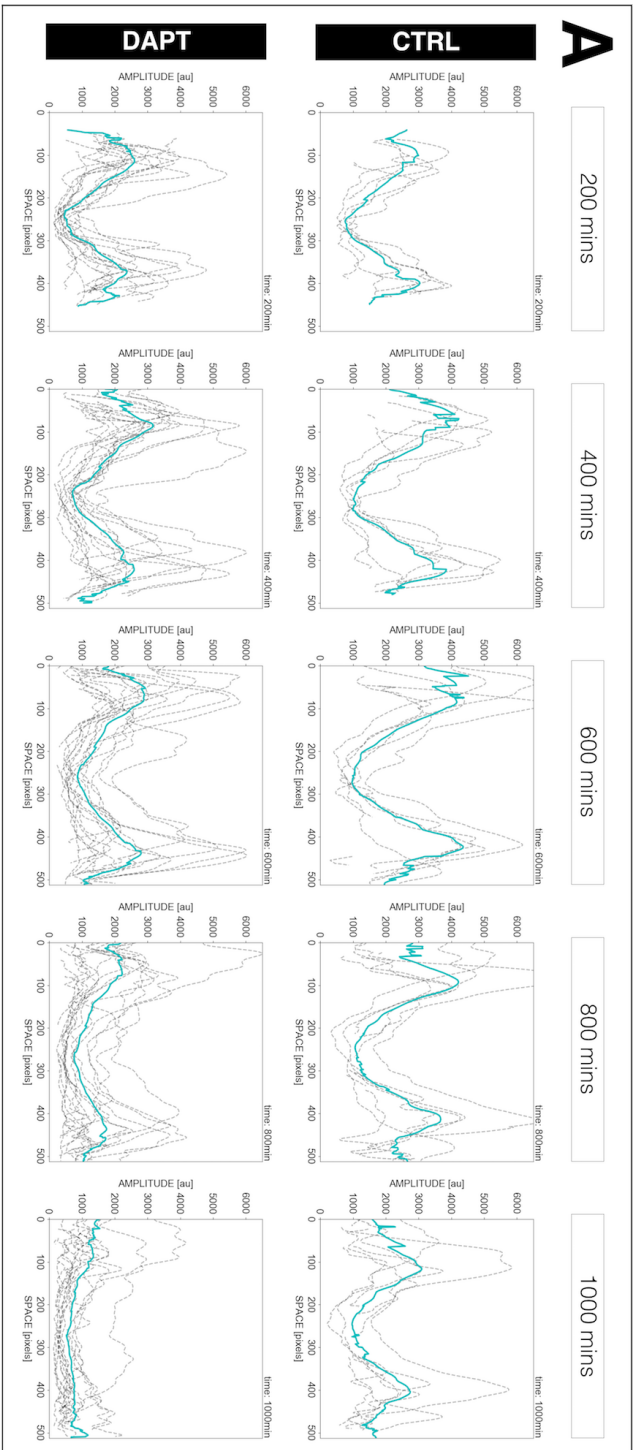


Figure 8.12 Oscillations at the posterior PSM (i.e. the center of spreadouts) have the lowest amplitude even when the segmentation clock is sped up. (A) Average amplitude gradient along the periphery-center-periphery axis of spreadouts subjected to 130-min periodic pulses of 2 μ M DAPT (or DMSO for controls) at different timepoints. Amplitude gradient tracing average amplitude over 50 pixels at different positions along the periphery-center-periphery axis at the equator (i.e. perpendicular to the dorsal-ventral axis) of the sample is marked with a dashed black line. The average of this amplitude gradient across multiple samples (for CTRL: $n = 6$ and $N = 5$, for DAPT: $n = 15$ and $N = 7$) is marked with a solid cyan line. Time is indicated as mins elapsed from the start of the experiment. Pixel size is 1.38 μ m and cells have a diameter of around 10 μ m. Plot for DAPT is the same as that for the 130-min condition in Figure 4.4A. (B) Temporal evolution of the amplitude gradient as an overlay of the average amplitude gradient across multiple samples at different timepoints. Colors mark progression in time, from purple to yellow. Pixel size is 1.38 μ m and cells have a diameter of around 10 μ m. Plot for DAPT is the same as that for the 130-min condition in Figure 4.3B.

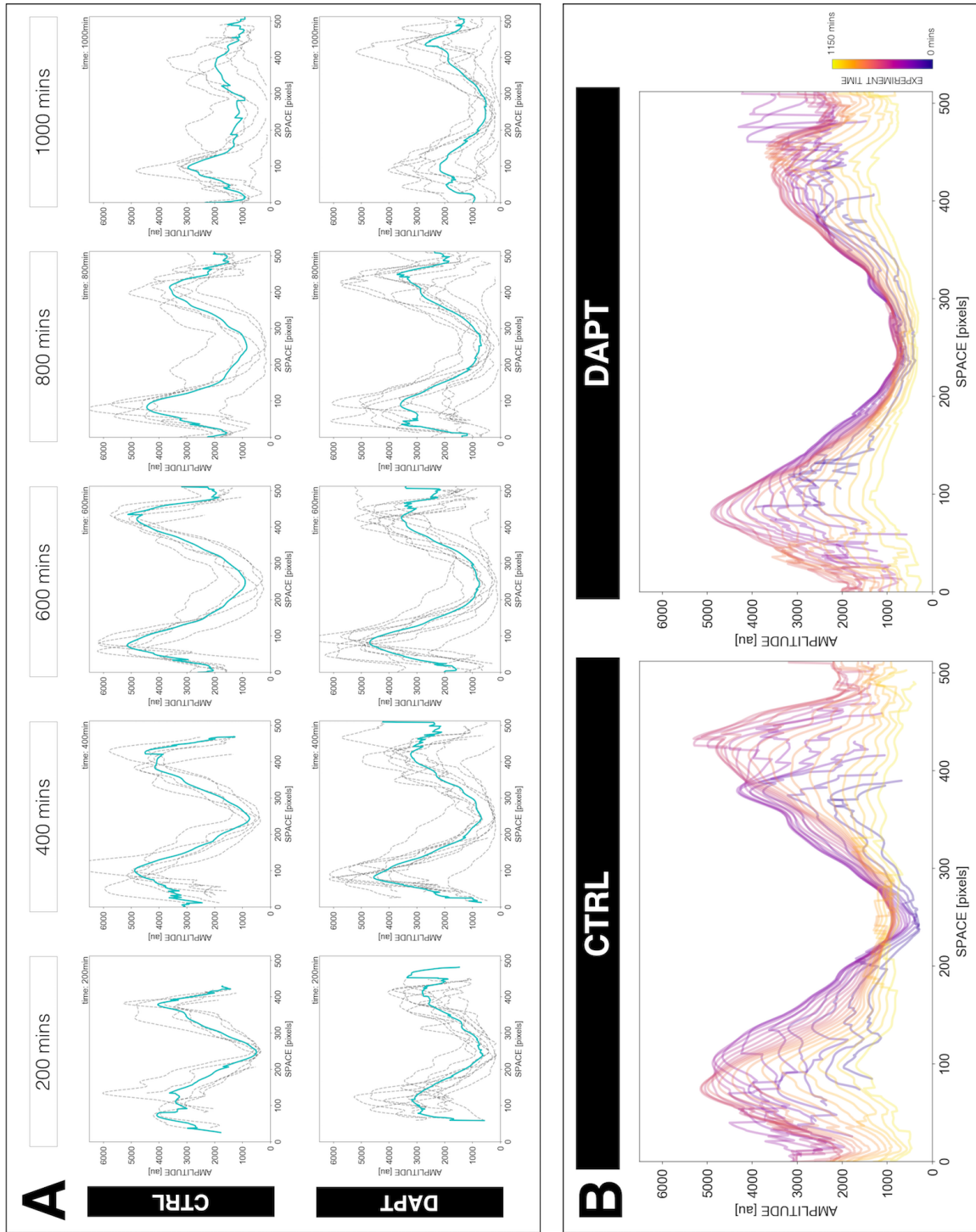


Figure 8.13 Oscillations at the posterior PSM (i.e. the center of spreadouts) have the lowest amplitude even when the segmentation clock is slowed down. (A) Average amplitude gradient along the periphery-center-periphery axis of spreadouts subjected to 170-min periodic pulses of 2 μ M DAPT (or DMSO for controls) at different timepoints. Amplitude gradient tracing average amplitude over 50 pixels at different positions along the periphery-center-periphery axis at the equator (i.e. perpendicular to the dorsal-ventral axis) of the sample is marked with a dashed black line. The average of this amplitude gradient across multiple samples (for CTRL: $n = 5$ and $N = 4$, for DAPT: $n = 9$ and $N = 6$) is marked with a solid cyan line. Time is indicated as mins elapsed from the start of the experiment. Pixel size is 1.38 μ m and cells have a diameter of around 10 μ m. Plot for DAPT is the same as that for the 170-min condition in Figure 4.4A. (B) Temporal evolution of the amplitude gradient as an overlay of the average amplitude gradient across multiple samples at different timepoints. Colors mark progression in time, from purple to yellow. Pixel size is 1.38 μ m and cells have a diameter of around 10 μ m. Plot for DAPT is the same as that for the 170-min condition in Figure 4.3B.

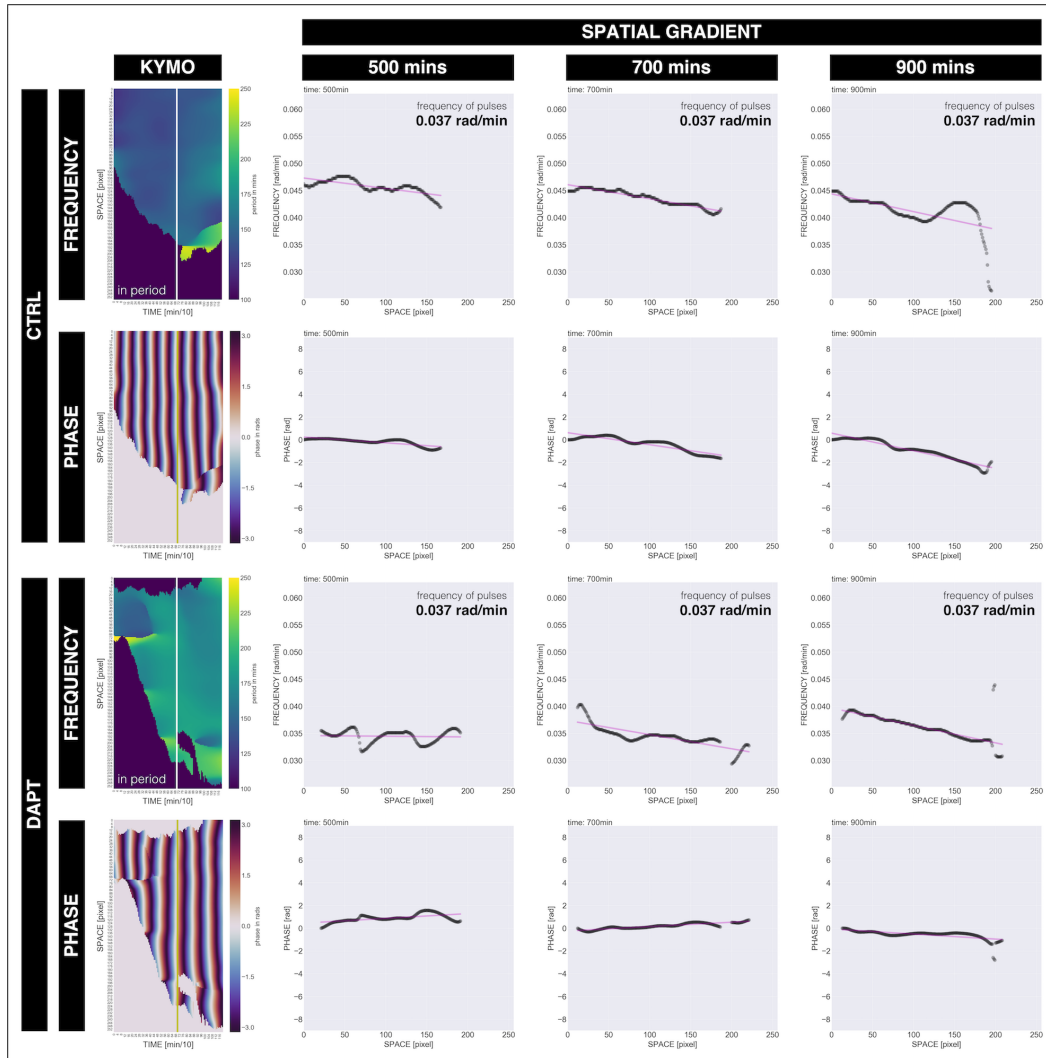


Figure 8.14 The frequency gradient precedes the phase gradient in samples entrained to 170-min periodic pulses of 2 μM DAPT. Spatial gradient in spreadout subjected to 170-min periodic pulses of 2 μM DAPT (or DMSO for control). Left: Kymographs plotting either the period or phase in space (y-axis) over time (x-axis). Center to periphery axis is from pixel 0 to pixel 256, from top to bottom of the kymograph. Kymographs include a line at time = 700 mins after the start of the experiment. Right: Spatial frequency gradient and spatial phase gradient at different timepoints. Center to periphery axis is from pixel 0 to pixel 256, from left to right of the spatial gradient plots. The faint magenta line denotes the linear fit to the experimental spatial gradient. Frequency of the DAPT (or DMSO) pulses is specified, and time is indicated as mins elapsed from the start of the experiment. Pixel size is 1.38 μm and cells have a diameter of around 10 μm .

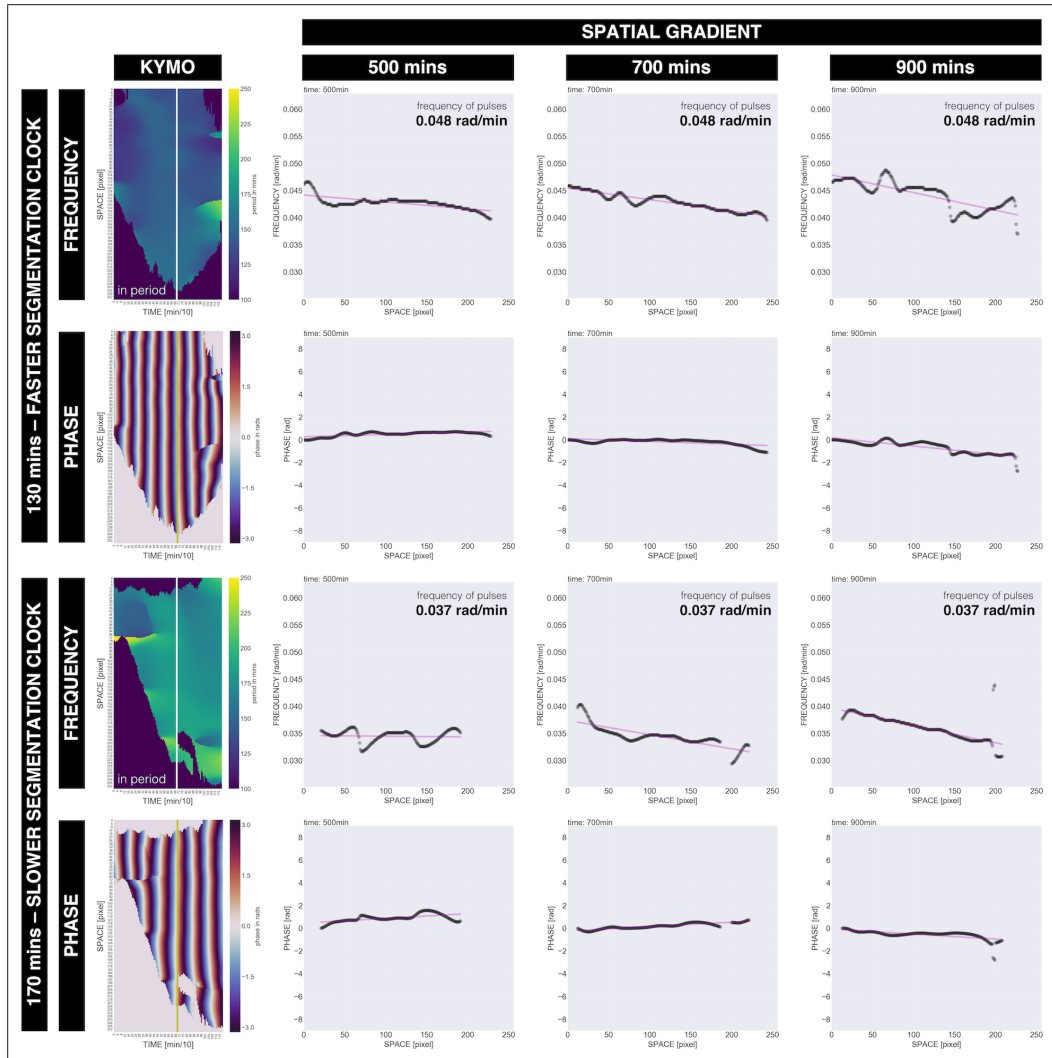


Figure 8.15 The frequency gradient precedes the phase gradient in samples entrained to periodic pulses of 2 μM DAPT. Spatial gradient in spreadout subjected to either 130-min or 170-min periodic pulses of 2 μM DAPT. Left: Kymographs plotting either the period or phase in space (y-axis) over time (x-axis). Center to periphery axis is from pixel 0 to pixel 256, from top to bottom of the kymograph. Kymographs include a line at time = 700 mins after the start of the experiment. Right: Spatial frequency gradient and spatial phase gradient at different timepoints. Center to periphery axis is from pixel 0 to pixel 256, from left to right of the spatial gradient plots. The faint magenta line denotes the linear fit to the experimental spatial gradient. Frequency of the DAPT pulses is specified, and time is indicated as mins elapsed from the start of the experiment. The plots for the 130-min condition are the same as those for the DAPT condition in Figure 4.5. The plots for the 170-min condition are the same as those for the DAPT condition in Figure 8.14. Pixel size is 1.38 μm and cells have a diameter of around 10 μm .

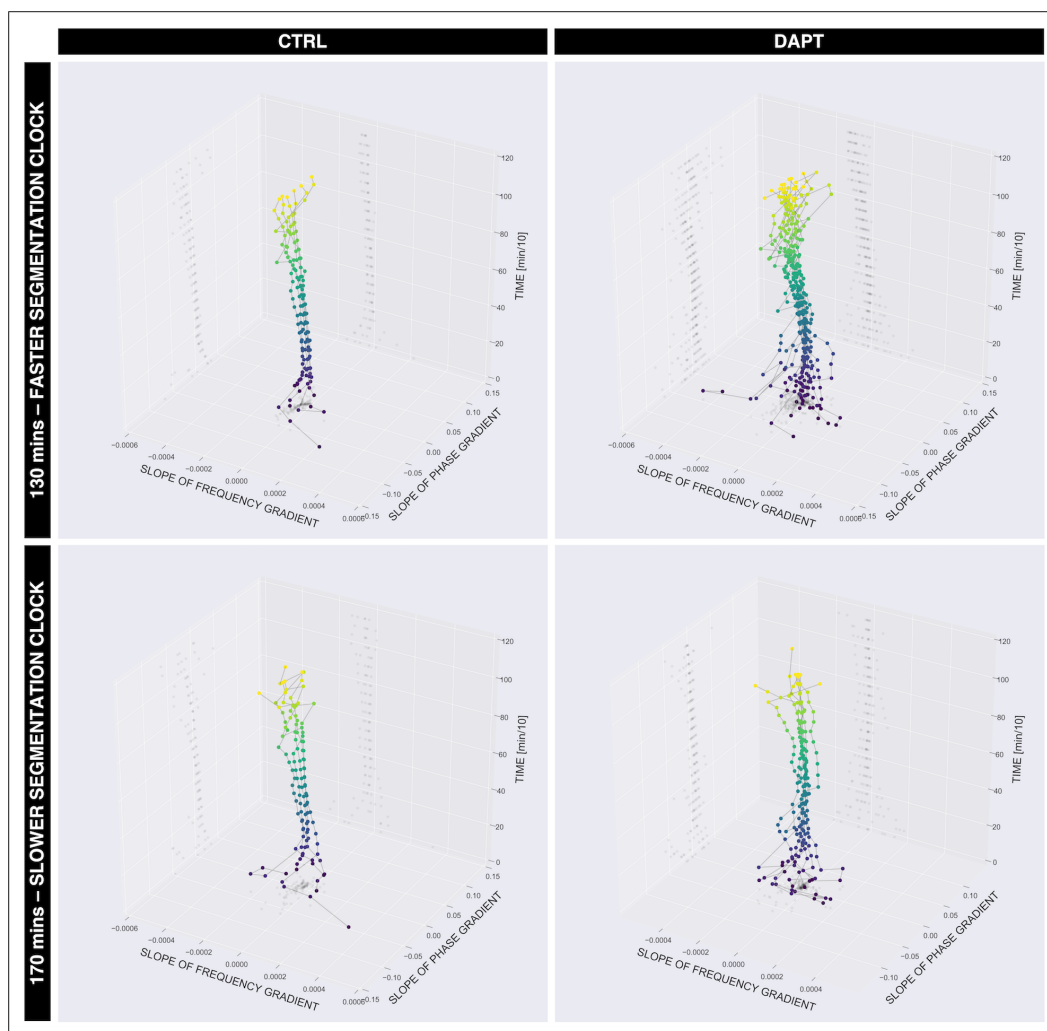


Figure 8.16 Entrainment of the segmentation clock to periodic pulses of 2 μM DAPT results in altered slopes of the frequency and phase gradients. 3D plot of the slope of frequency gradient, the slope of phase gradient, and time for spreadouts subjected to either 130-min or 170-min periodic pulses of 2 μM DAPT (or DMSO for controls). Plots include projections of (a) slope of frequency gradient versus time, (b) slope of phase gradient versus time, and (c) slope of frequency gradient versus slope of phase gradient. Colors mark progression in time, from purple to yellow. Pixel size is 1.38 μm and cells have a diameter of around 10 μm . **130-min**: (CTRL: $n = 6$ and $N = 5$) and (DAPT: $n = 15$ and $N = 7$), **170-min**: (CTRL: $n = 5$ and $N = 4$) and (DAPT: $n = 9$ and $N = 6$).

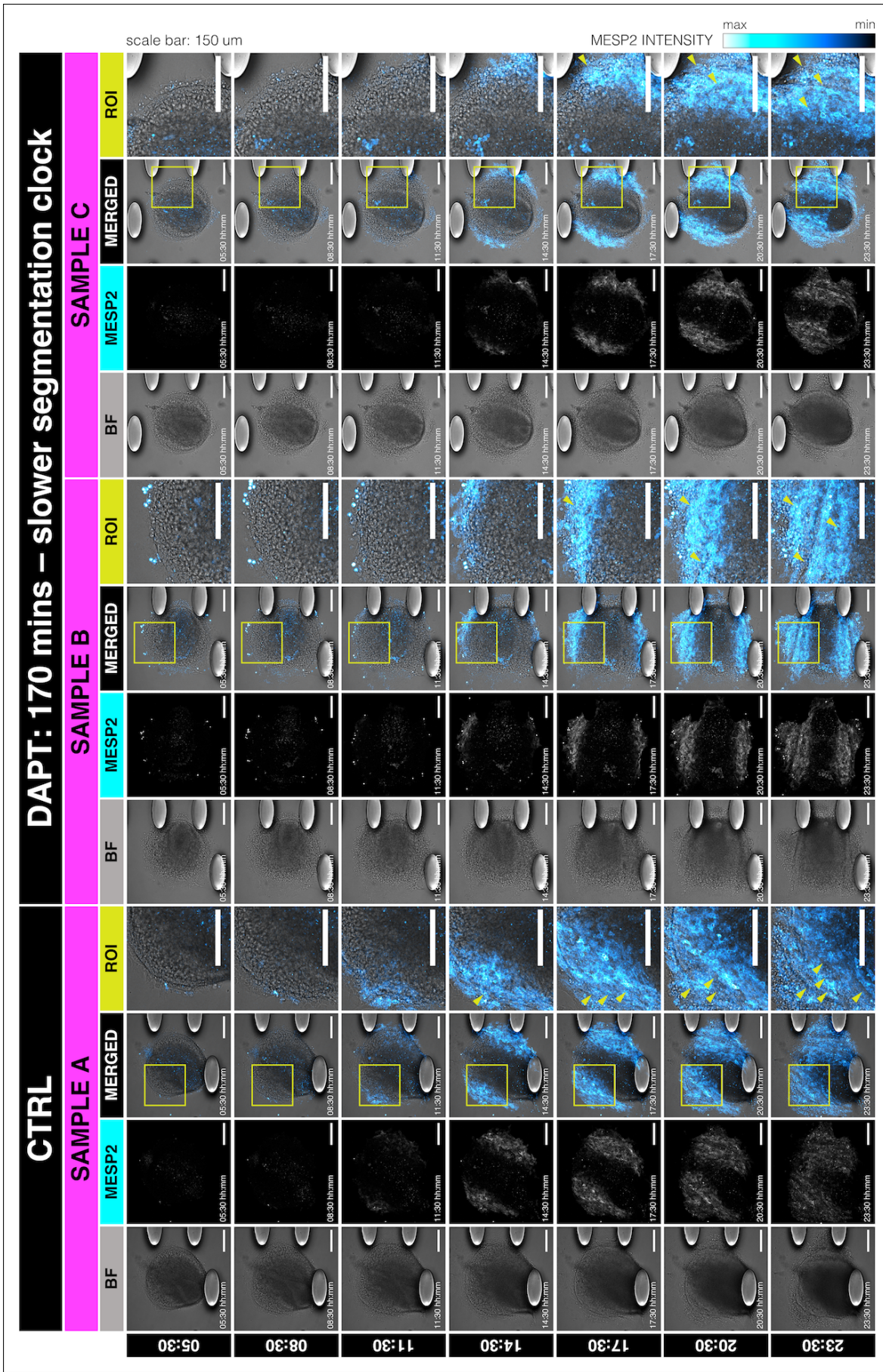


Figure 8.17 Spreadouts subjected to periodic pulses of 2 μ M DAPT show physical segment boundaries with polarized expression of *Mesp2*. Snapshots of timelapse imaging of spreadouts subjected to 170-min periodic pulses of 2 μ M DAPT (or DMSO for control). Shown are the brightfield channel, the *Mesp2*-GFP channel, and their merge. Also shown is a ROI in the merge of the two channels, with green arrowheads marking segment boundaries. Time is indicated as hh:mm elapsed from the start of the experiment.

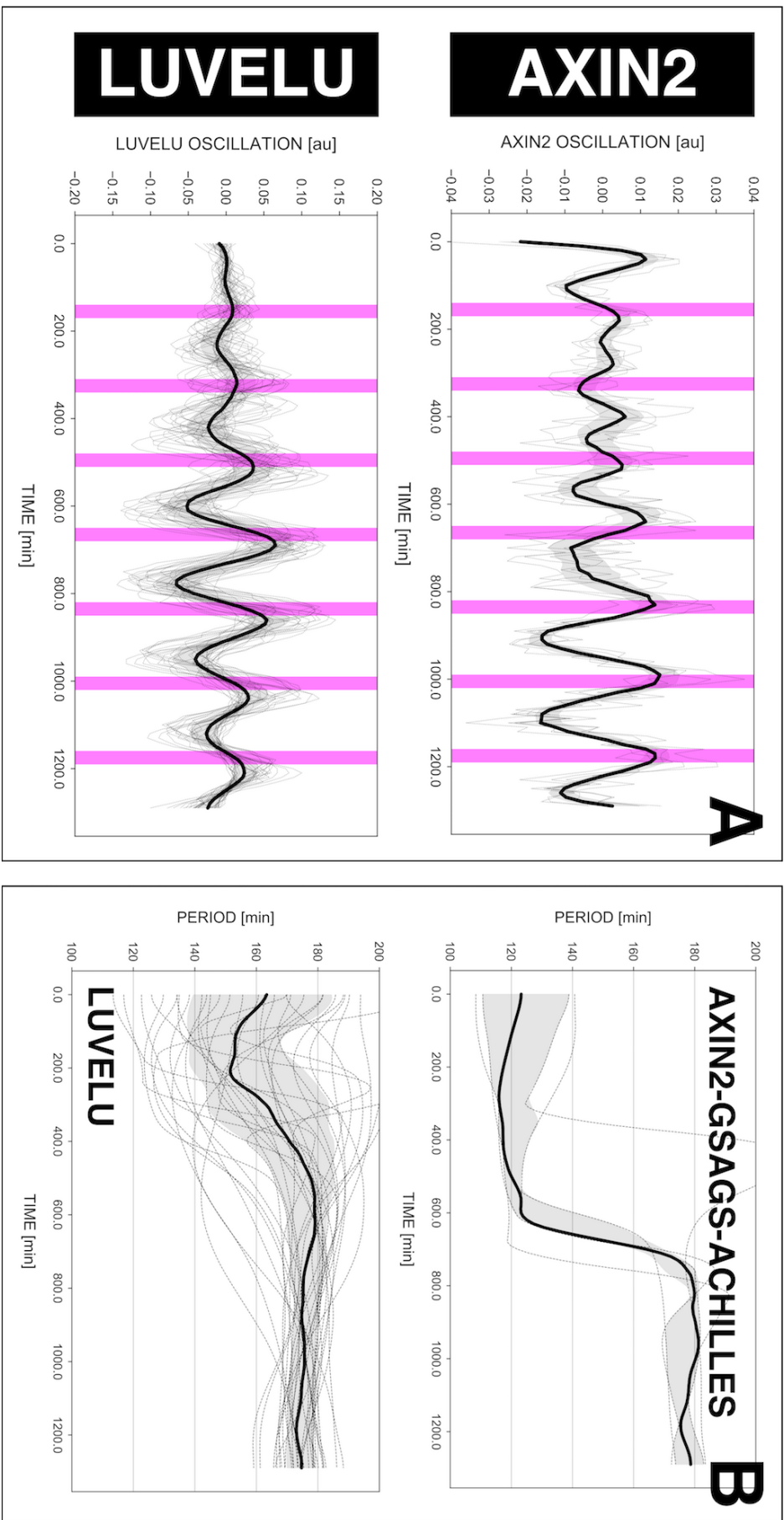


Figure 8.18 Tissue-level oscillations of Wnt signaling entrain to periodic pulses of DAPT later than tissue-level oscillations of Notch signaling. (A) Detrended timeseries of spreadouts expressing either Axin2-GSAGS-Achilles or LuVelu entrained to 170-min periodic pulses of 2 μ M DAPT. Periodic pulses are indicated as magenta bars and the timeseries of each sample (for AXIN2: $n = 5$ and $N = 1$, for LUVELU: $n = 34$ and $N = 8$) is marked with a dashed line. The median of the oscillations is represented here as a solid line, while the gray shaded area denotes the interquartile range. The plot for LuVelu is the same as that for the DAPT condition in Figure 3.2A. (B) Period evolution during entrainment, obtained from wavelet analysis. The period evolution for each sample and the median of the periods are represented here as a dashed line and a solid line, respectively. The gray shaded area corresponds to the interquartile range. The plot for LuVelu is the same as that for the DAPT condition in Figure 3.2B.

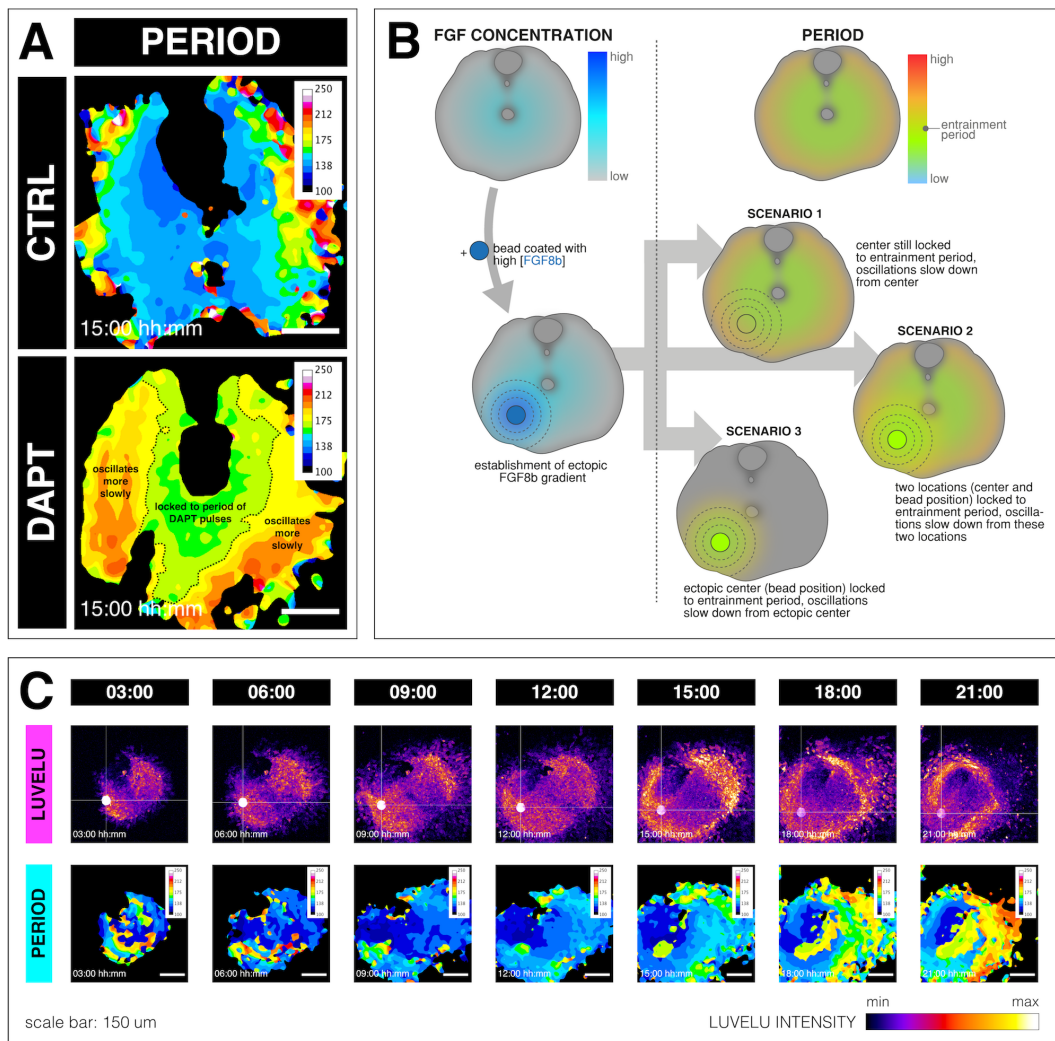


Figure 8.19 Oscillations locked to the periodic DAPT pulses are localized in region with high concentration of FGF. (A) Snapshot of period wavelet movie of spreadout subjected to 170-min periodic pulses of 2 μ M DAPT (or DMSO for control), taken 15 hours after the start of experiment. Samples are rotated so that the dorsal side is up. Region of oscillations locked to the periodic DAPT pulses and region of oscillations with period much slower than any oscillations in controls are highlighted. Scale bar: 150 μ m. (B) Top: Illustration of FGF gradient and emergent period gradient in a spreadout upon entrainment of the segmentation clock. Bottom: Illustration of spreadout embedded with bead coated with high concentration of FGF8b and possible outcomes after microfluidics-based entrainment. Illustration by Stefano Vianello. (C) Top: Snapshots of timelapse imaging of spreadout embedded with FGF-coated bead (white circle) and subjected to 170-min periodic pulses of 2 μ M DAPT. Time is indicated as hh:mm elapsed from the start of the experiment. Bead was soaked in 0.8 μ g/ μ L FGF8b overnight prior to embedding. Bottom: Snapshots of corresponding period wavelet movie of spreadout embedded with FGF-coated bead and subjected to 170-min periodic pulses of 2 μ M DAPT. Time is indicated as hh:mm elapsed from the start of the experiment. Experiments with FGF8b-coated bead ($n = 5$ and $N = 1$) were done and data were analyzed by Takehito Tomita.



Figure 8.20 Intact PSM subjected to periodic pulses of 2 μ M DAPT forms somites with polarized expression of *Tbx18* and *Uncx4.1*. In situ hybridization chain reaction (HCR) of tails of mouse embryos recovered after imaging and subjecting intact PSM (i.e. PSM and 2 somites) to 170-min periodic pulses of 2 μ M DAPT (or DMSO for controls). Samples were hybridized with probes against *Tbx6*, *Uncx4.1*, and *Tbx18* to mark the PSM, the posterior half of somites, and the anterior half of somites, respectively. Nuclei were stained with DAPI. White asterisks marks aberrant segment, while white arrowheads mark notably bigger somites. Culture times are indicated. Samples were squished on coverslip during imaging. Minimum and maximum intensity were set for each sample separately. Scale bar: 150 μ m.

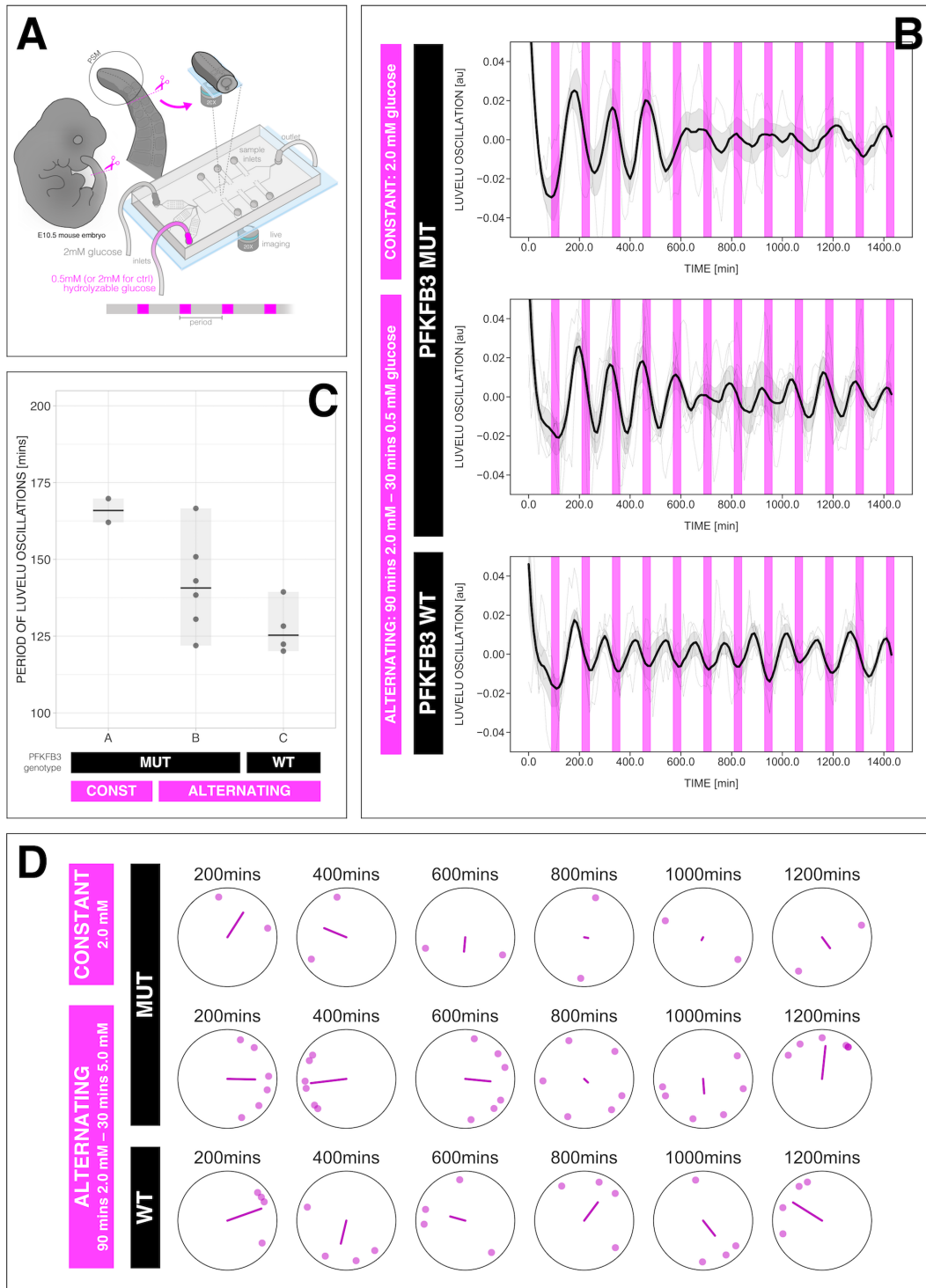


Figure 8.21 Segmentation clock in intact PSM adjusts to periodic perturbation of glycolytic flux. (A) Scheme of entrainment of segmentation clock in intact PSM to periodic perturbation of glycolytic flux (i.e. alternating concentrations of glucose). Illustration by Stefano Vianello. (B) Detrended timeseries of segmentation clock in intact PSM of mouse embryos having either the wild type (WT) or mutant form (MUT) of PFKFB3 subjected to 120-min periodic pulses of 0.5 mM glucose (or 2.0 mM glucose for constant glucose concentration control). Samples were cultured in 2.0 mM glucose in between pulses. Periodic pulses are indicated as magenta bars and the timeseries of each sample (for PFKFB3 MUT 2.0: $n = 2$ and $N = 1$, for PFKFB3 MUT 0.5: $n = 6$ and $N = 3$, for PFKFB3 WT 0.5: $n = 4$ and $N = 1$) is marked with a dashed line. The median of the oscillations is represented here as a solid line, while the gray shaded area denotes the interquartile range. (C) Mean period of the segmentation clock from 800 to 1000 mins after start of the experiment of samples in (B). Each sample is represented as a dot, while the median of all samples is denoted as a solid horizontal line. The gray shaded area denotes the range. (D) Polar plots at different timepoints showing phase of each sample and their first Kuramoto order parameter, represented as a magenta dot along the circumference of a circle and a magenta line segment at the circle's center, respectively. A longer line segment corresponds to a higher first Kuramoto order parameter, and thus to more coherent samples. The direction of the line denotes the vectorial average of the sample phases.

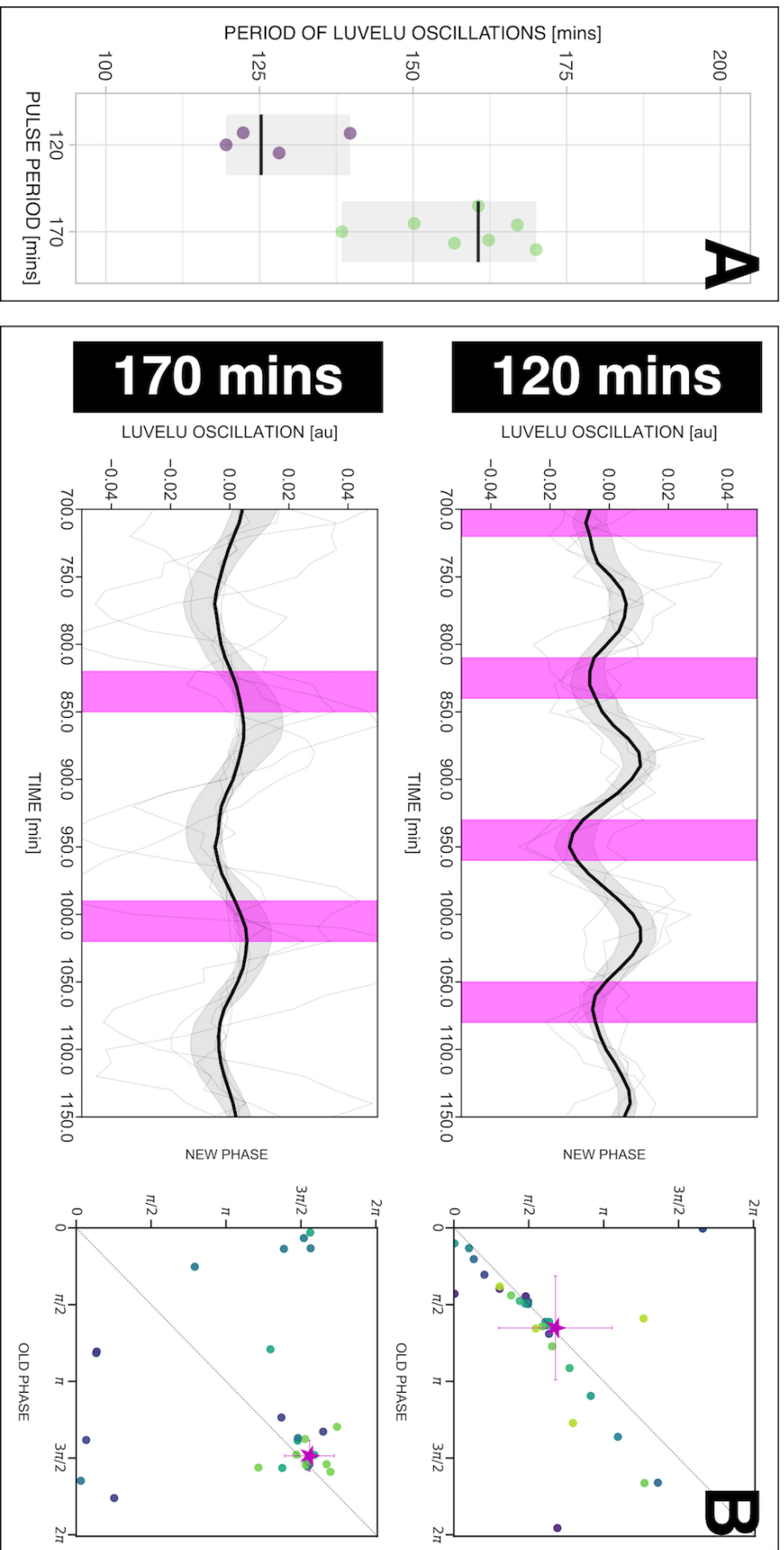


Figure 8.22 Phase and period of the segmentation clock in intact PSM is locked to the periodic perturbation of glycolytic flux. (A) Mean period of the segmentation clock from 800 to 1000 mins after start of the experiment of samples in (B). Each sample is represented as a dot, while the median of all samples is denoted as a solid horizontal line. The gray shaded area denotes the range. (B) Left: Detrended timeseries of segmentation clock in intact PSM of mouse embryos having wild type (WT) PPKFB3 subjected to either 120-min or 170-min periodic pulses of 0.5 mM glucose, zoomed in from 700 mins to 1150 mins. Samples were cultured in 2.0 mM glucose in between pulses. Periodic pulses are indicated as magenta bars and the timeseries of each sample (for 120-min: $n = 4$ and $N = 1$, for 170-min: $n = 7$ and $N = 1$) is marked with a dashed line. The median of the oscillations is represented here as a solid line, while the gray shaded area denotes the interquartile range. The full detrended timeseries for the 120-min condition can be seen in Figure 8.21B. Right: Stroboscopic maps of samples subjected to either 120-min or 170-min periodic pulses of 0.5 mM glucose. The localized region close to the diagonal in each map marks the entrainment phase for that detuning. This is highlighted with a magenta star, which corresponds to the centroid of the said region. The centroid (x_c, y_c) was calculated from the vectorial average of the phases of all samples at the end of the experiment, where x_c = vectorial average of old phase, y_c = vectorial average of new phase. The spread of the points in the region is reported in terms of the circular standard deviation ($\sqrt{-2/nR}$, where R is the first Kuramoto order parameter). Colors mark progression in time, from purple to yellow.

Bibliography

- Abe, Takaya, Hiroshi Kiyonari, Go Shioi, et al. (2011). “Establishment of conditional reporter mouse lines at ROSA26 locus for live cell imaging”. In: *genesis* 49.7, pp. 579–590. DOI: 10.1002/dvg.20753 (cit. on p. 107).
- Abraham, Ute, Adrián E Granada, Pål O Westermark, et al. (2010). “Coupling governs entrainment range of circadian clocks”. In: *Molecular Systems Biology* 6.1. DOI: 10.1038/msb.2010.92 (cit. on pp. 14, 29, 38, 49, 82).
- Anderson, P. W. (1972). “More Is Different”. In: *Science* 177.4047, pp. 393–396. DOI: 10.1126/science.177.4047.393 (cit. on pp. 4, 5).
- Arnol'd, Vladimir Igorevich and André Avez (1968). “Ergodic problems of classical mechanics”. In: (cit. on pp. 8, 59, 76).
- Aschoff, Jrgen and Hermann Pohl (1978). “Phase relations between a circadian rhythm and its zeitgeber within the range of entrainment”. In: *Naturwissenschaften* 65.2, pp. 80–84. DOI: 10.1007/BF00440545 (cit. on p. 13).
- Aulehla, A and R L Johnson (1999). “Dynamic expression of lunatic fringe suggests a link between notch signaling and an autonomous cellular oscillator driving somite segmentation.” In: *Developmental biology* 207.1, pp. 49–61. DOI: 10.1006/dbio.1998.9164 (cit. on p. 84).
- Aulehla, Alexander (2008). “About gradients and oscillations: the role of the Wnt-signaling pathway in somite formation during embryonic development”. PhD thesis (cit. on p. 99).
- Aulehla, Alexander and Olivier Pourquié (2010). “Signaling Gradients during Paraxial Mesoderm Development”. In: *Cold Spring Harbor Perspectives in Biology* 2.2, a000869. DOI: 10.1101/cshperspect.a000869 (cit. on p. 21).
- Aulehla, Alexander and Olivier Pourquié (2008). “Oscillating signaling pathways during embryonic development”. In: *Current Opinion in Cell Biology* 20.6, pp. 632–7. DOI: 10.1016/j.ceb.2008.09.002 (cit. on p. 21).
- Aulehla, Alexander, Christian Wehrle, Beate Brand-Saberi, et al. (2003). “Wnt3a plays a major role in the segmentation clock controlling somitogenesis.” In: *Developmental cell* 4.3, pp. 395–406. DOI: 10.1016/S1534-5807(03)00055-8 (cit. on pp. 21, 68, 72, 102).
- Aulehla, Alexander, Winfried Wiegraebe, Valerie Baubet, et al. (2007). “A beta-catenin gradient links the clock and wavefront systems in mouse embryo segmentation”. In: *Nature Cell Biology* 10.2, pp. 186–93. DOI: 10.1038/ncb1679 (cit. on pp. 21, 26, 32, 44, 48, 50, 72, 75, 83, 100, 102, 107).

- Baas, Nils Andreas and Claus Emmeche (1997). "On emergence and explanation". In: *Intellectica* 25.2, pp. 67–83 (cit. on p. 2).
- Bagheri, Neda, Jörg Stelling, and Francis J Doyle III (2008). "Circadian phase resetting via single and multiple control targets". In: *PLoS Comput Biol* 4.7, e1000104. DOI: 10.1371/journal.pcbi.1000104 (cit. on p. 14).
- Balanov, Alexander, Natalia Janson, Dmitry Postnov, and Olga Sosnovtseva (2008). *Synchronization: from simple to complex*. Springer Science & Business Media (cit. on pp. 7, 8, 10, 11, 38, 41, 54, 132).
- Belousov, BP (1959). "Sbornik Referatov po Radiacioni Medicine". In: *1958 Meeting*. Vol. 145 (cit. on p. 10).
- Bialek, William (2015). "Perspectives on theory at the interface of physics and biology". In: *arXiv*. _eprint: 1512.08954 (cit. on p. 5).
- Bordyugov, Grigory, Ute Abraham, Adrian Granada, et al. (2015). "Tuning the phase of circadian entrainment". In: *Journal of The Royal Society Interface* 12.108, p. 20150282. DOI: 10.1098/rsif.2015.0282 (cit. on pp. 12, 13, 29, 38, 40, 41, 48).
- Brown Jr, Frank A, H Marguerite Webb, and Miriam F Bennett (1955). "Proof for an endogenous component in persistent solar and lunar rhythmicity in organisms". In: *Proceedings of the National Academy of Sciences of the United States of America* 41.2, p. 93. DOI: 10.1073/pnas.41.2.93 (cit. on p. 12).
- Browne, William E, Alivia L Price, Matthias Gerberding, and Nipam H Patel (2005). "Stages of embryonic development in the amphipod crustacean, *Parhyale hawaiensis*". In: *genesis* 42.3, pp. 124–149. DOI: 10.1002/gene.20145 (cit. on p. 17).
- Brustis, JJ (1976). "Organisation et differenciation du mesoderme somitique cultive en presence des tissus adjacents (corde, tube nerveux, ectoderme, endoderme) chez les anoures." In: *Comptes rendus des seances de l'Academie des Sciences* 283.10, pp. 379–382 (cit. on p. 26).
- Buchholz, F, A Freund, and FW Schneider (1985). "Periodic perturbation of the BZ-reaction in a CSTR: chemical resonance, entrainment and quasi-periodic behavior". In: *Temporal Order*. Springer, pp. 116–121. DOI: 10.1007/978-3-642-70332-4_16 (cit. on p. 10).
- Buck, J (1988). "Synchronous rhythmic flashing of fireflies. II." In: *The Quarterly review of biology* 63.3, pp. 265–89 (cit. on p. 1).
- Buck, J and E Buck (1968). "Mechanism of rhythmic synchronous flashing of fireflies. Fireflies of Southeast Asia may use anticipatory time-measuring in synchronizing their flashing." In: *Science (New York, N.Y.)* 159.3821, pp. 1319–27 (cit. on pp. 1, 29).
- Burke, Ann C, Craig E Nelson, Bruce A Morgan, and Cliff Tabin (1995). "Hox genes and the evolution of vertebrate axial morphology". In: *Development* 121.2, pp. 333–346 (cit. on p. 17).
- Butcher, Earl O (1929). "The development of the somites in the white rat (*Mus norvegicus albinus*) and the fate of the myotomes, neural tube, and gut in the tail". In: *American Journal of Anatomy* 44.3, pp. 381–439. DOI: 10.1002/aja.1000440303 (cit. on p. 18).
- Camazine, Scott, Jean-Louis Deneubourg, Nigel R Franks, et al. (2003). *Self-organization in biological systems*. Princeton university press (cit. on p. 2).

- Carrieri, Francesca Anna, Philip J Murray, Dimitrinka Ditsova, et al. (2019). “CDK 1 and CDK 2 regulate NICD 1 turnover and the periodicity of the segmentation clock”. In: *EMBO reports* 20.7, e46436. DOI: 10.15252/embr.201846436 (cit. on p. 53).
- Chal, Jérôme, Masayuki Oginuma, Ziad Al Tanoury, et al. (2015). “Differentiation of pluripotent stem cells to muscle fiber to model Duchenne muscular dystrophy”. In: *Nature Biotechnology* 33.9, pp. 962–969. DOI: 10.1038/nbt.3297 (cit. on p. 26).
- Chapman, Deborah L, Irina Agulnik, Sarah Hancock, Lee M Silver, and Virginia E Papaioannou (1996). “Tbx6, a mouse T-Box gene implicated in paraxial mesoderm formation at gastrulation”. In: *Developmental biology* 180.2, pp. 534–542. DOI: 10.1006/dbio.1996.0326 (cit. on p. 92).
- Choi, Harry MT, Colby R Calvert, Naeem Husain, et al. (2016). “Mapping a multiplexed zoo of mRNA expression”. In: *Development* 143.19, pp. 3632–3637. DOI: 10.1242/dev.140137 (cit. on pp. 92, 115).
- Choi, Harry MT, Maayan Schwarzkopf, Mark E Fornace, et al. (2018). “Third-generation in situ hybridization chain reaction: multiplexed, quantitative, sensitive, versatile, robust”. In: *Development* 145.12. DOI: 10.1242/dev.165753 (cit. on pp. 92, 115).
- Chu, Li-Fang, Daniel Mamott, Zijian Ni, et al. (2019a). “An In Vitro Human Segmentation Clock Model Derived from Embryonic Stem Cells”. In: *Cell Reports* 28.9, 2247–2255.e5. DOI: 10.1016/j.celrep.2019.07.090 (cit. on p. 26).
- Chu, Li-Fang, Daniel Mamott, Zijian Ni, et al. (2019b). “An in vitro human segmentation clock model derived from embryonic stem cells”. In: *Cell reports* 28.9, pp. 2247–2255. DOI: 10.1016/j.celrep.2019.07.090 (cit. on p. 54).
- Clark, Erik (2020). “Time and Space in Segmentation”. In: *bioRxiv*. DOI: 10.1101/2020.09.12.294611 (cit. on p. 51).
- Cole, Susan E, John M Levorse, Shirley M Tilghman, and Thomas F Vogt (2002). “Clock regulatory elements control cyclic expression of Lunatic fringe during somitogenesis”. In: *Developmental cell* 3.1, pp. 75–84. DOI: 10.1016/s1534-5807(02)00212-5 (cit. on pp. 32, 48, 107).
- Cooke, J (1975). “Control of somite number during morphogenesis of a vertebrate, *Xenopus laevis*.” In: *Nature* 254.5497, pp. 196–9 (cit. on pp. 18, 19).
- Cooke, J and E.C. Zeeman (1976). “A clock and wavefront model for control of the number of repeated structures during animal morphogenesis”. In: *Journal of Theoretical Biology* 58.2, pp. 455–476. DOI: 10.1016/S0022-5193(76)80131-2 (cit. on pp. 19, 20, 77, 87, 100).
- Cooke, Jonathan (1998). “A gene that resuscitates a theory—somitogenesis and a molecular oscillator”. In: *Trends in Genetics* 14.3, pp. 85–88. DOI: 10.1016/S0168-9525(98)01396-1 (cit. on p. 99).
- Criswell, Katharine E and J Andrew Gillis (2020). “Resegmentation is an ancestral feature of the gnathostome vertebral skeleton”. In: *Elife* 9, e51696. DOI: 10.7554/eLife.51696 (cit. on p. 18).
- Cross, Frederick R and Eric D Siggia (2005). “Mode locking the cell cycle”. In: *Physical Review E* 72.2, p. 021910. DOI: 10.1103/PhysRevE.72.021910 (cit. on pp. 38, 52, 132).

- Cumming, Bruce G and Edger Wagner (1968). “Rhythmic processes in plants”. In: *Annual Review of Plant Physiology* 19.1, pp. 381–416. DOI: 10.1146/annurev.pp.19.060168.002121 (cit. on p. 12).
- Davis, Gregory K and Nipam H Patel (1999). “The origin and evolution of segmentation”. In: *Trends in Genetics* 15.12, pp. M68–M72. DOI: 10.1016/S0168-9525(99)01875-2 (cit. on p. 17).
- Dekkers, Johanna F, Maria Alieva, Lianne M Wellens, et al. (2019). “High-resolution 3D imaging of fixed and cleared organoids”. In: *Nature protocols* 14.6, p. 1756. DOI: 10.1038/s41596-019-0160-8 (cit. on p. 117).
- Dequéant, Mary-Lee, Earl Glynn, Karin Gaudenz, et al. (2006). “A Complex Oscillating Network of Signaling Genes Underlies the Mouse Segmentation Clock”. In: *Science* 314.5805, pp. 1595–1598. DOI: 10.1126/science.1133141 (cit. on pp. 21, 22, 26, 72, 102).
- Dequéant, Mary-Lee and Olivier Pourquié (2008). “Segmental patterning of the vertebrate embryonic axis”. In: *Nature Reviews Genetics* 9.5, pp. 370–382. DOI: 10.1038/nrg2320 (cit. on pp. 1, 21, 72, 102).
- Detwiler, SR (1934). “An experimental study of spinal nerve segmentation in *Amblystoma* with reference to the plurisegmental contribution to the brachial plexus”. In: *Journal of Experimental Zoology* 67.3, pp. 395–441. DOI: 10.1002/jez.1400670303 (cit. on p. 18).
- Detwiler, SR (1935). “The development of spinal ganglia following transplantation of the spinal cord with or without somites”. In: *The Anatomical Record* 61.4, pp. 441–455. DOI: 10.1002/ar.1090610407 (cit. on p. 18).
- Diaz-Cuadros, Margarete, Daniel E Wagner, Christoph Budjan, et al. (2020). “In vitro characterization of the human segmentation clock”. In: *Nature* 580.7801, pp. 113–118. DOI: 10.1038/s41586-019-1885-9 (cit. on pp. 21, 26, 54, 80).
- Echelard, Yann, Douglas J Epstein, Benoit St-Jacques, et al. (1993). “Sonic hedgehog, a member of a family of putative signaling molecules, is implicated in the regulation of CNS polarity”. In: *Cell* 75.7, pp. 1417–1430. DOI: 10.1016/0092-8674(93)90627-3 (cit. on p. 111).
- Ermentrout, B, J Flores, and A Gelperin (1998). “Minimal model of oscillations and waves in the *Limax* olfactory lobe with tests of the model’s predictive power.” In: *Journal of neurophysiology* 79.5, pp. 2677–89 (cit. on p. 81).
- Evrard, Yvonne A., Yi Lun, Alexander Aulehla, Lin Gan, and Randy L. Johnson (1998). “lunatic fringe is an essential mediator of somite segmentation and patterning”. In: *Nature* 394.6691, p. 28632. DOI: 10.1038/28632 (cit. on pp. 24, 84).
- Falk, Henning Johannes (2019). “Imaging the onset of the segmentation clock during mouse gastrulation”. PhD thesis. DOI: 10.11588/heidok.00024446 (cit. on pp. 24, 28, 44, 76, 102).
- Faraday, Michael (1831). “XVII. On a peculiar class of acoustical figures; and on certain forms assumed by groups of particles upon vibrating elastic surfaces”. In: *Philosophical transactions of the Royal Society of London* 121, pp. 299–340. DOI: 10.1098/rstl.1831.0018 (cit. on p. 48).

- Feller, Juliane, Andre Schneider, Karin Schuster-Gossler, and Achim Gossler (2008). “Non-cyclic Notch activity in the presomitic mesoderm demonstrates uncoupling of somite compartmentalization and boundary formation”. In: *Genes & Development* 22.16, pp. 2166–2171. DOI: 10.1101/gad.480408 (cit. on p. 96).
- Geling, Andrea, Harald Steiner, Michael Willem, Laure Bally-Cuif, and Christian Haass (2002). “A γ -secretase inhibitor blocks Notch signaling in vivo and causes a severe neurogenic phenotype in zebrafish”. In: *EMBO reports* 3.7, pp. 688–694. DOI: 10.1093/embo-reports/kvf124 (cit. on p. 53).
- Geyer, Delphine, David Martin, Julien Tailleur, and Denis Bartolo (2019). “Freezing a flock: Motility-induced phase separation in polar active liquids”. In: *Physical Review X* 9.3, p. 031043. DOI: 10.1103/PhysRevX.9.031043 (cit. on p. 5).
- Gillis, Freya I and J Andrew Gillis (2020). In: *The Bulletin of the Amateur Entomologists’ Society* 79.537, pp. 95–105 (cit. on p. 12).
- Glass, Leon and Michael C Mackey (1988). *From clocks to chaos: The rhythms of life*. Princeton University Press (cit. on p. 13).
- Goedhart, Joachim (2020). “PlotTwist: A web app for plotting and annotating continuous data”. In: *PLoS biology* 18.1, e3000581. DOI: 10.1371/journal.pbio.3000581 (cit. on p. 132).
- Gomez, Céline, Ertuğrul M. Özbudak, Joshua Wunderlich, et al. (2008). “Control of segment number in vertebrate embryos”. In: *Nature* 454.7202, p. 335. DOI: 10.1038/nature07020 (cit. on p. 48).
- Goodwin, Brian C. and Morrel H. Cohen (1969). “A phase-shift model for the spatial and temporal organization of developing systems”. In: *Journal of Theoretical Biology* 25.1, pp. 49–107. DOI: 10.1016/S0022-5193(69)80017-2 (cit. on pp. 19, 20, 80, 87, 100).
- Goodwin, Brian C et al. (1963). “Temporal organization in cells. A dynamic theory of cellular control processes.” In: *Temporal organization in cells. A dynamic theory of cellular control processes*. DOI: 10.5962/bhl.title.6268 (cit. on p. 21).
- Granada, A, R M Hennig, B Ronacher, A Kramer, and H Herzel (2009). “Phase response curves elucidating the dynamics of coupled oscillators.” In: *Methods in enzymology* 454, pp. 1–27. DOI: 10.1016/S0076-6879(08)03801-9 (cit. on p. 38).
- Granada, Adrián E, Grigory Bordyugov, Achim Kramer, and Hanspeter Herzel (2013). “Human Chronotypes from a Theoretical Perspective”. In: *PLoS ONE* 8.3, e59464. DOI: 10.1371/journal.pone.0059464 (cit. on pp. 13–15, 40, 41, 47, 48, 51, 52).
- Granada, Adrián E and Hanspeter Herzel (2009). “How to Achieve Fast Entrainment? The Timescale to Synchronization”. In: *PLoS ONE* 4.9, e7057. DOI: 10.1371/journal.pone.0007057 (cit. on p. 14).
- Haan, Jos de (2006). “How emergence arises”. In: *Ecological complexity* 3.4, pp. 293–301. DOI: 10.1016/j.ecocom.2007.02.003 (cit. on p. 2).
- Hannibal, Roberta L and Nipam H Patel (2013). “What is a segment?” In: *EvoDevo* 4.1, p. 35. DOI: 10.1186/2041-9139-4-35 (cit. on pp. 17, 92, 96).
- Harker, Janet E (1956). “Factors controlling the diurnal rhythm of activity of *Periplaneta americana* L”. In: *Journal of Experimental Biology* 33.1, pp. 224–234 (cit. on p. 12).

- Harris, Charles R., K. Jarrod Millman, Stéfan J. van der Walt, et al. (Sept. 2020). “Array programming with NumPy”. In: *Nature* 585.7825, pp. 357–362. DOI: 10.1038/s41586-020-2649-2 (cit. on p. 134).
- Haupaix, Nicolas, Camille Curantz, Richard Bailleul, et al. (2018). “The periodic coloration in birds forms through a prepattern of somite origin”. In: *Science* 361.6408. DOI: 10.1126/science.aar4777 (cit. on p. 18).
- Heltberg, Mathias, Ryan A Kellogg, Sandeep Krishna, Savaş Tay, and Mogens H Jensen (2016). “Noise Induces Hopping between NF-κB Entrainment Modes”. In: *Cell Systems* 3.6, 532–539.e3. DOI: 10.1016/j.cels.2016.11.014 (cit. on p. 16).
- Herrgen, Leah, Saúl Ares, Luis G Morelli, et al. (2010). “Intercellular Coupling Regulates the Period of the Segmentation Clock”. In: *Current Biology* 20.14, pp. 1244–1253. DOI: 10.1016/j.cub.2010.06.034 (cit. on pp. 21, 24, 47, 48, 75, 79, 82).
- Ho, Christine (2020). “Collective synchronization of coupled self-organizing mouse embryonic oscillators”. PhD thesis. DOI: 10.11588/heidok.00027590 (cit. on pp. 26, 28, 84).
- Huang, Tan-Chi and Nathanaël Grobelaar (1995). “The circadian clock in the prokaryote *Synechococcus* RF-1”. In: *Microbiology* 141.3, pp. 535–540. DOI: 10.1099/13500872-141-3-535 (cit. on p. 12).
- Huang, Yu-Wen and Chih-Yen King (2020). “A complete catalog of wild-type Sup35 prion variants and their protein-only propagation”. In: *Current Genetics* 66.1, pp. 97–122. DOI: 10.1007/s00294-019-01003-8 (cit. on p. 5).
- Hubaud, Alexis and Olivier Pourquié (2014). “Signalling dynamics in vertebrate segmentation”. In: *Nature Reviews Molecular Cell Biology* 15.11, pp. 709–721. DOI: 10.1038/nrm3891 (cit. on pp. 1, 16, 21, 22, 72, 102).
- Hubaud, Alexis, Ido Regev, L Mahadevan, and Olivier Pourquié (2017). “Excitable Dynamics and Yap-Dependent Mechanical Cues Drive the Segmentation Clock”. In: *Cell* 171.3, 668–682.e11. DOI: 10.1016/j.cell.2017.08.043 (cit. on pp. 21, 26, 54, 79).
- Hunter, John D (2007). “Matplotlib: A 2D graphics environment”. In: *Computing in science & engineering* 9.3, pp. 90–95. DOI: 10.1109/MCSE.2007.55 (cit. on p. 134).
- Ishimatsu, Kana, Tom W. Hiscock, Zach M. Collins, et al. (2018). “Size-reduced embryos reveal a gradient scaling based mechanism for zebrafish somite formation”. In: *Development*, dev.161257. DOI: 10.1242/dev.161257 (cit. on p. 18).
- Isomura, Akihiro, Fumiko Ogushi, Hiroshi Kori, and Ryoichiro Kageyama (2017). “Optogenetic perturbation and bioluminescence imaging to analyze cell-to-cell transfer of oscillatory information”. In: *Genes & development* 31.5, pp. 524–535. DOI: 10.1101/gad.294546.116 (cit. on pp. 16, 29, 38, 50, 52, 102, 132).
- Itō, Akira (1979). “Perturbation theory of self-oscillating system with a periodic perturbation”. In: *Progress of Theoretical Physics* 61.1, pp. 45–53. DOI: 10.1143/PTP.61.45 (cit. on p. 10).
- Izhikevich, Eugene M (2007). *Dynamical systems in neuroscience*. MIT press (cit. on pp. 13, 38, 52).

- Izquierdo, Emiliano, Theresa Quinkler, and Stefano De Renzis (2018). “Guided morphogenesis through optogenetic activation of Rho signalling during early *Drosophila* embryogenesis”. In: *Nature Communications* 9.1, p. 2366. DOI: 10.1038/s41467-018-04754-z (cit. on p. 50).
- Jacob, François (1977). “Evolution and tinkering”. In: *Science* 196.4295, pp. 1161–1166. DOI: 10.1126/science.860134 (cit. on pp. 4, 5).
- Jiang, Di, Edwin M Munro, and William C Smith (2005). “Ascidian prickle regulates both mediolateral and anterior-posterior cell polarity of notochord cells”. In: *Current Biology* 15.1, pp. 79–85. DOI: 10.1016/j.cub.2004.12.041 (cit. on p. 17).
- Johnson, Carl Hirschie (1999). “Forty years of PRCs-what have we learned?” In: *Chronobiology international* 16.6, pp. 711–743. DOI: 10.3109/07420529909016940 (cit. on pp. 13, 52).
- Kai, Tohru and Kazuhisa Tomita (1979). “Stroboscopic phase portrait of a forced nonlinear oscillator”. In: *Progress of Theoretical Physics* 61.1, pp. 54–73. DOI: 10.1143/PTP.61.54 (cit. on p. 10).
- Kalmus, Hans (1940). “New research in the diurnal periodicity of animals”. In: *Acta Medica Scandinavica* 103.S108, pp. 227–233. DOI: 10.1111/j.0954-6820.1940.tb11096.x (cit. on p. 38).
- Keller, RE, Michael Danilchik, Robert Gimlich, and John Shih (1985). “The function and mechanism of convergent extension during gastrulation of *Xenopus laevis*”. In: *Development* 89.Supplement, pp. 185–209 (cit. on p. 26).
- Kellogg, Ryan A and Savaş Tay (2015). “Noise Facilitates Transcriptional Control under Dynamic Inputs”. In: *Cell* 160.3, pp. 381–392. DOI: 10.1016/j.cell.2015.01.013 (cit. on pp. 16, 29).
- King, Chih-Yen (2001). “Supporting the structural basis of prion strains: induction and identification of [PSI] variants”. In: *Journal of molecular biology* 307.5, pp. 1247–1260. DOI: 10.1006/jmbi.2001.4542 (cit. on p. 5).
- Kopan, Raphael and Maria G Ilagan (2009). “The canonical Notch signaling pathway: unfolding the activation mechanism.” In: *Cell* 137.2, pp. 216–33. DOI: 10.1016/j.cell.2009.03.045 (cit. on p. 148).
- Kraus, Florian, Bénédicte Haenig, and Andreas Kispert (2001). “Cloning and expression analysis of the mouse T-box gene *Tbx18*”. In: *Mechanisms of development* 100.1, pp. 83–86. DOI: 10.1016/S0925-4773(00)00494-9 (cit. on pp. 92, 96).
- Krueger, Daniel, Emiliano Izquierdo, Ranjith Viswanathan, et al. (2019). “Principles and applications of optogenetics in developmental biology”. In: *Development* 146.20, dev175067. DOI: 10.1242/dev.175067 (cit. on p. 50).
- Lauschke, Volker M, Charisios D Tsiairis, Paul François, and Alexander Aulehla (2012). “Scaling of embryonic patterning based on phase-gradient encoding”. In: *Nature* 493.7430, p. 101. DOI: 10.1038/nature11804 (cit. on pp. 24, 25, 28, 31, 32, 44, 50, 62, 67, 75, 76, 80, 81, 87, 99).
- Lefever, René (1968). “Dissipative structures in chemical systems”. In: *The journal of chemical physics* 49.11, pp. 4977–4978. DOI: 10.1063/1.1669986 (cit. on p. 10).

- Lefever, René and Grégoire Nicolis (1971). “Chemical instabilities and sustained oscillations”. In: *Journal of theoretical Biology* 30.2, pp. 267–284. DOI: 10.1016/0022-5193(71)90054-3 (cit. on p. 10).
- Lewis, Julian (2003). “Autoinhibition with Transcriptional Delay A Simple Mechanism for the Zebrafish Somitogenesis Oscillator”. In: *Current Biology* 13.16, pp. 1398–1408. DOI: 10.1016/S0960-9822(03)00534-7 (cit. on pp. 21, 103).
- Liao, Bo-Kai, David J Jörg, and Andrew C Oates (2016). “Faster embryonic segmentation through elevated Delta-Notch signalling”. In: *Nature Communications* 7, p. 11861. DOI: 10.1038/ncomms11861 (cit. on p. 47).
- Liao, Bo-Kai and Andrew C Oates (2017). “Delta-Notch signalling in segmentation”. In: *Arthropod Structure & Development* 46.3, pp. 429–447. DOI: 10.1016/j.asd.2016.11.007 (cit. on pp. 24, 75, 79).
- Liu, Andrew C, David K Welsh, Caroline H Ko, et al. (2007). “Intercellular coupling confers robustness against mutations in the SCN circadian clock network”. In: *Cell* 129.3, pp. 605–616. DOI: 10.1016/j.cell.2007.02.047 (cit. on p. 14).
- Lucchetta, Elena M, Ji Lee, Lydia A Fu, Nipam H Patel, and Rustem F Ismagilov (2005). “Dynamics of Drosophila embryonic patterning network perturbed in space and time using microfluidics”. In: *Nature* 434.7037, pp. 1134–1138. DOI: 10.1038/nature03509 (cit. on p. 102).
- Makki, Rabih, Alberto P Muñuzuri, and Juan Perez-Mercader (2014). “Periodic perturbation of chemical oscillators: Entrainment and induced synchronization”. In: *Chemistry–A European Journal* 20.44, pp. 14213–14217. DOI: 10.1002/chem.201403647 (cit. on p. 10).
- Manson, Steven M (2001). “Simplifying complexity: a review of complexity theory”. In: *Geoforum* 32.3, pp. 405–414. DOI: 10.1016/S0016-7185(00)00035-X (cit. on p. 2).
- Mansouri, Ahmed, Yoshifumi Yokota, Roland Wehr, et al. (1997). “Paired-related murine homeobox gene expressed in the developing sclerotome, kidney, and nervous system”. In: *Developmental dynamics: an official publication of the American Association of Anatomists* 210.1, pp. 53–65. DOI: 10.1002/(SICI)1097-0177(199709)210:1<53::AID-AJA6>3.0.CO;2-0 (cit. on p. 111).
- Maroto, Miguel, Kim J Dale, Mary-Lee Dequéant, Anne-Cécile Petit, and Olivier Pourquié (2005). “Synchronised cycling gene oscillations in presomitic mesoderm cells require cell-cell contact.” In: *The International journal of developmental biology* 49.2-3, pp. 309–15. DOI: 10.1387/ijdb.041958mm (cit. on pp. 26, 48).
- Marr, David and Tomaso Poggio (1976). “From understanding computation to understanding neural circuitry”. In: (cit. on p. 4).
- Masamizu, Yoshito, Toshiyuki Ohtsuka, Yoshiki Takashima, et al. (2006). “Real-time imaging of the somite segmentation clock: revelation of unstable oscillators in the individual presomitic mesoderm cells.” In: *Proceedings of the National Academy of Sciences of the United States of America* 103.5, pp. 1313–8. DOI: 10.1073/pnas.0508658103 (cit. on pp. 21, 26, 44, 48, 75, 83).
- Matsuda, Mitsuhiko, Yoshihiro Yamanaka, Maya Uemura, et al. (2020). “Recapitulating the human segmentation clock with pluripotent stem cells”. In: *Nature* 580.7801, pp. 124–129. DOI: 10.1038/s41586-020-2144-9 (cit. on pp. 21, 54).

- Matsumiya, Marina, Takehito Tomita, Kumiko Yoshioka-Kobayashi, Akihiro Isomura, and Ryoichiro Kageyama (2018). “ES cell-derived presomitic mesoderm-like tissues for analysis of synchronized oscillations in the segmentation clock”. In: *Development* 145.4. DOI: 10.1242/dev.156836 (cit. on pp. 26, 54).
- Mazzocchi, Fulvio (2008). “Complexity in biology: exceeding the limits of reductionism and determinism using complexity theory”. In: *EMBO reports* 9.1, pp. 10–14. DOI: 10.1038/sj.embor.7401147 (cit. on pp. 2, 4, 5).
- McKinney, Wes et al. (2010). “Data structures for statistical computing in python”. In: *Proceedings of the 9th Python in Science Conference*. Vol. 445. Austin, TX, pp. 51–56. DOI: 10.25080/Majora-92bf1922-00a (cit. on p. 134).
- Mondragón-Palomino, Octavio, Tal Danino, Jangir Selimkhanov, Lev Tsimring, and Jeff Hasty (2011). “Entrainment of a Population of Synthetic Genetic Oscillators”. In: *Science* 333.6047, pp. 1315–1319. DOI: 10.1126/science.1205369 (cit. on p. 16).
- Mongera, Alessandro, Payam Rowghanian, Hannah J Gustafson, et al. (2018). “A fluid-to-solid jamming transition underlies vertebrate body axis elongation”. In: *Nature* 561.7723, pp. 401–405. DOI: 10.1038/s41586-018-0479-2 (cit. on p. 5).
- Mönke, Gregor, Frieda A Sorgenfrei, Christoph Schmal, and Adrián E Granada (2020). “Optimal time frequency analysis for biological data-pyBOAT”. In: *bioRxiv*. DOI: 10.1101/2020.04.29.067744 (cit. on pp. 131–133).
- Morales, Aixa V, Yuko Yasuda, and David Ish-Horowicz (2002). “Periodic Lunatic fringe expression is controlled during segmentation by a cyclic transcriptional enhancer responsive to notch signaling”. In: *Developmental cell* 3.1, pp. 63–74. DOI: 10.1016/s1534-5807(02)00211-3 (cit. on pp. 32, 48, 107).
- Morelli, Luis G, Saúl Ares, Leah Herrgen, et al. (2009). “Delayed coupling theory of vertebrate segmentation”. In: *HFSP Journal* 3.1, pp. 55–66. DOI: 10.2976/1.3027088 (cit. on pp. 24, 47, 75, 79, 82).
- Morimoto, Mitsuru, Makoto Kiso, Nobuo Sasaki, and Yumiko Saga (2006). “Cooperative Mesp activity is required for normal somitogenesis along the anterior–posterior axis”. In: *Developmental Biology* 300.2, pp. 687–698. DOI: 10.1016/j.ydbio.2006.08.043 (cit. on p. 107).
- Morimoto, Mitsuru, Yu Takahashi, Maho Endo, and Yumiko Saga (2005). “The Mesp2 transcription factor establishes segmental borders by suppressing Notch activity”. In: *Nature* 435.7040, pp. 354–359. DOI: 10.1038/nature03591 (cit. on p. 68).
- Mrosovsky, N (1999). “Masking: History, Definitions, and Measurement”. In: *Chronobiology International* 16.4, pp. 415–429. DOI: 10.3109/07420529908998717 (cit. on p. 48).
- Murray, Philip J, Philip K Maini, and Ruth E Baker (2011). “The clock and wavefront model revisited”. In: *Journal of theoretical biology* 283.1, pp. 227–238 (cit. on p. 99).
- Nagai, Takeharu, Keiji Ibata, Eun Sun Park, et al. (2002). “A variant of yellow fluorescent protein with fast and efficient maturation for cell-biological applications”. In: *Nature biotechnology* 20.1, pp. 87–90. DOI: 10.1038/nbt0102-87 (cit. on pp. 26, 107).
- Naganathan, Sundar Ram, Marko Popovic, and Andrew C Oates (2020). “Somite deformations buffer imprecise segment lengths to ensure left-right symmetry”. In: *bioRxiv*. DOI: 10.1101/2020.08.14.251645 (cit. on pp. 97, 102).

- Nawrocki, Steffan T, Patrick Griffin, Kevin R Kelly, and Jennifer S Carew (2012). “MLN4924: a novel first-in-class inhibitor of NEDD8-activating enzyme for cancer therapy”. In: *Expert opinion on investigational drugs* 21.10, pp. 1563–1573. DOI: 10.1517/13543784.2012.707192 (cit. on p. 53).
- Neidhardt, Lorenz M, Andreas Kispert, and BG Herrmann (1997). “A mouse gene of the paired-related homeobox class expressed in the caudal somite compartment and in the developing vertebral column, kidney and nervous system”. In: *Development genes and evolution* 207.5, pp. 330–339. DOI: 10.1007/s004270050120 (cit. on pp. 92, 96).
- Nishimura, Kohei, Tatsuo Fukagawa, Haruhiko Takisawa, Tatsuo Kakimoto, and Masato Kanemaki (2009). “An auxin-based degron system for the rapid depletion of proteins in nonplant cells”. In: *Nature Methods* 6.12, pp. 917–922. DOI: 10.1038/nmeth.1401 (cit. on p. 50).
- Niwa, Yasutaka, Hiromi Shimojo, Akihiro Isomura, et al. (2011). “Different types of oscillations in Notch and Fgf signaling regulate the spatiotemporal periodicity of somitogenesis”. In: *Genes & Development* 25.11, pp. 1115–1120. DOI: 10.1101/gad.2035311 (cit. on p. 21).
- Oates, Andrew C (2020). “Waiting on the Fringe: cell autonomy and signaling delays in segmentation clocks”. In: *Current Opinion in Genetics & Development* 63, pp. 61–70. DOI: 10.1016/j.gde.2020.04.008 (cit. on p. 24).
- Oates, Andrew C, Luis G Morelli, and Saúl Ares (2012). “Patterning embryos with oscillations: structure, function and dynamics of the vertebrate segmentation clock”. In: *Development* 139.4, pp. 625–639. DOI: 10.1242/dev.063735 (cit. on pp. 16, 23, 48).
- Oginuma, Masayuki, Yu Takahashi, Satoshi Kitajima, et al. (2010). “The oscillation of Notch activation, but not its boundary, is required for somite border formation and rostral-caudal patterning within a somite”. In: *Development* 137.9, pp. 1515–1522. DOI: 10.1242/dev.044545 (cit. on p. 96).
- Okubo, Yusuke, Takeshi Sugawara, Natsumi Abe-Koduka, et al. (2012). “Lfng regulates the synchronized oscillation of the mouse segmentation clock via trans-repression of Notch signalling”. In: *Nature Communications* 3.1, p. 1141. DOI: 10.1038/ncomms2133 (cit. on p. 84).
- Packard, David S (1980). “Somite formation in cultured embryos of the snapping turtle, *Chelydra serpentina*”. In: *Development* 59.1, pp. 113–130 (cit. on p. 26).
- Palmeirim, Isabel, Domingos Henrique, David Ish-Horowicz, and Olivier Pourquié (1997). “Avian hairy Gene Expression Identifies a Molecular Clock Linked to Vertebrate Segmentation and Somitogenesis”. In: *Cell* 91.5, pp. 639–48. DOI: 10.1016/S0092-8674(00)80451-1 (cit. on pp. 1, 21, 99).
- Pechenkin, Alexander (2009). “On the origin of the Belousov-Zhabotinsky reaction”. In: *Biological Theory* 4.2, pp. 196–206. DOI: 10.1162/biot.2009.4.2.196 (cit. on p. 10).
- Phillips, Rob (2015). “Theory in biology: Figure 1 or Figure 7?” In: *Trends in cell biology* 25.12, pp. 723–729. DOI: 10.1016/j.tcb.2015.10.007 (cit. on p. 5).
- Pikovsky, Arkady, Michael Rosenblum, and Jürgen Kurths (2003). *Synchronization: a universal concept in nonlinear sciences*. Vol. 12. Cambridge university press. DOI: 10.1017/CB09780511755743 (cit. on pp. 7–9, 13, 34, 41, 52).

- Pittendrigh, Colin S (1961). “On temporal organization in living systems”. In: *Harvey lectures* 56, pp. 93–125 (cit. on p. 12).
- Pittendrigh, Colin S and Dorothea H Minis (1964). “The entrainment of circadian oscillations by light and their role as photoperiodic clocks”. In: *The American Naturalist* 98.902, pp. 261–294. DOI: 10.2307/2459454 (cit. on p. 12).
- Pittendrigh, Collin S and Victor G Bruce (1957). “An oscillator model for biological clocks”. In: *Rhythmic and synthetic processes in growth*, pp. 75–109. DOI: 10.1515/9781400876167-006 (cit. on pp. 12, 13, 38).
- Pittendrigh, CS, VG Bruce, NS Rosensweig, and ML Rubin (1959). “Growth patterns in *Neurospora*: a biological clock in *Neurospora*”. In: *Nature* 184.4681, pp. 169–170. DOI: 10.1038/184169a0 (cit. on p. 12).
- Politi, Antonio Z, Yin Cai, Nike Walther, et al. (2018). “Quantitative mapping of fluorescently tagged cellular proteins using FCS-calibrated four-dimensional imaging”. In: *Nature protocols* 13.6, pp. 1445–1464. DOI: 10.1038/nprot.2018.040 (cit. on p. 128).
- Postma, Marten and Joachim Goedhart (2019). “PlotsOfData—A web app for visualizing data together with their summaries”. In: *PLOS Biology* 17.3, e3000202. DOI: 10.1371/journal.pbio.3000202 (cit. on pp. 35, 36, 70–72, 91, 92, 132).
- Postnov, DE, AG Balanov, OV Sosnovtseva, and Erik Mosekilde (2001). “Transition to synchronized chaos via suppression of the natural dynamics”. In: *Physics Letters A* 283.3-4, pp. 195–200. DOI: 10.1016/S0375-9601(01)00238-9 (cit. on pp. 10, 54).
- Pourquié, Olivier (2011). “Vertebrate segmentation: from cyclic gene networks to scoliosis”. In: *Cell* 145.5, pp. 650–663. DOI: 10.1016/j.cell.2011.05.011 (cit. on p. 97).
- Prigogine, Ilya and René Lefever (1968). “Symmetry breaking instabilities in dissipative systems. II”. In: *The Journal of Chemical Physics* 48.4, pp. 1695–1700. DOI: 10.1063/1.1668896 (cit. on p. 10).
- Prigogine, Ilya and Grégoire Nicolis (1967). “On symmetry-breaking instabilities in dissipative systems”. In: *The Journal of Chemical Physics* 46.9, pp. 3542–3550. DOI: 10.1063/1.1841255 (cit. on p. 10).
- Remak, Robert (1855). *Untersuchungen über die Entwicklung der Wirbelthiere*. Vol. 1. Walter De Gruyter Incorporated (cit. on p. 18).
- Roenneberg, Till, Zdravko Dragovic, and Martha Merrow (2005). “Demasking biological oscillators: Properties and principles of entrainment exemplified by the *Neurospora* circadian clock”. In: *Proceedings of the National Academy of Sciences of the United States of America* 102.21, pp. 7742–7747. DOI: 10.1073/pnas.0501884102 (cit. on p. 48).
- Roenneberg, Till, Lena K Keller, Dorothee Fischer, et al. (2015). “Human activity and rest in situ”. In: *Methods in enzymology*. Vol. 552. Elsevier, pp. 257–283. DOI: 10.1016/bs.mie.2014.11.028 (cit. on p. 12).
- Rogers, Scott, Rodney Wells, and Martin Rechsteiner (1986). “Amino acid sequences common to rapidly degraded proteins: the PEST hypothesis”. In: *Science* 234.4774, pp. 364–368. DOI: 10.1126/science.2876518 (cit. on p. 107).
- Rémi, Jan, Martha Merrow, and Till Roenneberg (2010). “A Circadian Surface of Entrainment: Varying T, τ , and Photoperiod in *Neurospora crassa*”. In: *Journal of Biological Rhythms* 25.5, pp. 318–328. DOI: 10.1177/0748730410379081 (cit. on p. 13).

- Schindelin, Johannes, Ignacio Arganda-Carreras, Erwin Frise, et al. (2012). “Fiji: an open-source platform for biological-image analysis”. In: *Nature methods* 9.7, pp. 676–682. DOI: 10.1038/nmeth.2019 (cit. on p. 130).
- Scholtz, Gerhard and Wolfgang Dohle (1996). “Cell lineage and cell fate in crustacean embryos—a comparative approach.” In: *International Journal of Developmental Biology* 40.1, pp. 211–220 (cit. on p. 17).
- Seymour, Philip A., Caitlin A. Collin, Anuska I. R. Egeskov-Madsen, et al. (2019). “Jag1 modulates an oscillatory Dll1-Notch-Hes1 signaling module to coordinate growth and fate of pancreatic progenitors”. In: *bioRxiv*, p. 336529. DOI: 10.1101/336529 (cit. on p. 53).
- Sonnen, Katharina F. and Alexander Aulehla (2014). “Dynamic signal encoding—From cells to organisms”. In: *Seminars in Cell & Developmental Biology* 34, pp. 91–8. DOI: 10.1016/j.semcdb.2014.06.019 (cit. on pp. 26, 32, 44).
- Sonnen, Katharina F, Volker M Lauschke, Julia Uraji, et al. (2018). “Modulation of Phase Shift between Wnt and Notch Signaling Oscillations Controls Mesoderm Segmentation”. In: *Cell* 172.5, 1079–1090.e12. DOI: 10.1016/j.cell.2018.01.026 (cit. on pp. 21, 24, 26, 28, 29, 31, 32, 50, 72, 73, 75, 80, 87, 94, 97, 99, 100).
- Soza-Ried, Cristian, Emre Öztürk, David Ish-Horowicz, and Julian Lewis (2014). “Pulses of Notch activation synchronise oscillating somite cells and entrain the zebrafish segmentation clock”. In: *Development* 141.8, pp. 1780–1788. DOI: 10.1242/dev.102111 (cit. on pp. 24, 29, 47, 49, 56, 75).
- Tam, PPL (1981). “The control of somitogenesis in mouse embryos”. In: *Development* 65.Supplement, pp. 103–128 (cit. on p. 18).
- Tautz, Diethard (2004). “Segmentation”. In: *Developmental Cell* 7.3, pp. 301–312. DOI: 10.1016/j.devcel.2004.08.008 (cit. on p. 17).
- Trepast, Xavier and Erik Sahai (2018). “Mesoscale physical principles of collective cell organization”. In: *Nature Physics* 14.7, pp. 671–682. DOI: 10.1038/s41567-018-0194-9 (cit. on p. 5).
- Tsiairis, Charisios D and Alexander Aulehla (2016). “Self-Organization of Embryonic Genetic Oscillators into Spatiotemporal Wave Patterns”. In: *Cell* 164.4, pp. 656–667. DOI: 10.1016/j.cell.2016.01.028 (cit. on pp. 4, 24, 26, 28, 48, 49, 56, 75).
- Tyson, John J (1973). “Some further studies of nonlinear oscillations in chemical systems”. In: *The Journal of Chemical Physics* 58.9, pp. 3919–3930. DOI: 10.1063/1.1679748 (cit. on p. 10).
- van den Brink, Susanne C, Anna Alemany, Vincent van Batenburg, et al. (2020). “Single-cell and spatial transcriptomics reveal somitogenesis in gastruloids”. In: *Nature*, pp. 1–5. DOI: 10.1038/s41586-020-2024-3 (cit. on p. 26).
- van der Walt, Stéfan, S Chris Colbert, and Gael Varoquaux (2011). “The NumPy array: a structure for efficient numerical computation”. In: *Computing in science & engineering* 13.2, pp. 22–30. DOI: 10.1109/MCSE.2011.37 (cit. on p. 134).
- van der Walt, Stéfan, Johannes L Schönberger, Juan Nunez-Iglesias, et al. (2014). “scikit-image: image processing in Python”. In: *PeerJ* 2, e453. DOI: 10.7717/peerj.453 (cit. on p. 134).

- van Regenmortel, Marc HV (2004). “Reductionism and complexity in molecular biology: Scientists now have the tools to unravel biological complexity and overcome the limitations of reductionism”. In: *EMBO reports* 5.11, pp. 1016–1020. DOI: 10.1038/sj.embor.7400284 (cit. on p. 5).
- Vibe, Carina Beatrice (2021). “The temperature response of the medaka segmentation clock and its link to robustness in embryonic patterning”. PhD thesis. DOI: 10.11588/heidok.00028769 (cit. on p. 103).
- Virtanen, Pauli, Ralf Gommers, Travis E Oliphant, et al. (2020). “SciPy 1.0: fundamental algorithms for scientific computing in Python”. In: *Nature methods* 17.3, pp. 261–272. DOI: 10.1038/s41592-019-0686-2 (cit. on p. 134).
- Waddington, C.H. (1965). “Autogenous cellular periodicities as (a) temporal templates and (b) the basis of “morphogenetic fields””. In: *Journal of Theoretical Biology* 8.2, pp. 367–369. DOI: 10.1016/0022-5193(65)90084-6 (cit. on pp. 21, 24).
- Ward, Lizzy, Susan E Evans, and Claudio D Stern (2017). “A resegmentation-shift model for vertebral patterning”. In: *Journal of anatomy* 230.2, pp. 290–296. DOI: 10.1111/joa.12540 (cit. on p. 18).
- Waskom, Michael, Olga Botvinnik, Paul Hobson, et al. (Nov. 2014). *seaborn: v0.5.0 (November 2014)*. Version v0.5.0. DOI: 10.5281/zenodo.12710 (cit. on p. 134).
- Webb, Alexis B, Iván M Lengyel, David J Jörg, et al. (2016). “Persistence, period and precision of autonomous cellular oscillators from the zebrafish segmentation clock”. In: *eLife* 5, e08438. DOI: 10.7554/eLife.08438 (cit. on pp. 26, 48).
- Wilkinson, David G and M Angela Nieto (1993). “Detection of messenger RNA by in situ hybridization to tissue sections and whole mounts”. In: *Methods in enzymology* 225, pp. 361–373. DOI: 10.1016/0076-6879(93)25025-w (cit. on p. 110).
- Williams, Leonard W (1910). “The somites of the chick”. In: *American Journal of Anatomy* 11.1, pp. 55–100. DOI: 10.1002/aja.1000110103 (cit. on p. 18).
- Wilson, Paul A, George Oster, and R Keller (1989). “Cell rearrangement and segmentation in *Xenopus*: direct observation of cultured explants”. In: *Development* 105.1, pp. 155–166 (cit. on p. 26).
- Yamaguchi, Shun, Hiromi Isejima, Takuya Matsuo, et al. (2003). “Synchronization of cellular clocks in the suprachiasmatic nucleus”. In: *Science* 302.5649, pp. 1408–1412. DOI: 10.1126/science.1089287 (cit. on p. 14).
- Yan, Siyuan, Xiaoli Wei, Shanshan Xu, et al. (2017). “6-Phosphofructo-2-kinase/fructose-2, 6-bisphosphatase isoform 3 spatially mediates autophagy through the AMPK signaling pathway”. In: *Oncotarget* 8.46, p. 80909. DOI: 10.18632/oncotarget.20757 (cit. on pp. 104, 107).
- Yoshioka-Kobayashi, Kumiko, Marina Matsumiya, Yusuke Niino, et al. (2020). “Coupling delay controls synchronized oscillation in the segmentation clock”. In: *Nature* 580.7801, pp. 119–123. DOI: 10.1038/s41586-019-1882-z (cit. on pp. 24, 26, 47, 73, 75, 79, 82, 84, 107).
- Yu, Chang-I and Chih-Yen King (2019). “Forms and abundance of chaperone proteins influence yeast prion variant competition”. In: *Molecular microbiology* 111.3, pp. 798–810. DOI: 10.1111/mmi.14192 (cit. on p. 5).

- Zantke, Juliane, Tomoko Ishikawa-Fujiwara, Enrique Arboleda, et al. (2013). “Circadian and circalunar clock interactions in a marine annelid”. In: *Cell reports* 5.1, pp. 99–113. DOI: 10.1016/j.celrep.2013.08.031 (cit. on p. 16).
- Zhabotinsky, Anatoly M (1964). “Periodic liquid phase reactions”. In: *Proc. Acad. Sci. USSR*. Vol. 157, pp. 392–395 (cit. on p. 10).
- Zitterbart, Daniel P, Barbara Wienecke, James P Butler, and Ben Fabry (2011). “Coordinated movements prevent jamming in an emperor penguin huddle”. In: *PLoS one* 6.6, e20260. DOI: 10.1371/journal.pone.0020260 (cit. on p. 5).

List of Figures

1.1	Collective dynamics emerging in complex systems are ubiquitous in nature	3
1.2	First known documentation of synchronization, an odd kind of sympathy	7
1.3	Entrainment is the synchronization of an autonomous, endogenous oscillation to an external oscillation	9
1.4	Entrainment of an electrical circuit (i.e. LC oscillator) to periodically oscillating voltage	11
1.5	On detuning, entrainment phase, and human chronotypes	15
1.6	Somites lay out the segmented body plan of the mouse, a vertebrate . .	17
1.7	Early descriptions of somites in chick and rat embryos	18
1.8	Theoretical models for periodic tissue patterning during somitogenesis	20
1.9	The segmentation clock is an elaborate molecular network of oscillatory signaling pathways	22
1.10	Levels of organization in the presomitic mesoderm (PSM)	23
1.11	Spreadouts recapitulate key features of mouse somitogenesis	25
1.12	A microfluidics PDMS chip for culture, imaging, and entrainment of an ex vivo model of somitogenesis	27
3.1	A microfluidics-based experimental platform enables simultaneous visualization and entrainment of signaling oscillations in a spreadout, an ex vivo model of somitogenesis	33
3.2	Entrainment to periodic pulses of DAPT allows control of the period of the segmentation clock	35
3.3	Changing the concentration of DAPT, equivalent to changing entrainment strength, affects entrainment of the segmentation clock to periodic DAPT pulses	37
3.4	The segmentation clock is phase-locked to the periodic DAPT pulses . .	39
3.5	The entrainment phase varies according to the detuning between the free-running segmentation clock and the periodic DAPT pulses	42
3.6	The segmentation clock can be entrained to a higher order	43
3.7	An altered period gradient emerges upon entrainment of the segmentation clock to a slower period	45
3.8	A period gradient emerges even upon entrainment of the segmentation clock to periodic pulses of 2 μ M DAPT	46

4.1	The rhythm of the segmentation clock matches the rhythm of oscillations in the posterior PSM (i.e. the center of spreadouts) regardless whether the clock is sped up or slowed down	57
4.2	The phase of oscillations in the posterior PSM (i.e. the center of spreadouts) matches the phase of the segmentation clock	58
4.3	A higher (or lower) period gradient correlates with a higher (or lower) amplitude gradient	60
4.4	Oscillations at the posterior PSM (i.e. the center of spreadouts) have the lowest amplitude regardless whether segmentation clock is sped up or slowed down	61
4.5	The frequency gradient precedes the phase gradient in samples entrained to 130-min periodic pulses of 2 μ M DAPT	64
4.6	Entrainment of the segmentation clock results in a less steep phase gradient	65
4.7	A change in slope of the frequency gradient translates less to a corresponding change in slope of the phase gradient when the segmentation clock is entrained to periodic DAPT pulses	66
4.8	Entrained spreadouts undergo segmentation even with a flatter phase gradient than respective controls, with samples with slower segmentation clock starting to segment later	69
4.9	Increasing entrainment strength abolishes the period gradient and its consequent phase wave	71
4.10	Tissue-level oscillations of Wnt signaling are also entrained to periodic pulses of DAPT and are phase-shifted to entrained tissue-level oscillations of Notch signaling	74
4.11	Possible outcomes of the change in the slope of the period/frequency gradient in a sample with slow segmentation clock (compared to a sample with fast segmentation clock) during tissue segmentation in the absence of axial elongation (e.g. in spreadouts)	78
5.1	A microfluidics PDMS chip for culture, imaging, and entrainment of intact PSM.	89
5.2	Intact PSM of mouse embryos can be cultured inside PDMS chip for microfluidics-based entrainment.	90
5.3	Segmentation clock in intact PSM is entrained to periodic DAPT pulses	91
5.4	Segment polarity is preserved in somites formed from intact PSM subjected to microfluidics-based entrainment	93
5.5	A slower segmentation clock does not always result in a proportionally bigger somite	95
5.6	Possible effects of slowing down the segmentation clock on somite size	98
6.1	Wholemout in situ hybridization of E10.5 mouse embryos against Dnm2114	

6.2	Correlative live imaging and immunofluorescence of spreadout	119
6.3	Microfluidics PDMS devices for culture, imaging, and entrainment of embryonic tissue samples	123
6.4	Customized box to mount microfluidics device on microscope for simultaneous culture, entrainment, and live imaging	129
8.1	Timeseries acquired from global intensity analysis corresponds to the ticking of the segmentation clock	139
8.2	The period of the segmentation clock can both be sped up and slowed down by modulating the period of DAPT pulses	140
8.3	The period of the segmentation clock becomes locked to the period of the DAPT pulses	141
8.4	Changing the concentration of DAPT, equivalent to changing entrainment strength, affects entrainment of the segmentation clock to 130-min periodic DAPT pulses	142
8.5	The segmentation clock keeps its adjusted rhythm even a few cycles after release from DAPT pulses	143
8.6	The segmentation clock establishes a stable phase relationship with the periodic DAPT pulses.	144
8.7	A period gradient emerges in the tissue even after globally slowing down the period of the LuVeLu oscillations.	145
8.8	An altered period gradient emerges upon entrainment of the segmentation clock to a faster period	146
8.9	Detuning affects the entrainment phase of the segmentation clock . . .	147
8.10	The segmentation clock adjusts its rhythm to periodic pulses of MLN4924, a Notch signaling activator	148
8.11	The segmentation clock is phase-locked to periodic pulses of MLN4924, a Notch signaling activator	149
8.12	Oscillations at the posterior PSM (i.e. the center of spreadouts) have the lowest amplitude even when the segmentation clock is sped up . .	150
8.13	Oscillations at the posterior PSM (i.e. the center of spreadouts) have the lowest amplitude even when the segmentation clock is slowed down	151
8.14	The frequency gradient precedes the phase gradient in samples entrained to 170-min periodic pulses of 2 uM DAPT	152
8.15	The frequency gradient precedes the phase gradient in samples entrained to periodic pulses of 2 uM DAPT	153
8.16	Entrainment of the segmentation clock to periodic pulses of 2 uM DAPT results in altered slopes of the frequency and phase gradients	154
8.17	Spreadouts subjected to periodic pulses of 2 uM DAPT show physical segment boundaries with polarized expression of Mesp2	155
8.18	Tissue-level oscillations of Wnt signaling entrain to periodic pulses of DAPT later than tissue-level oscillations of Notch signaling	156

8.19	Oscillations locked to the periodic DAPT pulses are localized in region with high concentration of FGF	157
8.20	Intact PSM subjected to periodic pulses of 2 uM DAPT forms somites with polarized expression of Tbx18 and Uncx4.1	158
8.21	Segmentation clock in intact PSM adjusts to periodic perturbation of glycolytic flux	159
8.22	Phase and period of the segmentation clock in intact PSM is locked to the periodic perturbation of glycolytic flux	160

List of Tables

3.1	Summary statistics on period-locking of the segmentation clock in E10.5 spreadouts to periodic pulses of 2 μ M DAPT	36
4.1	Temporal derivative of slope of frequency gradient and of slope of phase gradient in spreadouts subjected to periodic pulses of 2 μ M DAPT (or DMSO for controls)	63
4.2	Slope of phase gradient in spreadouts subjected to periodic pulses of 2 μ M DAPT (or DMSO for controls)	70
4.3	Slope of the spatial phase gradient corresponding to waves/pulses of LuVeLu in spreadouts subjected to 130-min periodic pulses of DAPT (or DMSO for controls)	72
6.1	PCR program for genotyping	108
6.2	List of primers for genotyping mouse lines used in this study	108
6.3	List of expected PCR products for genotyping mouse lines used in this study	108
6.4	Recipe for media preparation	109
6.5	List of solutions for in situ hybridization	110
6.6	Components of in vitro transcription mixture for synthesis of digoxigenin-labeled RNA probes	111
6.7	TBST washes post-incubation with anti-DIG antibody	113
6.8	List of oligonucleotides used as probes against Tbx6 in HCR	116
6.9	List of oligonucleotides used as probes against Tbx18 in HCR	117
6.10	List of oligonucleotides used as probes against Uncx4.1 in HCR	118
6.11	List of antibodies used in this study	118
6.12	List of PTFE tubing needed for a microfluidics-based entrainment experiment	124
6.13	List of syringe containing drug/medium for a microfluidics-based entrainment experiment	125
6.14	Pumping program of medium for entrainment to 170-min periodic pulses of drug	127
6.15	Pumping program of drug/control for entrainment to 170-min periodic pulses of drug	128
6.16	Re-orientation of some spreadouts that were subjected to 130-min periodic pulses of 2 μ M DAPT (or DMSO control)	131

6.17 Re-orientation of some spreadouts that were subjected to 170-min
periodic pulses of 2 uM DAPT (or DMSO control) 131

Colophon

This thesis was typeset with $\text{\LaTeX}2_{\epsilon}$. It uses the *Clean Thesis* style developed by Ricardo Langner. The design of the *Clean Thesis* style is inspired by user guide documents from Apple Inc.

Download the *Clean Thesis* style at <http://cleanthesis.der-ric.de/>.

សំគាល់ ៥៣៦៤